JOURNAL OF APPLIED PHYSICS

JOURNAL
OF
APPLIED PHYSICS

Vol. 18, No. 8 AUGUST, 1947

In This Issue

Page

Infinite-Rejection Filters ALBERT M. STONE AND JAMES L. LAWSON 691

Theory of Automatic Control Systems M. AVRAMY MELVIN 704

Computation of the Solutions of $(1+2\epsilon\cos 2z)y''+\theta y=0$; Frequency Modulation Functions N. W. MCLACHLAN 723

Sensitized Luminescence of Manganese-Activated Calcite JAMES H. SCHULMAN, LYLE W. EVANS, ROBERT J. GINTHER, AND K. J. MURATA 732

Electron Beam Deflection. Part I. Small-Angle Deflection Theory R. G. E. HUTTER 740

Electrostatic Dischargers for Aircraft WAYNE C. HALL 759

Slow Transverse Magnetic Waves in Cylindrical Guides G. G. BRUCK AND E. R. WICHER 766

Incandescent Lamps as Electrical Load for Testing S. KEILIEN 769

Capacity per Unit Length and Characteristic Impedance of Coaxial Cables with One Slightly Non-Circular Conductor PHILIP PARZEN 774

Thermal Conductivity of Aluminum; Solid and Liquid States C. C. BIDWELL AND C. L. HOGAN 776

Letters to the Editor:

Stabilization, Tempering, and Relaxation in the Austenite-Martensite Transformation J. H. HOLLOMON, L. D. JAFFE, AND D. C. BUFFUM 780

Remarks on Compressive and Tensile Strengths STANLEY THOMPSON 781

Reply to "Remarks on Compressive and Tensile Strengths" P. W. BRIDGMAN 782

European Induction Accelerators ROLF WIDERÖE 783

Direction of Maximum Crystal Elongation during Metal Cutting G. H. TOWNEND 784

In Every Issue

Here and There 784

New Books 786

New Booklets 788

Index to Advertisers xxx

BOARD OF EDITORS

ELMER HUTCHISSON, *Editor*

Associate Editors

R. BOWLING BARNES
OTTO BEECK
W. F. BUSSE
SELIG HECHT
W. JAMES LYONS
PHILIP MORRISON
PAUL E. SABINE
FREDERICK SEITZ
J. R. TOWNSEND
JOHN VON NEUMANN

Publication of the American Institute of Physics

ADMINISTRATIVE STAFF

HENRY A. BARTON, *Director*

CLEVELAND NORCROSS, *Assistant Director*

RUTH F. BRYANS, *Publication Manager*

THEODORE VORBURGER, *Business Manager*

JOHN T. TATE, *Adviser on Publications*

GOVERNING BOARD

GEORGE R. HARRISON, *Chairman*

WALLACE WATERFALL, *Secretary*

GEORGE B. PEGRAM, *Treasurer*

E. U. CONDON
A. J. DEMPSTER
W. F. FAIR, JR.
FLOYD A. FIRESTONE
HARVEY FLETCHER
R. C. GIBBS
K. S. GIBSON
PAUL E. KLOPSTEG
A. H. PFUND
JOHN T. TATE
M. W. WHITE
A. G. WORTHING

The JOURNAL OF APPLIED PHYSICS, published monthly at Prince and Lemon Sts., Lancaster, Pa., is devoted to physics in its role as the science basic to other natural sciences and to the arts and industries. Previous to 1937 this publication was known as PHYSICS. The JOURNAL OF APPLIED PHYSICS publishes editorials, news of physicists, and reviews, as well as technical papers of applied physics.

Manuscripts should be submitted to Elmer Hutchisson, Editor, Case School of Applied Science, Cleveland 6, Ohio.

Subscriptions and orders for back numbers should be addressed to Prince and Lemon Streets, Lancaster, Pa. or to the American Institute of Physics, 57 East 55 Street, New York 22, N. Y.

Subscription Price

	U.S. AND CANADA	ELSEWHERE
To members and associate members of the American Institute of Physics	$6.00	$7.00
To all others	8.00	9.00

Back Number Prices

Complete set: Vol. 1, July, 1931–Vol. 17, 1946—$124.00
Yearly back number rate: $10.00
Single copies: $1.00 each.

Changes of address and proofs should be addressed to the Publications Manager.

Advertising rates supplied on request. Orders, advertising copy, and cuts should be sent to the American Institute of Physics.

Entered as second class matter January 22, 1937, at the Post Office at Lancaster, Pennsylvania, under the Act of March 3, 1879. Accepted for mailing at the special rate of postage provided for in the Act of February 28, 1925, authorized May 2, 1932.

Copyright 1947, by the American Institute of Physics.

Journal
of
Applied Physics

Volume 18, Number 8 August, 1947

Infinite-Rejection Filters

ALBERT M. STONE AND JAMES L. LAWSON
Radiation Laboratory, Massachusetts Institute of Technology, Cambridge, Massachusetts*
(Received May 20, 1946)

The characteristics of certain bridged-T filter structures have been investigated theoretically and an experimental confirmation of this theory at u.h.f. has been obtained. In theory it is possible to obtain infinite attenuation at a designated frequency, while retaining essentially the same band width as that for the uncompensated filter. A model has been constructed which has a band width of ½ Mc/sec. at 3000 Mc/sec. with an attenuation at center frequency of over 70 db. This is to be compared with the attenuation from a similar uncompensated filter of 20 db. Certain other known filter expressions have also been reduced to forms readily utilizable at these frequencies. Their utility for u.h.f. applications is discussed. The distortion produced in otherwise rectangular pulses of short duration has been investigated both theoretically and experimentally. Curves are presented which show the resultant wave form as a function of the tuning of the filter.

I. INTRODUCTION

IT has been known for some time that a parallel-resonant filter of the bridged-T structure may be designed for complete (i.e., infinite) rejection of the frequency to which it is tuned. This infinite rejection is obtained regardless of the finite Q of the coils and condensers of the filter and is limited solely by one's skill in adjusting a single resistive element.[1] At the same time as long as the ratio of unloaded[2] Q to loaded Q (*viz.*, line loading plus external resistance loading) is large compared with unity, the band width, measured between the points where the power transmitted is 3 db below the off-resonance value, is virtually indistinguishable from that of the normal (i.e., finite rejection) filter consisting of the tuned circuit alone. The principal object of this article is to present these results in readily usable form for u.h.f. work and to point out some salient features hitherto unstressed.

The applications of infinite-rejection filters are as varied as ingenuity affords. The particular problem which prompted the present analysis was that of eliminating an interfering c-w (or low-frequency modulated) carrier without, at the same time, destroying the usefulness of a pulsed 10-cm radar system. The analysis, therefore, is divided into two parts: (1) an investigation of the criteria for infinite rejection at microwave frequencies, and (2) an investigation of the distortion produced in rectangular pulses by such filters.

* This paper is based on work done for the Office of Scientific Research and Development under Contract OEMsr-262 with the Massachusetts Institute of Technology.

[1] W. N. Tuttle, Proc. I.R.E. **28**, 23, 1940; H. W. Bode, U. S. Patent No. 2,002,216 (1933).

[2] The Q of a bandpass circuit will be defined as the ratio of the center frequency to the band width. For a simple circuit such as the single-tuned type, $Q = L\omega_0/r$, where r is the series resistance, L the inductance, and ω_0 the resonant radian frequency.

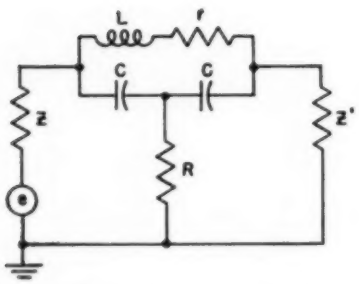

FIG. 1. Schematic diagram of an infinite-rejection filter with tap between condensers.

The essential modification of the ordinary filter consists of a tap from the center of the coil or condenser arm to ground (see Fig. 1) through a resistance R. (There may be reactance in this arm as well; it has been disregarded, however, as it merely complicates matters and leads to nothing fundamentally new.) It will be shown in Section II that a proper choice of R (see Fig. 1) can be made so that *no* power is passed from the generator to the load at the resonant frequency. In fact the resistance required is $R=(rQ_0^2)/4$, where Q_0 is the unloaded Q of the circuit, defined as $L\omega_0/r$, ω_0 is the resonant radian frequency, and the other symbols have conventional meanings. It is immaterial whether the coil or the condenser is center-tapped. However, if the circuit is considered to be an L, R'', C all in parallel, a center tap on the resistance R'' brought to ground through R will not achieve the desired result. Physically this must be so, for at resonance the parallel L, R'', C circuit is merely R''. A circuit of this type obviously cannot attenuate completely (see Fig. 2).

In the third section an alternative method of accomplishing this same result will be presented which, however, can be shown to be precisely equivalent to the methods mentioned above. The application of these results to *i-f* and video frequencies will appear obvious. Several possible methods for obtaining infinite-rejection u.h.f. filters will be discussed in this section and some experimentally obtained results will be presented.

Finally, in Section IV the results of an analysis of the pulse distortion produced by such a filter will be presented.

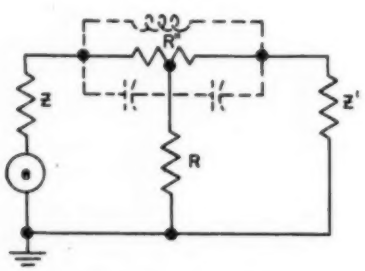

FIG. 2. Modification of Fig. 1 not leading to infinite rejection.

II. CIRCUIT ANALYSIS

The circuit of Fig. 1 is in the form of a bridged-T section with the capacitance tapped and hence can be developed by the usual methods of circuit analysis[3] into the symmetrical-lattice form, Fig. 3. This lattice is precisely equivalent to the bridged-T, having the same poles and zeros and the same frequency behavior. For simplicity the generator and its internal impedance (or the line impedance if we consider the generator matched to the line) and the load have been split off. The dotted lines signify repetition of the corresponding elements. It is not difficult to see that the symmetrical lattice is nothing more nor less than the usual four-arm bridge, as shown in Fig. 4, where Z_a is the series element and Z_b is the shunt element of the lattice. Now from this it is easy to picture physically why the circuit of Fig. 1 gives infinite rejection. To balance the bridge one tunes the resonant circuit as is customary, and then, by adjusting R, a condition of zero load current is obtained. In such a state the power that would normally pass on to the load is absorbed in the added resistance. This condition of balance is, obviously, the one that makes $Z_b=Z_a$. It is unnecessary to carry this calculation out in detail. The result may be

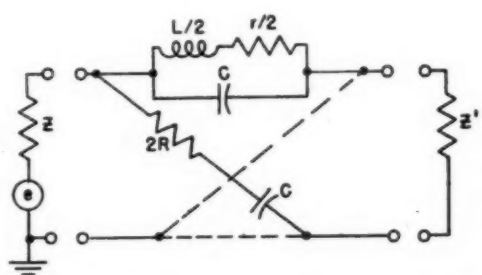

FIG. 3. Lattice development of infinite-rejection filter.

[3] E. A. Guillemin, *Communication Networks* (John Wiley and Sons, New York, 1935), Vol. 2, Chap. IV.

stated; the bridge is balanced when

$$\omega_0^2 = 2/LC, \tag{1}$$

and, simultaneously,

$$R = (rQ_0^2)/4. \tag{2}$$

Equation (1) states that the tuning of the circuit is independent of the added shunt element (but this is only true if it is non-reactive). Equation (2) gives the added condition that increases the maximum attenuation in the resonance curve indefinitely. It is clear that, for the ordinary values of Q_0 met in high frequency and u.h.f. work, R is easily realizable physically. If the two capacitances in Fig. 1 are unequal, the same conditions (1) and (2) hold, but $C/2$ is now the series sum of the two.

The case of the tapped coil leads to results which are expressed precisely by Eq. (1) and Eq. (2). (Compare Fig. 5 and Fig. 1.) The symmetrical-lattice development of the tapped-coil circuit is shown in Fig. 6. If the two half-coils are identical, the value of L to be used in Eq. (1) is

$$L = 2L_1 + 2kL_1, \tag{3}$$

where L_1 is the self-inductance of the half-coil, and k is the coefficient of coupling. (This choice of identical coils is not an essential restriction but leads to facility in computation.)

It is desirable for ease of discussion, once the criterion for infinite rejection has been established, to compute the actual output power

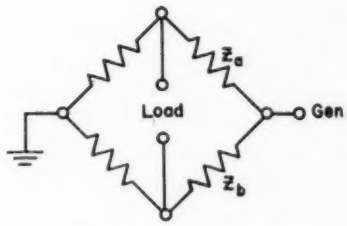

FIG. 4. Circuit equivalent to Fig. 3.

passed by the filter as a function of frequency; or, rather, to compute the dimensionless fraction, the output power divided by the output power in the absence of the filter. The latter output power is simply $e^2/4Z$, if it is assumed that load and line are matched and that e represents the generator voltage. It is sufficient to consider only the circuit of Fig. 1. Let i_L be the output current. We form the dimensionless quantity F by

$$F = \frac{4|i_L|^2Z^2}{e^2}. \tag{4}$$

We are not interested in any phase factor since the output of the filter usually is applied to the grid of a tube. The following definition is introduced:

$$\omega/\omega_0 \equiv m = \frac{\omega(LC)^{\frac{1}{2}}}{2}.$$

Then, with the previous definition of Q_0 and the balance condition, Eq. (2), one arrives at

$$F = \frac{4Z^2R^2[m^2Q_0^2(m^2-1)^2+(1-m^2)^2]}{(2R+Z)^2\left[mZQ_0(m^2-1)-\frac{4mR}{Q_0}\right]^2+\left[2RZ+\frac{4R^2}{Q_0^2}-m^2(Z^2+6RZ+4R^2)\right]^2}. \tag{5}$$

In simplifying this expression it is convenient to introduce the further definition

$$R \equiv \beta Z/4. \tag{6}$$

Thus β is the *standing-wave ratio at resonance looking toward the unbalanced filter terminating*

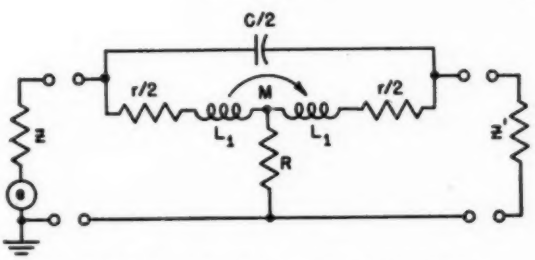

FIG. 5. Infinite-rejection filter with tapped coil.

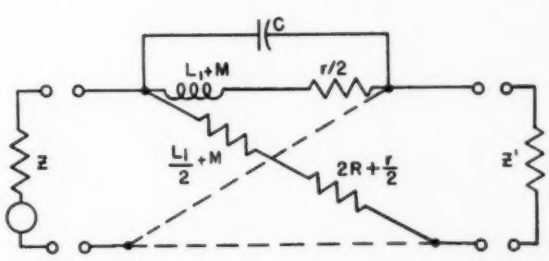

FIG. 6. Lattice development of Fig. 5.

the line.[4] (In this connection use is made of the fact that, for a reasonably high-Q filter, $L\omega_0/r = R'/L\omega_0$, where R' is the equivalent shunt resistance.) If terms in $1/Q^4$ and higher powers in the denominator of Eq. (5) are neglected, that equation can be written

$$F \cong \left[\frac{\beta}{\beta+2}\right]^2 \left[\frac{m^2(1-m^2)^2}{m^2(1-m^2)^2+\left(\frac{\beta+2}{2Q_0}\right)^2}\right]. \quad (7)$$

For most practical purposes $m=1$ very closely. Hence Eq. (7) becomes

$$F \cong \left[\frac{\beta}{\beta+2}\right]^2 \frac{(1-m^2)^2}{(1-m^2)^2+\left[\frac{\beta+2}{2Q_0}\right]^2}. \quad (8)$$

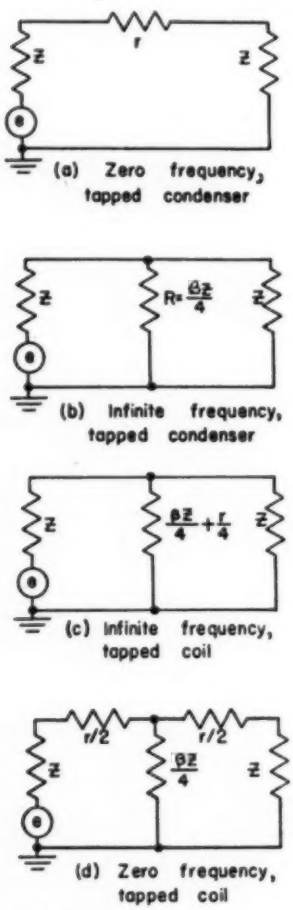

FIG. 7. Limiting cases of Figs. 1 and 5.

[4] The standing-wave ratio is the ratio of the sum of the incident and reflected wave peak amplitudes to their difference.

In the region far from resonance, the limiting value of F, from Eq. (5), is

$$F_\infty = \left[\frac{\beta}{\beta+2}\right]^2 \quad (9)$$

for high frequencies; and

$$F_0 = 1 \quad (10)$$

at low frequencies. The curve is symmetrical if $\beta \gg 2$ and $r \ll Z$, a condition which is usually realized in practice. (The value of β is often of the order of 10, Q_0 is often several hundred, and Z/r is often 2000 or more.) These limiting cases can be seen from simple reasoning. At zero frequency, the circuit of Fig. 1 becomes that of Fig. 7a. Here it is clear that

$$F = \frac{1}{\left(1+\frac{r}{2Z}\right)^2} \cong 1.$$

For very high frequencies, the circuit of Fig. 1 is similar to that of Fig. 7b, and it is again obvious that

$$F = \left[\frac{\beta}{\beta+2}\right]^2$$

as found above.

If, as in Fig. 5, the inductance is center-tapped to ground, the behavior is slightly different except near resonance. For very high frequencies, the circuit equivalent to Fig. 5 is that of Fig. 7c and

$$F_\infty = \left[\frac{\beta}{\beta+2}\right]^2.$$

For low frequencies, the circuit is that of Fig. 7d and likewise

$$F_0 = \left[\frac{\beta}{\beta+2}\right]^2.$$

Thus there is a slight difference in the low and high frequency behavior of the two cases, i.e., tapped coil or condenser, which disappears when β is large. (This difference is more apparent than real, for it arises solely because all the losses have been considered to be connected with the coil and none with the condenser.)

It is interesting to compare the expression (8) for F with that for the *unbalanced* network (R infinite). Details will be omitted. The result is, with β preserving the previously assigned meaning and value,

$$F' = \frac{4[Q_0^2(1-m^2)^2+m^2]}{4Q_0^2(1-m^2)^2+m^2(\beta+2)^2}. \tag{11}$$

Equation (8) reduces to Eq. (11) in the limit of large β as it must, i.e., when the equivalent shunt resistance of the resonant circuit is very large. However, F' approaches unity at both very high and very low frequencies and thus is symmetrical about $m=1$.

The band width of the infinite-rejection, or balanced, filter may be defined as the difference in the two frequencies where F has half its value at infinite frequency. From Eq. (8) this requires that

$$\frac{(1-m^2)^2}{(1-m^2)^2+\left[\dfrac{\beta+2}{2Q_0}\right]^2} = \tfrac{1}{2}. \tag{12}$$

The term $(1-m^2)$ can be replaced closely by $2\delta m$, where δm is the shift of frequency from the $(m=1)$-value. Thus Eq. (12) becomes

$$\delta m = \pm(\beta+2)/4Q_0,$$

and the band width at the half-power, or 3-db-down, point is thus

$$B = \frac{\beta+2}{2Q_0} f_0 \text{ cycles/sec.}, \tag{13}$$

where B is the band width and $\omega_0 = 2\pi f_0$.

For the unbalanced filter in this notation the band width is given simply by

$$B' = \frac{[(\beta+2)^2-8]^{\frac{1}{2}}}{2Q_0} f_0 \text{ cycles/sec.} \tag{14}$$

and hence reduces to Eq. (13) for large values of β. A sketch of the antiresonance behavior of the balanced and unbalanced filter is given in Fig. 8. In this figure the minimum in the unbalanced filter curve is given by Eq. (11) while, of course, for the balanced case,

$$F_{res} = 0. \tag{15}$$

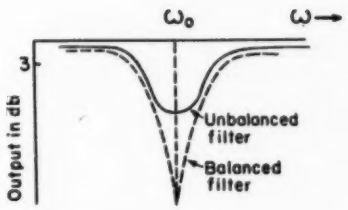

FIG. 8. Schematic behavior of antiresonance curve.

If one defines

$$\gamma \equiv Q_0/Q_L, \tag{16}$$

where Q_L is the loaded Q of the circuit (because of line loading and external resistance loading) γ can be related to β by

$$\frac{\beta+2}{2} = \gamma. \tag{17}$$

The value of the loaded Q of the unbalanced filter at resonance may be seen almost from inspection of Fig. 9. The quantity Q_0 is defined as $Q_0 \equiv \beta Z/L\omega_0$; Q_L is likewise defined as $R_1/L\omega_0$, where R_1 is the parallel resistance across the terminals of the inductance, i.e., $R_1 = 2\beta Z/(2+\beta)$. Hence:

$$\gamma \equiv Q_0/Q_L = (\beta+2)/2.$$

Now Eq. (11) may be rewritten at resonance as

$$F_{res}' = \left[\frac{2}{\beta+2}\right]^2 = \frac{1}{\gamma^2}, \tag{18}$$

which can be easily visualized. The depth of the attenuation cut taken by the filter depends only on the ratio of loaded to unloaded Q, and hence principally on the coefficient of coupling of the line to the filter. In principle, infinite attenuation at resonance could be obtained with the unbalanced filter by enormous coupling to the line. However, in such a case, the band width likewise

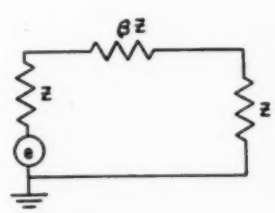

FIG. 9. Circuit for determining loaded Q.

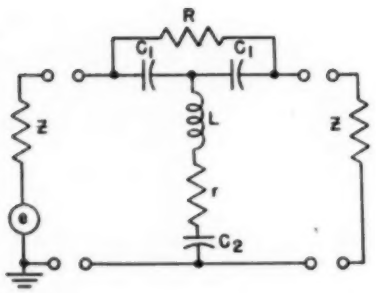

FIG. 10. Circuit equivalent to Fig. 5.

becomes enormous; for Eq. (14) may be written as

$$B' = \frac{f_0}{2Q_0}(\gamma^2-2)^{\frac{1}{2}} = \frac{f_0}{2Q_0}\left[\frac{1}{F_{res}'}-2\right]^{\frac{1}{2}}, \quad (19)$$

and as F' decreases B' increases.

In the case of the balanced circuit, while $F_{res}=0$, the band width however is still finite as found above in Eq. (13); *viz.*, in this notation,

$$B = \gamma f_0/2Q_0 = \frac{f_0}{2Q_L}, \quad (20)$$

and the attenuation at high frequencies, from Eq. (9), is

$$F_\infty = \left[\frac{\gamma-1}{\gamma}\right]^2. \quad (21)$$

It is interesting now to put in some figures for a possible u.h.f. application. Let the desired band width be ± 0.5 Mc/sec. at 3000 Mc/sec. Thus $Q_L=3000$. Let $Q_0=30{,}000$, and hence $\gamma=10$. Then, in this case, according to Eq. (21),

$$F_\infty = 0.81,$$

which represents an insertion loss of about 1 db and, of course, $F_{res}=0$. For the same filter unbalanced,

$$F_{res}' = 0.01,$$

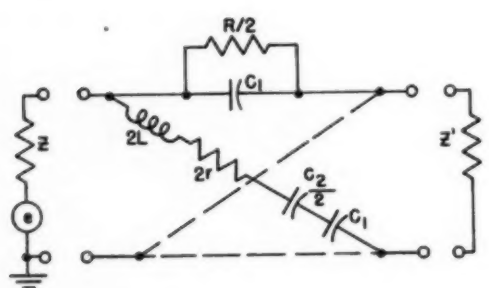

FIG. 11. Lattice development of Fig. 10.

and the band width would be ± 0.5 Mc/sec. within 1 percent for both filters.

The circuits of Fig. 1 and of Fig. 5, discussed in some detail in this section, by no means exhaust the possibilities of single-section infinite-rejection filters. In fact they are merely prototypes: variants can be obtained by standard transformation theorems. For example, the circuit of Fig. 10 is potentially equivalent to that of Fig. 5. From the symmetrical-lattice development in Fig. 11, it can be shown, with some manipulation, that the condition for infinite rejection is that

$$\omega_0^2 = \omega_2^2 + \frac{r}{R}\omega_1^2, \quad (22)$$

and

$$R/r = Q_0^2 n^2\left(\frac{n^2}{4}+m^2-1\right), \quad (23)$$

where

$$Q_0 = \frac{L\omega_0}{r}, \quad \omega_2^2 = \frac{1}{LC_2}, \quad \omega_1^2 = \frac{2}{LC},$$

$$n = \frac{\omega_2}{\omega_0}, \quad n = \frac{\omega_1}{\omega_0}.$$

The extension to the case where the capacitances C_1 are not equal is readily accomplished but leads to nothing essentially new.[5]

[5] Some interesting asymmetry properties are present in this filter. For instance, the possible values of R/r range from 4 to ∞; i.e., when $m=0$ the value of 4 obtains, and when $m=1$, $R/r \to \infty$ and $rn^2/R \to 0$. In the limiting case of small values of $n^2(C_1 \gg C_2)$, Eqs. (22) and (23) lead to

$$\omega_0^2 \leqq \omega_2^2, \quad (a)$$

$$R = 4r. \quad (b)$$

When n^2 becomes very large ($C_1 \ll C_2$), the limiting value of the frequency, again is

$$\omega_0^2 \leqq \omega_2^2, \quad (c)$$

but now we have

$$R = rQ_0^2 n^4/2 \quad (d)$$

and

$$\omega_1^2/\omega_0^2 \leqq (R/r)^{\frac{1}{2}}/Q_0. \quad (e)$$

(Cf. Eq. (d) and Eq. (2).) From Eqs. (d) and (c) it can be seen that the apparent pull of the resonant frequency from that of the shunt arm alone is somewhat illusory, despite Eq. (22). Thus one possible small advantage ensues. For a given value of R infinite rejection may be obtained by varying C_1, and, hence, n. If the frequency pulling (which is small as noted) is not serious, this may be a convenient method.

For reference, we write the expression for the fraction of the unfiltered energy transmitted by this balanced filter as a function of frequency.

$$F'' \leqq \frac{(f^2-1)^2 R/r}{\left[\frac{R}{4r}+\frac{R^2}{4}\right]\left[\frac{n^2(1+2r)^2}{4Rr}+\frac{4}{n^2}\left(f^2-m^2-\frac{n^2}{4}\right)^2\right]},$$

where $f=\omega/\omega_0$.

While the circuit of Fig. 10 may be better than that of Fig. 1 or Fig. 5 for some applications, it suffers from two defects: (1) six circuit elements are necessary *vs.* five in the former case, a defect of some importance in u.h.f. applications; (2) the frequency of infinite rejection only approximates the resonant frequency of the shunt resonant element, and each adjustment of R requires readjustment of ω_0. Furthermore, R cannot be readily visualized or calculated in terms of standing-wave ratios.

Finally, it should be mentioned that, for tuning the balanced filter of Fig. 1 over a comparatively narrow range of frequencies, it is desirable to change both L and C, although either one alone can be varied. The condition of balance, from Eq. (2), may be written as

$$R=\frac{\omega_0^2L^2}{4r}$$

and, if one eliminates ω_0^2 by noting that near resonance $\omega_0L\cong 2/C\omega_0$,

$$R\cong L/2rC. \tag{24}$$

Since r represents the losses in the tuned circuit, it is practically constant during the tuning, and hence the filter remains balanced with R fixed if L and C are changed together in such a way that their ratio stays constant. If, however, L alone is varied or C alone is varied as the frequency is varied, say by l percent or c percent, respectively, for a 1 percent change in ω_0, R must be changed by $(2+l)$ percent or $(1+c)/2$ percent, respectively. Depending on the method and difficulty of changing R, we can attempt to tune in one of the three ways.

III. APPLICATION TO u.h.f. FILTERS

In the previous section we found that a filter of unlimited attenuation could be realized practically, at least for cases where the circuit constants are lumped. The following question now arises: what modifications are necessary when one deals with corresponding distributed-parameter circuits, i.e., u.h.f. lines and u.h.f. resonant cavities? It turns out that this same analysis is applicable, for it is well known that a single-mode cavity resonator can be completely specified in terms of Q, ω_0, and R'' and, likewise, a u.h.f. line has a definite input impedance (usually real). The cavity resonator can be shunted across the line, or placed in series with one side of the line. In the latter case we have exactly the unbalanced filter of Fig. 1 or Fig. 5 discussed above. The only remaining question is how we can arrange the analogue of R, for there is no obvious condenser or inductance to be center-tapped.

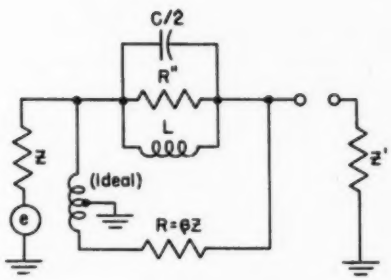

FIG. 12. Infinite-rejection filter in the form of a three-arm bridge.

Before proceeding to a discussion of the methods of realizing the balanced filter it is worth while to introduce still another circuit which can be shown to be precisely equivalent to the balanced filter.

Figure 12 shows essentially a three-arm bridge. Let us assume an ideal 1:1 (auto) transformer such that the impedances are infinite, and close coupled, so that the coefficient of coupling is unity. One is interested in the load current as a function of R and ω. This is given by

$$i_L=\frac{e\beta^2Z^2\left(1-\omega^2\frac{LC}{2}\right)}{Z(\beta+2)\left[2\beta Z^2\left(1-\omega^2\frac{LC}{2}\right)+j\omega LZ(\beta+2)\right]}, \tag{25}$$

where i_L is the load current and all other symbols have their previous meanings and R is taken

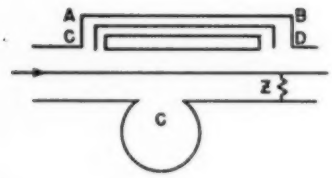

FIG. 13. u.h.f. realization of Fig. 12.

equal to R'', i.e., βZ. Again we form the fraction

$$F=\frac{4|i_L|^2Z^2}{e^2}$$

and find

$$F=\frac{4\beta^2(1-m^2)^2}{(\beta+2)^2\left[4(1-m^2)^2+\dfrac{(\beta+2)^2}{Q_0^2}m^2\right]}. \quad (26)$$

Remembering that m^2 is virtually unity, we note that Eq. (26) is identical with Eq. (8). Thus the attenuation for low frequencies is given by the ratio of β to $(\beta+2)$, just as was found before. The band width to the 3-db-down points therefore must be exactly the same. Hence it may be concluded that the bridge circuit is precisely equivalent to the balanced-filter circuit, even to the necessary loss of resonance.

This suggests at once a simple method to obtain the balanced-filter behavior at u.h.f. Consider the circuit of Fig. 13; C is a cavity which is equivalent to the lumped resonant circuit of Fig. 12. The power absorbed in the load Z is made up of two parts: one part comes directly through C to Z, the other through the branch line to Z. This latter suffers a 180° change of phase by making $\overline{AC}$ and $\overline{BD}$ each a quarter wave-length. Then the power through the branch path arrives at D with phase reversed from that of the power arriving directly. The amount of power bypassed is controlled by the probes in the stub lines. This circuit, as a little thought will show, is the u.h.f. analog of Fig. 12 and

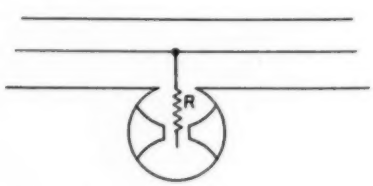

FIG. 14. u.h.f. analog of Fig. 1.

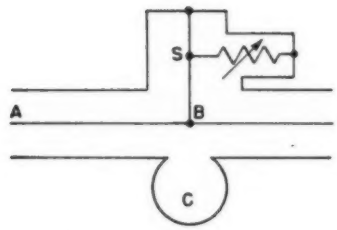

FIG. 15. Second u.h.f. analog of Fig. 1.

hence should possess its advantages. One device of this type has been constructed and will be discussed below.

Another application of these ideas to a u.h.f. filter is suggested by Fig. 1. Can this circuit be carried directly over to ultra high frequencies? Suppose one had a cavity as in Fig. 14. It is quite clear intuitively that by symmetry if a probe is placed midway between the interior posts of the cavity and connected by a resistor to the center conductor, i.e., ground, it is the complete analog of Fig. 1. However, this procedure is difficult experimentally. Alternatively we might connect R from ground, not to the center point between the posts, but to a point in the coupling window at the midpotential of the window. Thus we would be reasonably sure of obtaining again the analog of Fig. 5. Finally, we may incorporate this idea in a practical way as follows: C again is the cavity (Fig. 15), and A the center conductor of a coaxial line. This is stub-supported at the point B, symmetrically located with respect to the (symmetrical) cavity C. Now, if the stub center conductor S could be made lossy, with a real resistance between B and ground equal to $rQ_0^2/4$ (where r is the equivalent series loss of the cavity and Q_0 is the unloaded Q of the cavity), we would expect the balanced-filter results to apply. This can be achieved by coupling a real load to the stub cavity as shown. By adjusting

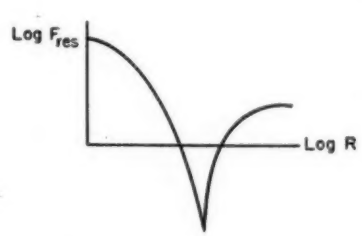

FIG. 16. Log F_{res} *vs.* log R.

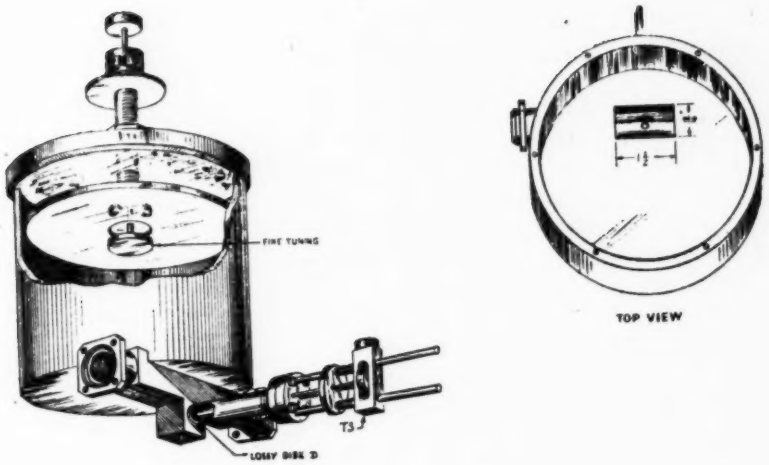

FIG. 17. Infinite-rejection filter.

the coupling, choosing the load properly, and placing it at the proper distance from the probe, any equivalent real value of impedance can be introduced into S, and the reactive part can effectively be absorbed in the cavity reactance. Thus, since B is essentially at the midpoint of the effective voltage across the cavity C, we can balance the filter by this adjustment and by tuning C. It should also be noted that there should be no "frequency-pulling" (to the extent that the added reactance at B is small) because the balanced filter and unbalanced filter have the same resonant frequency (see Fig. 8). Furthermore it is not essential that the voltage across the iris be completely symmetrical with respect to B. (Note discussion in first part of Section II.) A filter of this design has been constructed, and the data obtained from it will be presented below.[6]

A word should first be said, however, concerning how critical the tuning procedure can be. The sharpness of tuning as ω is varied can be seen from Fig. 8. In practice, however, this adjustment is usually not very difficult, for one may tune the cavity by stubs moving on fine threads in a region of weak field. The sharpness as R is varied can be calculated. The result is

$$F_{res}=\frac{4\left(1-\frac{4R}{\beta}\right)^2}{\frac{16}{Q^2}(R+1)^2+\left[(2R+1)\left(2+\frac{4}{\beta}\right)\right]^2} \quad (27)$$

[6] Acoustic applications of a filter of this type suggest themselves but will not be discussed here.

to the same degree of approximation as previously used.

It is noted that F_{res} becomes zero, as it should, for $R=\beta/4$. A logarithmic plot of F_{res} is given in Fig. 16. The adjustment of R is thus seen to be critical and, experimentally, needs a little care. (For the curve drawn, Q was assumed 3000 and $\beta=20$; then one can simplify further to obtain

$$F_{res}\cong\left[\frac{2\left(1-\frac{4R}{\beta}\right)}{[2R+1]\left[2+\frac{4}{\beta}\right]}\right]^2.)$$

For any particular cavity it is wise to choose the load and load position (or, failing this, to use the proper transformer) such that R at B is approximately the correct value to start with.

In order to retain full benefit of the infinite-rejection circuit, it is clear from Eq. (20) that the loaded Q should be high, and thus for large values of β, the unloaded Q must be very high. For a band width of 0.5 Mc/sec. at 3000 Mc/sec., a loaded Q of 6000 is needed, and clearly a cavity operating in the $TE_{0,1,1}$ mode[7] is indicated in order to obtain the necessary Q_0 of 30,000 or more so as to have a small loss off resonance (see Eq. 21). Conveniently enough, an "echo box" can be modified for this use.[8]

[7] See W. L. Barrow and W. W. Mieher, Proc. I.R.E. **28**, 184 (1940).

[8] The "echo box" is merely a high Q cavity. The ratio of stored to dissipated energy is so high that, once excited, the echo box will "ring" for a considerable time.

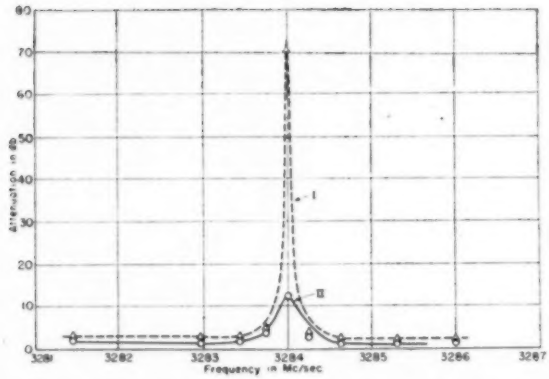

FIG. 18. Filter characteristics. Curve I, balanced filter; Curve II, unbalanced filter.

Although the tuning of the filter is exceedingly sharp for very high rejection ratios (cf. Figs. 8 and 16), and therefore the standard Radiation Laboratory echo box (1943) had to be eventually supplanted by a cavity of similar design but of $\frac{1}{4}$-in. steel plate for the sake of mechanical rigidity, the following results will be reported from a modified standard echo box. Figure 17 is a drawing of the cavity. The loss in the side stub is provided by the resistive disk D, whose resistance was adjusted by scraping to the (roughly) calculated value. Further adjustment was provided by the tuning stub TS which, if R_0 is the value of the resistance, makes the real impedance at B any value from 0 to R_0. Thus the resistance at A can be adjusted to the proper value. (The inevitable reactance introduced can be simply absorbed in that of the cavity.) Iris coupling to the $TE_{0,1,1}$ mode requires the rather peculiar off-set shown. With the filter coupled between the generator and receiver (through a standing-wave detector) by considerable lossy line, curves of filter output *vs.* frequency were obtained. These are shown in Fig. 18. Curve I is for the filter adjusted for infinite rejection; Curve II is for R considerably different from the correct value. It is seen that Curve II is the usual rejection-filter characteristic. Curve I is virtually identical with it at the half-power points and above, but increases the rejection ratio to very large values. The 70-db point was the last measured value and was limited by the receiver sensitivity. There is nothing to make one believe it could not be extended considerably further, although even at the 70-db point considerable difficulty is encountered merely in the frequency instability of the (klystron) signal generator. Table I summarizes the experimental measurements and compares them with the values computed from theory. It is clear that the agreement is satisfactory.

TABLE I. Comparison of theoretical and experimental results.

Design characteristics	Modified echo box		Cavity with center posts		Probe-type filter	
f_0 in Mc/sec.	3284		3160		3233	
β	5.78		16.8		2.7	
B' in Mc/sec.	0.5		14.7		1.04	
	Exp.	Theor.	Exp.	Theor.	Exp.	Theor.
γ	4.2	4.63	10	9.4	3.6	2.35
B/B'	1.02	1.05	1.14	1.01	1.15	1.21
Insertion loss in db	1.1	1.06	2.25*	1.0	6.1**	5
F_{res}/F_{res}' in db	60	∞	35	∞	11	∞

* There was an asymmetry in the resonance curve due to imperfect matching between line and load. This partly accounts for this discrepancy.
** Averaged over asymmetry.

A word might be said of two preliminary constructions. To check the theory, a cavity of the type sketched in Fig. 14 was constructed as a balanced filter. Figure 19 describes it, and Table I gives the experimental and theoretical results obtained with it. For cases where extreme sharpness is not required this filter is easy to make, easy to adjust, and easy to operate.

Finally, the u.h.f. analog of Fig. 12 has likewise been constructed from a modified echo box. This is shown in Fig. 20. Because of inability to couple properly by means of probes, the tabulated theoretical and experimental results shown in Table I are not in as good agreement as in the other two cases.

IV. PULSE DISTORTION PRODUCED BY FILTER

Although the results of investigations into the distortion introduced in an initially rectangular pulse emerging from a single-tuned filter (pass or rejection type) are probably well known for the case where the filter is tuned to the carrier frequency of the pulse, not as much information seems to be available for the case where the filter is not tuned precisely to the carrier.[3]

The mathematical expression for the transfer impedance of an infinite-rejection filter becomes too involved for tractability in Fourier analysis. Thus one is forced to idealize the actual problem. This can be done, however, with practically no modification of the actual state of affairs, for the

attenuation characteristic of an infinite-rejection filter very closely resembles that of a single-tuned circuit with a Q far too high to be realized experimentally. Thus the following is required of the single-tuned circuit: (1) it shall have the same band width as the infinite-rejection filter, and (2) it shall have the same attenuation at resonance. The correspondence in shape then follows automatically. The experimental filter described in Section III had a band width of 0.5 Mc/sec. at 3000 Mc/sec., with a loss off resonance of approximately 1 db. Let us take the attenuation at resonance as 60 db. Then the appropriate constants for the idealized filter are $Q_0=6\times10^6$ and $R=2000$, where Q_0, the unloaded Q of the filter, is defined by $Q_0=R/L\omega_0$. The term L is the equivalent lumped inductance of the filter, and R is the equivalent shunt resistance, measured in units of line impedance.

The system function, i.e., ratio of output to input voltage, is given by

$$h(\omega)=\frac{1+2j\dfrac{Q_0}{\omega_0}(\omega-\omega_0)}{2+R+4j\dfrac{Q_0}{\omega_0}(\omega-\omega_0)}. \qquad (28)$$

where $j\equiv(-1)^{\frac{1}{2}}$, and ω_0 is defined by

$$\omega_0^2\equiv\frac{1}{LC}.$$

Now, let e_1 be a rectangularly modulated sinusoidal carrier of radian frequency ω, with unit amplitude and pulse duration τ seconds.

Before we proceed to a mathematical formulation of the resulting output voltage e_2, we may describe the process in physical terms. The incoming pulse shock-excites the filter. The filter "rings" for the duration of the pulse at the frequency of the pulse, with a steady-state amplitude dependent on the resonance characteristic of the filter. To this steady-state value is added a transient oscillation decaying exponentially to zero at a rate determined by the Q and R of the filter. At the conclusion of the pulse, the steady oscillation disappears, and all that is left is the decaying term, but now to it is added a second decay term out of phase, initiated by the "shock" of returning the carrier level to zero. If, in addition, the filter is somewhat detuned from the carrier (of frequency ω_1) the decay terms, representing self-resonant transient oscillations, beat with the steady-state oscillations at a frequency equal to the difference between the two. Thus the resultant shape of the pulse is cooperatively determined by (a) the Q and R of the filter, and (b) the frequency difference $\Delta f=(\omega_0-\omega_1)/2\pi$ cycles/sec.

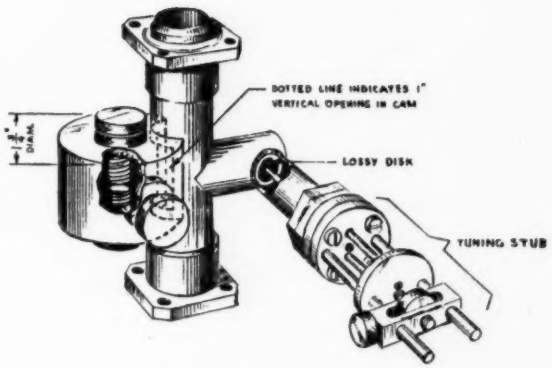

FIG. 19. u.h.f. filter.

Returning to a mathematical formulation of this result, we see that the function $e_2(t)$ can be obtained from $e_1(t)$ by a technique now fairly standard.[9] The Fourier spectral distribution of the unit pulse of duration τ is multiplied by $h(\omega)$, expanded into partial fractions, and reintegrated with respect to ω (with, of course, proper attention to the choice of path of integration in the complex plane). In short, there

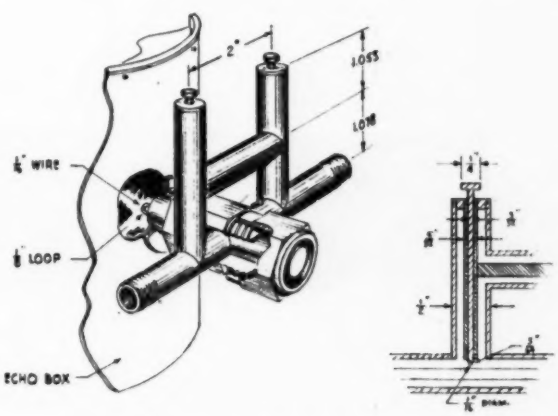

FIG. 20. Bridge-type filter.

[9] E. A. Guillemin, *Communication Networks* (John Wiley and Sons, New York, 1935), Vol 2, Chap. XI.

results

$$e_2(t)=\frac{\exp j\omega_1 t}{2+R+4j\dfrac{Q_0}{\omega_0}(\omega_1-\omega_0)}\left\{1+2j\frac{Q_0}{\omega_0}(\omega_1-\omega_0)+\frac{R}{2}\exp[j(\omega_0-\omega_1)t]\times\exp\left[-\omega_0 t\frac{R+2}{4Q_0}\right]\right\},\qquad 0\le t\le\tau;\quad(29)$$

$$e_2(t)=\frac{\dfrac{R}{2}\exp[j\omega_1 t]}{2+R+4j\dfrac{Q_0}{\omega_0}(\omega_1-\omega_0)}\left\{\exp[j(\omega_0-\omega_1)t\times\exp\left[-\omega_0 t\frac{R+2}{4Q_0}\right]-\exp\left[-\omega_0\frac{R+2}{4Q_0}(t-\tau)\right]\times\exp[j(\omega_0-\omega_1)(t-\tau)]\right\},\qquad \tau\le t\le\infty,\quad(30)$$

where, to repeat, ω_1 is the radian frequency of the carrier, ω_0 is the resonant radian frequency of the filter, and the factor multiplying $\exp[j\omega_1 t]$ is the resultant pulse shape.

Expressions (29) and (30) have been calculated for a 1-μsec. pulse and with differences of carrier frequency from filter frequency of 0, ±0.2, ±0.4, ±0.6, ±0.8, ±1, and ±1.5 Mc/sec. It is to be noted, of course, that the result is even in the difference frequency, as would be expected.

The final appearance of the pulse will depend strongly, of course, on further phase shifts, attenuation, and demodulation in the receiver. However, phase shift and attenuation can both be neglected in a well-constructed receiver (except possibly for a linear phase shift which merely shifts the origin of the pulse). A linear detector will have a video output, therefore proportional to $|e_2(t)|$ (disregarding the carrier frequency part). A square-law detector will have an output proportional to $|e_2(t)|^2$, and so on. The curves plotted from Eqs. (29) and (30) and shown in Fig. 21 are calculated from $|e_2(t)|^{\frac{3}{2}}$, i.e., for a three-halves power second detector.

The receiver on which measurements were made was carefully constructed, with an *i-f* band

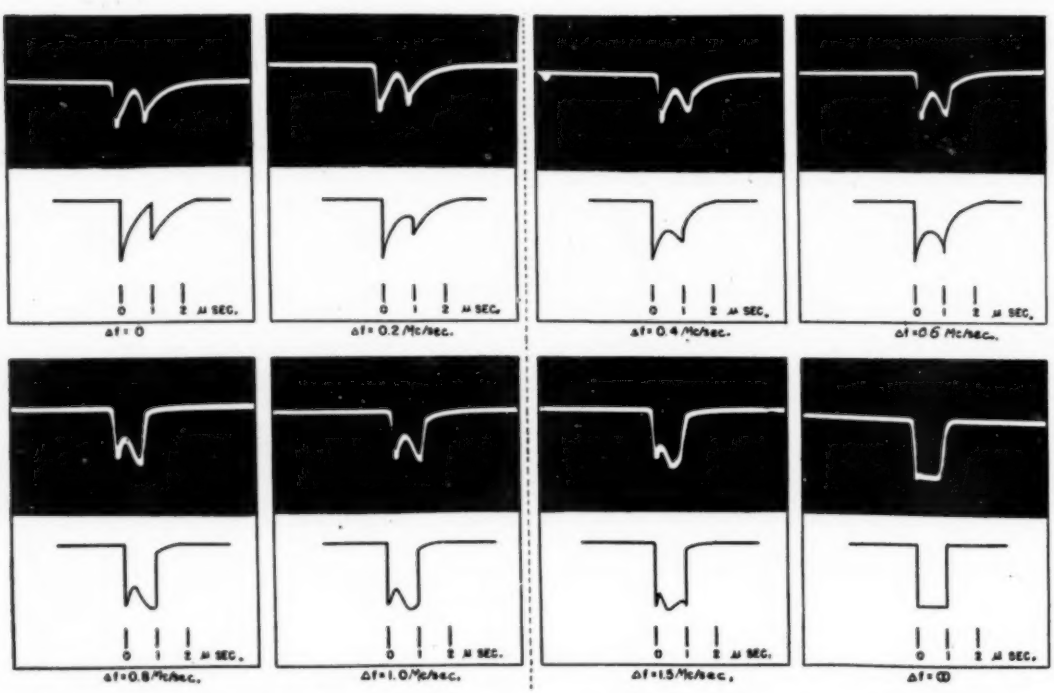

FIG. 21. Distortion produced in rectangular wave by a high Q rejection filter detuned from the pulse frequency by Δf Mc/sec.

width of some 13 Mc/sec. and a video band width of some 7 Mc/sec. The second detector was somewhere between linear and three-halves power law. One photograph reproduced in Fig. 21 shows the resultant rectangular wave form. The pulse was formed by driving the grid of a klystron amplifier (excited by a klystron oscillator) from cut-off to a conduction value. This resulted in a pulse virtually free from f-m. The output cavity of the amplifier was broadened in bandwidth by loading it externally. The other photographs carry self-evident explanations.

The agreement between experimentally determined and theoretically predicted curves is seen to be quite satisfactory, with the possible exception of the pulse for $\Delta f = 1.5$ Mc/sec., where $\Delta f \equiv (\omega_1 - \omega_0)/2\pi$. Such differences as remain can be accounted for by the lack of abruptness in the rise and fall of the pulse, somewhat inexact guesses as to Q_0 and R, and the slight difference in the law of the second detector assumed and that used. However, more accurate determination is hardly warranted.

It is clear that for small frequency differences the pulse is spread out to some two microseconds or so, with a more or less triangular shape, but in every case there is a fairly well defined discontinuity at $t = 1$ μsec. While the attenuation of the *center* frequencies in the pulse spectrum is essentially complete, enough energy remains to give respectable signals. One crude experiment showed a loss of about 2 db in the minimum discernible signal in receiver noise for a filter tuned so that $\Delta f = 0$. As $|\Delta f|$ increases, the depth of the cut in the pulse and the length of the tail decrease more or less uniformly until a case is reached where there is about one wiggle (due to the beat phenomenon mentioned above) across the top of the pulse ($\Delta f \cong 1$ Mc/sec.), then two wiggles with reduced amplitude, and so on. The explanation of the discrepancy between the theoretical and experimental curves for $\Delta f = 1.5$ Mc/sec. is probably that the difference frequency differs slightly from the nominal value. The larger Δf, the more phase change in the wiggles for a given error in frequency setting. The beats finally die out and a square pulse is regained when the filter is tuned far off resonance. It is therefore not hard to determine the tuning of the filter to a fairly considerable accuracy from the video appearance of a square pulse.

Theory of Automatic Control Systems*

M. Avramy Melvin
Columbia University, New York, New York

(Received June 7, 1946)

The theory of *robots* or reproducing power-amplifying systems is considered. After a general terminological orientation the study in the first part is confined to *simple robots*, the theory of which is equivalent to that of nonlinear springs with inertia and friction. The alacrity and fidelity of control are well exhibited by studying the behavior of a robot under constant tracking. Special emphasis is placed on the specification of conditions for *optimum performance*, i.e., minimum deviation or maximum fidelity after any given time. Curves are given for both proportional and on-off robots, from which the parameter values for optimum performance may be read.

In Part II the theory of proportional robots is analyzed in detail, especially from the point of view of conditions for optimum performance. Two subsequent papers will contain the theory for the on-off case and the general nonlinear robot case. The paper is organized as follows:

Part I. Descriptive account
- A. Terminology and kinematic description
- B. Dynamical equation of robots with usual load
- C. Optimum performance curves. Practical examples

Part II. Theory of simple robots with proportional control
- A. Complete solutions as functions of time. Optimum performance curves
- B. Path curves in the position-velocity plane

PART I. DESCRIPTIVE ACCOUNT

A. Terminology and Kinematic Description

A POWER ROBOT may be defined as a *reproducing power-amplifying system*. In other words the name refers to any automatic control system which reproduces the time variation of some quantity which is fed into it, but *with enormously amplified power*. Now, power (whether mechanical or electrical, see Glossary—Table I) is measured by a force-like quantity,** m, multiplied by the time variation of some position-like quantity, θ, i.e.,

$$\text{Power} = m\frac{d\theta}{dt} \equiv mv.$$

The robot may then be said to reproduce the time variation, v, of the position of some guide, θ_g, with an enormously increased m so that a heavy *load* may be made to follow. The manner in which this is accomplished is by having a delicate *pick-up* operate a *motor* which applies power to the load. The pick-up is so constructe l as to compare the position, θ_g, of the guide with θ of the load and apply a restoring force m' by

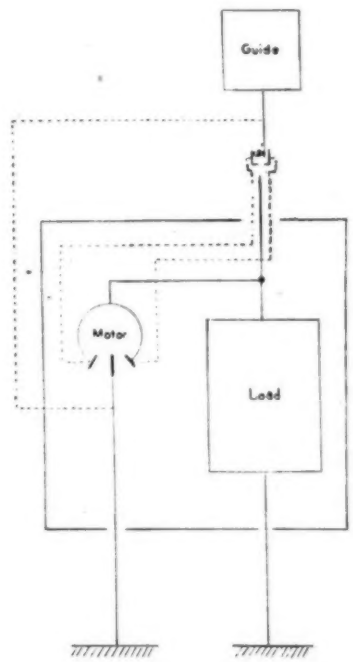

FIG. 1. Schematic diagram of a simple robot.

* This work was done in 1943–44 under Contract No. OEMsr-618 between Columbia University and the Office of Scientific Research and Development which assumes no responsibility for the accuracy of the statements contained herein. It was carried out with practically no reference to existing literature, which was, in any case, largely unavailable. Any deviations of terminology from that current among the workers in the field may be ascribed to this. It is hoped that the extensive glossary at the beginning will compensate somewhat for this deficiency. The terms used were carefully chosen with a view to suggestiveness, and some may recommend themselves to others.

** Apologies are here made for the notation, originally adopted in unpublished preceding reports for other reasons. It is to be noted that the theory is much more general than appears here, since m and θ may be any pair of conjugate physical quantities (original report). But, for simplicity, one may think of θ as a position variable (or angle) and of m as a force (or torque). The system then reproduces the motion or "tracking" of a *guide*, which is detected by the *pick-up* and applied *via* a *motor* to the *load* or controlled system.

means of the motor to reduce the magnitude of the difference, $D' = \theta_g - \theta$, between them. We shall call this difference the *output deviation*, and shall designate as a *simple robot* any system in which the operation of the pick-up is made to depend directly on this output deviation, D'. Other more general types, such as *transmission* robots, may be discussed in another paper.

A schematic diagram of a simple robot is given in Fig. 1. It will generally be arranged that all reaction of the controlled system back on the guide will be negligibly small. We shall further include in the specification of a simple robot the physically natural requirement:

m' is a single valued integrable function of D' in any finite domain. Let the phrase *apparent work* (i.e., as measured in the frame of reference moving with v_g) describe the integral $\int m' dD'$. We may then formulate the condition in words: *The apparent work done against the motor is finite in any finite deviation and is zero upon the completion of any closed cycle.*

In general one may write the equation of motion of a simple robot as

$$\boldsymbol{Z}[\theta] = m'(D'),$$

where $\boldsymbol{Z}$ is what we may call the "displacement operator" or "stiffness" of the load (usually involving differential operators) and m' is the restoring force function. In very many cases, including all those considered in this paper, the displacement operator is linear in θ and its derivatives (or integrals). Examples are translational inertia, rotational inertia about an axis, "1st power law" viscous resistance, magnetic damping, Hooke's law elastic stiffness, etc. In all such cases we may rewrite the equation of

TABLE I. Glossary and examples of terms used.

Symbol	Description	Translational motion	Rotational motion	Electric circuits	Dimensionless forms for usual load case
T	total time				$\mathbf{T} = BT/I.$ $\mathcal{T} = m_0 T/v_0 l$
t	time from beginning of a cycle				τ
θ	position-like variable	position	angle	work per unit current or time integrated voltage	$\phi = B^2\theta/m_0 l$
$v = d\theta/dt$	velocity-like variable	velocity	angular velocity	voltage	$\omega = Bv/m_0$
m	force-like variable	force	torque	current	$\mu = m/m_0$
I	inertance	mass	moment of inertia	capacitance	
$B = 1/R'$	friction coefficient $= \frac{1}{\text{respondance}}$	resisting force per unit velocity	torque per unit angular velocity	conductance $= \frac{1}{\text{resistance}}$	
$K = 1/I.'$	stiffness $= \frac{1}{\text{compliance}}$	elastic force per unit displacement	elastic torque per unit angle turned	inverse inductance	
g	as subscript indicates quantity associated with guide				
b	as subscript indicates quantity at beginning				
n	as subscript indicates quantity associated with n-th cycle if there is oscillation				
$n+\frac{1}{2}$	as subscript indicates quantity associated with second half of n-th cycle if there is oscillation				
∞	as subscript indicates quantity associated with steady state				
$D' = \theta_g - \theta$	total output deviation				$\Delta' = \frac{B^2}{m_0 l} D$
$D_i = \theta_g - \theta_i$	input deviation				Δ_i
D_{∞}'	mean steady state deviation from guide position				Δ_{∞}'
$D = D' - D_{\infty}'$	output deviation from steady state deviation = "deviation"				Δ
$\bar{D}_n$	maximum amplitude of deviation in n-th cycle				$\bar{\Delta}_n$
$V = v_g - v$	time rate of change of deviation				$\Omega = \frac{B}{m_0} V$
T''	time measured from the beginning of constant tracking				$\mathbf{T}'$
T_0'	interval between beginning of constant tracking and first vanishing of D				$\mathbf{T}_0'$
$T = T'' - T_0'$	time measured from first vanishing of D				$\mathbf{T}$
P_n	period of n-th cycle				π_n
$n(\bar{D})$	Number-Amplitude function giving number of cycles required for maximum amplitude to fall to $\bar{D}$				$n(\bar{\Delta})$
$\bar{D}(T)$	Amplitude-Time function giving maximum amplitude as a function of time				$\bar{\Delta}(\mathbf{T})$
$f = \frac{1}{P_n}\left(\frac{1}{\lvert V_n \rvert} + \frac{1}{\lvert V_{n+\frac{1}{2}} \rvert}\right)$	Fidelity Fraction: approximate fractional time per cycle spent within unit D interval about D_{∞}'				$f_{\Delta} = \frac{m_0 l}{B^2} f$
$B_{\min}$	optimum value of the friction coefficient for minimizing the deviation amplitude at any time				
$B_{\max}$	optimum value of the friction coefficient for maximizing the fidelity fraction at any time				

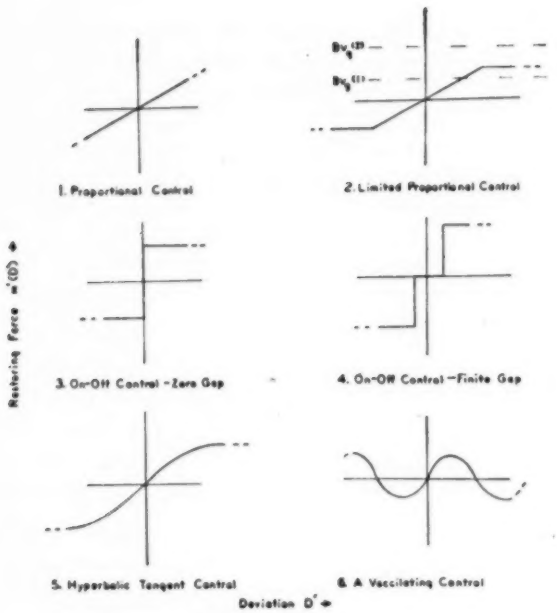

FIG. 2. Restoring force deviation graphs for various types of control.

motion in terms of D':

$$\boldsymbol{Z}[D'] = z(t) - m'(D')$$

where (I.01)

$$z(t) = \boldsymbol{Z}[\theta_g(t)]$$

is the result of operating with $\boldsymbol{Z}$ on the guide position as a function of time.

In general the pick-up is such that the restoring force (i.e., "cause") is not linearly proportional to the deviation ("effect"), so that the theory of robots will be in the domain of non-linear dynamics. The special linear case in which the pick-up does act to produce a restoring force proportional to the deviation is designated by the name of *proportional control*. It will be analyzed below so that it may serve as a standard of comparison for other, non-linear controls. The graphs of restoring force *versus* deviation for several types of control are given in Fig. 2.

A division which should be made from the point of view of a general theory is between *faithful* and *vacillating* (or faithless) robots as illustrated in Fig. 2. In a later paper[1] we shall give a precise and general definition of faithfulness, but tentatively we may indicate the distinction as follows: In a faithful robot the restoring force always acts so as to reduce the deviation, i.e., m is always positive for positive D. Not so for a vacillating robot, a type which may occur, for example, in rotating control systems where, if the deviation exceeds a certain value, a new guide (or the old one from the other side) takes over as the center of attraction and the old one is deserted. Certain theorems which may be proved, such as the approach in constant tracking of every simple robot to a steady state of zero oscillation, may be proved only for faithful robots. The others may vacillate throughout eternity.

In any case, the efficiency of a robot will be measured by the *fidelity with which the load is made to follow the guide*, i.e., by the smallness of the *time lag* and *oscillation* of the output deviation D' for changes in θ_g. The more ideal the control system, the smaller will these quantities be. It is one of our prime objectives not only to deduce the general description of the phenomena but also to determine what values of the parameters will minimize lag and oscillation.

There are two interesting special cases:

I. The amplification of power associated with an oscillatory motion.

II. The amplification of power in the case of constant tracking.

The first is the case in which the guide moves with a given oscillatory motion, and the problem is to determine what the amplitude, frequency, and phase of the output deviation are. This is a generalization of the problem of forced oscillations in linear mechanics and we shall not discuss it in this paper.

The second case is that in which, beginning at a certain time when the velocity of the load is v_b and the output deviation is D_b, the tracking velocity, v_g, of the guide becomes and remains constant. It is a generalization of the problem of free oscillations, or oscillations under a constant force, in linear mechanics. It is this *case of constant tracking* with which we shall primarily be concerned, for the fidelity of control of a robot is perhaps best brought out by studying its characteristics for this case (Fig. 3). After a certain time and number of cycles (finite or infinite) the system may attain a *steady state*. The steady state may be either one of no oscillation, i.e., perfect

[1] "Theory of damped non-linear oscillators with applications," referred to in the following as D.N.O.

following of the tracking motion, or of a steady oscillation with finite period and amplitude. The following or oscillation may be about the correct tracking motion or about a position lagging by a certain steady value behind the correct position. When it occurs, we shall denote this mean steady-state deviation from the guide position by the symbol D_x' (an explicit definition will be given later), and it will be convenient to separate it out from the total output deviation, so that we may write

$$D \equiv D' - D_x'.$$

Here then, D represents the deviation from the mean steady-state tracking position (Fig. 3). Since it is often relatively easy to correct for a steady space deviation like D_x', it is desirable to concentrate merely on minimizing the oscillation and time lag of D.

When there is oscillation it is often convenient to start counting time and number of cycles from the first time when $D=0$. Let the interval between the beginning of constant tracking and this first zero of D be represented by the symbol T_0' (Fig. 3) so that, if T' represents the time as measured from the beginning of constant tracking, we have

$$T = T' - T_0'.$$

When the general theory of a system for an arbitrary beginning time is worked out, T_0' may be determined by an auxiliary calculation. The advantage of this shift of the origin of time to the beginning of the first cycle is that it will often simplify the ensuing formulas by eliminating a phase-shift term. Sometimes T_0' is of interest for itself, in that a certain event for which the control is motivated in the first place is made to occur at that moment. Even in cases where steady permanent control is desired, it might be that the system could be brought immediately to the steady state at that moment by a suitable impulsive process.

If D does oscillate in time we may wish to analyze its variation in each cycle independently. In such circumstances it will be convenient to start the time scale anew at the beginning of each cycle. The time so measured within each cycle will be denoted by the symbol t.

Let us designate the maximum and minimum D in the n-th cycle (the *deviation amplitudes*) by $\bar{D}_n$ and D_n, respectively. Also let the period in the n-th cycle be represented by P_n. Upon inverting the expression for $\bar{D}_n$ as a function of n, one may arrive at the

number-amplitude function: $n(\bar{D})$

giving the number of cycles required for the maximum deviation to fall and remain below $\bar{D}$. The control characteristics of a system are per-

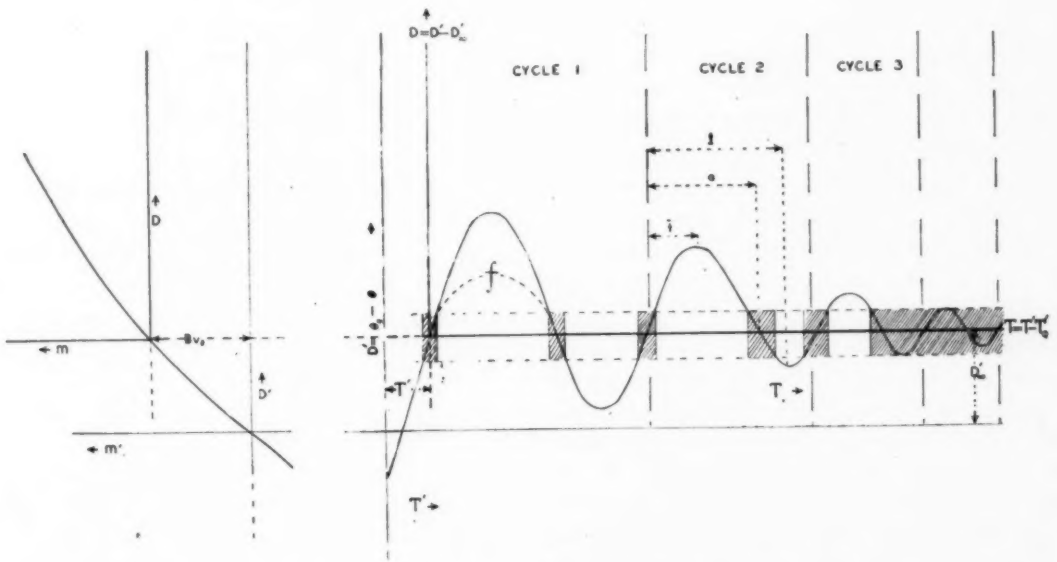

FIG. 3. Oscillations in a simple faithful robot under constant tracking.

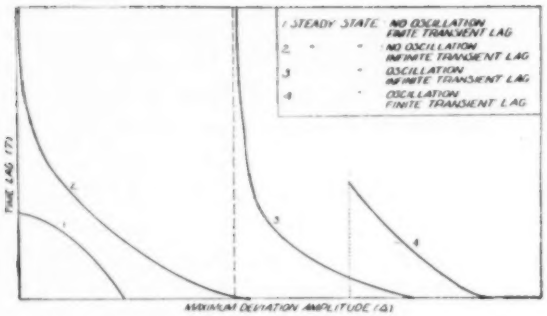
1 STEADY STATE NO OSCILLATION FINITE TRANSIENT LAG
2 " " NO OSCILLATION INFINITE TRANSIENT LAG
3 " " OSCILLATION INFINITE TRANSIENT LAG
4 " " OSCILLATION FINITE TRANSIENT LAG
TIME LAG (T)
MAXIMUM DEVIATION AMPLITUDE (D)

FIG. 4. Time lag *vs.* maximum deviation amplitude.

haps best exhibited by its

time-amplitude curves: $T(\bar{D}) = \sum_{n=0}^{n(\bar{D})-1} P_n$,

giving the time required up to the beginning of the cycle in which the maximum aplitude falls below $\bar{D}$. These may be plotted for various values of the relevant parameters.

The magnitude $\bar{D}_\infty$, after a steady state has been reached, will be finite or zero, depending on whether there is or is not a steady state of oscillation. The number of cycles and time required to reach the steady state exactly, which we designate

number of transient cycles: n_∞

and

transient lag, $T_\infty = \sum_{n=0}^{n_\infty-1} P_n$,

respectively, may be finite or infinite. Combining this with the possibility of zero or finite oscillation, we have the four main types of time-amplitude curves one may expect to encounter, sketched in Fig. 4. The functions should actually be represented as discrete, since the variables $\bar{D}$ and T take on discrete values but, for convenience, we have drawn smooth curves through the points.

Besides the $\bar{D}-T$ curves, which set upper limits to the deviations after any particular time, we may be concerned to know what fraction of the time of any cycle the system spends with a deviation in the interval dD between D and $D+dD$. In other words, we should like to know the "distribution function" for the probability of finding the system in the neighborhood of any given deviation about the mean tracking position. Since it is proportional to the time spent within unit interval about D, this distribution function is inversely proportional to the time rate of change of D at that point. Thus letting

$$V \equiv \partial D/\partial T,$$

and expressing it as a function $V(D)$ of D, we may write:

$$f(D)dD = \frac{1}{P}\left[\frac{1}{|V(D)|_R} + \frac{1}{|V(D)|_L}\right]dD,$$

where we have added together the time intervals for dD when the deviation is increasing and decreasing, respectively, since both contribute to the probability of finding the system in dD. division by the period P is merely to insure normalization, i.e.,

$$\int_{-D}^{D} f(D)dD = 1.$$

Because of the nature of oscillation (velocity zero at the amplitude limits) $f(D)$ will be of a general U-shape as sketched in Fig. 5. Now it is difficult to characterize this curve in a general way. For practical purposes, however, it will be of primary interest to know what fraction of the time of any cycle the system spends within any small interval in the *neighborhood* of the mean steady-state position, i.e., we wish to give *the value of the ordinate, f, of the distribution curve at the abscissa*, $D=0$. This we shall designate the *fidelity fraction*, since multiplying it by any small deviation interval ΔD about $D=0$ gives an approximation to the fractional time spent within that interval. Since the area under the total curve has been normalized to unity, it is clear that f is also represented by the shaded area in Fig. 5. An explicit formula for f in terms of the velocity V_n at the beginning of the n-th cycle and the velocity V at the time a of the return passage through zero D is

$$f = \frac{1}{P_n}\left(\frac{1}{|V_n|} + \frac{1}{|V(a)|}\right)^{***}$$

*** As pointed out by the referee, the quantity f here defined is more applicable to the first half of the cycle rather than to the total cycle. It is still, however, an approximate index of fidelity and may be taken as having certain advantages of simplicity. In any case, it had already been used in the treatment of the special cases given later.

B. Dynamical Equation of Robots with Usual Load

Thus far our considerations have been quite general. But it is convenient here to limit ourselves to the very important common case where the sluggishness of the load or controlled system is governed mainly by inertia and frictional resistance so that the equation of motion of the robot may be written

$$I\frac{dv}{dT'}+Bv=m'(D')$$

$$\left.\begin{aligned} v&=v_b \\ D'&=\theta_g-\theta_b \end{aligned}\right\}\text{at } T'=0, \tag{1.02}$$

where I is the inertia of the load and the B its frictional resistance per unit velocity and, as is the nature of the robot, the applied force m' is a function of the deviation D'. (In the case of a transmission robot, D' must be taken as representing the input deviation.) The subscript b in the initial condition equations represents the values of the indicated quantities at the beginning $T'=0$. In terms of θ, the differential equation may be written

$$I\frac{d^2\theta}{dT^2}+B\frac{d\theta}{dT}=m'(\theta_g-\theta)=m_0\mu'(\theta_g-\theta)$$

where we have taken out a constant *characteristic strength* factor m_0 (which may be defined conveniently in any particular type of system) and have left the functional dependence in the dimensionless restoring force function $\mu'(\theta_g-\theta)$.

Now, in developing the theory for this usual load case, it is convenient to choose new dimensionless measures of time, velocity, and force such that

$$\frac{m'}{m_0}\equiv\mu' \quad \frac{B}{I}T\equiv\mathrm{T} \quad \frac{B}{m_0}v\equiv\omega \quad \frac{B^2}{m_0 I}\theta\equiv\phi.$$

Therefore,

$$\frac{B}{I}t\equiv\tau \quad \frac{B}{m_0}V\equiv\omega_g-\omega\equiv\Omega \quad \frac{B^2}{m_0 I}D'\equiv\Delta' \tag{1.02'}$$

$$\frac{I}{m_0}\frac{dv}{dt}\equiv\frac{d\omega}{d\tau} \quad \text{etc.,}$$

where

$$\kappa\equiv m_0 I/B^2.$$

Thus we are measuring *all forces in fractions of the characteristic strength* and *all times in fractions of the time constant* of the load when slowing down freely under no applied load; and we are measuring *all velocities in fractions of the characteristic steady-state velocity of the load*, i.e., its motion against friction when the constant characteristic strength of the motor is applied steadily. With these notations the basic robot equation (1.02) takes the form

$$\frac{d^2\phi}{d\mathrm{T}'^2}+\frac{d\phi}{d\mathrm{T}'}=\mu'[\kappa(\phi_g-\phi)],$$

or if we express the equation in terms of

$$\Delta'=\phi_g-\phi$$

we get

$$\frac{d^2\Delta'}{d\mathrm{T}'^2}+\frac{d\Delta'}{d\mathrm{T}'}=\left(\frac{d^2}{d\mathrm{T}'^2}+\frac{d}{d\mathrm{T}'}\right)\phi_g-\mu'(\kappa\Delta').$$

This is the form which the fundamental operator equation (1.01) assumes in usual load systems.

If we confine ourselves to the case of constant tracking beginning at $\mathrm{T}'=0$,

$$\phi_g=\omega_g\mathrm{T}'$$

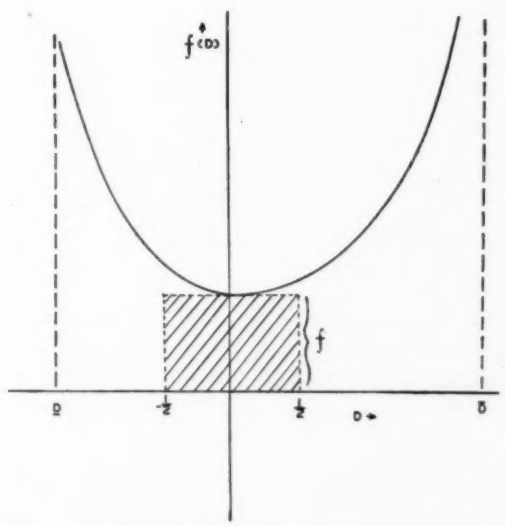

FIG. 5. Distribution function for probability of finding deviation in any neighborhood.

TABLE II. Steady-state deviations and modified force functions for various types of robots.

Type of control	Restoring force-deviation relation $\mu'(\Delta')$	Steady-state deviation Δ_s'	Modified restoring force function
Proportional	$\kappa\Delta'$	$\frac{\omega_g}{\kappa}$	$\kappa\Delta$
Quadratic	$\hat{\Delta}'(\kappa\Delta')^2$	$\hat{\omega}_g\frac{1}{\kappa}(\lvert\omega_g\rvert)^{\frac{1}{2}}$	$\pm\lvert\kappa\Delta\pm(\lvert\omega_g\rvert)^{\frac{1}{2}}\rvert^2-\omega_g \quad (\pm=\hat{\omega}_g)$
Cubic	$(\kappa\Delta')^3$	$\frac{1}{\kappa}\omega_g^{\frac{1}{3}}$	$(\kappa\Delta+\omega_g^{\frac{1}{3}})^3-\omega_g$
m-th power	$\hat{\Delta}'\lvert\kappa\Delta'\rvert^m$	$\hat{\omega}_g\frac{1}{\kappa}\lvert\omega_g\rvert^{1/m}$	$\pm\lvert\kappa\Delta\pm\lvert\omega_g\rvert^{1/m}\rvert^m-\omega_g \quad (\pm=\hat{\omega}_g)$
Exponential	$\hat{\Delta}'[e^{\kappa\lvert\Delta'\rvert}-1]$	$\hat{\omega}_g\frac{1}{\kappa}\ln[1+\lvert\omega_g\rvert]$	$\pm[e^{\lvert\kappa\Delta\pm\ln(1+\lvert\omega_g\rvert)\rvert}-(1+\lvert\omega_g\rvert)] \quad (\pm=\hat{\omega}_g)$
Hyperbolic sine	$\sinh(\kappa\Delta')$	$\frac{1}{\kappa}\sinh^{-1}\omega_g$	$\sinh(\kappa\Delta+\sinh^{-1}\omega_g)-\omega_g$
		$\lvert\omega_g\rvert<1$: $\quad\lvert\omega_g\rvert>1$:	
Hyperbolic tangent	$\tanh(\kappa\Delta')$	$\frac{1}{\kappa}\tanh^{-1}\omega_g$ or $\pm\infty$	$\tanh(\kappa\Delta+\tanh^{-1}\omega_g)-\omega_g$
On-off zero-gap		0 or $\pm\infty$	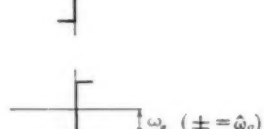 $(\pm=\hat{\omega}_g)$
On-off finite-gap		$\pm\delta$ or $\pm\infty$	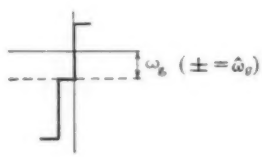 $(\pm=\hat{\omega}_g)$

$\hat{a}$ means "sign of a" or $\frac{a}{|a|}$

and we have:

$$\frac{d^2\Delta'}{d\mathrm{T}'^2}+\frac{d\Delta'}{d\mathrm{T}'}=\omega_g-\mu'(\kappa\Delta')\equiv-\mu$$

$$(\mu')\qquad \left.\begin{aligned}\Delta'&=-\phi_b\\ \frac{d\Delta'}{d\mathrm{T}'}&=\omega_g-\omega_b\equiv\Omega_b\end{aligned}\right\}\ \text{at } \mathrm{T}'=0, \tag{I.03}$$

where κ, ω_g, ϕ_b, ω_b, Ω_b are then constants calculable in terms of the given data, and where we have introduced the symbol

$$\mu\equiv\mu'-\omega_g$$

for the *modified force function*, i.e., the restoring force measured from the level ω_g instead of zero.

Now it is demonstrated in D.N.O.[1] that the final steady state in constant tracking of any faithful robot is one of zero oscillation, and consists of a constant steady deviation given by setting the right-hand side of the differential equation (I.03) equal to zero:

$$\omega_g-\mu'(\kappa\Delta')=0$$

or

$$\Delta_s'=\frac{1}{\kappa}\mu'^{-1}(\omega_g)$$

where μ'^{-1} is the inverse function corresponding to μ'. Applications of this result to various types of control are given in Table II. It is thus possible to simplify the system of equations of motion (I.03) by introducing the modified force function and expressing everything in terms of the modified deviation Δ:

$$\mu(\kappa\Delta)\equiv\mu'[\kappa\Delta']-\omega_g=\mu'[\kappa(\Delta+\Delta_s')]-\omega_g.$$

This shift of reference level of μ is illustrated in

Fig. 3. If Δ becomes zero at some finite time, T_0', before the steady state is reached, i.e., in case of at least one oscillation, it is possible to simplify the equations a little further. Introducing the modified force function, and measuring the time in terms of T from the first zero of Δ, we have:

$$\frac{d^2\Delta}{d\mathrm{T}^2}+\frac{d\Delta}{d\mathrm{T}}=-\mu(\kappa\Delta)$$

$$\left.\begin{aligned}\Delta&=0\\ \frac{d\Delta}{d\mathrm{T}}&=\omega_g-\omega_0\equiv\Omega_0\end{aligned}\right\}\text{at } \mathrm{T}=0, \tag{I.04}$$

where, if the solution to the problem for arbitrary beginning data is known, ω_0 or Ω_0 may be calculated readily. Conversely, if one has the solution for general values of Ω_0 as a parameter, one may determine the particular value required to fit the initial data

$$\Delta=-\phi_b-\Delta_\infty' \quad \Omega=\Omega_b \text{ at } \mathrm{T}=-\mathrm{T}_0'.$$

In general, if μ' is of any other functional form but linear, the differential equation is non-linear in that the right-hand side is a function of the *dependent* variable, and the solution of the system will require special devices in various cases. We shall discuss this question in D.N.O.[1] and in a subsequent paper[2], but for the present we confine ourselves to noting that, once the problem is solved, all the control characterizing concepts defined above may be found, translated, of course, in dimensionless terms. These are listed for reference in Table III. All these quantities generally depend, of course, on the parameters κ, ω_0, and ω_g as well as the indicated arguments.

The visualization of the motion is facilitated if it is represented on a diagram on which Ω is plotted as ordinate against Δ as abscissa. This gives the "path curve" in the "state plane" (or "phase space") of our damped non-linear oscillator. The differential equation governing the path of the representative point in the state plane follows from a simple rearrangement of (I.04)

$$\frac{d\Omega}{d\Delta}=-1-\frac{\mu(\kappa\Delta)}{\Omega} \tag{I.04'}$$

[2] "Theory of on-off and relay control systems," J. App. Phys. (To be published.)

with the same initial conditions. The time is now merely a parameter tracing the representative point as it moves along the path curve.

It will be shown in D.N.O.[1] that for every faithful robot the path curve is a continuous right-handed (clockwise) spiral closing in on the point Δ_∞' which lies on the Δ axis. This spiral may be bounded between two comparison spirals beginning at the same initial point and made up of successive pieces of linear oscillator spirals with certain frequencies which may be worked out in each case. In this way follow immediately criteria for oscillation and overdamping, and the possible existence of any finite number of oscillations in the transient state of non-linear oscillators. Upper and lower bounds to the number of oscillations and times required for the deviation to fall to any desired value may then be set.

C. Optimum Performance Curves

If after solving the constant tracking case as represented in (I.04) for any particular system, and finding for instance

$$\bar{\Delta}(\mathrm{T}, \kappa, \Omega_0, \omega_g)$$

and

$$f_\Delta(\mathrm{T}, \kappa, \Omega_0, \omega_g),$$

we return to the ordinary measures of time and

TABLE III. Control characterizing concepts translated in dimensionless terms.

Δ_∞'	mean steady-state deviation from guide position
Δ	deviation from mean steady-state deviation
T_0'	time when Δ first becomes zero after the beginning of constant tracking
$\bar{\Delta}_n$	maximum value of Δ in n-th cycle
$\underline{\Delta}_n$	minimum value of Δ in n-th cycle
π_n	period of oscillation in n-th cycle
$n(\bar{\Delta})$	number-amplitude function
$\bar{\Delta}(\mathrm{T})$	amplitude-time function
n_∞	number of transient cycles required to reach the steady state
T_∞	transient lag, i.e., time required to reach the steady state
$f_\Delta=\frac{1}{\pi_n}\left[\frac{1}{\lvert\Omega_n\rvert}+\frac{1}{\lvert\Omega(a)\rvert}\right]\equiv\kappa f$	fidelity fraction, i.e., approximate fractional time per cycle spent within unit Δ interval about steady-state deviation

position, we may write

$$(D)\quad \bar{D}=\frac{m_0 I}{B^2}\bar{\Delta}\left(\frac{B}{I}T,\ \frac{m_0 I}{B^2},\ \frac{B}{m_0}V_0,\ \frac{B}{m_0}v_g\right), \tag{1.05}$$

$$(f)\quad f=\frac{B^2}{m_0 I}f_\Delta\left(\frac{B}{I}T,\ \frac{m_0 I}{B^2},\ \frac{B}{m_0}V_0,\ \frac{B}{m_0}v_g\right). \tag{1.06}$$

It is interesting to investigate the dependence of $\bar{D}$ upon the various system parameters. We shall illustrate by considering the dependence upon the friction coefficient B, whose influence on the times required for reducing $\bar{D}$ and for increasing f may be considerable. It is then important practically to determine (with a given time) for what value of B, $\bar{D}$ is a minimum, and for what value f is a maximum. We shall designate these two values (or sets of values) by the symbols $B_{\min}$ and $B_{\max}$, respectively.

Consider first the determination of $B_{\min}$: This is obtained from the conditions

$$\frac{\partial \bar{D}}{\partial B}=0;\quad \frac{\partial^2 \bar{D}}{\partial B^2}>0.$$

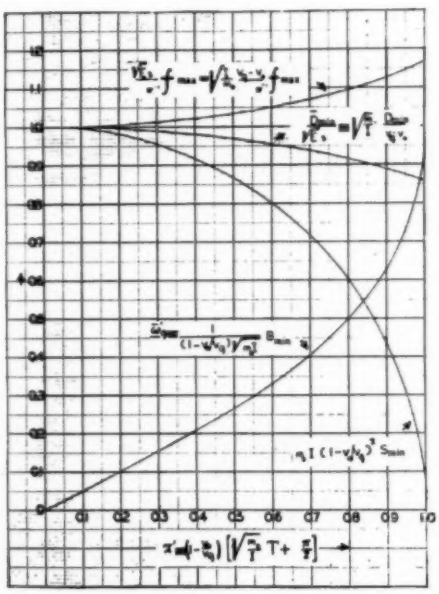

FIG. 6. Optimum performance curves for minimum deviation and maximum fidelity—proportional robot in constant tracking.

In general this value of $B_{\min}$ will depend on the time as well as the parameters, and to every time there will be associated a minimizing value $B_{\min}$. The value of $\bar{D}$ associated with $B_{\min}$ may be obtained by substituting into Eq. (1.06). $\bar{D}_{\min}$ and $B_{\min}$ as ordinates may both be plotted against the associated time T. Examples of such curves for proportional and on-off control robots obtained from the mathematical analysis in Part II and a subsequent paper are given in Figs. 6, 7, and 8. The curves are approximate only, and valid under the conditions for short period oscillations, i.e., for low damping B relative to motor strength m_0. It is further shown in the mathematical analysis that real minimum values of $\bar{D}_{\min}$, and maximum values of $f_{\max}$, may be obtained only for certain ranges of B and T. These ranges are diagrammed in Fig. 9. For generality the ranges of negative B and T are also given.

The actual value of T, and therefore $B_{\min}$, to be chosen depends of course on the requirements of the situation. In many cases ($\bar{D}_x=0$) it will be found that $\bar{D}_{\min}$ may be made as small as desired by choosing a sufficiently large T. But generally we do not wish this time to be unduly long. The most practical procedure to be followed for systems with adjustable B is then probably this:

For a given power source m_0, load inertia I, constant velocity of tracking v_g, and initial load velocity v_0, if we designate a deviation amplitude which is not to be exceeded, we determine a point on the $(\bar{D}_{\min}-T)$ curve. By making the friction coefficient in the system have the value $B_{\min}$ associated with the abscissa of this point, we ensure that the desired diminution in $\bar{D}$ will occur in the shortest possible time. This time is given by the common abscissa.†

† The formal proof that the conditions for

$\bar{D}$ minimum with respect to B at constant T

are entirely equivalent to those for

T minimum with respect to B at constant $\bar{D}$

is easy. It follows immediately from the expression

$$\bar{D}-\bar{D}(B,T)=0$$

that

$$\left(\frac{\partial T}{\partial B}\right)_{\bar{D}}=-\frac{(\partial \bar{D}/\partial B)_T}{(\partial \bar{D}/\partial T)_B}$$

and from this the desired conclusion may be drawn except in the case where the denominator on the right-hand side also vanishes (i.e., in the steady state).

As indicated above, just as one may seek to find an optimum value of B for minimizing the deviation, one may instead determine a B_{max} to maximize the fidelity fraction. B_{max} is determined to satisfy the conditions

$$\partial f/\partial B=0; \quad \partial^2 f/\partial B^2<0.$$

Plots of f_{max} and B_{max} curves analogous to the $\bar{D}_{min}$ and B_{min} curves may be made and the following prescription carried out:

For a given power source m_0, load inertia I, constant velocity of tracking v_g, and initial velocity v_0, if we designate a fidelity fraction which is to be exceeded, we determine a point on the f_{max} curve. By making the friction coefficient in the system have the value B_{max} associated with the abscissa of this point, we ensure that the desired increase in f will occur in the shortest possible time. This time is given by the abscissa.

Such curves as $\bar{D}_{min}$–B_{min} and f_{max}–B_{max} may conveniently be referred to as *curves for optimum performance.*

We may define the *sensitivity* of a maximum or minimum as *the relative change in the ordinate for a unit change in the abscissa* away from the extremum. It is proposed that this is a fairly

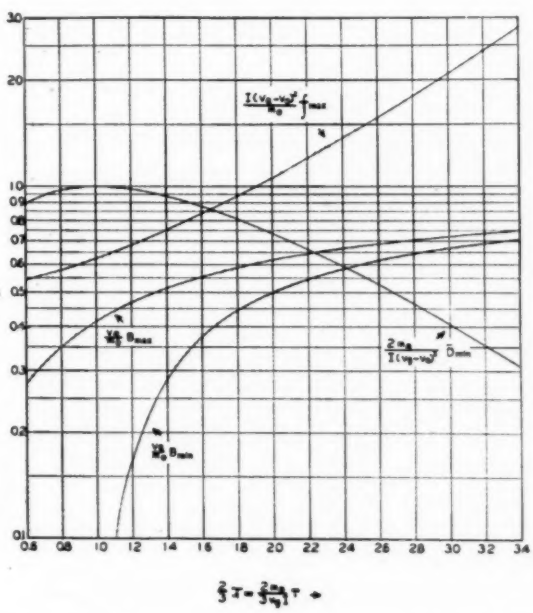

FIG. 7. Optimum performance curves for minimum deviation and maximum fidelity—on-off robot in constant tracking.

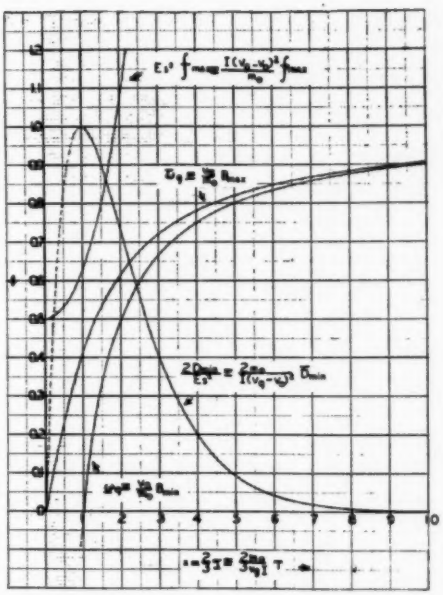

FIG. 8. Optimum performance curves on a semi-logarithmic plot—on-off robot in constant tracking.

relevant criterion in most cases where the local importance of a maximum or minimum is to be estimated. With application to the functions $\bar{D}(B)$ and $f(B)$ this yields

$$S_{min}=\frac{1}{\bar{D}_{min}}\frac{\partial^2\bar{D}}{\partial B^2}\bigg|_{B_{min}} \qquad S_{max}=\frac{1}{f_{max}}\frac{\partial^2 f}{\partial B^2}\bigg|_{B_{max}},$$

where in each case the second derivative is evaluated at the extremum, i.e., where the first derivative vanishes. Once the extremum problems have been solved, plots of S_{min} and S_{max} similar to those described for $\bar{D}_{min}$ and f_{max} may of course be made.

So far, in the interest of clarity we have described the curves for optimum performance in general without specifying the restrictions which may be placed, by dimensional considerations, on the manner of occurrence of the various parameters. But it may be of *considerable practical value* to determine in general *upon what involvements of the parameters the optimum performance curves depend.* Various minimal sets of such variables may be found, with differing advantages.

Here we shall make a particular choice which brings out clearly the dependence on B: If the

abbreviations

$$\frac{m_0 T}{v_g I} \equiv \mathcal{T} \quad \frac{I v_g^2}{m_0} \equiv E \quad 1 - \frac{v_0}{v_g} \equiv s \qquad (1.07)$$

are introduced, it is readily seen that (I.05) and (I.06) may be rewritten

$$(D') \quad \bar{D} = \frac{E}{\omega_g^2} \bar{\Delta}\left(\omega_g \mathcal{T}, \ \frac{E}{\omega_g^2}, \ \omega_g s, \ \omega_g\right) \qquad (1.08)$$

$$(f') \quad f = \frac{\omega_g^2}{E} f_\Delta\left(\omega_g \mathcal{T}, \ \frac{E}{\omega_g^2}, \ \omega_g s, \ \omega_g\right). \qquad (1.09)$$

It is clear from the definitions (I.07) of $\mathcal{T}$, E, and s that they in no way involve B. The functions in (D') and (f') depend on B only through

$$\omega_g \equiv \frac{B}{m_0} v_g.$$

Therefore all extremalizing values of B may be obtained by setting

$$\frac{\partial \bar{D}}{\partial \omega_g} = 0, \quad \frac{\partial f}{\partial \omega_g} = 0.$$

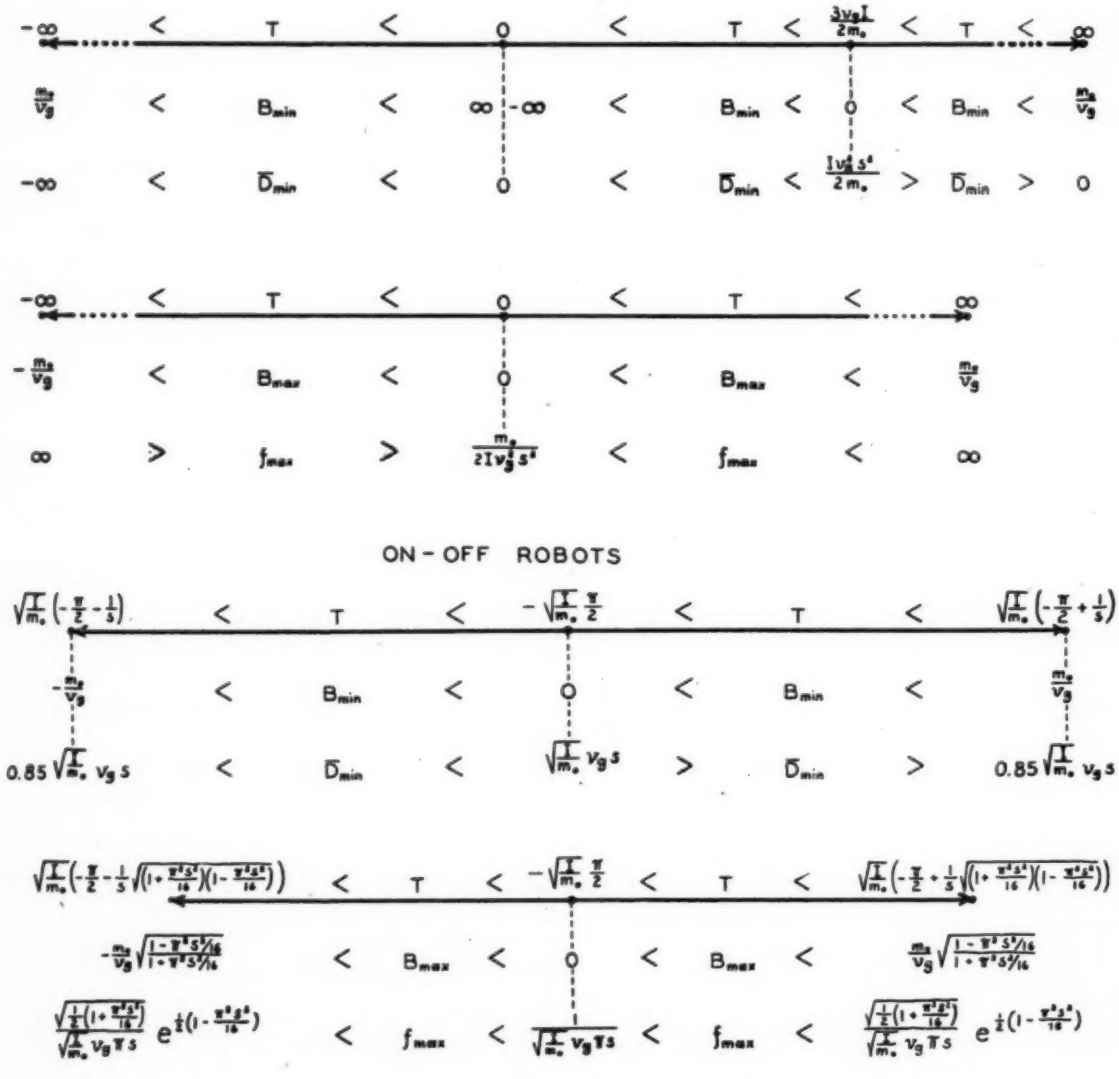

FIG. 9. Domain of real $\bar{D}_{\min}$ and $f_{\max}$ with associated ranges of the time and the friction coefficient.

These equations yield

$$(\omega_g)_{\min} \quad (\omega_g)_{\max}$$
$$\bar{D}_{\min} \qquad f_{\max}$$

and the sensitivities, etc., solely in terms of the quantities

$$\mathcal{T} \quad E \quad s$$

and no others. *Thus for any simple robot the optimum performance curves depend upon the time and physical parameters only in the three combinations defined in* (*I.07*). When quantities are expressed in terms of $\mathcal{T}$, E, and s, we shall say that they are "in $\mathcal{T}Es$ measure."

We shall now illustrate the use of the optimum performance curves by a practical example. Consider a system with the following parameters:

motor strength	$m_0 = 1$ kw. $= 10^{10}$ erg/sec.
inertia	$I = 1000$ kg $= 10^6$ g
guide velocity	$v_g = 3.6$ km/hr. $= 100$ cm/sec.
initial load velocity	$v_0 = 1.8$ km/hr. $= 50$ cm/sec.
$E = 1$	$s = \frac{1}{2}$.

Suppose we wish to determine the optimum conditions for the deviation amplitude not to exceed 0.45 cm, i.e.,

$$\frac{\bar{D}_{\min}}{(E)^{\frac{1}{3}}s} = 0.9.$$

We find from Fig. 6 for proportional robots:

$$\mathcal{T}' = 0.86 \qquad \mathrm{T} = \left(\frac{I}{m_0}\right)^{\frac{1}{3}}\left(-\frac{\pi}{2}+\frac{\mathcal{T}'}{s}\right) = 0.0015 \text{ sec.}$$

$$\bar{\omega}_g' = 0.57 \qquad B = 28\times 10^6 \text{ dynes per cm/sec.}$$
$$= 28.6 \text{ kg per cm/sec.}$$

$$(E)^{\frac{1}{3}}\pi s f_{\max} = 1.11 \qquad f_{\max} = 0.707 \text{ cm}^{-1}.$$

Thus the optimal friction coefficient is such as to produce a drag of about 29 kg for a velocity 1 cm/sec. After 15 ten thousandths of a second the deviation amplitude will have fallen below 0.45 cm. To use the fidelity fraction, we consider the sample question: What fraction of a cycle does the system spend within a deviation equal to $\frac{1}{5}$ the deviation amplitude, i.e., within 0.09 cm of the correct position? The answer is $0.707\times 2\times 0.09 = 0.127 \simeq \frac{1}{8}$ of a cycle.

When we now consider an on-off robot with the same parameters we find we can no longer choose the minimizing deviation at 0.45 cm, since this already exceeds the upper limit for which $\bar{D}_{\min}$ is real. In fact we have a real minimum only when

$$\bar{D}_{\min} \leqslant \frac{I(v_g - v_0)^2}{2m_0} = 0.125 \text{ cm}$$

in this case. Taking $\bar{D}_{\min}$ equal to $\frac{1}{4}$ its value in the preceding example, i.e., at 0.1125 cm, we find

$$\frac{2\bar{D}_{\min}}{Es^2} = 0.9,$$

for which Fig. 7 yields:

$$\tfrac{2}{3}\mathcal{T} = 1.53 \qquad T = 0.023 \text{ sec.}$$
$$\underline{\omega}_g = 0.35 \qquad B_{\min} = 35.7 \text{ kg per cm/sec.}$$
$$\bar{\omega}_g = 0.54 \qquad B_{\max} = 55 \text{ kg per cm/sec.}$$
$$Es^2 f_{\max} = 0.81 \qquad f_{\max} = 3.24 \text{ cm}^{-1}.$$

The fidelity fraction in this case yields the result that the system will probably spend a fraction

$$3.24\times 2\times \frac{0.1125}{5} = 0.146 \text{ of a cycle}$$

within a deviation equal to $\frac{1}{5}$ the amplitude about the correct position.

PART II. THEORY OF SIMPLE ROBOTS WITH PROPORTIONAL CONTROL

A. Complete Solutions as Functions of Time Optimum Performance Curves

We shall now consider a particular type of control for which detailed analytical and graphical solutions will be given. This is the case of the simple robot with *proportional control* in which the restoring force is linearly proportional to the deviation, i.e.,

$$m = m_0(\theta_g - \theta).$$

The basic equation for the robot with usual load may then be written

$$I\frac{d^2\theta}{dT'^2} + B\frac{d\theta}{dT'} = m_0(\theta_g - \theta)$$
$$\left.\begin{aligned}\theta &= \theta_b \\ \frac{d\theta}{dT'} &= \omega_b\end{aligned}\right\} \text{at } T' = 0. \qquad \text{(II.01)}$$

Introducing the dimensionless measures given by (I.02′) and taking the case of constant tracking, we have

$$\frac{d^2\Delta'}{d\mathrm{T}'^2}+\frac{d\Delta'}{d\mathrm{T}'}+\kappa\Delta'=\omega_g$$

$$\left.\begin{aligned}\Delta'=\Delta_b'&=-\phi_b\\ \frac{d\Delta'}{d\mathrm{T}'}&=\omega_g-\omega_b\equiv\Omega_b\end{aligned}\right\}\text{at } \mathrm{T}'=0. \tag{II.02}$$

Upon integration of (II.02) we get:

$$\Delta'=\frac{\omega_g}{\kappa}+(\phi_b+\omega_g/\kappa)e^{-\mathrm{T}'/2}\frac{\sin\nu_0(\mathrm{T}'-\mathrm{T}_0')}{\sin\nu_0\mathrm{T}_0'} \tag{II.02′}$$

with

$$\mathrm{T}_0'=\frac{1}{\nu_0}\left[\pi-\sin^{-1}\frac{1}{[1+(-z_b/\nu_0)^2]^{\frac{1}{2}}}\right]$$

$$=\frac{1}{\nu_0}\left[\pi-\tan^{-1}\left(\frac{\nu_0}{-z_b}\right)\right]$$

$$=\frac{1}{\nu_0}\left[\frac{\pi}{2}-\tan^{-1}\frac{z_b}{\nu_0}\right]$$

where we have introduced the convenient abbreviations

$$z_b\equiv\frac{\Omega_b}{\phi_b+\omega_g/\kappa}-\tfrac{1}{2}\equiv\frac{I}{B}\frac{v_g-v_b}{\theta_b+Bv_g/m_0}-\tfrac{1}{2}$$

$$\nu_0\equiv(\kappa-\tfrac{1}{4})^{\frac{1}{2}}\equiv\frac{(4m_0I-B^2)^{\frac{1}{2}}}{2B} \tag{II.03}$$

It is clear that the mean steady-state deviation in this type of system with proportional control is then

$$\Delta_\infty'=\frac{\omega_g}{\kappa}\qquad D_\infty'=\frac{B}{m_0}v_g$$

and is just *the deflection which evokes the restoring force required to drag the system along against friction at the velocity* v_g. This is of course only a special case of the general result for Δ_∞' described in the preceding section. For the time dependent deviation from Δ_∞' there are three cases:

Case I: $\nu_0^2>0$. *Oscillatory Approach to Steady State*

$$\Delta=(\phi_b+\omega_g/\kappa)e^{-\mathrm{T}'/2}\frac{\sin\nu_0(\mathrm{T}'-\mathrm{T}_0')}{\sin\nu_0\mathrm{T}_0'}.$$

As v_0 approaches 0, T_0' may be represented approximately by

$$\mathrm{T}_0'\simeq\frac{\pi}{\nu_0}+\frac{1}{z_b}\quad\text{if}\quad z_b<0,$$

$$\mathrm{T}_0'\simeq\frac{1}{z_b}\quad\text{if}\quad z_b>0.$$

The deviation amplitude in the steady state $\bar{\Delta}_\infty$ is zero, and the number of transient cycles n_∞ and time T_∞ required to reach the steady state are both infinite.

Case II: $\nu_0^2=0$. *Critically Damped Approach to Steady State*

$$\Delta=(\phi_b+\omega_g/\kappa)e^{-\mathrm{T}'/2}\left(\frac{\mathrm{T}'}{\mathrm{T}_0'}-1\right)$$

where

$$\mathrm{T}_0'=\infty\quad\text{if}\quad z_b<0,$$

$$\mathrm{T}_0'=\frac{1}{z_b}\quad\text{if}\quad z_b>0.$$

Thus we see that the number of cycles n_∞ before the asymptotically approached steady state is either 0 or $\frac{1}{2}$, depending on whether z_b is less than or greater than zero. In the latter case Δ becomes zero once at T_0', and overshoots the mark, later subsiding asymptotically to zero again. Examining the structure of z_b, we see that this occurs under the following sets of circumstances:

I/B sufficiently large
v_g-v_b sufficiently large
θ_b small, m_0/Bv_g sufficiently large.

Case III: $\nu_0^2<0$. *Overdamped Approach to Steady State*

$$\Delta=(\phi_b+\omega_g/\kappa)e^{-\mathrm{T}'/2}\frac{\sinh|\nu_0|(\mathrm{T}'-\mathrm{T}_0')}{\sinh|\nu_0|\mathrm{T}_0'}$$

where

$$T_0' = \frac{1}{|\nu_0|} \sinh^{-1} \frac{1}{[(-z_b/\nu_0)^2 - 1]^{\frac{1}{2}}}$$

$$= -\frac{1}{|\nu_0|} \tanh^{-1} \frac{|\nu_0|}{-z_b}$$

$$= \ln \left| \frac{z_b + |\nu_0|}{z_b - |\nu_0|} \right|^{1/2|\nu_0|}.$$

It appears that T_0' has a real positive finite value only for $z_b > |\nu_0|$. Thus the smallest possible real values of T_0' and the number n_x of transient cycles during the approach to the steady state of zero deviation are governed by the rule

$$T_0' \text{ finite} \quad n_x = \tfrac{1}{2} \quad \text{if } z_b > |\nu_0|$$
$$T_0' = \infty \quad n_x = 0 \quad \text{if } z_b < |\nu_0|.$$

This is to be compared with the corresponding condition in Case II: A schedule of the possible real T_0' in the various cases, together with an analysis, by means of the unit circle in the trigonometric plane, of the limits approached, is given in Table IV.

For fixed $z_b > 0$, it is clear from the nature of the function $(1/x) \tanh^{-1} x$ that T_0' has its minimum value at $\nu_0 = 0$, i.e., for critical damping. Thus, *if the objective is to attain T_0' as quickly as possible, we shall certainly strive to keep the damping below the critical value.*

We pass now to the consideration of the amplitude time dependence in the various cases. The most interesting circumstances are those in which there is oscillation as in Case I, or when there is overshoot in Cases II and III.

Case I: If we shift to the time scale

$$T = T' - T_0'$$

$$\Delta = (\phi_b + \omega_g/\kappa) e^{-(T+T_0')/2} \frac{\sin \nu_0 T}{\sin \nu_0 T_0'}$$

TABLE IV. Smallest real T_0' as a function of ν_0 and z_b for the proportional robot.

$\leftarrow \nu_0^2$

	ν_0 Real: oscillation $T_0' = \frac{1}{\nu_0}\left[\pi - \tan^{-1}\frac{\nu_0}{-z_b}\right] = \frac{[\ ]}{\nu_0}$		$\nu_0 \to$ zero	zero $\leftarrow \lvert\nu_0\rvert$	ν_0 Imaginary: overdamping
			Critical damping		
z_b plus			$T_0' = \frac{1}{z_b}$	$T_0' = \frac{1}{z_b}$	if $z_b > \lvert\nu_0\rvert$: $T_0' = \frac{1}{\lvert\nu_0\rvert} \tanh^{-1} \frac{\lvert\nu_0\rvert}{z_b}$ if $z_b \leq \lvert\nu_0\rvert$: ∞
z_b zero	$T_0' = \frac{1}{\nu_0}\left[\pi - \frac{\pi}{2}\right] = \pi/2\nu_0$		$\frac{\pi}{2\nu_0} \to \infty$	∞	∞
z_b					
z_b zero	$T_0' = \pi/2\nu_0$		$\frac{\pi}{2\nu_0} \to \infty$	∞	∞
z_b minus			$\frac{\pi}{\nu_0} \to \infty$	∞	∞

z_b can be plus or minus.
ν_0 can be real or imaginary.

we may represent the beginning of each cycle by

$$\mathrm{T}_n=\frac{2n\pi}{\nu_0} \qquad (n=0,\ 1,\ 2,\ \cdots)$$

and the middle (node) by

$$\mathrm{T}_{n+\frac{1}{2}}=\frac{(2n+1)\pi}{\nu_0}=\mathrm{T}_n+\frac{\pi}{\nu_0}.$$

The times when the maximum and minimum deviations occur in the cycle are found by examining the zeros of the velocity

$$\Omega\equiv\frac{d\Delta}{d\mathrm{T}}=\frac{\phi_b+\omega_g/\kappa}{\sin\nu_0\mathrm{T}_0'}e^{-(\mathrm{T}+\mathrm{T}_0')/2}\times[-\tfrac{1}{2}\sin\nu_0\mathrm{T}+\nu_0\cos\nu_0\mathrm{T}]$$

to be

$$\bar{\mathrm{T}}_n=\mathrm{T}_n+\frac{1}{\nu_0}\tan^{-1}2\nu_0$$

$$\underline{\mathrm{T}}_n=\mathrm{T}_n+\frac{1}{\nu_0}\tan^{-1}2\nu_0+\frac{\pi}{\nu_0}.$$

In particular,

$$\bar{\mathrm{T}}_0=\frac{1}{\nu_0}\tan^{-1}2\nu_0.$$

The maximum amplitude of deviation in the n-th cycle, or the amplitude-time function, is then:

$$\bar{\Delta}_n=\bar{\Delta}_0e^{-\mathrm{T}_n/2},$$

where Δ_0, the maximum deviation amplitude in the first cycle, is

$$\bar{\Delta}_0=(\phi_b+\omega_g/\kappa)e^{-(\bar{\mathrm{T}}_0+\mathrm{T}_0')/2}\frac{\sin\nu_0\bar{\mathrm{T}}_0}{\sin\nu_0\mathrm{T}_0'}.$$

But

$$\bar{\mathrm{T}}_0+\mathrm{T}_0'=\frac{1}{\nu_0}\left[\pi-\tan^{-1}\frac{\nu_0}{-z_b}+\tan^{-1}2\nu_0\right]$$

$$=\frac{1}{\nu_0}\left[\pi-\tan^{-1}\left(\nu_0\frac{2z_b+1}{-z_b+2\nu_0^2}\right)\right],$$

and

$$\frac{\sin\kappa_0\bar{\mathrm{T}}_0}{\sin\nu_0\mathrm{T}_0'}=\left(\frac{1+(z_b/\nu_0)^2}{1+(1/2\nu_0)^2}\right)^{\frac{1}{2}},$$

so that

$$\bar{\Delta}_0=(\phi_b+\omega_g/\kappa)\left(\frac{\nu_0^2+z_b^2}{\nu_0^2+\frac{1}{4}}\right)^{\frac{1}{2}}\times\exp-\frac{1}{2\nu_0}\left[\pi-\tan^{-1}\left(\nu_0\frac{2z_b+1}{-z_b+2\nu_0^2}\right)\right].$$

Case II, $z_b>0$: The time when the maximum deviation amplitude occurs is here given by

$$\bar{\mathrm{T}}=2 \quad \text{or} \quad \bar{\mathrm{T}}'=\mathrm{T}_0'+2=\frac{1}{z_b}+2,$$

and the associated maximum deviation amplitude is

$$\bar{\Delta}=2z_b(\phi_b+\omega_g/\kappa)e^{-(1+1/2z_b)}.$$

Case III, $z_b>|\nu_0|$: With respect to the shifted time scale, Δ may here be written:

$$\Delta=(\phi_b+\omega_g/\kappa)((z_b/\nu_0)^2-1)^{\frac{1}{2}}\left[\frac{z_b-|\nu_0|}{z_b+|\nu_0|}\right]^{1/4|\nu_0|}e^{-\mathrm{T}/2}\sinh|\nu_0|\mathrm{T}.$$

The time when the maximum amplitude of overshoot is reached is found by examining the zero of $d\Delta/d\mathrm{T}'$, to be

$$\bar{\mathrm{T}}=\frac{1}{\nu_0}\tanh^{-1}2|\nu_0|=\ln\left[\frac{1+2|\nu_0|}{1-2|\nu_0|}\right]^{1/2|\nu_0|}$$

which, upon insertion into the expression for Δ, yields the maximum amplitude

$$\bar{\Delta}=(\phi_b+\omega_g/\kappa)\left(\frac{z_b^2-|\nu_0|^2}{\frac{1}{4}-|\nu_0|^2}\right)^{\frac{1}{2}}\times\left[\frac{1-2|\nu_0|}{1+2|\nu_0|}\frac{z_b-|\nu_0|}{z_b+|\nu_0|}\right]^{1/4|\nu_0|}.$$

It is clear from the above expressions that in order that there shall actually be finite real values for T and Δ, it is also necessary that

$$|\nu_0|<\tfrac{1}{2} \ (\nu_0 \text{ pure imaginary}).$$

But this is merely the condition that

$$\kappa\equiv\frac{m_0I}{B^2}>0$$

i.e., *in order that the time and amplitude of overshoot may not increase indefinitely it is necessary that the restoring force factor be positive.* This requirement is otherwise obvious on physical grounds.

We shall now determine the fidelity fraction for Case I, which is the only case in which the concept has much interest. The expression for Ω given above may be rewritten

$$\Omega(T) = -\Delta_b \nu_0 (1+(z_b/\nu_0)^2)^{\frac{1}{2}} e^{-(T+T_0')/2} \cos \nu_0 T - \tfrac{1}{2}\Delta(T),$$

and if we evaluate this at $T = T_n$ and $T = T_{n+1}$, we find

$$\Omega(T_n) = \nu_0 \bar{\Delta}_n e^{\bar{T}_0/2} (1+1/4\nu_0^2)^{\frac{1}{2}} = \nu_0 \exp \frac{1}{2\nu_0} \tan^{-1} 2\nu_0 (1+1/4\nu_0^2)^{\frac{1}{2}} \bar{\Delta}_n$$

$$\Omega(T_{n+1}) = -\Omega(T_n) e^{-\pi/2\nu_0}.$$

Inserting these expressions into the formulas for f_Δ, and remembering that the period π_n is given by the constant $2\pi/\nu_0$, we have

$$f_\Delta = \frac{1}{2\pi} \exp - \frac{1}{2\nu_0} \tan^{-1} 2\nu_0 (1+e^{\pi/2\nu_0}) \frac{1}{\bar{\Delta}_n (1+1/4\nu_0^2)^{\frac{1}{2}}}.$$

Thus, except for a constant factor, the fidelity fraction varies inversely with the deviation amplitude.

In ordinary dimensional and $\mathcal{T}Es$ measure (see definitions (I.11) Section (C) Part I) the amplitude-time function may be written.

$$\bar{D} = \bar{D}_0 e^{-(B/2I)T} \equiv \bar{D}_0 e^{-(\omega_g/2)\mathcal{T}}$$

and the fidelity fraction is:

$$f = f_0 e^{(B/2I)T} \equiv f_0 e^{(\omega_g/2)\mathcal{T}},$$

where

$$\bar{D}_0 = \left(\theta_b + \frac{B}{m_0} v_g\right) \left(\frac{\nu_0^2 + z_b^2}{\nu_0^2 + \frac{1}{4}}\right)^{\frac{1}{2}} \times \exp - \frac{1}{2\nu_0} \left[\pi - \tan^{-1}\left(\nu_0 \frac{2z_b+1}{-z_b+2\nu_0^2}\right)\right],$$

$$f_0 = \frac{1}{2\pi} \exp - \frac{1}{2\nu_0} \tan^{-1} \times 2\nu_0 (1+e^{\pi/2\nu_0}) \frac{1}{\bar{D}_0 (1+1/4\nu_0^2)^{\frac{1}{2}}}.$$

For simplicity we shall set $\theta_b = 0$ in the following analysis. The definitions (I.03) may then be written in $\mathcal{T}Es$ measure

$$\nu_0 = \left(\frac{E}{\omega_g^2} - 1\right)^{\frac{1}{2}}$$
$$z_b = \frac{Es}{\omega_g^2} - \tfrac{1}{2} \equiv s(\nu_0^2+1) - \tfrac{1}{2}. \qquad \text{(II.04)}$$

The argument of the arc-tangent in the exponent of $\bar{D}_0$ then takes the form

$$\nu_0 \frac{2z_b+1}{2\nu_0^2 - z_b} = \nu_0 \frac{2s(\nu_0^2+1)}{\nu_0^2(2-s) - s + \frac{1}{2}}.$$

We shall examine in detail only the approximation $\nu_0 >> 1$ corresponding to short period oscillations, or low damping B relative to the square root of the product of motor strength m_0 by inertia I. For this limit the arc-tangent approaches $\pi/2$ and we may write

$$\bar{D}_0 \simeq \omega_g (1+s^2\nu_0^2)^{\frac{1}{2}} e^{-(\pi/4\nu_0)}$$

or, making use of the fact that in this approximation

$$\nu_0 = \frac{(E)^{\frac{1}{2}}}{\omega_g},$$

we may write

$$\bar{D} = (\omega_g^2 + Es^2)^{\frac{1}{2}} \exp - \left(\frac{\pi}{4(E)^{\frac{1}{2}}} + \frac{\mathcal{T}}{2}\right) \omega_g = \left(\left(\frac{Bv_g}{m_0}\right)^2 + \frac{Iv_g^2}{m_0}\left(1 - \frac{v_0}{v_g}\right)^2\right)^{\frac{1}{2}} \times \exp\left(-\frac{B}{2I}T - \frac{\pi B}{4(m_0 I)^{\frac{1}{2}}}\right).$$

We pause here for a moment to draw some general conclusions. It is clear from the expression that *the deviation amplitude at any given time will be smaller the smaller the guide velocity v_g and its difference from the initial velocity of the system v_0, the smaller the inertia of the load I, and the greater the strength of the power source m_0* (above the maximizing value $m_0^* = 8(I)^{\frac{1}{2}}/\pi B$). As mentioned before, the inertia of the load, the strength of the power source, etc., will often be fixed by other considerations. The most controllable factor is likely to be the friction coefficient B as

contained in the parameter ω_g. We now proceed to determine for what values of ω_g, $\bar{D}$ is a minimum, the value of this minimum, and its sensitivity (defined in the introduction).

It will be convenient to introduce the abbreviations

$$\mathcal{T}' \equiv (E)^{\frac{1}{2}} s\left(\tau + \frac{\pi}{2(E)^{\frac{1}{2}}}\right) \equiv \left(1 - \frac{v_0}{v_g}\right)\left(\left(\frac{m_0}{I}\right)^{\frac{1}{2}} T + \frac{\pi}{2}\right)$$

$$\omega_g' \equiv \frac{\omega_g}{(E)^{\frac{1}{2}} s} \equiv \frac{B}{(m_0 I)^{\frac{1}{2}}} \frac{v_g}{v_g - v_0}$$

as measures of the time and guide velocity in this case. With these notations we may write

$$\bar{D} = (E)^{\frac{1}{2}} s (1 + \omega_g'^2)^{\frac{1}{2}} e^{-(\omega_g'/2)\mathcal{T}'}.$$

From the formula for $\bar{D}$ we find, consecutively,

$$\frac{\partial \bar{D}}{\partial \omega_g'} = \bar{D}\left[\frac{\omega_g'}{1+\omega_g'^2} - \frac{\mathcal{T}'}{2}\right],$$

$$\frac{\partial^2 \bar{D}}{\partial \omega_g'^2} = \frac{1}{\bar{D}}\left(\frac{\partial \bar{D}}{\partial \omega_g'}\right)^2 + \bar{D}\frac{1-\omega_g'^2}{1+\omega_g'^2}.$$

Thus

$$(\omega_g')_{\min} \equiv \underline{\omega}_g' = \frac{1-(1-\mathcal{T}'^2)^{\frac{1}{2}}}{\mathcal{T}'} \qquad \underline{\omega}_g'^2 = \frac{2\underline{\omega}_g'}{\mathcal{T}'} - 1$$

$$\bar{D}_{\min} = (E)^{\frac{1}{2}} s\left(\frac{2\underline{\omega}_g'}{\mathcal{T}'}\right)^{\frac{1}{2}} e^{-(\underline{\omega}_g'/2)\mathcal{T}'}$$

$$S_{\min} \equiv \frac{1}{\bar{D}_{\min}} \frac{\partial^2 \bar{D}}{\partial \underline{\omega}_g'^2}\left(\frac{d\omega_g'}{dB}\right)^2 = \frac{1}{m_0 I (1 - v_0/v_g)^2}\left(\frac{\mathcal{T}'}{\underline{\omega}_g'} - 1\right) > 0,$$

where we have indicated the necessary condition that the extreme value represent a minimum by the inequality on S.

In the neighborhood of $\mathcal{T}' = 0$ we have

$$(\omega_g')_{\min} \simeq \frac{\mathcal{T}'}{2}$$

$$\frac{\bar{D}_{\min}}{(E)^{\frac{1}{2}} s} \simeq e^{-(\mathcal{T}'/2)^2} \qquad \text{(II.05)}$$

$$m_0 I (1 - v_0/v_g)^2 S_{\min} \simeq 1,$$

and in the neighborhood of $\mathcal{T}' = 1$

$$\omega_g' \to 1 \quad \frac{d\omega_g'}{d\mathcal{T}'} \to \infty \quad \text{(cusp)}$$

$$\frac{\bar{D}_{\min}}{(E)^{\frac{1}{2}} s} \to (2)^{\frac{1}{2}} e^{-\frac{1}{2}} \simeq 0.85 \qquad \text{(II.06)}$$

$$S_{\min} \to 0.$$

This limiting behavior, as well as the variation throughout the interval, is exhibited in Fig. 2, where ω_g', $\bar{D}_{\min}/(E)^{\frac{1}{2}} s$, and $m_0 I (1 - v_0/v_g)^2 S_{\min}$ are all plotted as functions of the time variable $\mathcal{T}'$. Beyond $\mathcal{T}' = 1$ there is no real minimum for $\bar{D}$.

In similar fashion to the above we may carry out the analysis for the fidelity fraction. We find

$$f_0 = \frac{1}{\pi} \frac{\cosh \frac{\pi}{4(E)^{\frac{1}{2}}} \omega_g}{\bar{D}_0} \equiv \frac{1}{\pi} \frac{\cosh \frac{\pi}{4} s\omega_g'}{\bar{D}_0},$$

so that

$$f = \frac{1}{\pi} \frac{\cosh \frac{\pi}{4} s\omega_g'}{\bar{D}}.$$

Making use of the preceding analysis of $\bar{D}$, we find

$$\frac{\partial f}{\partial \omega_g'} = f\left[\frac{\pi s}{4} \tanh \frac{\pi s}{4} \omega_g' - \frac{\omega_g'}{1+\omega_g'^2} + \frac{\mathcal{T}'}{2}\right]$$

$$\frac{\partial^2 f}{\partial \omega_g'^2} = \frac{1}{f}\left(\frac{\partial f}{\partial \omega_g'}\right)^2 + f\left[\left(\frac{\pi s}{4}\right)^2 \operatorname{sech}^2 \frac{\pi s}{4} \omega_g' - \frac{1-\omega_g'^2}{(1+\omega_g'^2)^2}\right]. \qquad \text{(II.07)}$$

If we set

$$\frac{\pi s}{4} \omega_g' \simeq 0$$

corresponding to the inequality $E >> \omega_g^2$, we may rewrite these expressions in the simplified form

$$\frac{\partial f}{\partial \omega_g'} = -f\left[\frac{\omega_g'}{1+\omega_g'^2} - \frac{\mathcal{T}'}{2}\right]$$

$$\frac{\partial^2 f}{\partial \omega_g'^2} = \frac{1}{f}\left(\frac{\partial f}{\partial \omega_g'}\right)^2 + f\left[\left(\frac{\pi s}{4}\right)^2 - \frac{1-\omega_g'^2}{1+\omega_g'^2}\right].$$

From these we may deduce that to this approximation $(\omega_g')_{max}$ *is equal to* $(\omega_g')_{min}$. Thus

$$(\omega_g')_{max} = \underline{\omega_g}' = \frac{1-(1-\mathcal{T}'^2)^{\frac{1}{2}}}{\mathcal{T}'}$$

$$f_{max} = \frac{1}{\pi \bar{D}_{min}} = \frac{1}{\pi(E)^{\frac{1}{2}}s}\left(\frac{\mathcal{T}'}{2\underline{\omega_g}'}\right)^{\frac{1}{2}} e^{(\omega_g'/2)\mathcal{T}'}$$

$$m_0 I(1-v_0/v_g)^2 S_{max} = \frac{\pi^2 s^2}{16} + 1 - \frac{\mathcal{T}'}{\underline{\omega_g}'} \leq 0.$$

$\pi(E)^{\frac{1}{2}}s\, f_{max}$ is also plotted in Fig. 6. We note that the only difference in the conditions determining f_{max} and $\bar{D}_{min}$ here is that the maximizing condition holds in a more restricted range, i.e.,

$$\frac{\underline{\omega_g}'}{\mathcal{T}'} \leq \frac{1}{1+(\pi s/4)^2},$$

which, together with the preceding equations, determines the following inequalities for the domain in which f is still maximized

$$-\left(\frac{1-\pi^2 s^2/16}{1+\pi^2 s^2/16}\right)^{\frac{1}{2}} \leq \omega_g' \leq \left(\frac{1-\pi^2 s^2/16}{1+\pi^2 s^2/16}\right)^{\frac{1}{2}}$$

$$-[(1+\pi^2 s^2/16)(1-\pi^2 s^2/16)]^{\frac{1}{2}} \leq \mathcal{T}' \leq [(1+\pi^2 s^2/16)(1-\pi^2 s^2/16)]^{\frac{1}{2}}$$

$$\frac{1}{(E)^{\frac{1}{2}}\pi s} \leq f_{max} \leq \frac{1}{(E)^{\frac{1}{2}}\pi s}[\tfrac{1}{2}(1+\pi^2 s^2/16)]^{\frac{1}{2}} e^{\frac{1}{2}(1-\pi^2 s^2/16)}.$$

The formulas given here and above are the base for the general summary diagram (Fig. 9) at the end of the Part I indicating the domains of the variables in which we get real extrema for $\bar{D}_{min}$ and f_{max}.

B. PATH CURVES IN THE POSITION-VELOCITY PLANE

For future use[1,2] we shall now work out the result of eliminating the time between the expression (II.02′) and its time derivative $\Omega \equiv d\Delta'/d\tau$ which satisfies the relation

$$\Omega + \tfrac{1}{2}(\Delta' - \omega_g/\kappa) = -\nu_0(\Delta_b' - \omega_g/\kappa) \times e^{-T'/2}\frac{\cos\nu_0(T'-T_0')}{\sin\nu_0 T_0'}. \quad (II.02'')$$

Making the substitutions (which correspond to an "affine" transformation in the $\Omega-\Delta$ plane)

$$\Delta \equiv \Delta' - \omega_g/\kappa \quad y \equiv \Omega + \tfrac{1}{2}(\Delta' - \omega_g/\kappa),$$

with some rearrangement we may write (II.02′) and (II.02″):

$$\nu_0\Delta = -((\nu_0\Delta_b)^2 + y_0^2)^{\frac{1}{2}} e^{-T'/2}\sin\nu_0(T'-T_0'),$$

$$y = -((\nu_0\Delta_b)^2 + y_0^2)^{\frac{1}{2}} e^{-T'/2}\cos\nu_0(T'-T_0'),$$

from which we may find

$$T' = T_0' + \frac{1}{\nu_0}\tan^{-1}\frac{\nu_0\Delta}{y} = \frac{1}{\nu_0}\left[\tan^{-1}\frac{z}{\nu_0} - \tan^{-1}\frac{z_b}{\nu_0}\right],$$

where we have introduced the "clock-hand variable"

$$z \equiv -y/\Delta \equiv -(\Omega/\Delta + \tfrac{1}{2}).$$

Thus

$$(\nu_0\Delta)^2 + y^2 = [(\nu_0\Delta_b)^2 + y_b^2] \times \exp -\frac{1}{\nu_0}\left[\tan^{-1}\frac{z}{\nu_0} - \tan^{-1}\frac{z_0}{\nu_0}\right] \quad (II.08)$$

which becomes in polar coordinates the equation of a right-handed (clockwise) equiangular spiral

$$\rho = \rho_b e^{-(\psi-\psi_b)/2\nu_0}$$

with

radius vector $\rho \equiv ((\nu_0\Delta)^2 + y^2)^{\frac{1}{2}}$

(clockwise) angle $\psi \equiv \tan^{-1}(z/\nu_0)$.

Thus, in the case of underdamping (Case I) *the "path" of the linear robot in the phase-plane* ($\Omega-\Delta'$ *plane*) *is an affine distortion of a right-handed logarithmic spiral with center at* ω_g/κ (*or* $\Delta=0$). For the further analysis it is desirable to elucidate the meaning of what we have called the "clock-hand variable" z. We note that, in the $\Omega-\Delta$ plane, the successive values of z correspond to straight lines through the origin arranged in clockwise increasing order. z, which equals the

negative slope $-\tfrac{1}{2}$

of these lines, goes from $-\infty$ to $+\infty$ twice in making one complete circuit; once in going from the $+\Omega$ axis to the $-\Omega$ axis, and a second time in going from the $-\Omega$ axis back to the $+\Omega$ axis. The zero of z is not the Δ axis but rather the line

$$\Omega/\Delta = -\tfrac{1}{2}$$

In the case of overdamping $\nu_0^2<0$ (Case III) we may write $\nu_0=i|\nu_0|$ and our basic Eq. (11.08) goes over to the form

$$y^2-|\nu_0|^2\Delta^2=(y_b^2-|\nu_0|^2\Delta_b^2)\times\left|\frac{z_b-|\nu_0|}{z_b+|\nu_0|}\frac{z+|\nu_0|}{z-|\nu_0|}\right|^{1/2|\nu_0|}. \quad (11.08')$$

We see that all the curves beginning in the region $z_b<-|\nu_0|$ (i.e., the right-upper or left-lower portion of the plane) go in to zero touching along the line $z=-|\nu_0|$. All curves beginning in the region $z>|\nu_0|$ (i.e., right-lower or left-upper portion of the plane) overshoot $\Delta=0$, crossing the Δ axis at the points

$$\Omega=\pm[y_b^2-|\nu_0|^2\Delta_b^2]\left|\frac{z_b-|\nu_0|}{z_b+|\nu_0|}\right|^{1/4|\nu_0|}.$$

Finally all curves beginning in the intermediate region

$$-|\nu_0|<z_b<|\nu_0|$$

move counter-clockwise into the origin, touching the line $z=-|\nu_0|$ like all the others. If extrapolated backward (z fixed, z_b shifting) these lines are all asymptotically parallel to the line $z=|\nu_0|$.

In the case of critical damping $\nu_0=0$ (Case II), the equation of the path-curve takes the form

$$y^2\equiv(\Omega+\Delta/2)^2=(\Omega_b+\Delta_b/2)^2e^{1/z-1/z_b}, \quad (11.08'')$$

and the intermediate region of Case III has shrunk down to the line $y=0$ or $\Omega=-\Delta/2$.

It is interesting and important to note that if one takes the limit of (11.08') as the restoring force constant $\kappa\to0$ and $|\nu_0|\to\frac{1}{2}$, one obtains in the limit

$$\Omega=\Omega_b,$$

which is definitely *not* the general solution in this case.[2] This situation, where the limit of the solution when a coefficient *approaches zero* is not the same as the solution when the coefficient *is zero*, seems to be not uncommon in differential equations. Knowing that it occurs, one must then make special examination of the case at the limit. This case is contained in the analysis in the succeeding paper dealing with on-off systems.

Computation of the Solutions of $(1+2\epsilon\cos 2z)y''+\theta y=0$; Frequency Modulation Functions

N. W. McLachlan
London, England

(Received January 9, 1947)

This equation pertains to a loss-free frequency modulation circuit. Floquet's theory is applied to obtain stable solutions when θ, ϵ are outside the range of the approximation solution given by Carson in 1922. A method is described by means of which solutions may be computed to any degree of accuracy. The necessary formulae associated with the solution are derived, and convergence is discussed. A numerical example, illustrating the procedure to be followed, is worked out in detail. An appropriate normalization of the solutions is suggested in order to obtain standard frequency modulation functions. It is shown how the analysis may be extended to cover the case of the equation

$$d^2Q/dt^2+(R/L)(dQ/dt)+[Q/LC_0(1+2\epsilon\cos 2\omega_1 t)]=0,$$

which applies to a frequency modulation circuit having constant resistance R.

1. INTRODUCTION

THIS equation occurs in the theory of a method used for transmitting signal characters in radio broadcasting. The method is known as frequency modulation, and it is also the basis of the warble tone employed to reduce standing wave effects in acoustical test rooms. In the circuit shown schematically in Fig. 1A, the capacitance C is a periodic function of the time t, being represented by the formula $C=C_0(1+2\epsilon\cos 2\omega_1 t)$, where C_0 and ϵ are parameters with $|\epsilon|<0.5$. If Q is the quantity of electricity on the capacitance at any instant, the differential equation for the circuit is

$$(d^2Q/dt^2)+Q/LC_0(1+2\epsilon\cos 2\omega_1 t)=0. \quad (1)$$

By writing $\omega_0^2=1/LC_0$, $\theta=(\omega_0/\omega_1)^2$, $\omega_1 t=z$, $y=Q$, (1) becomes

$$d^2y/dz^2+\theta y/(1+2\epsilon\cos 2z)=0. \quad (2)$$

Expressed in this way, we see that if $|\epsilon|\geqslant 0.5$, $(1+2\epsilon\cos 2z)$ has zeros, and, therefore, $\theta/(1+2\epsilon\cos 2z)$ has corresponding infinities. These are avoided by imposing the restriction $|\epsilon|<0.5$. In radio broadcasting $|\epsilon|<<<0.5$, and to an adequate approximation (2) may be written

$$y''+(a-2q\cos 2z)y=0, \quad (3)$$

where $a=\theta$, and $q=\theta\epsilon$. Then (3) is the canonical form of Mathieu's differential equation. When (a), a is very large and positive, (b) $a>>>q>0$, an approximate solution of (3) is given by

$$y=C\sum_{-\infty}^{\infty}J_r(q/2a^{\frac{1}{2}})\cos[(a^{\frac{1}{2}}-2r)z-\psi], \quad (4)$$

$$=C\sum_{-\infty}^{\infty}J_r(\omega_0\epsilon/2\omega_1)\cos[(\omega_0-2r\omega_1)t-\psi], \quad (5)$$

C and ψ being arbitrary constants. This form of solution was obtained by Carson in 1922.[1] Typical values of the various parameters in radio frequency modulation are: $f_0=\omega_0/2\pi=5\times 10^7$ c.p.s., $f_1=\omega_1/2\pi=5\times 10^3$ c.p.s., $f_0\epsilon=\omega_0\epsilon/2\pi$, $=\Delta f=\Delta\omega/2\pi=10^4$ c.p.s., this being the frequency deviation on either side of the central frequency f_0. Thus $\epsilon=2\times 10^{-4}$, so in (2) it is justifiable to take $(1+2\epsilon\cos 2z)^{-1}\simeq(1-2\epsilon\cos 2z)$. We also have $a=\theta=(f_0/f_1)^2=10^8$, and $q=\theta\epsilon=2\times 10^4$, so the conditions for (4) to be an approximate solution of (3) are satisfied. The values of the parameters for the acoustical warble tone do not always satisfy these conditions, and we have then to solve the equation

$$(1+2\epsilon\cos 2z)y''+\theta y=0 \quad (6)$$

without using the above approximation. In succeeding sections it is shown how this may be accomplished to any desired degree of accuracy.

2. THEORETICAL CONSIDERATIONS

Since the coefficient of y'' in (6) Section 1 is single-valued and periodic in z, that of y being

[1] J. R. Carson, "Notes on the theory of frequency modulation," Proc. I.R.E. 10, 62 (1922).

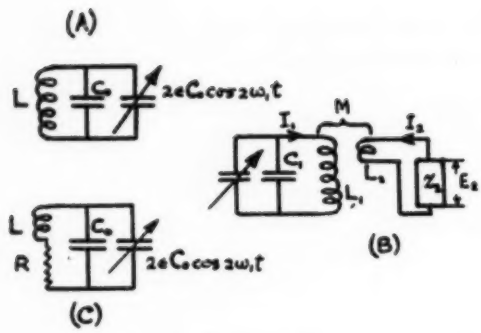

FIG. 1. (A) Schematic representation of loss-free oscillatory circuit with periodically variable capacitance $C=C_0(1+2\epsilon\cos 2\omega_1 t)$. (B) As at (A) but the circuit loosely coupled by L_2 to a second circuit. (C) As at (A) but the circuit having constant resistance R.

constant, Floquet's theory may be applied.[2] Thus the solutions are either stable, unstable, or neutral, according to the values of θ and ϵ. For present purposes we shall consider stable solutions. Thus linearly independent formal solutions are[3]

$$y_1(z)=\sum_{-\infty}^{\infty} c_{2r}\cos(2r+\rho)z, \qquad (1)$$

and

$$y_2(z)=\sum_{-\infty}^{\infty} c_{2r}\sin(2r+\rho)z, \qquad (2)$$

provided the point (θ, ϵ) lies in certain regions of the (θ, ϵ) plane defined below, and $0<\rho<1$. For other regions of the plane, the solutions take the forms

$$y_1(z)=\sum_{-\infty}^{\infty} c_{2r+1}\cos(2r+1+\rho)z, \qquad (3)$$

and

$$y_2(z)=\sum_{-\infty}^{\infty} c_{2r+1}\sin(2r+1+\rho)z. \qquad (4)$$

These forms will be comprehended readily by reference to McLachlan,[3] Chapter 4, in which there are stability charts for Mathieu's equation (3) Section 1. In these the (a, q) plane is mapped out into regions where the solutions are (a) stable, (b) unstable. A similar chart may be drawn for Eq. (6) Section 1, but in this case although θ is unlimited, ϵ is restricted to the strip $|\epsilon|<0.5$, as illustrated in Fig. 2. The values of (θ, ϵ) in which we are interested, lie *within* the stable regions, being on the iso-ρ curves. The full-line curves correspond to the characteristic curves for solutions of Mathieu's equation of positive integral order, and pertain to kindred solutions of (6) Section 1. They are designated α_m, β_m, with $m=2n$, $2n+1$, or $2n+2$. When the point (θ, ϵ) lies *between* α_{2n} and β_{2n+1}, the solutions (1), (2) are used, whereas for the regions *between* α_{2n+1} and β_{2n+2}, (3), (4) are used. If these solutions are normalized as shown in Section 12, they may then be regarded as *frequency modulation functions*, or f-m functions for brevity.

3. RECURRENCE RELATIONS FOR THE COEFFICIENTS IN (1)-(4) SECTION 2

Substituting either (1) or (2) into (6) Section 1, and equating the coefficient of $\cos(2r+\rho)z$, or that of $\sin(2r+\rho)z$ to zero, $r=-\infty$ to $+\infty$, we obtain the recurrence relation

$$[\theta-(2r+\rho)^2]c_{2r}-\epsilon[(2r+2+\rho)^2c_{2r+2}+(2r-2+\rho)^2c_{2r-2}]=0. \quad (1)$$

The relation for (3), (4) Section 2 is

$$[\theta-(2r+1+\rho)^2]c_{2r+1}-\epsilon[(2r+3+\rho)^2c_{2r+3}+(2r-1+\rho)^2c_{2r-1}]=0. \quad (2)$$

Both (1), (2) are linear difference equations of the second order, and each has two independent solutions, the character of which we shall now investigate. Dividing (1) throughout by c_{2r} and writing $v_{2r}=c_{2r+2}/c_{2r}$ we get

$$(2r+2+\rho)^2v_{2r}+(2r-2+\rho)^2v_{2r-2}^{-1}=[\theta-(2r+\rho)^2]\epsilon^{-1}, \quad (3)$$

or

$$v_{2r}+\left(\frac{2r-2+\rho}{2r+2+\rho}\right)^2 v_{2r-2}^{-1}=\left[\frac{\theta-(2r+\rho)^2}{(2r+2+\rho)^2}\right]\epsilon^{-1}. \quad (4)$$

With θ finite, $|\epsilon|<0.5$, $0<\rho<1$, when $r\to+\infty$ (4) may be written

$$v_{2r}+v_{2r-2}^{-1}\sim-\epsilon^{-1}. \qquad (5)$$

Then as $r\to+\infty$, $|v_{2r}|$ is either $\gtrless 1$. For the convergence of (1), (2) Section 2, $|c_{2r}|\to 0$ as $r\to+\infty$, so this solution rests on the condition

[2] G. Floquet, "Sur les equations differentielles lineares," Ann. de l'École Normale Superieure, 12, 47 (1883).
[3] N. W. McLachlan, *Theory and Application of Mathieu Functions* (Oxford Press, New York, 1947).

$|v_{2r}|<1$. The second solution d_{2r} pertains to $|v_{2r}|>1$, which means that $|d_{2r}|\to\infty$ with r, so in the present instance it is inadmissible. Suppose that $|\epsilon|<0.1$, then to a first approximation we may write

$$v_{2r}\simeq-\epsilon. \tag{6}$$

Substituting from (6) into (5) leads to

$$|v_{2r-2}|\simeq|\epsilon/(1-\epsilon^2)|<1. \tag{7}*$$

As $r\to+\infty$, the ratio of consecutive coefficients tends to this approximate value. The same conclusion may be reached if $r\to-\infty$.

The formulas corresponding to (3), (4) Section 2 may be derived from those above by writing $(2r+1)$ for $2r$.

4. MINIMUM RATIO OF CONSECUTIVE COEFFICIENTS

If the order of the solution (function) is $(m+\rho)$, where $m^2=4r_m^2$, it is convenient to regard $c_m=c_{2r_m}$ as the *central* coefficient in the solution. Then, if $s\geq r_m$, $|v_{2s}|=|c_{2s+2}/c_{2s}|<1$, and for $p\leq r_m$, $|1/v_{2p}|=|c_{2p-2}/c_{2p}|<1$, so $|v_{2p}|>1$. In (4) Section 3 let $r=-1$, and we get

$$v_{-2}+\left(\frac{4-\rho}{\rho}\right)^2 v_{-4}^{-1}=\left[\frac{\theta-(2-\rho)^2}{\rho^2\epsilon}\right]. \tag{1}$$

Now $0<\rho<1$, $|\epsilon|<0.5$, and if $\theta\gg1$, the r.h.s. of (1) may be relatively large. The second member of (1) is then negligible and, therefore,

$$v_{-2}\simeq[\theta-(2-\rho)^2]/\rho^2\epsilon. \tag{2}$$

For instance if $\theta=100$, $\epsilon=0.2$, $\rho=0.323$,

$$v_{-2}=c_0/c_{-2}\simeq4650/1, \tag{3}$$

so the minimum ratio of consecutive coefficients is 1/4650. As r decreases below -1, the ratio increases and tends ultimately to the value at (7) Section 3. Hence, as r increases above $r=s$, $|v_{2r}|$ decreases slowly to an ultimate value of $|\epsilon/(1-\epsilon^2)|$; and as r decreases below $r=p$, $1/v_{2r}$ attains a minimum value of $\epsilon\rho^2/[\theta-(2-\rho)^2]$ at $r=-1$, but thereafter rises and ultimately approaches $-\epsilon/(1-\epsilon^2)$. Between $r=-1$ and $r=r_m$, the ratio is positive if $\epsilon>0$.

* The sign of v_{2r-2} is minus.

The formulas corresponding to (3), (4) Section 2, are

$$v_{-3}+\left(\frac{5-\rho}{1-\rho}\right)^2 v_{-5}^{-1}=[\theta-(3-\rho)^2]/(1-\rho)^2\epsilon, \tag{4}$$

and

$$v_{-3}\simeq[\theta-(3-\rho)^2]/(1-\rho)^2\epsilon, \tag{5}$$

this being the reciprocal of the minimum ratio. The behavior of the coefficients with variation in r is that already described.

5. CONVERGENCE OF (1)–(4) SECTION 2

In Section 4 it is shown that as $r\to\pm\infty$, the ratio of consecutive coefficients is less than unity, and that $|c_{2r}|\to0$. Now $\left|\begin{matrix}\cos\\ \sin\end{matrix}(2r+\rho)z\right|\leq1$, if z is real, so by a known theorem the series concerned are absolutely and uniformly convergent. When differentiated term by term repeatedly, the ratio of the moduli of consecutive coefficients is less than unity as $r\to\pm\infty$. Hence the resulting series have the same properties as above, as also have those obtained by integrating term by term, for a similar reason.

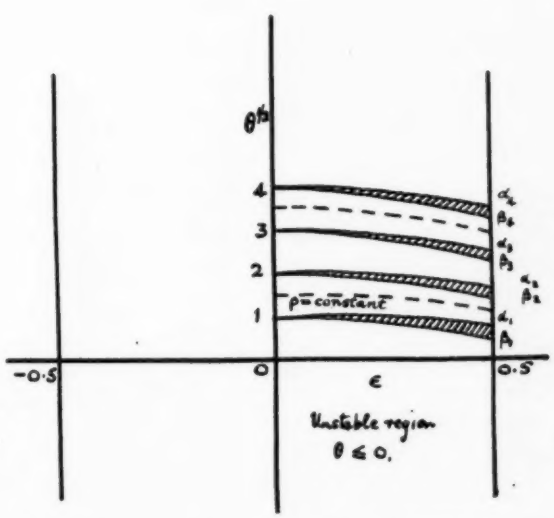

FIG. 2. Illustrating form of iso-ρ chart for $(1+2\epsilon\cos2z)y''+\theta y=0$. α_1, β_1, α_2, β_2, $\cdots$ are the characteristic curves (solid) for solutions of integral order—not considered herein. The even-order characteristics are symmetrical about the θ^1 axis, but those of odd order are asymmetrical although the chart is symmetrical. Iso-ρ curves are indicated by broken lines. When $\theta>0$ and the point (θ^1, ϵ) lies in an unshaded area, the solution is stable. If it lies in a shaded area between α_m and β_m, the complete solution is unstable and $\to\pm\infty$ as $z\to\pm\infty$.

6. FORMULAS FOR CALCULATING TRIAL VALUES OF ρ

a

Let

$$y=\cos\nu z+\epsilon c_1(z)+\epsilon^2 c_2(z)+\cdots, \quad (1)$$

and

$$\theta=\nu^2+\gamma_1\epsilon+\gamma_2\epsilon^2+\cdots, \quad (2)$$

where the $c(z)$ are continuous single-valued even functions of z; $\nu=(m+\rho)$ being real and positive. By substituting (1), (2) into (6) Section 1, taking the solution to be stable and the coefficient of $\cos\nu z$ unity, we may determine γ_1, γ_2, $\cdots$.[3] Then to a first approximation we find that

$$\theta\simeq\nu^2[1-(3\nu^2+4)\epsilon^2/2(\nu^2-1)]. \quad (3)$$

If $\theta\gg1$, and ϵ is small enough, (3) may be expressed in the form

$$\nu=(m+\rho)$$
$$\simeq[\theta(\theta-1)/\{\theta(1-\tfrac{3}{2}\epsilon^2)-(1+2\epsilon^2)\}]^{\frac{1}{2}}. \quad (4)$$

Thus m is the integral, and ρ the fractional part of the r.h.s. of (4).

b

We choose the form of differential equation at (2) Section 1 and expand $(1+2\epsilon\cos2z)^{-1}$. Then

$$\begin{aligned}(1+2\epsilon\cos2z)^{-1}=&(1+2\epsilon^2+6\epsilon^4+\cdots)\\&-2\epsilon(1+3\epsilon^2+10\epsilon^4+\cdots)\cos2z\\&+2\epsilon^2(1+4\epsilon^2+\cdots)\cos4z\\&-2\epsilon^3(1+5\epsilon^2+\cdots)\cos6z+\cdots. \quad (1)\end{aligned}$$

If ϵ is such that terms in $\cos4z$, $\cos6z$, etc., may be neglected, we can write (2) Section 1 in the approximate form

$$y''+(a-2q\cos2z)y=0, \quad (2)$$

with

$$a=\theta(1+2\epsilon^2+6\epsilon^4+\cdots), \quad (3)$$

and

$$q=\theta\epsilon(1+3\epsilon^2+10\epsilon^4+\cdots). \quad (4)$$

Then from reference 3, page 83,

$$(m+\rho)\simeq[a-(a-1)q^2/\{2(a-1)^2-q^2\}]^{\frac{1}{2}}. \quad (5)$$

The values of ρ computed from either (4) **a**, or (5) are to be regarded as "trial" values, which may need to be improved during the process of computing the coefficients.

7. COMPUTATION OF THE COEFFICIENTS

Having obtained a "trial" ρ, the c's are calculated by the method described in reference 3, Chapter 5. Unlike the c therein, those to be computed for (1), (2) Section 2 do not decrease rapidly with increase in $r>r_m$, unless ϵ is very small. Moreover, it is necessary to introduce an approximate correction based upon (7) Section 3, when starting the computation.

8. EXAMPLE

a

The following data pertain to an acoustical warble tone circuit: $f_0=\omega_0/2\pi=500$ c.p.s., $f_1=\omega_1/2\pi=50$ c.p.s., $\epsilon=0.2$. f_0 is the central frequency which corresponds to the unmodulated condition $\epsilon=0$. $\Delta f\simeq\epsilon f_0=100$ c.p.s., so the frequency range is approximately 400–600 c.p.s. The frequency of deviation or rate at which f_0 is modulated is $2f_1=100$ c.p.s., the modulation coefficient being $2\epsilon=0.4$. As shown in Section 1, $|2\epsilon|<1$. In the above data f_1 and ϵ are much greater than is usual in practice, where it is probable that $f_1=10$ c.p.s., and $\epsilon=0.05$.

Using (4) **a** Section 6 with $\theta=(f_0/f_1)^2=100$ $\epsilon=0.2$, yields

$$(m+\rho)=10.322,$$
so $$m=10, \quad \text{and} \quad \rho=0.322. \quad (1)$$

Using (3)–(5) **b** Section 6, we find that $a=109$, $q=22.72$, giving

$$(m+\rho)=10.323,$$
so $$m=10, \quad \text{and} \quad \rho=0.323. \quad (2)$$

Then c_{10} is the central coefficient. The close agreement between the trial values of ρ at (1), (2) should be noted, but this does not prove that they are accurate!

Taking one of the values of ρ, or the average, we calculate

$$\rightarrow \quad c_2,\ c_4,\ c_6,\ c_8,\ c_{10},\ \bar{c}_{12},\ \bar{c}_{14},$$
$$\bar{c}_6,\ \bar{c}_8,\ c_{10},\ c_{12},\ c_{14},\ c_{16},\ c_{18}, \quad \leftarrow$$

proceeding in the direction of the arrow in each case. Thus (a) we start at c_2 and work towards the central coefficient c_{10}, and (b) we start at c_{18} and work towards c_{10}. In each case there is an overlap of two (or more if desired) coefficients, and if we have started far enough away from c_{10}

on either side, and the trial ρ is sufficiently accurate, there ought to be adequate agreement between the pairs of coefficients c_6, $\bar{c}_6$; c_8, $\bar{c}_8$; etc. Failing this, re-computation using another value of ρ, and interpolation as in reference 3, Chapter 5, must be employed to attain the desired accuracy of the results.

b. Procedure

First we shall show that, to the degree of accuracy contemplated in demonstrating the method of calculation (using a 10-inch slide rule) that c_0 may be neglected. By (3) Section 4, $c_{-2}=c_0/4650$, so with $r=0$, $\epsilon=0.2$, and $\rho=0.323$ in (1) Section 3, by neglecting c_{-2} we obtain

$$c_0 = \epsilon(2+\rho)^2 c_2/(\theta-\rho^2) \simeq 0.0108 c_2. \tag{1}$$

With $r=1$ in (1) Section 3,

$$4.323^2 c_4 = 5(100-2.323^2)c_2 - 0.323^2 c_0, \tag{2}$$

$$= 472.8c_2 - 0.00113c_2, \tag{3}$$

by aid of (1). Thus the term $0.323^2 c_0$ in (2) may be ignored, and we get

$$c_4 = 472.8c_2/4.323^2 = 25.1c_2. \tag{4}$$

$r=2$ $\qquad 6.323^2 c_6 = 5(100-4.323^2)c_4 - 2.323^2 c_2.$

Substituting from (4) for c_4 we have

$$c_6 = 254.4c_2. \tag{5}$$

$r=3$ $\qquad 8.323^2 c_8 = 5(100-6.323^2)c_6 - 4.323^2 c_4,$

so $\qquad c_8 = 1090c_2. \tag{6}$

$r=4$ $\qquad 10.323^2 c_{10} = 5(100-8.323^2)c_8 - 6.323^2 c_6,$

so $\qquad c_{10} = 1465c_2$, *the central coefficient.* (7)

It will be seen that owing to repetition, the squares of various numbers, e.g., 4.323^2, need be obtained once only. We now continue and calculate the overlap coefficients $\bar{c}_{12}$, $\bar{c}_{14}$.

$r=5$ $\qquad 12.323^2 \bar{c}_{12} = 5(100-10.323^2)c_{10} - 8.323^2 c_8,$

so $\qquad 12.323^2 \bar{c}_{12} = 5(100-106.56)c_{10} - 8.323^2 c_8, \tag{8}$

and, therefore, $\qquad \bar{c}_{12} = -814c_2. \tag{9}$

This may be regarded as the "critical" point of the computation, because here $[100-(2r+0.323)^2]$ is smaller than for any other value of r. Consequently the influence of an inaccurate trial ρ is greatest when $r=5$.

$r=6$ $\qquad 14.323^2 \bar{c}_{14} = 5(100-12.323^2)\bar{c}_{12} - 10.323^2 c_{10},$

so $\qquad \bar{c}_{14} = 270c_2. \tag{10}$

c

We now calculate the coefficients on the upper side of c_{10}, commencing with c_{20}. From (7) Section 3, the *limiting* value of the ratio of consecutive coefficients is approximately $-\epsilon/(1-\epsilon^2) = -0.2/0.96 = -0.208$. But $|c_{20}/c_{18}| > 0.208$, so we shall tentatively assume that $c_{20}/c_{18} = -0.23$. Using (1) Section 3 with

$r=9$ $\qquad 16.323^2 c_{16} = 5(100-18.323^2)c_{18} - 20.323^2 c_{20}.$ (1)

Since $\qquad c_{20} = -0.23 c_{18},$

the last member of (1) is $95c_{18}$, so (1) yields

$$16.323^2c_{16} = -1180c_{18} + 95c_{18}, \tag{2}$$

giving

$$c_{16} = -4.07c_{18}. \tag{3}$$

The second term on the r.h.s. of (2) is 8.05 percent of the first, so the error in taking $c_{20}/c_{18} = -0.23$ cannot exceed 1.85 percent, and in fact it is very much less. Enhanced accuracy would ensue by commencing with, say, c_{26}, but this is not justifiable for slide rule work. Continuing, we have

$r=8$ $\quad 14.323^2c_{14} = 5(100-16.323^2)c_{16} - 18.232^2c_{18},$

so $\quad c_{14} = 14.8c_{18}.$ (4)

$r=7$ $\quad 12.323^2c_{12} = 5(100-14.323^2)c_{14} - 16.323^2c_{16},$

so $\quad c_{12} = -44.5c_{18}.$ (5)

$r=6$ $\quad 10.323^2c_{10} = 5(100-12.323^2)c_{12} - 14.323^2c_{14},$

so $\quad c_{10} = 80c_{18}$, *the central coefficient.* (6)

$r=5$ $\quad 8.323^2\bar{c}_8 = 5(100-10.323^2)c_{10} - 12.323^2c_{12},$

so $\quad \bar{c}_8 = 59.5_8c_{18}$ (critical point). (7)

$r=4$ $\quad 6.323^2\bar{c}_6 = 5(100-8.323^2)c_8 - 10.323^2c_{10},$

so $\quad \bar{c}_6 = 13.93c_{18}.$ (8)

d. Results in Terms of the Central Coefficient c_{10}

			Difference between overlap coefficients
$c_2 = 0.00068\ 3c_{10}$			
$c_4 = 0.01715\ c_{10}$			
$c_6 = 0.1737\ c_{10}$	$\bar{c}_6 = 0.1741\ c_{10}$		$0.0004\ c_{10}$
$c_8 = 0.745\ c_{10}$	$\bar{c}_8 = 0.7444\ c_{10}$		$-0.0006\ c_{10}$
$c_{10} = 1.00000\ 0c_{10}$	$c_{10} = 1.0000\ c_{10}$		$0.0000\ c_{10}$
$\bar{c}_{12} = -0.556\ c_{10}$	$c_{12} = -0.556\ c_{10}$		$0.0000\ c_{10}$
$\bar{c}_{14} = 0.1845\ c_{10}$	$c_{14} = 0.185\ c_{10}$		$0.0005\ c_{10}$
	$c_{16} = -0.051\ c_{10}$		
	$c_{18} = 0.0125\ c_{10}$		

The agreement between c_6, $\bar{c}_6$; etc., is satisfactory for present purposes.

e. Check on ρ

The agreement between the overlap coefficients in **d** does not warrant a check. When necessary, however, an improved value of ρ may be found as follows: Put $r=5$ in (1) Section 3, and we get

$$[100-(10+\rho)^2]c_{10} - 0.2[(12+\rho)^2c_{12} + (8+\rho)^2c_8] = 0. \tag{1}$$

The computed values of c_8, c_{12} are inserted in (1), which is then solved as a quadratic equation for ρ. Provided the difference between the trial ρ and that obtained from (1) is a small fraction of the former, the new value of ρ is likely to be the better value of the two. To the order of accuracy contemplated herein, the ρ from (1) agrees with 0.323.

The complete computation may be checked by substituting (1) Section 2 into (6) Section 1 using the values of the c in **d**, with $z=0$, or any other convenient value.

In **b** and **c** the computation has been set out deliberately in such a manner as to make the procedure easy to follow. For a systematic series

of computations, the arrangement may be improved in a way which the professional computer will readily discern. Accuracy to as many decimal places as desired may be attained by well-known processes.

9. THE SOLUTION OF (1) SECTION 1

Writing $z=\omega_1 t$, $Q=y$ in (1), (2) Section 2, and using the c in **d** Section 8, to the desired degree of approximation, we have

$$Q_1(t)\simeq\sum_1^9 c_{2r}\cos(2r+0.323)\omega_1 t, \qquad (1)$$

and

$$Q_2(t)\simeq\sum_1^9 c_{2r}\sin(2r+0.323)\omega_1 t. \qquad (2)$$

Hence the complete solution with two arbitrary constants is

$$Q(t)\simeq AQ_1(t)+BQ_2(t), \qquad (3)$$

$$=C\sum_1^9 c_{2r}\cos[(2r+0.323)\omega_1 t-\phi], \qquad (4)$$

where $C=(A^2+B^2)^{\frac{1}{2}}$, $\phi=\tan^{-1}(B/A)$. In practice either the circuit current or the e.m.f. induced in a coupled circuit is needed. The current is dQ/dt, while the e.m.f. is proportional to $dI/dt=d^2Q/dt^2$. Hence

$$dQ/dt\simeq -C\sum_1^9 (2r+0.323)\omega_1 c_{2r}\times\sin[(2r+0.323)\omega_1 t-\phi], \qquad (5)$$

and

$$dI/dt\simeq -C\sum_1^9 (2r+0.323)^2\omega_1^2 c_{2r}\times\cos[(2r+0.323)\omega_1 t-\phi]. \qquad (6)$$

The ratios of the coefficients in (4)–(6) in terms of the central coefficient, taken to be unity in each case, are set out in Table I.

10. SALIENT DIFFERENCES BETWEEN THE FORMS OF SOLUTIONS (4) OR (5) SECTION 1 AND (4) SECTION 9

If the numerical data satisfy conditions (a), (b) Section 1, the two forms of solution yield substantially the same results. But when this is not so, the procedure given in Section 8 must be used, and the following salient differences are exhibited:

TABLE I. Showing relative amplitudes of the side frequencies corresponding to Q, I, and E.

r	$Q(t)$	$Q'(t)$	$Q''(t)$
1	0.00068 3	0.00015 37	0.00003 47
2	0.01715	0.00719	0.00302
3	0.1737	0.1062	0.0649
4	0.745	0.6	0.483
5	1.00000 0	1.00000 0	1.00000 0
6	−0.556	−0.664	−0.795
7	0.185	0.255	0.356
8	−0.051	−0.0806	−0.127
9	0.0125	0.0222	0.0393

1. In (4) Section 1, the moduli of the coefficients equidistant from the central coefficient are equal, whereas in (4) Section 9 they are unequal, as will be seen from column 2 in Table I.

2. The coefficients in the series for $Q'(t)$, and $Q''(t)$ obtained by term differentiation of (4) Section 1, bear the same relation to each other as those in the series for $Q(t)$. The relative ratios for $Q'(t)$, and $Q''(t)$ obtained from (4) Section 9 differ from those for $Q(t)$, and the discrepancies are more marked the higher the derivative. Thus differentiation enhances the asymmetry about the central coefficient.

3. In (4) Section 1 the central frequency f_0, and the various side frequencies are affected to a trifling extent by capacitance variation, since ϵ is so small in a radio circuit. But owing to the relatively large value of ϵ in the warble tone circuit, in (4) Section 9, f_0 is increased by 3.23 percent to $1.0323f_0$, when $\epsilon=0.2$. Also each side frequency is increased by an amount dependent upon the value of r. For instance when $r=1$, the side frequency is $2.323f_1$ instead of $2f_1$, and when $r=9$, the corresponding values are $18.323f_1$ and $18f_1$. A common feature of the two forms of solution is that the side frequencies are spaced at integral multiples of $2f_1$ about the central frequency.

11. PROCEDURE WHEN m IS LARGE

In Section 8 suppose that $f_1=10$ c.p.s., $\epsilon=0.05$, then $\theta=2500$, and $(m+\rho)\simeq\theta^{\frac{1}{2}}(1+3\epsilon^2/4)=50.375$. Thus $m=50$ and $\rho=0.375$. If the computation started at c_2 and were symmetrical about c_{50}, 49 coefficients would have to be calculated, thereby entailing considerable labor, especially if the trial ρ were insufficiently accurate. When θ is large, this may be circumvented by calculating

only the *significant* coefficients on each side of c_m. For a given θ the greater ϵ the larger is the number of significant coefficients. To determine the significant coefficient of lowest order, namely, c_{2s} or c_{2s+1}, we use (1) or (2) Section 3, according as m is even or odd. If m, $(m-2s)$ are large enough, the last member of (1) Section 3 may be neglected. Then if $s \gg 1$, we have

$$v_{2r}^{-1} = c_{2r}/c_{2r+2} \simeq 4(s+1)^2\epsilon/(\theta - 4s^2). \quad (1)$$

Provided adequate accuracy ensues when $v_{2r}^{-1} = h$, (1) yields the approximate formula

$$2s \simeq [h\theta/(h+\epsilon)]^{\frac{1}{2}}. \quad (2)$$

With $\theta = 2500$, $\epsilon = 0.05$, $h = 0.05$, (2) gives $2s = 36$, so the number of significant coefficients on the lower side of c_{50} is $(25-18) = 7$. As in **b** Section 8 the value of c_{34}, the first coefficient omitted, may be calculated from $c_{34}/c_{36} = h$.

On the upper side of c_m, (1) Section 3 gives

$$v_{2r-2} = c_{2r}/c_{2r-2} \simeq 4(s-1)^2\epsilon/(\theta - 4s^2), \quad (3)$$

and (2) is usable here also. Hence including c_m, the total number of significant coefficients is $7+1+7 = 15$. If $h = 0.1$ gave adequate accuracy, there would be eleven significant coefficients. Formula (2) is applicable when m is odd, provided that $(2s+1)$ be written for $2s$. If m is very large and ϵ very small (2) Section 1 may be written with adequate approximation

$$y'' + \theta(1 - 2\epsilon\cos 2z)y = 0, \quad (4)$$

so the solution takes the form at (4) Section 1.

12. FREQUENCY MODULATION FUNCTIONS AND THEIR NORMALIZATION

Consider the coupled circuit shown schematically in Fig. 1B. If the coefficient of coupling is small, and the impedance of Z_2 much greater than that of the remainder of the circuit, the P.D. on Z_2 is nearly $E_2 = MdI_1/dt$. Thus $I_2 \simeq E_2/Z_2$. If another circuit is coupled electromagnetically to Z_2, the P.D. across Z_3 will be approximately proportional to d^2I_2/dt^2, and so on. Thus the relative amplitudes of the side frequency P.D.S. in a particular circuit depend upon the number of circuits preceding it. In the nth circuit, the P.D. may be found by differentiating the series for $Q(t)$ in the first circuit $(n+1)$ times. This procedure is valid by virtue of uniform convergence as treated in Section 5. Accordingly it is proposed to base our definitions of the frequency modulation functions upon (1)–(4) Section 2, these being the forms of solution for the quantity $Q(t)$.

If in (1), (2) Section 2, $\rho = p/s$, a rational fraction in its lowest terms, the solutions are periodic in z real, with period $2s\pi$, $s \geq 2$. Then if K is a normalizing constant, we shall adopt the convention that[3]

$$\frac{K}{\pi s}\int_0^{2\pi s} [\sum c_{2r}\cos(2r+\rho)z]^2 dz = \frac{K}{\pi s}\int_0^{2\pi s} [\sum c_{2r}\sin(2r+\rho)z]^2 dz = K\sum_{-\infty}^{\infty} c_{2r}^2 = 1, \quad (1)$$

so

$$K = \left[\sum_{-\infty}^{\infty} c_{2r}^2\right]^{-\frac{1}{2}}. \quad (2)$$

When ρ is irrational, we use definition (2) above, i.e. we make $s \to +\infty$ in (1). Writing $E_{2r}^{(2n+\rho)} = Kc_{2r}$, we define the f-m functions of order $(2n+\rho)$ to be

$$\left.\begin{matrix} cf \\ sf \end{matrix}\right\}_{2n+\rho}(z, \epsilon) = \sum_{r=-\infty}^{\infty} E_{2r}^{(2n+\rho)} \begin{matrix}\cos \\ \sin\end{matrix}(2r+\rho)z, \quad (3, 4)$$

and those of order $(2n+1+\rho)$ to be

$$\left.\begin{matrix} cf \\ sf \end{matrix}\right\}_{2n+1+\rho}(z, \epsilon) = \sum_{r=-\infty}^{\infty} E_{2r+1}^{(2n+2+\rho)} \times \begin{matrix}\cos \\ \sin\end{matrix}(2r+1+\rho)z. \quad (5, 6)[4]$$

In this notation c, s, signify cos, sin, while f indicates frequency modulation. When $\epsilon \to 0$, (3), (4) $\to \cos(2n+\rho)z$, $\sin(2n+\rho)z$, while (5), (6) $\to \cos(2n+1+\rho)z$, and $\sin(2n+1+\rho)z$, respectively. Thus all the E tend to zero, except $E_{2n+1}^{(2n+\rho)}$, which tends to unity. Also when $\epsilon = 0$, $\theta = (2n+\rho)^2$ or $(2n+1+\rho)^2$, as the case may be.

[4] For this case use (1), (2) with $(2r+1)$ for $2r$, and K_1 for K.

13. CHANGING THE SIGN OF ϵ

This may be effected by writing $(\frac{1}{2}\pi - z)$ for z in (6) Section 1. Making this change in (3)–(6) Section 12 yields solutions having the following properties: (a) they are neither odd nor even, (b) they do not reduce to the limiting forms in Section 12 when $\epsilon \to 0$, (c) they are unduly complicated. If we write $(-1)^r c_{2r}$ for c_{2r}, $(-1)^r c_{2r+1}$ for c_{2r+1} in the respective recurrence relations (1), (2) Section 3, the sign of ϵ is changed. Using this substitution in (3)–(6) Section 12 with $-0.5 < \epsilon < 0$, we obtain the simple even and odd solutions (f-m functions)

$$\left.\begin{matrix} cf \\ sf \end{matrix}\right\}_{2n+\rho}(z, -\epsilon) = (-1)^n \sum_{-\infty}^{\infty} (-1)^r E_{2r}^{(2n+\rho)} \begin{matrix} \cos \\ \sin \end{matrix} (2r+\rho)z, \quad (1, 2)$$

and

$$\left.\begin{matrix} cf \\ sf \end{matrix}\right\}_{2n+1+\rho}(z, -\epsilon) = (-1)^n \sum_{-\infty}^{\infty} (-1)^r E_{2r+1}^{(2n+1+\rho)} \begin{matrix} \cos \\ \sin \end{matrix} (2r+1+\rho)z. \quad (3, 4)$$

The purpose of the multiplier $(-1)^n$ is to insure a conventional positive sign when $\epsilon = 0$, and the functions reduce to $+\cos(m+\rho)z$, and $+\sin(m+\rho)z$, respectively, with $m = 2n$ or $2n+1$.

14. OSCILLATORY CIRCUIT HAVING CONSTANT RESISTANCE BUT PERIODICALLY VARIABLE CAPACITANCE

This is shown schematically in Fig. 1C, the differential equation being

$$d^2Q/dt^2 + (R/L)dQ/dt + Q/LC_0(1 + 2\epsilon \cos 2\omega_1 t) = 0. \quad (1)$$

Using the substitutions given in Section 1, and putting $R/2L = \kappa$, we get

$$(1 + 2\epsilon \cos 2z)(y'' + 2\kappa y') + \theta y = 0. \quad (2)$$

Writing $y = e^{-\kappa z}u(z)$, (2) is transformed to

$$(1 + 2\epsilon \cos 2z)u'' + (\theta_1 - 2\epsilon_1 \cos 2z)u = 0, \quad (3)$$

with $\theta_1 = (\theta - \kappa^2)$, and $\epsilon_1 = \epsilon\kappa^2$. The formal solutions of (3) are of the type given at (1)–(4) Section 3. Substituting (1) Section 2 into (3) above, and equating the coefficient of $\cos(2r+\rho)z$ to zero for $r = -\infty$ to $+\infty$ yields the recurrence relation

$$[\theta_1 - (2r+\rho)^2]c_{2r} - [\epsilon(2r-2+\rho)^2 + \epsilon_1]c_{2r-2} - [\epsilon(2r+2+\rho)^2 + \epsilon_1]c_{2r+2} = 0. \quad (4)$$

The recurrence relation corresponding to (3), (4) Section 2, is (4) with $(2r+1)$ for $2r$. By analysis akin to that in Section 6, formulas for calculating m and ρ may be derived. Then the procedure follows on the lines of that in Section 8 *et seq.* Approximate solutions of (1) Section 1 and (1) above are given in reference 3, pages 280 and 283, the form being quite different from that herein.

The Sensitized Luminescence of Manganese-Activated Calcite

JAMES H. SCHULMAN, LYLE W. EVANS, AND ROBERT J. GINTHER
Naval Research Laboratory, Washington, D. C.

AND

K. J. MURATA
*Geological Survey, U. S. Department of the Interior, Washington, D. C.**

(Received January 20, 1947)

Synthetic manganese-activated calcites are shown to be practically inert to ultraviolet excitation in the range 2000–3500A, while they are luminescent under cathode-ray excitation. The incorporation of small amounts of an auxiliary impurity along with the manganese produces the strong response to ultraviolet radiation hitherto ascribed to $CaCO_3$:Mn itself. Three such impurities have been studied: lead, thallium, and cerium. The first two induce excitation in the neighborhood of the mercury resonance line, while the cerium introduces a response principally to longer wave ultraviolet. The strong response to 2537A excitation shown by some natural calcites is likewise found to be due to the presence of lead along with the manganese, rather than to the manganese alone. The data do not warrant ascribing the longer wave-length ultraviolet-excited luminescence of all natural calcites to the action of an auxiliary impurity. The essential identity of the cathode-ray excited luminescence spectra of $CaCO_3$:Mn, $CaCO_3$:(Pb+Mn), $CaCO_3$:(Tl+Mn), and $CaCO_3$:(Ce+Mn) with the 2537A-excited spectra of the latter three is evidence that the luminescent center in all cases is the manganese ion or the MnO_6 group. It is shown that a "cascade" mechanism for the action of the auxiliary impurities, lead, thallium, and cerium, is incorrect; and that the phenomenon must be considered as a case of sensitized luminescence. Owing to the nature of cathode-ray excitation, the manganese activator can be excited by this agent even in the absence of a second impurity. For optical excitation, however, an absorption band for the ultraviolet must be established by building into the $CaCO_3$:Mn a second impurity or "sensitizer."

THE rose to orange-red luminescence of natural calcite has been studied by many investigators[1–5] and has been ascribed to the presence of manganese as an activator. The preparation of a synthetic manganese-activated calcite phosphor was described by Fonda,[6] who precipitated $CaCO_3$:Mn from a $CaCl_2$-$MnCl_2$ solution by means of $(NH_4)_2CO_3$. This material fluoresced with a rose color under 2537A excitation, the best preparation having 30 percent of the brightness of calcite from Franklin, New Jersey. Our attempts to duplicate this preparation yielded material much inferior in brightness to Fonda's product, judging by comparison with the best sample of calcite that we could obtain from the above locality.

It has recently been shown by Murata and Smith[7] that manganese-activated sodium chloride is not excited by 2537A radiation unless lead is also present as a "co-activator" in the phosphor. This observation, together with our inability to duplicate Fonda's work, suggested that an unsuspected impurity—possibly lead—was at least partially responsible for the luminescence of his preparations, and that the amount of this impurity was smaller in our work. This was found to be the case. When the reagents used to prepare the calcite were first purified before following Fonda's procedure for precipitation of the phosphor,** the product was almost completely inert to both 2537A*** and "3650A"*** excitation.

* Data on natural calcites published by permission of the Director, Geological Survey, U. S. Department of Interior.

[1] E. L. Nichols, H. L. Howes, and D. T. Wilber, Phys. Rev. **12**, 351 (1918).

[2] T. Tanaka, J. Opt. Soc. Am. **8**, 287 (1924).

[3] E. L. Nichols, H. L. Howes, and D. T. Wilber, Carnegie Inst. Rep. **384**, 367 (1928).

[4] W. L. Brown, Univ. Toronto Studies, Geol. Series **36**, 45 (1934).

[5] P. Pringsheim, *Fluoreszenz and Phosphoreszenz* (Julius Springer, Berlin, 1928), p. 312.

[6] G. R. Fonda, J. Phys. Chem. **44**, 435 (1939).

[7] K. J. Murata, and R. L. Smith, Am. Mineral **31**, 527 (1946).

** Preparation of the phosphors was carried out by Fonda's procedure, precipitation of the $CaCO_3$ from a $CaCl_2-MnCl_2$ solution at 70° by means of 50 percent excess $(NH_4)_2CO_3$ solution, followed by aging of the precipitate in its supernatant liquor for 10 minutes at the boiling point. 100 ml volumes of $CaCl_2-MnCl_2$ solution

Luminescence could be produced in the final calcite product by adding to the calcium chloride solution an auxiliary component—either a lead, thallium, or cerium salt—along with the manganese chloride prior to precipitation of the phosphor. The addition of lead or thallous chlorides as auxiliary impurities, giving $CaCO_3$:(Pb+Mn) and $CaCO_3$:(Tl+Mn), respectively, induced strong luminescence under 2537A excitation, but only a minor increase in the "3650A" excited luminescence. The color of the luminescence was rose, in samples of low brightness, to orange-red in samples of high brightness.† The brightest preparations of $CaCO_3$:(Pb+Mn) were 90 percent as bright, under 2537A excitation, as an outstandingly efficient specimen of calcite from Langban, Sweden.

The addition of cerium to the $CaCl_2$-$MnCl_2$ solution (as cerous ammonium nitrate) prior to the precipitation gave a product that luminesced both under 2537A and "3650A" excitation, with a rose color in both cases. Enhancement of the response to the latter excitation was greater with cerium than with lead or thallium as the auxiliary impurity, cerium-bearing samples being much brighter than the $CaCO_3$:Mn.

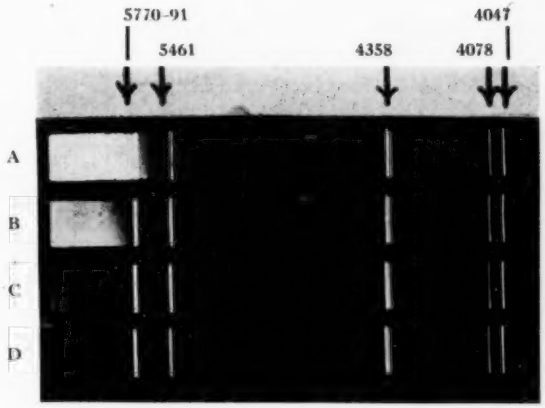

FIG. 1. Luminescence of synthetic manganese-activated calcites under 2537A excitation. Gaertner L231 spectrometer with camera attachment. Type II-F plate. Exposure times: 25 minutes. Exciting source: "Mineralite" lamp without filter.

A. Cadmium borate:Mn
B. Calcite:(Pb+Mn)
C. Calcite:(Tl+Mn)
D. Calcite:(Ce+Mn).

LUMINESCENCE UNDER OPTICAL EXCITATION

The 2537A-excited luminescence spectra of synthetic calcites containing lead, thallium, and cerium additions are shown in Figs. 1 and 2. Included also in Fig. 1 is the 2537A-excited luminescence spectrum of a sample of manganese-activated cadmium borate phosphor having a quantum efficiency of 75–80 percent under this excitation. The spectra given by the three calcite preparations are essentially identical, starting at about 5780A and extending beyond the limits of sensitivity of the plate used.

Measurements of the brightness of a series of preparations of $CaCO_3$:(Pb+Mn), $CaCO_3$:(Tl+Mn), and $CaCO_3$:(Ce+Mn) are given in

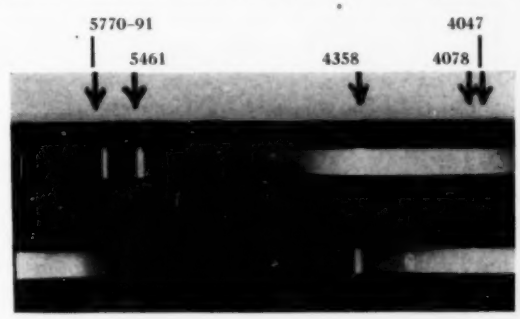

FIG. 2. Luminescence of synthetic calcite:(Ce+Mn) under 2537A excitation. Gaertner L231 spectrometer with camera attachment. Type II-F plate.

A. "Mineralite" lamp, no filter, 1 minute exposure.
B. Calcite:(Ce+Mn) excited by "Mineralite" through Corning 9863 filter. Exposure time: 16 hours. Luminescence between 4000–5000A caused by fused silica of lamp.

---

were used in all the experiments. The concentrations of our solutions were: $CaCl_2$, 0.162 molar; $(NH_4)_2CO_3$, 0.25 molar. These concentrations are twice as high as those employed by Fonda.

Purification of the $CaCl_2$ solution was accomplished by partial (33 percent) precipitation with $(NH_4)_2CO_3$ at 70°. Judging by the inertness of the final product, a greater degree of purification was effected by this procedure than by treatment of the $CaCl_2$ solution with H_2S. The $(NH_4)_2CO_3$ solution was purified by partial (33 percent) precipitation with $CaCl_2$ solution at 70°. It was not found necessary to purify the $MnCl_2$ solution, but this is desirable in general. Purification of the $MnCl_2$ may be effected by the same procedure used for purification of the $CaCl_2$.

*** 2537A excitation was provided by a low pressure mercury vapor lamp ("Mineralite" or "germicidal" lamp) equipped with a Corning No. 9863 filter. "3650A" excitation was provided by a 360BL lamp with the same filter, giving a broad band in the near ultraviolet (3300–4200A) with a peak near 3650A.

† Spectroscopic comparison of the luminescence of several preparations showed that the rose-colored fluorescence of the weaker samples is due to the superposition of visible (violet and blue) light from the exciting source upon the light emitted by the sample; during the brief afterglow following cessation of excitation the orange-red color of the luminescence is seen, since visible light from the lamp is no longer superimposed. The reflection of light from the exciting source becomes less important the brighter the phosphor, and the true orange-red luminescence color is therefore observed with these brighter samples even during excitation.

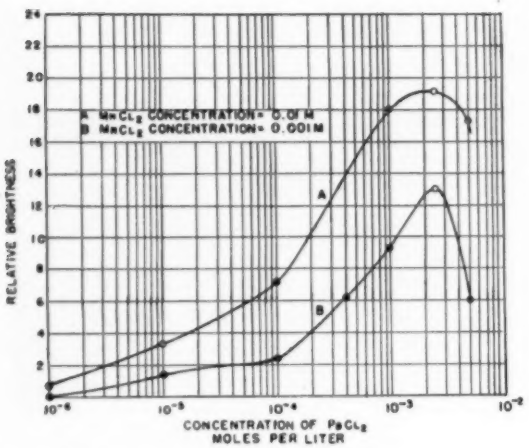

FIG. 3. Effect of lead concentration on brightness of synthetic calcites.

Table I, relative to the brightness of the above mentioned cadmium borate phosphor. In these measurements, circular plaques of the samples, one inch in diameter, were illuminated by a "Mineralite" lamp with a Corning 9863 filter and viewed by a barrier layer photo-cell through a red filter cutting off visible light below 5500A. A plaque of unactivated $CaCO_3$ was used to obtain the "dark response" of the system, which was due to the small amount of visible radiation from the lamp passed by both filters. The small correction obtained in this way was applied to all the readings.

The data on $CaCO_3$:(Pb+Mn) are further graphically illustrated in Figs. 3 and 4. An x-ray diffraction study of all the samples indicated that a number of them were mixtures of calcite and aragonite, instead of pure calcite. Those preparations in which aragonite was found are indicated by • in the figures, while the pure calcite samples are indicated by ○.††

†† The preparation of the pure calcite form of $CaCO_3$, $CaCO_3$:Pb, $CaCO_3$:Tl, and $CaCO_3$:Ce by the hot precipitation, recommended by Fonda and used by us in most of the work, was found to be impossible, aragonite or, at best, mixtures of calcite and aragonite being formed instead. Apparently manganese has to be co-precipitated with the calcium carbonate in order to generate the calcite phase, although even in this case the formation of aragonite is not always prevented. Manganese-free calcite, with or without Pb, Tl, or Ce impurity, could be prepared only by low temperature precipitation. To obtain these materials a saturated calcium bicarbonate solution was made by bubbling carbon dioxide through a calcium carbonate suspension, filtering off the excess solid, and adding $PbCl_2$, TlCl, or $CeCl_3$ solution to the filtrate. From such solutions calcite was deposited at room temperature after a day or two.

LUMINESCENCE UNDER CATHODE-RAY AND SPARK-COIL EXCITATION

Visual observations were made of the cathode-ray excited luminescence of a group of synthetic calcite phosphors of the same manganese concentration, including a sample containing manganese alone, and samples containing manganese plus one of each of the auxiliary impurities: lead, thallium, and cerium. The phosphor samples were mounted side by side in $\frac{1}{8}$" diameter $\times \frac{1}{16}$" deep wells drilled into a brass plate, which was placed inside a demountable cathode-

TABLE I. Brightness of $CaCO_3$:(Pb+Mn), $CaCO_3$:(Tl+Mn), and $CaCO_3$:(Ce+Mn) phosphors under 2537A excitation.

Molality of solution** with respect to		Relative brightness
Pb^{++}	Mn^{++}	
5×10^{-3}	10^{-2}	17.2
5×10^{-3}	10^{-3}	6.1
2.5×10^{-3}	10^{-2}	19.2
2.5×10^{-3}	10^{-3}	13.0
10^{-3}	5×10^{-2}	0.26
10^{-3}	3×10^{-2}	2.32
10^{-3}	10^{-2}	18.0
10^{-3}	5×10^{-3}	19.2
10^{-3}	3×10^{-3}	18.2
10^{-3}	10^{-3}	9.3
10^{-3}	10^{-4}	Too weak to measure
4×10^{-4}	10^{-3}	6.3
10^{-4}	10^{-2}	7.2
10^{-4}	10^{-3}	2.44
10^{-4}	10^{-4}	Too weak to measure
10^{-5}	10^{-2}	3.3
10^{-5}	10^{-3}	1.52
10^{-5}	10^{-4}	Too weak to measure
10^{-6}	10^{-2}	0.76
10^{-6}	10^{-3}	Too weak to measure
10^{-6}	10^{-4}	0.
Tl^{+}	Mn^{++}	
10^{-3}	10^{-2}	5.8
10^{-3}	10^{-3}	Too weak to measure
10^{-3}	10^{-4}	0.
10^{-4}	10^{-2}	1.55
10^{-4}	10^{-3}	Too weak to measure
10^{-4}	10^{-4}	0.
Ce^{+++}	Mn^{++}	
10^{-3}	10^{-2}	0.64*(*b*)
10^{-3}	10^{-3}	0.71*(*a*)
10^{-3}	10^{-4}	0.
10^{-4}	10^{-2}	0.79*(*c*)
10^{-4}	10^{-3}	Too weak to measure
10^{-4}	10^{-4}	0.
Calcite, Franklin, New Jersey		12.4
Calcite, Langban, Sweden		21.3
Cadmium borate: manganese		100.

* Brightness under "3650A" excitation: $(a)>(b)>(c)$.

** Polarographic and colorimetric analyses of several of the above samples showed that the mole ratios of Mn/Ca, Pb/Ca, and Ce/Ca in the solid were substantially the same as in the solution prior to precipitation, while in the case of thallium the Tl/Ca ratio in the phosphor was only one seventh of its value in the solution prior to precipitation. These results are in agreement with what is expected from elementary chemical considerations concerning the solubilities of the various carbonates, basic carbonates, and hydroxides involved.

ray tube. There was no perceptible color difference between the luminescence of $CaCO_3$:Mn, $CaCO_3$:(Pb+Mn), $CaCO_3$:(Tl+Mn) and $CaCO_3$:(Ce+Mn) when they were simultaneously bombarded with cathode rays (accelerating voltage, 800 volts; current density approximately 100 μamps/cm^2). The close proximity of the samples would tend to make any differences between them readily detectable.

Since the design of the demountable cathode-ray tube used in making these visual observations was not suited for use as a spectrographic source unit, the luminescence spectra of the above phosphors under spark-coil excitation, in air at a pressure of 10^{-2} mm Hg, were photographed instead (Fig. 5). It has been our observation that this type of excitation and cathode-ray excitation give the same luminescence spectrum with all the standard sulfide, silicate, fluoride, and tungstate phosphors. The visual observations and the spectrograms of Fig. 5 show the essential identity of the luminescence under corpuscular excitation of manganese-activated calcites with or without auxiliary impurities.

NATURAL CALCITES

In order to determine whether or not the luminescence of natural manganese-bearing calcites is due to an auxiliary impurity, as with our synthetic samples, preliminary qualitative spectrographic analyses were made of brightly orange-red fluorescing (2537A excitation) natural calcites from the following localities: (1) Franklin, New Jersey; (2) Langban, Sweden; (3) Mount Spurr, Alaska Peninsula, Alaska; (4) Sunset Mine, Superior, Arizona; and (5) Guanajuato, Mexico. All of them were found to contain both manganese and lead. The manganese content of the samples ranged from tenths of a percent to several percent; and the lead from hundredths of a percent to over a percent. Neither thallium nor cerium could be detected in any of the samples, which therefore are samples of lead-induced luminescence. It follows that the "3650A" excited luminescence of these natural calcites is induced by some other impurity than those put into our synthetic samples, or is due to the manganese alone.

Chemical analysis of the outstandingly bright

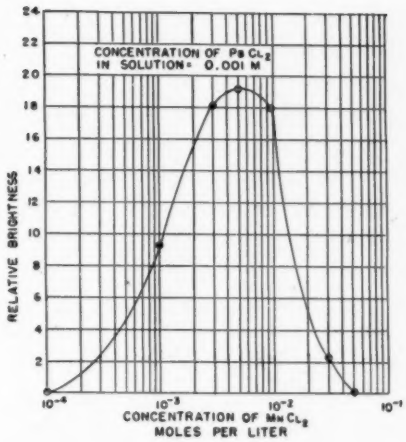

FIG. 4. Effect of manganese concentration on brightness of synthetic calcites.

Langban calcite showed that it contained 1.3 weight percent of lead and 3.0 weight percent of manganese, which is the order of magnitude of both impurities present in our synthetic samples.

The well-formed crystals from Guanajuato, Mexico, showed a sharply-zoned fluorescence that was restricted to the outermost millimeter of the crystals. Spectrographic analysis of the fluorescent and non-fluorescent portions showed that the manganese content was approximately 0.1 percent in both. The fluorescent portion, however, also contained several tenths of a

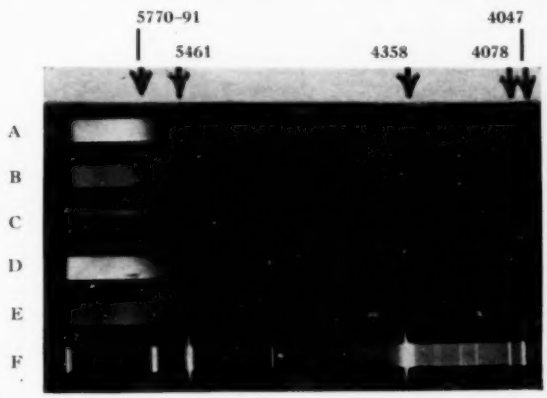

FIG. 5. Luminescence of manganese-activated calcites under spark-coil excitation. Gaertner L231 spectrometer with camera attachment. Type II-F plate. Exposure times: 5 minutes. Density differences between samples not significant.

A. Cadmium borate: Mn
B. Calcite: Mn
C. Calcite: (Pb+Mn)
D. Calcite: (Tl+Mn)
E. Calcite: (Ce+Mn)
F. "Mineralite" lamp, no filter, 1 minute exposure (for wave-length calibration).

percent of lead, whereas the non-fluorescent portion had no detectable lead.

The preliminary study of natural calcites thus confirms the results obtained with our synthetic samples, and demonstrates that the luminescence of natural calcites under excitation in the region of mercury resonance radiation is due—not to manganese alone, as has hitherto been believed—but to the simultaneous presence of manganese and lead in the crystal.

DISCUSSION

The lack of fluorescence response of $CaCO_3$:Mn to optical excitation by ultraviolet radiation in the neighborhood of the mercury resonance line, and the development of such a response by the incorporation of auxiliary impurities such as lead, thallium, or cerium, may be considered from three different viewpoints. First, it may be postulated that the manganese activator alone in the calcite structure does not constitute a luminescent center, but that luminescence emission is possible only from a more complex center containing lead, thallium, or cerium in addition to the manganese. The auxiliary impurities and the manganese are accordingly interpreted as "co-activators."[7] This interpretation is ruled out by the fact that all samples of manganese-activated calcite, whether or not they luminesced under ultraviolet excitation, responded to cathode-ray and spark-coil excitation with the same luminescence emission spectrum. The cathode-ray excited luminescence is essentially identical with the optically-excited luminescence of the preparations responsive to the latter type of excitation. This luminescence is of the typical orange-red color associated with manganese in sixfold coordination with oxygen,[8,9] as would be expected if Mn^{++} replaced Ca^{++} substitutionally in calcite. This shows that the Mn^{++} ions or the MnO_6 groups existing in the crystal constitute in themselves luminescent centers, independent of the presence or absence of an auxiliary impurity and of the nature of the impurity when present.

A second interpretation is that we are dealing here with a "cascade" process in the case of ultraviolet excitation of the phosphors containing an auxiliary impurity along with the manganese. According to this simple picture, the manganese and the auxiliary impurity need not be considered as forming a manganese ion-impurity ion complex, but act as two separate luminescent centers. The auxiliary impurity absorbs the exciting "short" ultraviolet radiation and emits as fluorescence longer wave ultraviolet or even visible radiation capable of exciting the manganese activator to its typical luminescence. This interpretation assumes, then, a greater or less degree of coincidence between the position of the manganese absorption band in $CaCO_3$:Mn and the emission bands of $CaCO_3$:Pb, $CaCO_3$:Tl, and $CaCO_3$:Ce. This interpretation is contradicted by simple experiments in which intimate mechanical mixtures of $CaCO_3$:Mn with $CaCO_3$:Pb, $CaCO_3$:Tl, and $CaCO_3$:Ce, respectively, were examined under 2537A excitation. In no case was luminescence observed.

The third interpretation of our results is that the $CaCO_3$:(Pb+Mn), $CaCO_3$:(Tl+Mn), and $CaCO_3$:(Ce+Mn) phosphors are cases of "sensitized luminescence," such as those first described by Rothschild[10] in the group of rare-earth activated alkaline earth sulfide phosphors. In this model it is assumed that (a) $CaCO_3$:Pb, $CaCO_3$:Tl, and $CaCO_3$:Ce have an absorption band in the short wave-length ultraviolet region in question; (b) $CaCO_3$:Mn does not have an absorption band in this region of the ultraviolet, but may have absorption bands in another spectral range; (c) the simultaneous incorporation of manganese and lead, thallium, or cerium in calcite leaves conditions (a) and (b) substantially unchanged; (d) energy absorbed in the lead, thallium, or cerium-induced absorption bands is transferred to the manganese by a process analagous to collisions of the second kind rather than by a radiative ("cascade") process; and (e) the luminescence emission is due to the Mn^{++} ion alone and is independent in spectral characteristics of how the energy is imparted to this ion.

The fundamental lattice absorption of pure calcite lies at wave-lengths shorter than about

[8] S. H. Linwood, and W. A. Weyl, J. Opt. Soc. Am. **32**, 443 (1942).
[9] J. H. Schulman, J. App. Phys. **17**, 902 (1946).
[10] S. Rothschild, Physik Zeits. **35**, 557 (1934); *ibid.* **37**, 757 (1936).

2250A.[11] The introduction of absorption bands at longer ultraviolet wave-lengths than the fundamental crystal absorption by the incorporation of lead, thallium, silver, and other heavy metal impurities in the alkali halides is well-known,[12] and a similar effect is to be expected in crystals with anions other than the halogens, although the position of the absorption peak produced by a given cation impurity will differ with the nature of the host crystal. The absorption produced by the impurity ion may be due to the excitation of this ion itself, as proposed by Seitz[13] for the alkali halide-thallium phosphors; or to the higher ionization potential of the substituting cation compared to that of the cation of the crystal itself[14]; or to a greater polarizing power of the impurity ion compared to the cation of the host crystal. In our manganese-activated calcites, the lead, thallium, and cerium impurities would act in this way as "absorbers" or "sensitizers," and this function would be performed whether the "sensitizers" themselves are capable of emitting luminescent radiation of their own or not. The manganese activator and the lead, thallium, or cerium "sensitizer" would have to be near neighbors in the calcite structure for the energy to be transferred from the sensitizer to the manganese, but this requirement is different from the concept of a $Mn^{++}-Pb^{++}$ (or $-Tl^{+}$ or $-Ce^{+++}$) complex as the luminescent center.

According to this picture of sensitized luminescence, no sensitizer should be required for the appearance of the manganese luminescence under cathode-ray bombardment. Under this type of excitation, energy is absorbed primarily by the atoms of the host crystal, the absorbed energy then being capable of transmission over large distances through the lattice to the site of the manganese activator by means of excitons or by the movement of electrons and positive holes through the crystal.[15]

The validity of the above interpretation of sensitized luminescence is supported by a more detailed study of the excitation and absorption (reflection method) of manganese-activated calcite phosphors being made by Mr. Elias Burstein and Mrs. Margaret White, Crystal Section, N.R.L., whom we thank for permission to present a summary of their preliminary results. Data on the excitation and reflection spectra of the lead, thallium, and cerium sensitized phosphors, as well as of calcites containing lead, thallium, cerium, and manganese separately, and of pure calcite are given in Figs. 6 and 7.

For the excitation studies, plaques of phosphor powder were irradiated with ultraviolet from a Beckman hydrogen discharge lamp, monochromatized by a Beckman quartz spectrophotometer, and the irradiated surface viewed by an RCA 1P21 multiplier photo-tube through a Corning 2418 filter. The design of the apparatus allowed the continuous automatic plotting of the photo-cell response *vs.* excitation wave-length in about 15 minutes over the range of 2000 to 3500A. The data are presented in Fig. 6 as cell response *vs.* wave-length instead of as a true excitation spectrum, since no means was provided for keeping constant ultraviolet energy incident on the phosphor at all wave-lengths or for measuring the intensity of the incident ultraviolet as a function of wave-length. Since the hydrogen lamp employed gives a continuous spectrum without sharp changes in output with wave-length, and the transmission of the monochroma-

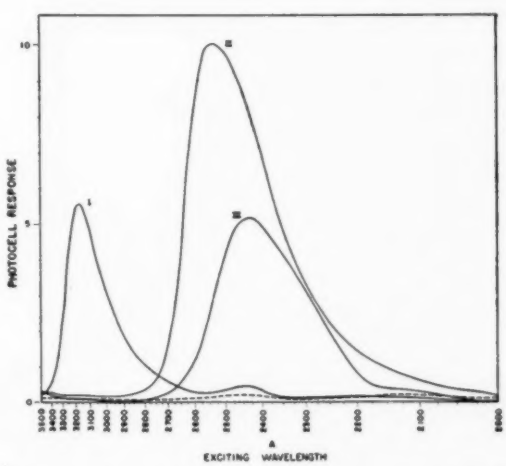

FIG. 6. Ultraviolet excitation spectra of synthetic manganese-activated calcites.

I. Calcite: (Ce+Mn)
II. Calcite: (Pb+Mn)
III. Calcite: (Tl+Mn)
Dotted curve—calcite: Mn.

[11] International Critical Tables, Vol. VII, pp. 270–273.
[12] R. Hilsch, Physik. Zeits. **38**, 1031 (1927).
[13] F. Seitz, J. Chem. Phys. **6**, 150 (1938).
[14] N. F. Mott, and R. W. Gurney, *Electronic Processes in Ionic Crystals* (Oxford University Press, 1940), p. 102.
[15] See reference 14, p. 207.

tor likewise varies continuously, the data suffice to locate qualitatively, at least, the positions of excitation bands. Pure natural calcite (curve not shown in Fig. 6) gave no response over the whole range. Synthetic calcite, activated with manganese alone (dotted curve, Fig. 6) showed only a very faint luminescence under excitation near 2150A and again near 2450A. It is not yet known whether this very slight response is due to manganese alone or to traces of a sensitizing impurity which our purification method failed to remove. With $CaCO_3$:(Ce+Mn) (curve I) the 2450A excitation peak is somewhat higher, but a much more important effect is the far stronger excitation band created by the cerium at longer wave-lengths, peaking at about 3170A. $CaCO_3$:(Tl+Mn) (curve III) has a strong excitation region peaking at 2435A, while $CaCO_3$:(Pb+Mn) (curve II) shows a very intense excitation region with a peak at 2540A. This last band coincides almost exactly with the wave-length of mercury resonance radiation, which probably accounts for the much higher efficiency of luminescence of the $CaCO_3$:(Pb+Mn) phosphors under this excitation compared to that of $CaCO_3$:(Tl+Mn) and $CaCO_3$:(Ce+Mn) (*cf.* Table I).

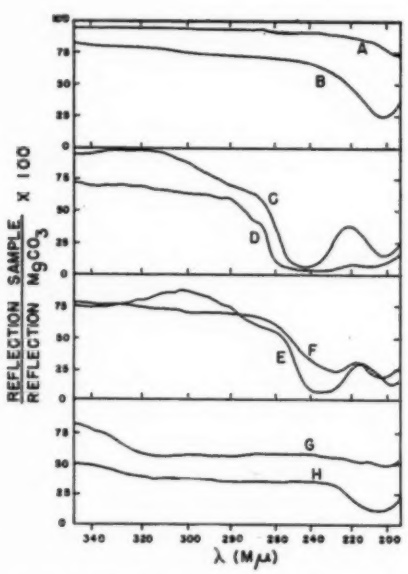

FIG. 7. Reflection spectra of calcite preparations.

A. Unactivated calcite (optical quality, non-luminescent natural specimen)
B. Calcite:Mn
C. Calcite:Pb
D. Calcite:(Pb+Mn)
E. Calcite:Tl
F. Calcite:(Tl+Mn)
G. Calcite:Ce
H. Calcite:(Ce+Mn).

In Fig. 7 are given the results of reflection measurements on the above materials. For these measurements the samples were illuminated with a Hanovia hydrogen-discharge lamp, and the reflected light analyzed by a Gaertner quartz monochromator, using a 1P28 multiplier phototube as a receiver. A plaque of magnesium carbonate[16] was used as a standard and the photocell response to the reflection from the samples was compared to the response from the standard. Absolute measurements cannot be made by this method, of course, since the reflectivity is a function of particle size, packing of the sample, angles of illumination and viewing. Comparison of the results obtained with this system with true absorption measurements on materials obtainable in the form of single plates or crystals has, however, given good agreement as to the location of absorption bands and qualitative information as to their intensity. The difference in reflection between different samples in regions where they are both quite transparent is not to be considered significant on account of the disturbing factors mentioned above; significance should be attached only to the shape of each curve and the structure or absence of structure found therein. The measurements were made point by point, with data being taken every 50A between 2000 and 3400A. The data indicate that the introduction of manganese into calcite does not introduce any pronounced absorption beyond that present in pure calcite in the wave-length range investigated except at wave-lengths shorter than about 2400A. The introduction of lead in the calcite calls forth two fairly sharp absorption bands, which persist when manganese is introduced in addition to the lead.††† The absorption band lying at the longer wave-lengths in $CaCO_3$:Pb and $CaCO_3$(Pb+Mn) coincides fairly well with the position of the excitation band of the latter phosphor. The same situation applies in the case of $CaCO_3$:Tl and $CaCO_3$:(Tl+Mn). The results with cerium are less satisfactory because there is no sharp peak in

[16] C. F. Goodeve, Trans. Faraday Soc. **34**, 902 (1938).

††† The greater absorption and overlapping of the peaks in $CaCO_3$:(Pb+Mn) compared to $CaCO_3$:Pb is due to the higher Pb concentration in the former, 1.60 mole percent *vs.* 0.4 mole percent Pb in the latter.

the absorption coinciding with the peak of the excitation spectrum of $CaCO_3$:(Ce+Mn). However, even here a considerable increase in absorption over pure $CaCO_3$ is evident, there being a drop of approximately 20–30 percent in the reflection between 3400A and 3150A for both $CaCO_3$:Ce and $CaCO_3$:(Ce+Mn).

A study of the literature reveals a number of known phosphors which appear to be based upon the mechanism of sensitized luminescence outlined above. Among these are alkaline earth borates, phosphates, silicates, and silico-phosphates,[17,18] and the NaCl:(Pb+Mn) of Murata and Smith.[7] In principle it should be possible to introduce excitation bands for any desired ultraviolet spectral region by choice of the proper sensitizer for any phosphor showing response to cathode-ray or x-ray excitation but not to ultraviolet excitation. Investigations under way at the Naval Research Laboratory are concerned with further studies along these lines.

SUMMARY

It is shown that synthetic preparations of calcite, with manganese as an activator, are luminescent under cathode-ray excitation, but are substantially non-luminescent under ultraviolet irradiation. By co-precipitation of small amounts of lead, thallium, or cerium with the manganese-activated calcium carbonate, there is produced no essential change in the cathode-ray luminescence spectrum, but the products are then strongly excited by ultraviolet radiation as well. Spectrographic analyses of natural calcites from a number of different localities show that in the strongly luminescent (2537A excitation) specimens of the natural mineral, lead accompanies the manganese activator, while in the non-luminescent (2537A excitation) specimens the manganese is present without lead. The near-ultraviolet excited luminescence of most natural calcites is not connected with the lead, and has not as yet been ascribed to the presence of any specific auxiliary impurity.

The interpretation of these results is shown to be most consistent with the concept of a "sensitized" luminescence, and the possible application of this viewpoint to known phosphors and to the synthesis of new phosphors having specific excitation bands is pointed out.

ACKNOWLEDGMENT

We wish to express our thanks to Mrs. Esther Claffy for the chemical analyses of our synthetic calcites. The chemical analysis of the Langban calcite was obtained through the kindness of Professor C. Palache, Department of Mineralogy, Harvard University.

[17] Hüniger and Panke, U. S. Patents 2,241,950 and 2,241,951 of May 13, 1941.
[18] Aschermann and Strubing, U. S. Patent 2,308,736 of January 19, 1943.

Electron Beam Deflection

Part I. Small-Angle Deflection Theory

R. G. E. HUTTER
Sylvania Electric Products, Inc., Flushing, New York
(Received February 26, 1947)

Two general mathematical methods are discussed which may be used to study the effects of electric and/or magnetic deflection fields on electron beams. The basic equations for the "path method" are the equations of motion of Newton or Euler-Lagrange. The "iconal method" makes use of certain properties of the Hamiltonian function.

These methods are then applied to describe the action of balanced, two-dimensional electric deflection fields on electron beams. It is shown that both methods yield essentially the same results. Expressions are derived describing the magnitude of deflection and the distortions of an electron beam.

Only the path method is used in a similar investigation of magnetic-type deflection fields.

A. INTRODUCTION AND GENERAL OUTLINE OF THE THEORY

1. Introduction

THE problems of the formation and the control of electron beams are the concern of "Geometrical Electron Optics," a term chosen to imply the analogy which exists between the behavior of electron beams and light beams, and which manifests itself in the terminology and the fact that many light-optical instruments have an electron-optical equivalent. Electron beams may be focused, deflected, and reflected by electric or magnetic fields which are called electron lenses, deflection fields, and electron mirrors, respectively. The deflection fields might be termed electron prisms if it were not for the fact that deflection fields produce both prismatic *and* focusing effects on electron beams. A deflection field may be considered as a prism having a weak cylinder lens joined to each face.

If the deflection fields are classified as those making use of focusing effects and those for which these effects are undesirable, it is found that these two classes represent the deflection fields producing large-angle deflections and those producing small-angle deflections, respectively. Deflection fields of the former group are employed in mass spectrometers, cyclotrons, and microanalyzers, while fields of the latter group are used in cathode-ray and television tubes, ion traps, scanning-type electron microscopes, etc.

This paper will deal exclusively with small-angle deflection fields in the manner now used for the treatment of electron-optical phenomena; the terms "deflection field," and "deflection system" will hereafter be assumed to relate only to small-angle deflection fields or systems. Large-angle deflection fields have been discussed elsewhere.[1–4]

It is the writer's purpose to provide certain mathematical tools which should be found useful in the design of improved deflection systems. In spite of the practical importance of an understanding of the problems of deflection, little attention has been paid to a systematic study of deflection fields. Approximate formulae are still used to determine the magnitude of deflection, and qualitative reasoning is applied to obtain information about the type of distortion of the deflected beam. Two exceptions exist: J. Picht and J. Himpan[5] have investigated single and crossed two-dimensional electric fields, and G. Wendt[6] has studied single and crossed magnetic deflection fields.

A thorough discussion of the subject is indicated for a number of reasons:

(1) Because of war conditions, the work of Picht, Himpan, and Wendt appears to have escaped the attention of the workers in the field of electron optics.

[1] R. G. E. Hutter, Phys. Rev. **67**, 248 (1945).
[2] R. Herzog, Zeits. f. Physik **89**, 447 (1934).
[3] W. Henneberg, Ann. d. Physik **19**, 335 (1934), *ibid.* **20**, 1 (1934), *ibid.* **21**, 390 (1934).
[4] N. D. Coggeshall, Phys. Rev. **70**, 270 (1946).
[5] J. Picht and J. Himpan, Ann. d. Physik **39**, 409 (1941), *ibid.* **43**, 53 (1943).
[6] G. Wendt, Die Telefunkenröhre **15**, 100 (1939); Zeits. f. Physik **118**, 593 (1942).

(2) These authors used a method of investigation which is known in electron optics as the "path method." It is of interest to show that another method, called the "iconal method," may also be employed.

(3) The method of Picht, Himpan, and Wendt, as well as the results, may be simplified. This simplification results in greater ease of application.

(4) The investigations may be generalized to include three-dimensional electric deflection fields.*

(5) A number of applications of the simplified and extended theory have now been made resulting in design charts for the determination of the magnitude of deflection, and in quantitative information on spot and pattern distortions of some of the commonly employed deflection fields.

The work is to be divided into two parts.** In Part I the general framework of the theory will be discussed, and the theory will be specialized for the case of single two-dimensional electric deflection fields, and single and crossed magnetic deflection fields. In Part II the magnitude of deflection and the distortion effects are computed for a number of typical electric and magnetic deflection fields.

2. General Outline of the Theory

Cathode-ray and television tubes are the most important devices employing the kinds of deflection fields to be investigated here. Although the theory to be developed may also be applied to small-angle deflection fields used in other devices, the terminology is that pertaining to cathode-ray tubes. The tube for which the theory will be developed is, however, an ideal rather than an actual cathode-ray tube. In order not to complicate the theory unduly, a number of assumptions had to be made chiefly concerning the electron beam and the focusing system.

The electron beam is assumed to be a rectilinear flow of electrons, homogeneous in velocity, and either conically or cylindrically shaped; space-charge effects are ignored. Such assumptions are not essential to the theory but were made to simplify its application. If it is necessary to explain the effects in an actual cathode-ray tube, such effects might have to be taken into account separately.

Furthermore, field distortions of the deflection fields due to the presence of other electrodes were not taken into account. This means that the deflection fields were taken as being determined solely by the current conductors and electrodes intended for the formation of the field.

These idealizations and approximations are permissible if one is interested in a comparative study of deflection fields, but not in an explanation of the performance of a particular cathode-ray tube which employs deflection fields.

The Cartesian system of coordinates will be used throughout this work. The z axis is taken as the optical axis of the focusing system. If undeflected, the electrons of the beam will travel in the $+z$ direction. The x direction is also called the "horizontal" direction while the y direction is called the "vertical" direction.

The initial coordinates of an electron, whose path through the deflection field is to be deter-

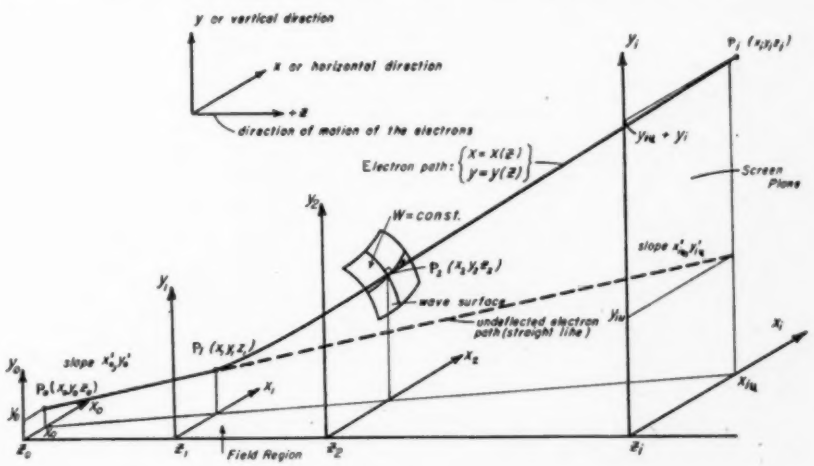

FIG. 1. The geometry of deflection.

* To be published at a later date.

** A part of the material presented in these papers was given in an abbreviated form at the National Electronics Conference in Chicago, October 3–5, 1946.

mined, are z_0, x_0, and y_0. The slope of the path at this point is given by x_0', y_0', the prime indicating the derivative of the quantity with respect to z. The position coordinates of an electron after deflection in a plane perpendicular to the z axis at a point z_i are given by z_i, x_i, and y_i. The coordinates x_i, y_i at a specified coordinate z_i are the quantities which ordinarily have to be determined. In cathode-ray and television tubes, z_i is the axial coordinate of the plane of the fluorescent screen. For simplicity, it is assumed that the screen is flat, although in many tubes the screen is actually a curved surface. Since z_i will remain a variable which may be chosen arbitrarily, it will also be possible to determine the position of the electron on a curved screen, in which case the calculations might be a little more cumbersome.

In most practical cases z_0 and z_i are axial coordinates which are in regions where the influence of the deflection field is negligibly small. The deflection action of the field takes place between two xy planes with axial coordinates z_1 and z_2, where $z_0<z_1<z_2<z_i$ (see Fig. 1).

There are four quantities—two coordinates and two slopes—which are of importance. If the deflecting field is zero, the electron with the above mentioned initial conditions x_0, y_0, x_0', y_0' at z_0, would proceed in a straight line from x_0, y_0, z_0 to the screen. Its coordinates at the screen are given by x_{iu} and y_{iu}, where

$$x_{iu}=x_0+x_0'(z_i-z_0), \quad y_{iu}=y_0+y_0'(z_i-z_0). \tag{1}$$

Its slopes at that point are

$$x_{iu}'=x_0', \quad y_{iu}'=y_0'. \tag{2}$$

The second subscript u indicates that x_{iu}, y_{iu} are the coordinates of the undeflected electron at the screen. (See Fig. 1.)

Equations (1) and (2) may be used to express x_0, y_0 in terms of x_{iu}, y_{iu}, x_{iu}', y_{iu}' as follows:

$$x_0=x_{iu}-x_{iu}'(z_i-z_0), \quad y_0=y_{iu}-y_{iu}'(z_i-z_0). \tag{3}$$

The coordinates x_i, y_i of the deflected electron at the axial coordinate z_i may be expanded formally in power series of powers of x_{iu}, y_{iu}, and x_{iu}', y_{iu}':

$$\left.\begin{aligned} x_i&=\sum_{a,b,c,d} M_{a,b,c,d}\cdot x_{iu}{}^a\cdot y_{iu}{}^b\cdot x_{iu}{}'^c\cdot y_{iu}{}'^d,\\ y_i&=\sum_{a,b,c,d} N_{a,b,c,d}\cdot x_{iu}{}^a\cdot y_{iu}{}^b\cdot x_{iu}{}'^c\cdot y_{iu}{}'^d,\end{aligned}\right\} \tag{4}$$

where $a+b+c+d=n$ with $n=0, 1, 2, \cdots$. There are $[(n+1)(n+2)(n+3)]/6$ terms of degree n.

The coefficients $M_{a,b,c,d}$ and $N_{a,b,c,d}$ will, of course, be functions of z_0, z_i and the field-strength parameters of the electric and magnetic deflection fields. The problem of determining x_i, y_i reduces to one of determining these coefficients. It will be shown that the series, Eq. (4), are rapidly converging if small-angle deflections are considered only. In most practical cases, n need not be taken as higher than three. The condition of smallness of the deflection angle will have to be stated mathematically.

Before going to the discussion of the two methods by which the coefficients $M_{a,b,c,d}$ and $N_{a,b,c,d}$ may be determined, a few remarks will be made concerning some general properties of these coefficients.

All electric and magnetic fields used as deflection fields are, strictly speaking, three-dimensional fields; i.e., the electrostatic potential function φ and the magnetic field strength vector **H** will be functions of all three coordinates x, y, and z. However, certain fields employed in actual devices exhibit in certain regions the properties of two-dimensional fields. This is especially the case for some electric deflection fields. In this case the potential function φ may be considered as depending only on x, z, or y, z. If the variation of φ with the third coordinate is negligibly small in regions passed by the electron beam, a considerable simplification of the theory appears possible. This simplification finds its expression in the end result, Eq. (4), in which a number of the coefficients $M_{a,b,c,d}$ and $N_{a,b,c,d}$ will vanish. It is, however, unnecessary to prove which of the coefficients are zero, since the methods by which the coefficients are to be determined will automatically assign the value of zero to the proper coefficients.

Often, in practice, two deflection fields are used which are rotated 90 degrees about the z axis with respect to each other. In this case only one set of coefficients $M_{a,b,c,d}$ or $N_{a,b,c,d}$ need be determined, the other set being obtained by interchanging a and b as well as c and d, and interchanging the field quantities. In order to get y_i from x_i, x_{iu} must be replaced by y_{iu}, x_{iu}' by y_{iu}', and *vice versa*. It should be pointed out, however, that the numerical values of the corre-

sponding coefficients will be different if different field functions are used for the two deflection fields.

The study of the motion of electrons in deflection fields requires a knowledge of the field distributions. An electric field may be given in terms of a potential distribution $\varphi=\varphi(x, y, z)$, while the magnetic field may be described by the magnetic vector potential distribution $\mathbf{A}=\mathbf{A}(x, y, z)$. It will be assumed that those functions are known.

Two essentially different methods are available to determine the position coordinates of an electron moving in the fields. (Both methods have been used to solve the analogous problem for focusing fields.)

If we consider electrons as small charged particles moving through electric and magnetic force fields, the concepts of electron ballistics can be applied. The Newton-Lorentz equations may be used as the basic set of equations. This method has been used by J. Picht and J. Himpan[5] for two-dimensional electrostatic deflection fields, and by G. Wendt[6] for a single magnetic deflection field. It is called the "path method."

If, on the other hand, waves are associated with a moving electron which travels through electric or magnetic fields of slowly-varying electron optical index of refraction, the wave approach to geometric optics can be applied. One of the basic concepts is that of the "point iconal." The method is based on the properties of the iconal function and is, therefore, called the "iconal method."

The common root of both methods is Hamilton's principle which states that the electron path,

$$x=x(s), \quad y=y(s), \quad z=z(s), \tag{5}$$

is such that

$$W=\int_{P_0(x_0,\,y_0,\,z_0)}^{P_i(x_i,\,y_i,\,z_i)}\left\{\left[\frac{2e}{m}\varphi(x, y, z)\right]^{\frac{1}{2}}-\frac{e}{m}(\mathbf{A}\cdot\mathbf{s})\right\}ds=\text{minimum}, \tag{6}$$

or with

$$\mathbf{s}=\frac{x'}{[1+x'^2+y'^2]^{\frac{1}{2}}}\mathbf{i}+\frac{y'}{[1+x'^2+y'^2]^{\frac{1}{2}}}\mathbf{j}+\frac{1}{[1+x'^2+y'^2]^{\frac{1}{2}}}\mathbf{k}, \tag{7}$$

and

$$ds=(1+x'^2+y'^2)^{\frac{1}{2}}dz, \tag{8}$$

that the electron path $x=x(z), y=y(z)$ is such that

$$W=\int_{z_0}^{z_i}F(x, y, z, x', y')dz=\int_{z_0}^{z_i}\left\{\left[\frac{2e}{m}\varphi(x, y, z)\right]^{\frac{1}{2}}\cdot[1+x'^2+y'^2]^{\frac{1}{2}}-\frac{e}{m}(A_x x'+A_y y'+A_z)\right\}dz=\text{minimum}, \tag{9}$$

where the primes indicate differentiation with respect to z.

The necessary conditions for the electron path Eq. (5) to satisfy Eq. (9) are certain differential equations. These equations are the Euler-Lagrange differential equations for the electron path obtained by carrying out the operations indicated by

$$\left.\begin{aligned}(d/dz)(\partial F/\partial x')-\partial F/\partial x=0,\\(d/dz)(\partial F/\partial y')-\partial F/\partial y=0.\end{aligned}\right\} \tag{10}$$

These equations are equivalent to Newton's equations

$$m\frac{d^2\mathbf{r}}{dt^2}=e\mathbf{E}+e[\mathbf{v}\times\mathbf{H}], \tag{11}$$

with

$$\mathbf{r}\cdot\mathbf{i}+y\cdot\mathbf{j}+z\cdot\mathbf{k}. \tag{12}$$

The iconal method utilizes the properties of the function W. If $x(z)$ and $y(z)$ are taken as the functions describing the actual electron path, and if the initial point $P_0(x_0, y_0, z_0)$ is kept fixed, W becomes a function of the end point $P_i(x_i, y_i, z_i)$. The equation $W=$const. describes a surface about P_0. This is the wave surface of the electron radiation diverging from P_0. Assuming that we know the wave surface configuration in the space where electric and magnetic fields exist, the path of an electron beyond this space (with the boundary point $P_2(x_2, y_2, z_2)$) and into field-free regions to the point $P_i(x_i, y_i, z_i)$ is then given by[7] (see Fig. 1)

$$\left.\begin{aligned}x_i=x_2+(1/n_i)(\partial W/\partial x_2)[(x_i-x_2)^2+(y_i-y_2)^2+(z_i-z_2)^2]^{\frac{1}{2}},\\y_i=y_2+(1/n_i)(\partial W/\partial y_2)[(x_i-x_2)^2+(y_i-y_2)^2+(z_i-z_2)^2]^{\frac{1}{2}}.\end{aligned}\right\} \tag{13}$$

[7] V. K. Zworykin, G. A. Morton, E. G. Ramberg, J. Hillier, and A. W. Vance, *Electron Optics and the Electron Microscope* (John Wiley and Sons, New York, 1945).

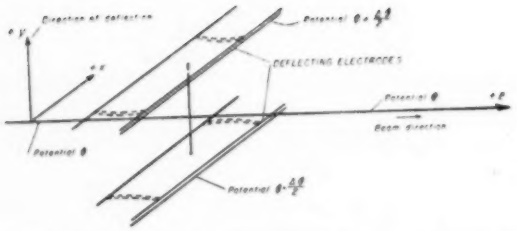

FIG. 2. The electrode geometry of a two-dimensional electric deflection field.

The slope of this straight line is that of the normal $\mathbf{n}$ to the wave surface at the point P_2, since $\mathbf{n}$ is given by

$$\mathbf{n}=\frac{1}{n_i}\frac{\partial W}{\partial x_2}\mathbf{i}+\frac{1}{n_i}\frac{\partial W}{\partial y_2}\mathbf{j}+\frac{1}{n_i}\frac{\partial W}{\partial z_2}\mathbf{k},$$

$$n_i=\phi_i^{\frac{1}{2}}=[(\partial W/\partial x_2)^2+(\partial W/\partial y_2)^2+(\partial W/\partial z_2)^2]^{\frac{1}{2}}. \tag{14}$$

It would appear that we have to know the electron path, i.e., the solution of the problem, in order to use the iconal method, since W can only be determined if $x=x(z)$ and $y=y(z)$ are known. However, the restrictions on the magnitude of the deflection angle mentioned above, together with the property of W as expressed by Eq. (9), eliminate the necessity of an exact knowledge of the path.

If the angle of deflection is small, the deflection itself must be small in the region where the field strengths are of appreciable magnitude. Large deflections are obtained by letting the beam travel in essentially field-free space before it reaches the screen; $x(z)$, $y(z)$, $x'(z)$, $y'(z)$ are, therefore, small quantities in regions of appreciable field strength. For their determination by means of Eq. (10), methods of successive approximations can be applied to yield electron paths of increasing accuracy. After the first-order approximation*** has been determined, either method may be used to find the higher order solutions.

In Part B, Section 2, the coordinates of the electron at the screen will be computed, including terms up to $n=2$ or $n=3$, which is, in general, sufficiently accurate to obtain quantitative information about the deflection, and the spot and pattern distortions occurring in common designs of cathode-ray and television tubes.

*** The first-order solution corresponds to the so-called "paraxial ray solution" of the focusing systems.

B. TWO-DIMENSIONAL ELECTRIC DEFLECTION FIELDS

1. The Field Distribution

Electric fields which deflect the electron beam in cathode-ray and television tubes are ordinarily produced by metal electrodes connected to potential sources. The location of these electrodes with respect to the electron beam and the direction of deflection are shown in Fig. 2. The Cartesian system of coordinates is chosen so that $+z$ is in the direction of motion of the undeflected electrons, and $+y$ is in the direction of deflection. Two assumptions will be made about the shape and the potentials of the deflecting electrodes. These assumptions will be expressed in terms of the potential distribution $\varphi=\varphi(x, y, z)$ of the field produced by the deflecting system.

$$\varphi=\varphi(y, z) \quad \text{i.e., } \varphi \text{ is independent of } x, \tag{15}$$

where

$$\left.\begin{aligned}\varphi(y, z)&=\phi+\varphi^*(y, z),\\ -\varphi^*(+y, z)&=\varphi^*(-y, z),\\ \text{so that}\quad \varphi(-y, z)&=\phi-\varphi^*(+y, z),\end{aligned}\right\} \tag{16}$$

where ϕ is the potential of the last anode of the electron gun.

The first assumption, Eq. (15), means that the electrodes producing φ are considered to be of infinite extent in the x direction, or, in other words, that the edge effects of the electrodes of finite extent in the x direction are neglected. The error introduced by this assumption ordinarily is negligible, since most electrodes are of sufficient width in the x direction. It follows from the assumption that the equipotential plots, as well as the cross section of the electrodes, are identical in all planes parallel to the (y, z) plane.

The second assumption, Eq. (16), restricts the validity of the following investigations to so-called balanced fields.**** The electrodes are located symmetrically with respect to the center or (x, z) plane. This center plane is at potential ϕ. The potentials of the electrodes are $\phi+\frac{1}{2}\Delta\phi$ and $\phi-\frac{1}{2}\Delta\phi$, respectively; $\Delta\phi$ is the potential difference between the electrodes.

The potential function φ must satisfy the

**** The theory of unbalanced deflection fields has also been worked out and will be published at a later date.

Laplace equation:

$$[\partial^2\varphi(y,z)/\partial y^2]+[\partial^2\varphi(y,z)/\partial z^2]\equiv 0. \quad (17)$$

Since $\varphi^*(y,z)=-\varphi^*(-y,z)$, the power series expansion of φ^* in powers of y can have only terms of odd power in y.

$$\varphi^*(y,z)=a_1(z)\cdot y+a_3(z)\cdot y^3+\cdots +a_{2n+1}(z)\cdot y^{2n+1}+\cdots. \quad (18)$$

Substituting Eq. (18) in Eq. (17), a recurrence formula for the coefficients is obtained, in which $a_1(z)$ remains arbitrary. With

$$a_1(z)=-E(z) \quad (19)$$

the following series is derived:

$$\varphi(y,z)=\phi-E(z)\cdot y+\tfrac{1}{6}E''(z)y^3-(1/120)E^{(IV)}(z)y^5+\cdots(-1)^{n+1}\times[1/(2n+1)!]E^{(2n)}(z)\cdot y^{2n+1}+\cdots. \quad (20)$$

It is seen that

$$E(z)=-\left.\frac{\partial\varphi(y,z)}{\partial y}\right|_{y=0}, \quad (21)$$

i.e., $E(z)$ is the axial field-strength distribution.

The electron-optical theory described below will be based on the general form of the potential distribution Eq. (20). It should be noted that edge effects of electrodes in the z direction are not excluded, since $E(z)$ is left arbitrary. The axial field-strength distribution $E(z)$ determines, except for a constant, the equipotential distribution of deflection fields satisfying the condition expressed by Eq. (15).

Ordinarily, two fields of the type described by Eq. (20) are employed in cathode-ray and television tubes. The electrodes are rotated 90 degrees with respect to each other about the z axis; one field deflects in the y direction, the other in the x direction. The two pairs of electrodes are generally spaced sufficiently far apart along the z axis to prevent the distortion of the potential distribution of one field by the electrodes producing the other field. It is assumed here that a plane exists midway between the two fields where neither field has sufficient strength to affect the electrons. A study of crossed electric fields reduces, then, to a study of two single fields.

2. Path Method for a Single Two-Dimensional Electric Deflection Field

Integration of the path differential Eqs. (10) becomes possible if it is assumed that $x(z)$, $y(z)$, $x'(z)$, and $y'(z)$ are small quantities. The expressions $\varphi^{\frac{1}{2}}$ and $(1+x'^2+y'^2)^{\frac{1}{2}}$ of Eq. (9) may be written in series form

$$\varphi^{\frac{1}{2}}(y,z)=\phi^{\frac{1}{2}}\left(1-\frac{1}{2}\frac{E}{\phi}y+\frac{1}{12}\frac{E''}{\phi}y^3-\frac{1}{8}\frac{E^2}{\phi^2}y^2-\frac{1}{16}\frac{E^3}{\phi^3}y^3+\cdots\right), \quad (22)$$

and

$$(1+x'^2+y'^2)^{\frac{1}{2}}=1+\tfrac{1}{2}(x'^2+y'^2)-\tfrac{1}{8}(x'^2+y'^2)^2+\cdots. \quad (23)$$

The expression for W then becomes

$$W=\left(\frac{2e}{m}\phi\right)^{\frac{1}{2}}\int_{z_0}^{z_i}\left\{[1]-\left[\frac{1}{2}\frac{E}{\phi}y\right]+\left[\tfrac{1}{2}(x'^2+y'^2)-\frac{1}{8}\frac{E^2}{\phi^2}y^2\right]+\left[-\tfrac{1}{4}(x'^2+y'^2)\frac{E}{\phi}y+\left(\frac{1}{12}\frac{E''}{\phi}-\frac{1}{16}\frac{E^3}{\phi^3}\right)y^3\right]+\left[-\tfrac{1}{8}(x'^2+y'^2)^2-\tfrac{1}{16}(x'^2+y'^2)y^2\frac{E^2}{\phi^2}-\left(-\frac{1}{24}\frac{EE''}{\phi^2}+\frac{5}{128}\frac{E^4}{\phi^4}\right)y^4\right]+\text{higher order terms}\right\}dz, \quad (24)$$

or

$$W=\left(\frac{2e}{m}\phi\right)^{\frac{1}{2}}\int_{z_0}^{z_i}\{F_0+F_1+F_2+F_3+F_4+\text{higher order terms}\}dz,$$

if the bracketed expressions are called F_0, F_1, F_2, F_3, and F_4. The Euler-Lagrange differential equations

$$\left.\begin{aligned}(d/dz)[(\partial/\partial x')(F_1+F_2+F_3+F_4)]-0=0,\\ (d/dz)[(\partial/\partial y')(F_1+F_2+F_3+F_4)]-(\partial/\partial y)(F_1+F_2+F_3+F_4)=0,\end{aligned}\right\} \tag{25}$$

yield

$$\left.\begin{aligned}&\frac{d}{dz}\left[x'-\frac{1}{2}\frac{E}{\phi}yx'-\tfrac{1}{2}x'^3-\tfrac{1}{2}y'^2x'-\frac{1}{8}\frac{E^2}{\phi^2}y^2x'\right]=0,\\ &\frac{d}{dz}\left[y'-\frac{1}{2}\frac{E}{\phi}yy'-\tfrac{1}{2}y'^3-\tfrac{1}{2}x'^2y'-\frac{1}{8}\frac{E^2}{\phi^2}y^2y'\right]-\left[-\frac{1}{2}\frac{E}{\phi}-\frac{1}{4}\frac{E^2}{\phi^2}y-\frac{1}{4}\frac{E}{\phi}x'^2-\frac{1}{4}\frac{E}{\phi}y'^2\right.\\ &\left.-\frac{3}{16}\frac{E^3}{\phi^3}y^2+\frac{1}{4}\frac{E''}{\phi}y^2-\frac{1}{8}\frac{E^2}{\phi^2}x'^2y-\frac{1}{8}\frac{E^2}{\phi^2}y'^2y+\frac{1}{6}\frac{EE''}{\phi^2}y^3-\frac{5}{32}\frac{E^4}{\phi^4}y^3\right]=0.\end{aligned}\right\} \tag{26}$$

The restriction that the deflection be small where the field strength is of appreciable magnitude may be expressed mathematically as

$$\left|\frac{1}{2}\frac{E}{\phi}y\right|\ll 1. \tag{27}$$

Taking Eq. (27) and $|x'^2|\ll 1$ and $|y'^2|\ll 1$ into account, the approximate solution of Eq. (26) may then be obtained in two steps. To the first order of approximation, the electron path will be given by

$$(d/dz)(x')=0, \quad (d/dz)(y')=-\tfrac{1}{2}(E/\phi). \tag{28}$$

The solution of Eq. (28) is

$$\left.\begin{aligned}x_g(z)&=x_0+x_0'(z-z_0),\\ y_g(z)&=y_0+y_0'(z-z_0)+Y(z),\end{aligned}\right\}^{\dagger} \tag{29}$$

where x_0, x_0', y_0, and y_0' are the initial conditions of the electron path. Here

$$Y(z)=-(1/2\phi)\int_{z_0}^{z}d\zeta\int_{z_0}^{\zeta}E(u)du, \tag{30}$$

is the deflection caused by the electrostatic field. If $z=z_i$ is the position coordinate of the screen, the deflection, d, at the screen for an electron with the initial conditions $x_0=y_0=x_0'=y_0'=0$ is given by

$$d=Y_i=Y(z_i)=-(1/2\phi)\int_{z_0}^{z_i}d\zeta\int_{z_0}^{\zeta}E(u)du. \tag{31}$$

Since $E(z)$ is proportional to the potential difference $\Delta\phi$ between the electrodes, it can be seen from Eq. (31) that d is a linear function of $\Delta\phi$. This is a desirable property of a deflection field, but an actual field has this property only to the extent that it is permissible to neglect the higher order terms in Eq. (26). A more accurate solution of Eq. (26) will be given which shows the extent to which the actual paths deviate from the first-order paths.

The quantities x', y', $|\frac{1}{2}(E/\phi)y|$, are still assumed to be small, but not negligibly so. It may be expected that the actual solution of Eq. (26) will differ but little from the first-order solution Eq. (29). Only a small error will therefore be made if y and x of Eq. (29) are substituted in all terms of Eq. (26) which were previously neglected. The terms x_0, x_0', y_0, and y_0' would then appear in the new solutions for $x=x(z)$ and $y=y(z)$. It is, however, more convenient to use four other quantities, namely, the coordinates and slopes of the undeflected electron at the

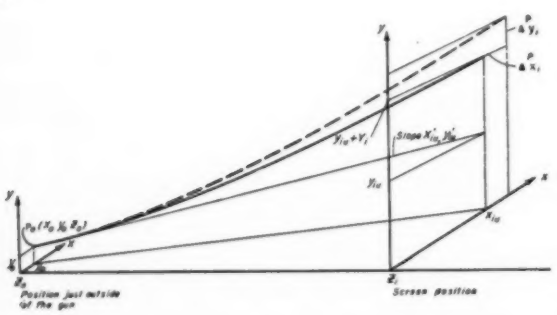

FIG. 3. The geometry of deflection (path method).

† This solution corresponds to the "paraxial ray" equation of the theory of focusing fields. In this theory the equation describes a path called the Gaussian path. It was for this reason that the subscript g was chosen.

screen defined by Eq. (1). Replacing x_0, y_0, x_0', and y_0' in Eq. (29) by x_{iu}, y_{iu}, x_{iu}', and y_{iu}' (using Eqs. (2), (3)), the following equations are obtained for x_g and y_g:

$$\left.\begin{aligned} x_g(z) &= x_{iu}+x_{iu}'(z-z_i), \\ y_g(z) &= y_{iu}+y_{iu}'(z-z_i)+Y(z). \end{aligned}\right\} \tag{32}$$

Substituting Eq. (32) in Eq. (26), the solutions $x(z)$ and $y(z)$ of the resulting differential equations are obtained by simple integrations. The terms of this solution may be arranged in powers of x_{iu}, y_{iu}, x_{iu}', y_{iu}'. If the difference between the new and the former solution is taken and the integrals are extended from z_0 to z_i, two quantities $\Delta^P x_i$, $\Delta^P y_i$ are derived which describe the deviations at the screen of the actual electron path from the first-order path given by Eq. (29). (See Fig. 3.) These quantities $\Delta^P x_i$ and $\Delta^P y_i$ may be written as

$$\left.\begin{aligned} \Delta^P x_i &= \alpha_{0010}x_{iu}'+\alpha_{0110}x_{iu}'y_{iu}+\alpha_{0011}x_{iu}'y_{iu}'+\alpha_{0210}x_{iu}'y_{iu}^2+\alpha_{0111}x_{iu}'y_{iu}'y_{iu}+\alpha_{0012}x_{iu}'y_{iu}'^2, \\ \Delta^P y_i &= \beta_{0000}+\beta_{0100}y_{iu}+\beta_{0001}y_{iu}'+\beta_{0200}y_{iu}^2+\beta_{0020}x_{iu}'^2+\beta_{0002}y_{iu}'^2+\beta_{0101}y_{iu}'y_{iu} \\ &\quad +\beta_{0300}y_{iu}^3+\beta_{0120}x_{iu}'^2y_{iu}+\beta_{0102}y_{iu}y_{iu}'^2+\beta_{0021}x_{iu}'^2y_{iu}'+\beta_{0201}y_{iu}^2y_{iu}'+\beta_{0003}y_{iu}'^3. \end{aligned}\right\} \tag{33}$$

Here the notation, similar to that for the expressions x_i and y_i, Eqs. (4), has been used to describe the expansion of the additional deflections $\Delta^P x_i$ and $\Delta^P y_i$. Since

$$x_i \cong x_g(z_i)+\Delta^P x_i = x_{iu}+\Delta^P x_i,$$

$$y_i \cong y_g(z_i)+\Delta^P y_i = y_{iu}+Y_i+\Delta^P y_i.$$

Then, to the degree of approximation considered here

$$M_{1000}=1+\alpha_{1000}, \quad \text{otherwise} \quad M_{a,b,c,d}\equiv\alpha_{a,b,c,d}$$

and

$$N_{0000}=\beta_{0000}+Y_i, \quad N_{0100}=1+\beta_{0100}, \quad \text{otherwise} \quad N_{a,b,c,d}\equiv\beta_{a,b,c,d}.$$

The coefficients $\alpha_{a,b,c,d}$ and $\beta_{a,b,c,d}$ are certain definite integrals from z_0 to z_i which can be written in various forms. After carrying out the operations mentioned above, some of these coefficients contain double integrals which can be changed to single integrals by the use of the formula

$$\int_{z_0}^{z_i} d\zeta \int_{z_0}^{\zeta} F(u)du = -\int_{z_0}^{z_i} F(u)(u-z_i)du. \tag{34}$$

Some integrands have the second derivative of the axial field distribution $E''(z)$ as a factor. In general, $E(z)$ is known from experiment and $E''(z)$ can then only be obtained by numerical differentiation. This leads to inaccuracies which can be avoided by eliminating $E''(z)$ from all integrands employing the method of partial integration. This method and the equations

$$Y''(z) = -\frac{1}{2\phi}E(z), \tag{35}$$

and

$$Y_i = Y(z_i) = (1/2\phi)\int_{z_0}^{z_i}(\alpha-z_i)E(\alpha)d\alpha \tag{36}$$

were used to simplify the coefficients $\alpha_{a,b,c,d}$ and $\beta_{a,b,c,d}$ which were first derived by J. Picht and

J. Himpan[5] in a different form. They may be written as follows:

$$\left.\begin{aligned}
\alpha_{0100} &= \tfrac{1}{2}Y_iY_i' + \frac{3}{4\phi}\int_{z_0}^{z_i} EYdz + \frac{1}{8\phi^2}\int_{z_0}^{z_i} E^2Y^2dz,\\
\alpha_{0110} &= -\frac{1}{2\phi}E_0(z_i-z_0) - Y_i' + \frac{1}{4\phi^2}\int_{z_0}^{z_i} E^2Ydz,\\
\alpha_{0011} &= 2Y_i + \frac{1}{2\phi}E_0(z_i-z_0)^2 + \frac{1}{4\phi^2}\int_{z_0}^{z_i} E^2Y(z-z_i)dz,\\
\alpha_{0210} &= -\frac{1}{8\phi^2}E_0^2(z_i-z_0) + \frac{1}{8\phi^2}\int_{z_0}^{z_i} E^2dz,\\
\alpha_{0012} &= -\frac{1}{8\phi^2}E_0^2(z_i-z_0)^3 + \frac{1}{8\phi^2}\int_{z_0}^{z_i} E^2(z-z_i)^2dz,\\
\alpha_{0111} &= \frac{1}{4\phi^2}E_0^2(z_i-z_0)^2 + \frac{1}{4\phi^2}\int_{z_0}^{z_i} E^2(z-z_i)dz;
\end{aligned}\right\} \tag{37}$$

$$\begin{aligned}
\beta_{0000} &= \tfrac{1}{3}Y_iY_i'^2 + \frac{1}{4\phi}E_iY_i^2 - \frac{1}{6\phi}\int_{z_0}^{z_i} EYY'dz + \frac{1}{2\phi^2}\int_{z_0}^{z_i} E^2Y(z-z_i)dz\\
&\quad + \frac{1}{12\phi^2}E_i^2Y_i^3 - \frac{3}{8\phi^2}\int_{z_0}^{z_i} E^2YY'^2(z-z_i)dz - \frac{3}{8\phi^2}\int_{z_0}^{z_i} E^2Y^2Y'dz + \frac{1}{6\phi^2}\int_{z_0}^{z_i} E'^2Y^3(z-z_i)dz\\
&\quad + \frac{5}{16\phi^3}\int_{z_0}^{z_i} E^3Y^2(z-z_i)dz + \frac{5}{32\phi^4}\int_{z_0}^{z_i} E^4Y^3(z-z_i)dz,\\
\beta_{0100} &= \tfrac{1}{2}Y_i'^2 + \frac{1}{2\phi}E_iY_i + \frac{1}{4\phi^2}E_i^2Y_i^2 + \frac{1}{2\phi^2}\int_{z_0}^{z_i} E^2(z-z_i)dz - \frac{3}{8\phi^2}\int_{z_0}^{z_i} E^2Y'^2(z-z_i)dz\\
&\quad + \frac{1}{2\phi^2}\int_{z_0}^{z_i} E'^2Y^2(z-z_i)dz - \frac{3}{4\phi^2}\int_{z_0}^{z_i} E^2YY'dz + \frac{5}{8\phi^3}\int_{z_0}^{z_i} E^3Y(z-z_i)dz\\
&\quad + \frac{15}{32\phi^4}\int_{z_0}^{z_i} E^4Y^2(z-z_i)dz,\\
\beta_{0001} &= \tfrac{1}{2}Y_iY_i' - \frac{1}{4\phi}\int_{z_0}^{z_i} EYdz + \frac{1}{2\phi^2}\int_{z_0}^{z_i} E^2(z-z_i)^2dz - \frac{3}{8\phi^2}\int_{z_0}^{z_i} E^2Y^2dz\\
&\quad - \frac{3}{2\phi^2}\int_{z_0}^{z_i} E^2YY'(z-z_i)dz - \frac{3}{8\phi^2}\int_{z_0}^{z_i} E^2Y'^2(z-z_i)^2dz + \frac{1}{2\phi^2}\int_{z_0}^{z_i} E'^2Y^2(z-z_i)^2dz\\
&\quad + \frac{5}{8\phi^3}\int_{z_0}^{z_i} E^3Y(z-z_i)^2dz + \frac{15}{32\phi^4}\int_{z_0}^{z_i} E^4Y^2(z-z_i)^2dz,
\end{aligned} \tag{38}$$

(Equation 38 continued on following page)

$$\beta_{0200}=-\frac{1}{4\phi}[E_0'(z_i-z_0)+(E_0-E_i)]+\frac{1}{4\phi^2}E_i^2Y_i-\frac{3}{8\phi^2}\int_{z_0}^{z_i}E^2Y'dz+\frac{1}{2\phi^2}\int_{z_0}^{z_i}E'^2Y(z-z_i)dz$$
$$+\frac{5}{16\phi^3}\int_{z_0}^{z_i}E^3(z-z_i)dz+\frac{15}{32\phi^4}\int_{z_0}^{z_i}E^4Y(z-z_i)dz,$$

$$\beta_{0020}=Y_i+\frac{1}{8\phi^2}\int_{z_0}^{z_i}E^2Y(z-z_i)dz,$$

$$\beta_{0002}=-\frac{1}{4\phi}E_0'(z_i-z_0)^3-\frac{1}{4\phi}E_0(z_i-z_0)^2-\frac{9}{8\phi^2}\int_{z_0}^{z_i}E^2Y(z-z_i)dz-\frac{9}{8\phi^2}\int_{z_0}^{z_i}E^2Y'(z-z_i)^2dz \tag{38}$$
$$+\frac{1}{2\phi^2}\int_{z_0}^{z_i}E'^2Y(z-z_i)^3dz+\frac{5}{16\phi^3}\int_{z_0}^{z_i}E^3(z-z_i)^3dz+\frac{15}{32\phi^4}\int_{z_0}^{z_i}E^4Y(z-z_i)^3dz,$$

$$\beta_{0101}=Y_i'+\frac{1}{2\phi}E_0'(z_i-z_0)^2+\frac{1}{2\phi}E_0(z_i-z_0)-\frac{3}{4\phi^2}\int_{z_0}^{z_i}E^2Ydz-\frac{3}{2\phi^2}\int_{z_0}^{z_i}E^2Y'(z-z_i)dz$$
$$+\frac{1}{\phi^2}\int_{z_0}^{z_i}E'Y(z-z_i)^2dz+\frac{5}{8\phi^3}\int_{z_0}^{z_i}E^3(z-z_i)^2dz+\frac{15}{16\phi^4}\int_{z_0}^{z_i}E^4Y(z-z_i)^2dz,$$

$$\beta_{0300}=-\frac{1}{6\phi^2}E_0E_0'(z_i-z_0)+\frac{1}{12\phi^2}(E_i^2-E_0^2)+\frac{1}{6\phi^2}\int_{z_0}^{z_i}E'^2(z-z_i)dz+\frac{5}{32\phi^4}\int_{z_0}^{z_i}E^4(z-z_i)dz,$$

$$\beta_{0120}=\frac{1}{8\phi^2}\int_{z_0}^{z_i}E^2(z-z_i)dz,$$

$$\beta_{0102}=-\frac{1}{2\phi^2}E_0^2(z_i-z_0)^2-\frac{1}{2\phi}E_0E_0'(z_i-z_0)^3-\frac{9}{8\phi^2}\int_{z_0}^{z_i}E^2(z-z_i)dz$$
$$+\frac{1}{2\phi^2}\int_{z_0}^{z_i}E'^2(z-z_i)^3dz+\frac{15}{32\phi^4}\int_{z_0}^{z_i}E^4(z-z_i)^3dz,$$

$$\beta_{0021}=\frac{1}{8\phi^2}\int_{z_0}^{z_i}E^2(z-z_i)^2dz,$$

$$\beta_{0201}=\frac{3}{8\phi^2}E_0^2(z_i-z_0)+\frac{1}{2\phi^2}E_0E_0'(z_i-z_0)^2-\frac{3}{8\phi^2}\int_{z_0}^{z_i}E^2dz$$
$$+\frac{1}{2\phi^2}\int_{z_0}^{z_i}E'^2(z-z_i)^2dz+\frac{15}{32\phi^4}\int_{z_0}^{z_i}E^4(z-z_i)^2dz,$$

$$\beta_{0003}=\frac{5}{24\phi^2}E_0^2(z_i-z_0)^3+\frac{1}{6\phi^2}E_0E_0'(z_i-z_0)^4-\frac{3}{4\phi^2}\int_{z_0}^{z_i}E^2(z-z_i)^2dz$$
$$+\frac{1}{6\phi^2}\int_{z_0}^{z_i}E'^2(z-z_i)^4dz+\frac{5}{32\phi^4}\int_{z_0}^{z_i}E^4(z-z_i)^4dz.$$

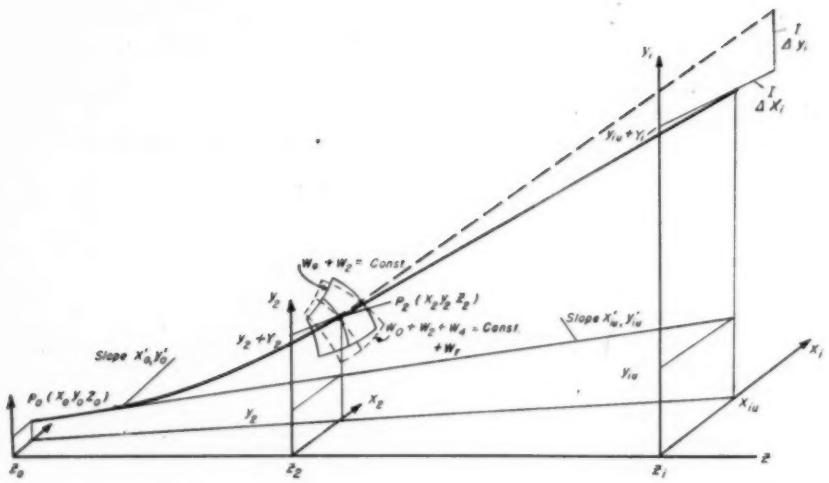

FIG. 4. The geometry of deflection (iconal method).

3. Iconal Method for a Single Electrostatic Deflection Field

Essentially the same coefficients can also be obtained by the use of the iconal method, as will now be shown. The point iconal function will be written in the form

$$W=\left(\phi\frac{2e}{m}\right)^{\frac{1}{2}}\int_{z_0}^{z_2}\left\{[1]+\left[-\frac{1}{2}\frac{E}{\phi}y+\tfrac{1}{2}(x'^2+y'^2)\right]+\left[-\frac{1}{8}\frac{E^2}{\phi^2}y^2-\tfrac{1}{8}(x'^2+y'^2)^2-\tfrac{1}{4}(x'^2+y'^2)y\frac{E}{\phi}\right.\right.$$
$$\left.+\frac{1}{12}\frac{E''}{\phi}y^3\right]+\left[-\frac{1}{16}\frac{E^3}{\phi^3}y^3-\tfrac{1}{16}(x'^2+y'^2)y^2\frac{E^2}{\phi^2}+\frac{1}{24}\frac{EE''}{\phi^2}y^4-\frac{5}{128}\frac{E^4}{\phi^4}y^4\right]$$
$$\left.+\text{higher order terms}\right\}dz, \tag{39}$$

or

$$W=W_0+W_2+W_4+W_r+\text{higher order terms.}$$

If $P_0(x_0, y_0, z_0)$ remains fixed, $W=$const. is the wave surface of electron radiation diverging from $P_0(x_0, y_0, z_0)$ and passing through the point $P_2(x_2, y_2, z_2)$. It is assumed that the space between the plane of the screen and the plane through z_2 parallel to the screen plane is field-free.†† (See Fig. 4.) The coordinates $x_i^{(1)}$ and $y_i^{(1)}$ of the electron path at the screen will then be given to the first degree approximation by

$$\left.\begin{aligned}x_i^{(1)}&=x_2+[(z_i-z_2)/\phi_i^{\frac{1}{2}}][\partial W_2/\partial x_2],\\ y_i^{(1)}&=y_2+[(z_i-z_2)/\phi_i^{\frac{1}{2}}][\partial W_2/\partial y_2].\end{aligned}\right\} \tag{40}$$

Equation (40) is derived from Eq. (13) by admitting only first-order terms. The expression W_2 has been determined by using the electron path equation in the form

$$\left.\begin{aligned}x_g(z)&=x_0[(z_2-z)/(z_2-z_0)]+x_2[(z-z_0)/(z_2-z_0)],\\ y_g(z)&=y_0[(z_2-z)/(z_2-z_0)]+y_2[(z-z_0)/(z_2-z_0)]-Y_2[(z-z_0)/(z_2-z_0)]+Y(z),\end{aligned}\right\} \tag{41}$$

with

$$Y(z)=-\frac{1}{2\phi}\int_{z_0}^{z}d\zeta\int_{z_0}^{\zeta}E(u)du. \tag{42}$$

The wave surface through the point $P_2(x_2, y_2, z_2)$, to a first approximation, is given by $W_0+W_2=$const. More accurately, this surface will be given by $W_0+W_2+W_4+W_r=$const. A new solution

†† This assumption can be discarded by an argument similar to that presented for focusing fields in the book by Zworykin, reference 7, p. 563.

for the coordinates of the electron path at the screen may be obtained in the form

$$\left.\begin{aligned} x_i^{(3)} &= x_2+\frac{z_i-z_2}{\phi_i^{\frac{1}{2}}}\frac{\partial W_2}{\partial x_2}\left[1+\frac{1}{2}\left(\frac{x_i^{(1)}-x_2}{z_i-z_2}\right)^2+\frac{1}{2}\left(\frac{y_i^{(1)}-y_2}{z_i-z_2}\right)^2\right]+\frac{z_i-z_2}{\phi_i^{\frac{1}{2}}}\frac{\partial(W_4+W_r)}{\partial x_2}, \\ y_i^{(3)} &= y_2+\frac{z_i-z_2}{\phi_i^{\frac{1}{2}}}\frac{\partial W_2}{\partial y_2}\left[1+\frac{1}{2}\left(\frac{x_i^{(1)}-x_2}{z_i-z_2}\right)^2+\frac{1}{2}\left(\frac{y_i^{(1)}-y_2}{z_i-z_2}\right)^2\right]+\frac{z_i-z_2}{\phi_i^{\frac{1}{2}}}\frac{\partial(W_4+W_r)}{\partial y_2}. \end{aligned}\right\} \tag{43}$$

The differences between the new and the former values of the coordinates are

$$\left.\begin{aligned} \Delta^I x_i &= x_i^{(3)}-x_i^{(1)}=\frac{z_i-z_2}{\phi_i^{\frac{1}{2}}}\frac{\partial(W_4+W_r)}{\partial x_2}+\frac{z_i-z_2}{\phi_i^{\frac{1}{2}}}\left[\frac{1}{2}\left(\frac{x_i^{(1)}-x_2}{z_i-z_2}\right)^2+\frac{1}{2}\left(\frac{y_i^{(1)}-y_2}{z_i-z_2}\right)^2\right]\frac{\partial W_2}{\partial x_2}, \\ \Delta^I y_i &= y_i^{(3)}-y_i^{(1)}=\frac{z_i-z_2}{\phi_i^{\frac{1}{2}}}\frac{\partial(W_4+W_r)}{\partial y_2}+\frac{z_i-z_2}{\phi_i^{\frac{1}{2}}}\left[\frac{1}{2}\left(\frac{x_i^{(1)}-x_2}{z_i-z_2}\right)^2+\frac{1}{2}\left(\frac{y_i^{(1)}-y_2}{z_i-z_2}\right)^2\right]\frac{\partial W_2}{\partial y_2}. \end{aligned}\right\} \tag{44}$$

Carrying out the indicated differentiations, the additional deflections $\Delta^I x_i$ and $\Delta^I y_i$ may be compared with the values $\Delta^P x_i$ and $\Delta^P y_i$ of the path method. The result of such a comparison is expressed by the following relations:

$$\left.\begin{aligned} \Delta^I x_i &= \Delta^P x_i-[(z_i-z_0)/(z_2-z_0)]\Delta^P x_2, \\ \Delta^I y_2 &= \Delta^P y_i-[(z_i-z_0)/(z_2-z_0)]\Delta^P y_2. \end{aligned}\right\} \tag{45}$$

Both methods give essentially the same result if the plane through z_2 terminates the deflection field where the deflection itself is still very small; then $\Delta^P x_2$ and $\Delta^P y_2$ will be small compared with $\Delta^P x_i$ and $\Delta^P y_i$, respectively.

The small difference between the results obtained by the two methods arises mainly from the fact that the path method corrects the first-order approximation path through the whole region from z_0 to z_i, while the iconal method corrects essentially only for the difference in slope at z_2, i.e., at the end of the field.

4. Some Remarks Concerning Applications

There are three problems which can be solved with the aid of the theory here presented. These are: (1) the determination of the "deflection" of the electron beam by any electric deflection system when the dimensions of the deflecting electrodes and their potentials are known; (2) the computation of the defocusing effects by a deflection system; and (3) the determination of deflection fields having less defocusing and distortion effects than those in common use.

The solution of the deflection problem requires a knowledge of the axial field-strength distribution $E(z)$. If the electrode shapes and potentials are known, $E(z)$ may, in some cases, be determined mathematically. In general, however, an experimental method must be used. The deflection may then be computed by means of Eq. (31). The problem of computing the defocusing and distortion effects requires a knowledge of $E(z)$, $E'(z)$, $Y(z)$, and $Y'(z)$. The defects of the deflection system are described by Eq. (33), the coefficients $\alpha_{a,b,c,d}$ and $\beta_{a,b,c,d}$ of Eqs. (37) and (38), ordinarily being determined by means of a planimeter. The coordinate z_0 is chosen to be outside the deflection field; $\alpha_{a,b,c,d}$ and $\beta_{a,b,c,d}$ are determined for any given screen position z_i and any given potentials ϕ and $\Delta\phi$. Since $E(z)$ is proportional to $\Delta\phi$, the various terms in the coefficients may be arranged in powers of $\Delta\phi/\phi$. Terms other than the lowest in each coefficient may ordinarily be neglected, reducing the amount of work involved in making computations. In order to compute the spot distortion, x_{iu}, y_{iu}, and x_{iu}', y_{iu}' are chosen to be the coordinates and slopes, respectively, of an electron in the undeflected beam. It should be noted that if the electron beam is considered to be a rectilinear flow of electrons with sharp boundaries, either cylindrically or conically shaped, the computations need only be applied to a number of electrons on the circumference of the beam.

Equation (33) can also be used to determine pattern distortion. It has been pointed out that crossed electrostatic fields, necessary to obtain a

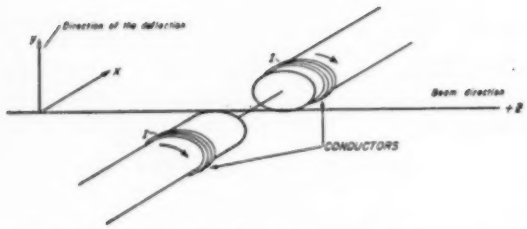

FIG. 5. Conductors and pole pieces producing a magnetic deflection field.

pattern, are arranged successively along the optical axis of the tube; it is assumed that a field-free plane exists between the two deflecting fields. The effects of both fields can then be superimposed linearly upon each other. An electron moving along the axis of the focusing system is deflected first by the vertical deflection system by the amount $Y(z_i)+\Delta^P y_i$ in the y direction, and zero in the x direction. Shortly after passing the vertical deflection field it passes through the horizontal deflection field, the effect of which is computed by replacing x by y, and y by x in all equations written so far. The horizontal deflection will be

$$x_i = -\frac{1}{2\phi}\int_{z_0}^{z_i} d\zeta \int_{z_0}^{\zeta} E_h(u)du,$$

where $E_h(z)$ symbolizes the axial field-strength distribution of the horizontal deflection field. The quantities $\Delta^P y_i$ and $\Delta^P x_i$ determine the additional deflections when x and y are interchanged in Eq. (33). The "initial conditions" x_{iu}, y_{iu}, x_{iu}', y_{iu}' are given by

$$x_{iu}=0, \quad y_{iu}=Y_i, \quad x_{iu}'=0, \quad y_{iu}'=Y_i'.$$

Spot and pattern distortions were computed for a number of deflection systems and will be presented in Part II.

The third problem, namely, that of determining deflection fields having smaller defocusing and distortion effects than those ordinarily encountered, means, mathematically, to find a function $E(z)$ such that Y_i has a prescribed value and yields coefficients $\alpha_{a,b,c,d}$ and $\beta_{a,b,c,d}$ smaller than those of known systems for the same value of Y_i. Various auxiliary conditions may be imposed such as those of constant electrode-to-screen distance, "reasonable" physical size of deflecting electrodes, etc. Solutions of these problems by mathematical procedures such as those used in the calculus of variations appear extremely difficult. It is more likely that trial and error methods, guided by the theory as expressed by Eqs. (31), (33), (37), and (38), will lead to improved deflection fields.

C. MAGNETIC DEFLECTION FIELDS

1. The Field Distribution

Magnetic deflection fields of cathode-ray and television tubes are produced by a pair of iron or air-cored electromagnets placed in "ear-muff" position on the outside of the tube. This is illustrated in Fig. 5 by a single deflection field. In order to obtain a pattern on the screen of the tube, two such fields are needed, rotated 90 degrees about the optical axis with respect to each other. Ordinarily these two fields exist over the same interval along the axis. Electrostatic deflection fields were arranged one after the other along the axis. This difference between the arrangements necessitates a difference in theoretical treatment. The effects of the crossed magnetic fields can only be described by treating them as a single field obtained by superposition of the two fields, since both magnetic fields act simultaneously on the electron beam.

Series expressions for magnetic field distributions will now be derived in a manner similar to that used for electrostatic fields. Fields of the type pictured in Fig. 5 show a certain kind of symmetry. Again using Cartesian coordinates x, y, and z, with $+z$ in the direction of the original motion of the electrons, and with y and x in the direction of vertical and horizontal deflections, respectively, a mirror-type symmetry of the fields exists with respect to the (x, z) and $(y; z)$ planes. The lines of force are mirror-symmetrical with respect to these planes. This condition may be expressed mathematically for the two fields by the following two sets of equations.

(1) Horizontal deflection field:

$$\left.\begin{aligned} H_z^h(x,y,z) &= -H_z^h(-x,y,z) \\ &= -H_z^h(x,-y,z), \\ H_y^h(x,y,z) &= +H_y^h(-x,y,z) \\ &= +H_y^h(x,-y,z), \\ H_x^h(x,y,z) &= +H_x^h(-x,y,z) \\ &= -H_x^h(x,-y,z). \end{aligned}\right\} \quad (46)$$

(2) Vertical deflection field:

$$\left.\begin{aligned} H_x^v(x, y, z) &= +H_x^v(-x, y, z) \\ &= +H_x^v(x, -y, z), \\ H_y^v(x, y, z) &= -H_y^v(-x, y, z) \\ &= -H_y^v(x, -y, z), \\ H_z^v(x, y, z) &= -H_z^v(-x, y, z) \\ &= +H_z^v(x, -y, z), \end{aligned}\right\} \quad (47)$$

where H_x^h, H_y^h, H_z^h, and H_x^v, H_y^v, H_z^v are the components of the magnetic field-strength vectors $\mathbf{H}^h$ and $\mathbf{H}^v$, respectively.

In current-free regions the relations

$$\mathrm{div}\mathbf{A}=0, \quad \nabla^2\mathbf{A}\equiv 0 \quad (48)$$

must hold for the magnetic vector potential $\mathbf{A}$, which is related to the magnetic field strength $\mathbf{H}$ by

$$\mathbf{H}=\mathrm{curl}\mathbf{A}. \quad (49)$$

The functions describing the components of the magnetic field strength may be expanded in power series of powers in x and y in which the coefficients are functions of z. Hence for the vertical deflection field one may write

$$\left.\begin{aligned} H_x^v &= p_{00}+p_{20}x^2+p_{02}y^2+p_{22}x^2y^2+p_{40}x^4+p_{04}y^4+p_{44}x^4y^4+p_{24}x^2y^4+p_{42}x^4y^2+\cdots, \\ H_y^v &= q_{11}xy+q_{13}xy^3+q_{31}x^3y+q_{33}x^3y^3+\cdots, \\ H_z^v &= r_{10}x+r_{12}xy^2+r_{32}x^3y^2+r_{14}xy^4+r_{34}x^3y^4+r_{30}x^3+\cdots. \end{aligned}\right\} \quad (50)$$

The procedure for the horizontal deflection field is the same.

In Eq. (50) use was made of the symmetry relations expressed by Eq. (47). The series for the components of the magnetic vector potential must then be (to give a relation expressed by (49)) of the form

$$\left.\begin{aligned} A_x^v &= a_{11}xy+a_{31}x^3y+a_{13}xy^3+a_{33}x^3y^3+a_{15}xy^5+\cdots, \\ A_y^v &= b_{00}+b_{20}x^2+b_{02}y^2+b_{22}x^2y^2+b_{40}x^4+b_{04}y^4+b_{24}x^2y^4+\cdots, \\ A_z^v &= c_{01}y+c_{21}x^2y+c_{03}y^3+c_{41}x^4y+c_{23}x^2y^3+c_{05}y^5+c_{43}x^4y^3+c_{25}x^2y^5+\cdots. \end{aligned}\right\} \quad (51)$$

The relations between the two sets of coefficients ($p_{\alpha\beta}$, $q_{\alpha\beta}$, $r_{\alpha\beta}$) and ($a_{\alpha\beta}$, $b_{\alpha\beta}$, $c_{\alpha\beta}$) may be found by the use of Eq. (49). Two more sets of relations between the coefficients of the set ($a_{\alpha\beta}$, $b_{\alpha\beta}$, $c_{\alpha\beta}$) may be found by use of the Eq. (48).

Redefining these coefficients p_{00}, p_{02}, and p_{04} by

$$p_{00}\equiv -V_0(z), \quad p_{02}\equiv -V_2(z), \quad p_{04}\equiv -V_4(z), \quad (52)$$

the following series for the components H_x^v, H_y^v, and H_z^v are obtained:

$$\left.\begin{aligned} H_x^v &= -V_0+(V_2+\tfrac{1}{2}V_0'')x^2-V_2y^2-[V_4+\tfrac{1}{6}V_2''+(1/24)V_0^{(IV)}]x^4 \\ &\qquad +(6V_4+\tfrac{1}{2}V_2'')x^2y^2-V_4y^4+\cdots, \\ H_y^v &= -2V_2xy-4V_4xy^3+(4V_4+\tfrac{1}{3}V_2'')x^3y+\cdots, \\ H_z^v &= -V_0'x-V_2'xy^2+(\tfrac{1}{3}V_2'+\tfrac{1}{6}V_0''')x^3+\cdots. \end{aligned}\right\} \quad (53)$$

The series for the components of the horizontal deflection field may be obtained by interchanging x and y in Eq. (53) and replacing V_0 by $-H_0$, V_2 by $-H_2$, and V_4 by $-H_4$. This yields

$$\left.\begin{aligned} H_x^h &= 2H_2xy+4H_4x^3y-(4H_4+\tfrac{1}{3}H_2'')xy^3+\cdots, \\ H_y^h &= H_0-(H_2+\tfrac{1}{2}H_0'')y^2+H_2x^2+[H_4+\tfrac{1}{6}H_2''+(1/24)H_0^{(IV)}]y^4 \\ &\qquad -(6H_4+\tfrac{1}{2}H_2'')x^2y^2+H_4x^4+\cdots, \\ H_z^h &= H_0'y+H_2'x^2y-(\tfrac{1}{3}H_2'+\tfrac{1}{6}H_0''')y^3+\cdots. \end{aligned}\right\} \quad (54)$$

The field strength of the combined fields is then given by

$$\left.\begin{aligned}
H_x &= -V_0+(V_2+\tfrac{1}{2}V_0'')x^2+2H_2xy-V_2y^2-[V_4+\tfrac{1}{6}V_2''+(1/24)V_0^{(\mathrm{IV})}]x^4+4H_4x^3y \\
&\qquad +(6V_4+\tfrac{1}{2}V_2'')x^2y^2-(4H_4+\tfrac{1}{3}H_2'')xy^3-V_4y^4+\cdots, \\
H_y &= H_0+H_2x^2-2V_2xy-(H_2+\tfrac{1}{2}H_0'')y^2+H_4x^4+(4V_4+\tfrac{1}{3}V_2'')x^3y \\
&\qquad -(6H_4+\tfrac{1}{2}H_2'')x^2y^2-4V_4xy^3+[H_4+\tfrac{1}{6}H_2''+(1/24)H_0^{(\mathrm{IV})}]y^4+\cdots, \\
H_z &= -V_0'x+H_0'y-V_2'xy^2+H_2'x^2y+(\tfrac{1}{3}V_2'+\tfrac{1}{6}V_0''')x^3-(\tfrac{1}{3}H_2'+\tfrac{1}{6}H_0''')y^3+\cdots.
\end{aligned}\right\} \tag{55}$$

The functions $-V_0$ and $+H_0$ are the axial field-strength distributions of the vertical and horizontal field strengths, respectively.

2. Theory of Magnetic Deflection

Either the path method or the iconal method may be used to describe the deflection and deflection defocusing effects of magnetic fields. Only the path method will be presented here; both methods give substantially the same result.

The equations of motion of an electron through any magnetic field are

$$\left.\begin{aligned}
\sqrt{\phi}(d/dz)[x'/(1+x'^2+y'^2)^{\frac{1}{2}}] &= \eta[-y'H_z+H_y], \\
\sqrt{\phi}(d/dz)[y'/(1+x'^2+y'^2)^{\frac{1}{2}}] &= \eta[x'H_z-H_x],
\end{aligned}\right\} \tag{56}$$

where ϕ is the potential of the space in which the electrons are moving and $\eta=(e/2m)^{\frac{1}{2}}$, where e and m are charge and mass, respectively, of the electron. Equations (56) may be obtained either from

$$\delta\int_{P_0}^{P_i}\{[2(e/m)\phi]^{\frac{1}{2}}-e/m(\mathbf{A}\cdot\mathbf{s})\}ds=0, \tag{57}$$

with $\mathbf{H}=\mathrm{curl}\mathbf{A}$, or from Newton's equations of motion, written

$$m\frac{d^2\mathbf{r}}{dt^2}=-e[\mathbf{v}\times\mathbf{H}], \quad \text{with} \quad \mathbf{r}=x\mathbf{i}+y\mathbf{j}+z\mathbf{k}. \tag{58}$$

If the magnetic field is that given by Eqs. (55), the Eqs. (56) become

$$\left.\begin{aligned}
(d/dz)[x'-\tfrac{1}{2}x'^3-\tfrac{1}{2}x'y'^2] &= (\eta/\sqrt{\phi})[V_0'y'x-H_0'y'y+H_0+H_2x^2-2V_2xy-(H_2+\tfrac{1}{2}H_0'')y^2], \\
(d/dz)[y'-\tfrac{1}{2}y'^3-\tfrac{1}{2}y'x'^2] &= (\eta/\sqrt{\phi})[-V_0'x'x+H_0'x'y+V_0-(V_2+\tfrac{1}{2}V_0'')x^2-2H_2xy+V_2y^2],
\end{aligned}\right\} \tag{59}$$

where only terms of zero, first and second order of x, x', y, and y' are considered. To a first approximation, the equations of motion are

$$x''=(\eta/\sqrt{\phi})H_0, \quad y''=(\eta/\sqrt{\phi})V_0. \tag{60}$$

The solution of these equations is

$$x_g(z)=x_0+x_0'(z-z_0)+X(z), \quad y_g(z)=y_0+y_0'(z-z_0)+Y(z), \tag{61}$$†††

where

$$X(z)=\frac{\eta}{\sqrt{\phi}}\int_{z_0}^{z}d\zeta\int_{z_0}^{\zeta}H_0(u)du, \quad Y(z)=\frac{\eta}{\sqrt{\phi}}\int_{z_0}^{z}d\zeta\int_{z_0}^{\zeta}V_0(u)du. \tag{62}$$

The quantities $X=X(z)$ and $Y=Y(z)$ at $z=z_i$ (the screen position) are the deflections at the screen.

††† This solution corresponds to the paraxial ray equation of the theory of focusing fields.

The deflections in the two directions x and y are independent of each other in this first-order approximation.

It was assumed that the quadratic terms in Eq. (59) were negligibly small. They are still assumed to be small, but will now be taken into account. Following the procedure used for electric deflection fields, x, x', y, and y' of Eq. (59) will be replaced by x_g, x_g', y_g, and y_g' of Eq. (61). This yields

$$\left.\begin{aligned}
(d/dz)[x'-\tfrac{1}{2}x_g'^3-\tfrac{1}{2}x_g'y_g'^2] &= (\eta/\sqrt{\phi})\{V_0'[y_0'+Y'][x_0+x_0'(z-z_0)+X] \\
&\quad -H_0'[y_0'+Y'][y_0+y_0'(z-z_0)+Y]+H_0+H_2[x_0^2+x_0'^2(z-z_0^2)+X^2+2x_0x_0'(z-z_0) \\
&\quad +2x_0X+2x_0'(z-z_0)X]-2V_2[x_0y_0+x_0'y_0(z-z_0)+y_0X+x_0y_0'(z-z_0) \\
&\quad +x_0'y_0'(z-z_0)^2+y_0'(z-z_0)X+x_0Y+x_0'(z-z_0)Y+XY] \\
&\quad -(H_2+\tfrac{1}{2}H_0'')[y_0^2+y_0'^2(z-z_0)^2+Y^2+2y_0y_0'(z-z_0)+2y_0Y+2y_0'(z-z_0)Y]\}, \\
(d/dz)[y'-\tfrac{1}{2}y_g'^3-\tfrac{1}{2}y_g'x_g'^2] &= (\eta/\sqrt{\phi})\{-V_0'[x_0'+X'][x_0+x_0'(z-z_0)+X] \\
&\quad +H_0'[x_0'+X'][y_0+y_0'(z-z_0)+Y]+V_0-(V_2+\tfrac{1}{2}V_0'')[x_0^2+x_0'^2(z-z_0)^2+X^2 \\
&\quad +2x_0x_0'(z-z_0)+2x_0X+2x_0'(z-z_0)X]-2H_2[x_0y_0+x_0'y_0(z-z_0)+y_0X \\
&\quad +x_0y_0'(z-z_0)+x_0'y_0'(z-z_0)^2+y_0'(z-z_0)X+x_0Y+x_0'(z-z_0)Y+XY] \\
&\quad +V_2[y_0^2+y_0'^2(z-z_0)^2+Y^2+2y_0y_0'(z-z_0)+2y_0Y+2y_0'(z-z_0)Y]\}.
\end{aligned}\right\} \tag{63}$$

The initial conditions x_0, x_0', y_0, and y_0' may be replaced by x_{iu}, x_{iu}', y_{iu}, and y_{iu}' of the undeflected electron. The relation between these quantities is

$$x_0=x_{iu}+x_{iu}'(z_0-z_i), \quad y_0=y_{iu}+y_{iu}'(z_0-z_i), \quad x_0'=x_{iu}', \quad y_0'=y_{iu}'. \tag{64}$$

The solution of the differential equations, Eqs. (63) can be obtained by simple integrations. If the differences $\Delta^M x_i$ and $\Delta^M y_i$ between the new solution and that given by Eqs. (61) are taken, one obtains

$$\left.\begin{aligned}
\Delta^M x_i &= \gamma_{0000}+\gamma_{1000}x_{iu}+\gamma_{0100}y_{iu}+\gamma_{0010}x_{iu}'+\gamma_{0001}y_{iu}'+\gamma_{2000}x_{iu}^2 \\
&\quad +\gamma_{1100}x_{iu}y_{iu}+\gamma_{0200}y_{iu}^2+\gamma_{0020}x_{iu}'^2+\gamma_{0011}x_{iu}'y_{iu}'+\gamma_{0110}x_{iu}'y_{iu} \\
&\quad +\gamma_{1001}x_{iu}y_{iu}'+\gamma_{1010}x_{iu}x_{iu}'+\gamma_{0101}y_{iu}y_{iu}'+\gamma_{0002}y_{iu}'^2, \\
\Delta^M y_i &= \delta_{0000}+\delta_{1000}x_{iu}+\delta_{0100}y_{iu}+\delta_{0010}x_{iu}'+\delta_{0001}y_{iu}'+\delta_{2000}x_{iu}^2 \\
&\quad +\delta_{1100}x_{iu}y_{iu}+\delta_{0200}y_{iu}^2+\delta_{0020}x_{iu}'^2+\delta_{0011}x_{iu}'y_{iu}'+\delta_{0110}x_{iu}'y_{iu} \\
&\quad +\delta_{1001}x_{iu}y_{iu}'+\delta_{1010}x_{iu}x_{iu}'+\delta_{0101}y_{iu}y_{iu}'+\delta_{0002}y_{iu}'^2.
\end{aligned}\right\} \tag{65}$$

The coefficients $\gamma_{a,b,c,d}$ and $\delta_{a,b,c,d}$ in Eq. (65) are

$$\left.\begin{aligned}
\gamma_{0000} &= \tfrac{1}{2}\int X'^3dz+\tfrac{1}{2}\int X'Y'^2dz-(\eta/\sqrt{\phi})\int Y'XV_0'(z-z_i)dz \\
&\quad +(\eta/\sqrt{\phi})\int YY'H_0(z-z_i)dz-(\eta/\sqrt{\phi})\int H_2X^2(z-z_i)dz \\
&\quad +(\eta/\sqrt{\phi})\int Y^2H_2(z-z_i)dz+(2\eta/\sqrt{\phi})\int XYV_2(z-z_i)dz+\tfrac{1}{2}(\eta/\sqrt{\phi})\int Y^2H_0''(z-z_i)dz, \\
\gamma_{1000} &= -(2\eta/\sqrt{\phi})\int XH_2(z-z_i)dz+(2\eta/\sqrt{\phi})\int YV_2(z-z_i)dz-(\eta/\sqrt{\phi})\int Y'V_0'(z-z_i)dz,
\end{aligned}\right\}$$

(Equation 66 continued on following page)

$$\gamma_{0100}=(\eta/\sqrt{\phi})\int Y'H_0'(z-z_i)dz+(2\eta/\sqrt{\phi})\int XV_2(z-z_i)dz$$
$$+(2\eta/\sqrt{\phi})\int YH_2(z-z_i)dz+(\eta/\sqrt{\phi})\int YH_0''(z-z_i)dz,$$

$$\gamma_{0010}=\tfrac{3}{2}\int X'^2dz+\tfrac{1}{2}\int Y'^2dz-(\eta/\sqrt{\phi})\int Y'V_0'(z-z_i)^2dz$$
$$-(2\eta/\sqrt{\phi})\int XH_2(z-z_i)^2dz+(2\eta/\sqrt{\phi})\int YV_2(z-z_i)^2dz,$$

$$\gamma_{0001}=\int X'Y'dz-(\eta/\sqrt{\phi})\int XV_0'(z-z_i)dz$$
$$+(\eta/\sqrt{\phi})\int YH_0'(z-z_i)dz+(\eta/\sqrt{\phi})\int Y'H_0'(z-z_i)^2dz+(2\eta/\sqrt{\phi})\int XV_2(z-z_i)^2dz$$
$$+(2\eta/\sqrt{\phi})\int YH_2(z-z_i)^2dz+(\eta/\sqrt{\phi})\int YH_0''(z-z_i)^2dz, \quad (66)$$

$$\gamma_{2000}=-(\eta/\sqrt{\phi})\int H_2(z-z_i)dz,$$

$$\gamma_{1100}=(2\eta/\sqrt{\phi})\int V_2(z-z_i)dz,$$

$$\gamma_{0200}=(\eta/\sqrt{\phi})\int H_2(z-z_i)dz+\tfrac{1}{2}(\eta/\sqrt{\phi})\int H_0''(z-z_i)dz,$$

$$\gamma_{0020}=\tfrac{3}{2}\int X'dz-(\eta/\sqrt{\phi})\int H_2(z-z_i)^3dz,$$

$$\gamma_{0011}=\int Y'dz+(2\eta/\sqrt{\phi})\int V_2(z-z_i)^3dz-(\eta/\sqrt{\phi})\int V_0'(z-z_i)^2dz,$$

$$\gamma_{0110}=(2\eta/\sqrt{\phi})\int V_2(z-z_i)^2dz,$$

$$\gamma_{1001}=-(\eta/\sqrt{\phi})\int V_0'(z-z_i)dz+(2\eta/\sqrt{\phi})\int V_2(z-z_i)^2dz,$$

$$\gamma_{1010}=-(2\eta/\sqrt{\phi})\int H_2(z-z_i)^2dz,$$

$$\gamma_{0101}=(\eta/\sqrt{\phi})\int H_0'(z-z_i)dz+(2\eta/\sqrt{\phi})\int H_2(z-z_i)^2dz+(\eta/\sqrt{\phi})\int H_0''(z-z_i)^2dz,$$

$$\gamma_{0002}=\tfrac{1}{2}\int X'dz+(\eta/\sqrt{\phi})\int H_0'(z-z_i)^2dz+(\eta/\sqrt{\phi})\int H_2(z-z_i)^3dz+\tfrac{1}{2}(\eta/\sqrt{\phi})\int H_0''(z-z_i)^3dz;$$

$$
\begin{aligned}
\delta_{0000} &= \tfrac{1}{2}\int Y'^3 dz + \tfrac{1}{2}\int X'^2 Y' dz \\
&\quad + (\eta/\sqrt{\phi})\int XX'V_0'(z-z_i)dz - (\eta/\sqrt{\phi})\int X'YH_0'(z-z_i)dz \\
&\quad + (\eta/\sqrt{\phi})\int X^2 V_2(z-z_i)dz + \tfrac{1}{2}(\eta/\sqrt{\phi})\int X^2 V_0''(z-z_i)dz \\
&\quad + (2\eta/\sqrt{\phi})\int XYH_2(z-z_i)dz - (\eta/\sqrt{\phi})\int Y^2 V_2(z-z_i)dz, \\
\delta_{1000} &= (2\eta/\sqrt{\phi})\int XV_2(z-z_i)dz + (\eta/\sqrt{\phi})\int XV_0''(z-z_i)dz \\
&\quad + (2\eta/\sqrt{\phi})\int YH_2(z-z_i)dz + (\eta/\sqrt{\phi})\int X'V_0'(z-z_i)dz, \\
\delta_{0100} &= -(\eta/\sqrt{\phi})\int X'H_0'(z-z_i)dz + (2\eta/\sqrt{\phi})\int XH_2(z-z_i)dz - (2\eta/\sqrt{\phi})\int YV_2(z-z_i)dz, \\
\delta_{0010} &= \int X'Y'dz + (\eta/\sqrt{\phi})\int XV_0'(z-z_i)dz + (\eta/\sqrt{\phi})\int X'V_0'(z-z_i)^2 dz \\
&\quad - (\eta/\sqrt{\phi})\int YH_0'(z-z_i)dz + (2\eta/\sqrt{\phi})\int XV_2(z-z_i)^2 dz \\
&\quad + (\eta/\sqrt{\phi})\int XV_0''(z-z_i)^2 dz + (2\eta/\sqrt{\phi})\int YH_2(z-z_i)^2 dz, \\
\delta_{0001} &= \tfrac{3}{2}\int Y'^2 dz + \tfrac{1}{2}\int X'^2 dz - (\eta/\sqrt{\phi})\int X'H_0'(z-z_i)^2 dz \\
&\quad + (2\eta/\sqrt{\phi})\int XH_2(z-z_i)^2 dz - (2\eta/\sqrt{\phi})\int YV_2(z-z_i)^2 dz, \\
\delta_{2000} &= (\eta/\sqrt{\phi})\int V_2(z-z_i)dz + \tfrac{1}{2}(\eta/\sqrt{\phi})\int V_0''(z-z_i)dz, \\
\delta_{1100} &= (2\eta/\sqrt{\phi})\int H_2(z-z_i)dz, \\
\delta_{0200} &= -(\eta/\sqrt{\phi})\int V_2(z-z_i)dz, \\
\delta_{0020} &= \tfrac{1}{2}\int Y'dz + (\eta/\sqrt{\phi})\int V_0'(z-z_i)^2 dz + (\eta/\sqrt{\phi})\int V_0(z-z_i)^3 dz + \tfrac{1}{2}(\eta/\sqrt{\phi})\int V_0''(z-z_i)^3 dz,
\end{aligned}
\tag{67}
$$

(Equation 67 continued on following page)

$$\delta_{0011}=\int X'dz-(\eta/\sqrt{\phi})\int H_0'(z-z_i)^2dz+(2\eta/\sqrt{\phi})\int H_2(z-z_i)^3dz,$$

$$\delta_{0110}=-(\eta/\sqrt{\phi})\int H_0'(z-z_i)dz+(2\eta/\sqrt{\phi})\int H_2(z-z_i)^2dz,$$

$$\delta_{1001}=(2\eta/\sqrt{\phi})\int H_2(z-z_i)^2dz,$$

$$\delta_{1010}=(\eta/\sqrt{\phi})\int V_0'(z-z_i)dz+(2\eta/\sqrt{\phi})\int V_2(z-z_i)^2dz+(\eta/\sqrt{\phi})\int V_0''(z-z_i)^2dz,$$

$$\delta_{0101}=-(2\eta/\sqrt{\phi})\int V_2(z-z_i)^2dz,$$

$$\delta_{0002}=\tfrac{3}{2}\int Y'dz-(\eta/\sqrt{\phi})\int V_2(z-z_i)^3dz.$$

The path method was applied by G. Wendt[6] to obtain expressions $\Delta^M x_i$ and $\Delta^M y_i$ for a single magnetic field. His equations may be obtained from Eqs. (65)–(67) by letting either H_0, H_2, and H_4, or V_0, V_2, and V_4 be identically equal to zero.

The two crossed magnetic deflection fields of actual cathode-ray tubes are ordinarily superimposed. The simultaneous deflecting action finds its expression in the existence of cross-terms with integrals of the type

$$\int X'Y'dz, \quad \int X V_2(z-z')dz,$$

$$\int Y H_2(z-z_i)dz \quad \text{etc.}$$

3. Some Remarks Concerning Applications

The solution of the deflection problem requires a knowledge of the axial field-strength distributions $V_0(z)$ and $H_0(z)$. Experimental methods are ordinarily the only means to determine these functions. It is rarely possible to compute them from the shapes of current conductors or pole pieces. The axial field strengths V_0 and H_0 could be measured by means of a number of methods described in the literature.[7]

In order to compute the distortion and defocusing effects, two other functions are required, namely $V_2(z)$ and $H_2(z)$. From Eq. (55) it can be seen that

$$(\partial^2 H_x/\partial y^2)\,|_{\substack{x=0\\y=0}}=-2V_2(z).$$

A similar equation holds for $H_2(z)$:

$$(\partial^2 H_y/\partial x^2)\,|_{\substack{x=0\\y=0}}=2H_2(z).$$

These relations provide the means to determine V_2 and H_2 experimentally. H_x is measured in the y, z plane at z for a number of values of y in the neighborhood of $y=0$. It is then possible to determine for each z the quantity $(\partial^2 H_x/\partial y^2)\,|_{x=0,\,y=0}$ and hence $V_2(z)$. A similar procedure for H_y will give $H_2(z)$. The measurements are made for each field alone.

The coefficients may be determined for any screen position coordinate z_i. Pattern and spot distortions are computed in a manner similar to that described for electrostatic fields.

Comparing the two sets of coefficients, a remark made above can now be verified easily. The set of coefficients $\gamma_{a,b,c,d}$ goes over into the set $\delta_{b,a,d,c}$ if H_0 is replaced by V_0, H_2 by V_2 and x_{iu} by y_{iu}, and x_{iu}' by y_{iu}'. If the functional dependency of the field-strength functions H_0, H_2 is the same as those of V_0, V_2, corresponding coefficients will also be alike numerically and only one set of coefficients need be calculated.

Electrostatic Dischargers for Aircraft

WAYNE C. HALL
Naval Research Laboratory, Washington, D. C.
(Received February 27, 1947)

Methods of discharging static electricity from aircraft in flight so as to reduce or eliminate corona interference, commonly known as precipitation static, are discussed. These methods have been classified into those employing either gaseous ions (high mobility), or those employing charge carriers such as water spray or dust particles (low mobility). Devices within the first classification offer the better solution to the problem from a practical standpoint. A discharger invented and developed at the Naval Research Laboratory is described.

INTRODUCTION

AIRCRAFT flying in stormy weather, at a time when radio communication becomes particularly important, often encounter a severe form of radio interference sufficient to prevent all reception.[1] The interference, which is commonly known as "precipitation static," results when the aircraft, acting as an isolated conductor, becomes electrically charged. When the charging is caused by rain, snow, ice particles, or dust, that is, by friction with atmospheric particles, it is found[2] that the charging is roughly proportional to the cube of the air speed and to the frontal area of the aircraft. Consequently, this effect may be expected to increase on the larger, higher speed aircraft of the future.

The reason for precipitation static may be seen from the following. Charging the aircraft results in generating a potential gradient between the aircraft and its surroundings sufficiently large to cause a corona discharge. Corona discharges on aircraft are also caused by electrical fields existing around the aircraft in the vicinity of highly charged clouds. The corona will occur from the regions of high electrical field surrounding sharp projections on the plane, such as the antennae, antenna masts, and propellers. Ordinarily, a corona discharge creates steep wave front impulses which will induce transient voltages of considerable magnitude in the antenna circuit of a radio receiver nearby. This results because the usual corona discharge occurs in the form of bursts which are cut off in a quasi-periodic fashion by accumulations of space charge about the discharge point. In exceptional cases, as from a very sharp point, non-pulsating corona currents causing no radio interference may be observed; however, the equilibrium which permits this type of discharge is unstable and is quickly destroyed by any effect which dulls the point. If the point of discharge is on the antenna itself, a corona current as small as one microampere may cause severe static.[3]

The radio interference resulting from corona can occasionally be removed by noise suppressor circuits. Usually, however, the interference created is continuous and covers so broad a frequency range that noise reduction circuits have little or no beneficial effects. In general, precipitation static—that is, radio interference induced by corona, is best prevented by removing the cause: that is, by preventing the formation of corona on the aircraft.

An interfering corona will be prevented or reduced only if the electrical charge is drained off from the aircraft so rapidly that a potential gradient sufficient to cause corona does not develop. Evidently, any modification of the aircraft which will raise the minimum potential gradient required to cause corona will be very beneficial. It can be accomplished by the use of electrostatic shielding, or by dielectric treatment, which will tend to prevent corona discharge from the antenna or the aircraft itself. Discussion of such treatments, however, is beyond the scope of this article, which is limited to the description of discharge devices capable of removing electrostatic charge from the aircraft.

[1] H. M. Hucke, Proc. I.R.E. **27**, 301–316 (May, 1939); R. Gunn, W. C. Hall, and G. D. Kinzer, *ibid.* **34**, 156–161 (April, 1946).
[2] R. G. Stimmel, E. H. Rogers, F. E. Waterfall, and R. Gunn, Proc. I.R.E. **34**, 167–177 (April, 1946).
[3] G. D. Kinzer, and J. W. McGee, Proc. I.R.E. **34**, 234–240 (April, 1946).

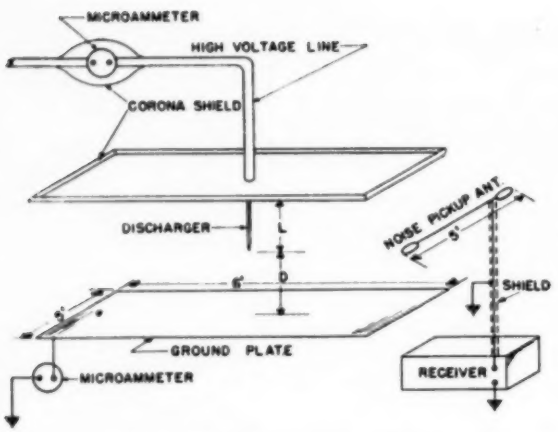

FIG. 1. Laboratory set-up to obtain discharger characteristics.

Electrostatic dischargers have the function of removing electric charge from the aircraft at a rate which substantially equals the rate of accumulation, and/or permitting the passage of electrical current to or from the aircraft when it is in the vicinity of charged clouds. Such dischargers may be classified into those using ions of high mobility (mobilities of 1.2 centimeters/second per volt/centimeter, or greater) and those using charge carriers, such as water particles or dust particles (mobilities varying from 0.002 to 0.01 centimeter/second per volt/centimeter). In the first classification are those dischargers involving the use of discharge wires or discharge points, while in the second classification are those involving the use of water spray or dust particles charged by induction or triboelectric processes.

GASEOUS-ION DISCHARGERS

Consider, first, the static dischargers which involve the highly mobile gaseous ions and electrons. Steps involved in operating these dischargers are: (1) the production of ions, and (2) the subsequent removal of ions with one sign only from the charged aircraft by the surrounding electric field. The discharge current resulting will remove charge of the same sign as that on the aircraft, and will be limited primarily by the space charge that forms about the discharge points. An example of a discharger in this class is the so-called trailing wire discharger, which consists of a five-foot strand of small wire extending in flight from the tail of the aircraft. This discharger has had some use and does help. Another example of this class of discharger is one using needle points located on the extremities of the aircraft, or on the propellers. In these examples, the electric field causing separation of charge is fixed largely by the potential of the aircraft, a factor which may not be increased greatly without causing interfering corona on the aircraft. Hence, in an investigation of possible increased output for this class of dischargers, it is sufficient to consider only whether the discharger will benefit from more profuse generation of ions, and whether the number of dischargers to be used may be increased with beneficial effects.

For a laboratory study of the static discharger, an experimental arrangement was constructed consisting of two parallel plates, between which a d.c. potential difference of up to 60,000 volts could be established. The discharger under investigation was attached to one of these plates. Nearby, a short antenna attached to an aircraft type receiver was arranged so as to pick up the radiated interference created by the discharger; then simultaneous measurements of the potential difference between the plates, current from the discharger, and radio noise picked up by the antenna were taken. All noise measurements were made in terms of the equivalent signal required from a signal generator coupled to the

TABLE I. Characteristics of sharp point dischargers.

Type of discharger	Distance D to plate	Voltage	Discharge (micro-amperes)	Radio noise at 300 kc
Needle point* (sharp and clean)	40 cm	+30,000	4	Less than 3 μv
		+45,000	11	Less than 3 μv
		+60,000	23	Less than 3 μv
		−30,000	−5	Less than 3 μv
		−45,000	−14	Less than 3 μv
		−60,000	−26	Less than 3 μv
Needle point (sharp and clean)	2.5 cm	−45,000	−350	160 μv
		−57,000	−520	Sparkover above this
		+15,000	30	16 μv
		+19,000	80	~400 μv— Sparkover above this
Two needle points (40 cm separation parallel to plate)	40 cm	+45,000	20	Less than 3 μv
		+60,000	38	Less than 3 μv
		−45,000	−25	Less than 3 μv
		−60,000	−45	Less than 3 μv
Blunt point with superimposed r-f arc r-f—8.0 Mc Generator—50 watts**	18 cm	−40,000	−33	Less than 3 μv
		−60,000	−68	~4 μv
		+40,000	27	<3 μv
		+60,000	60	~6 μv
Metallicized wick***	18 cm	+60,000	68	<3 μv
		−60,000	−74	<3 μv

* Using blunt points, it was observed that discharge currents were reduced and noise signals up to 400 μv were obtained.
** Estimated r-f dissipation in arc =5 to 10 watts.
*** See Table 3. Presented here for comparison purposes.

receiver through a 100-micromicrofarad condenser to cause a receiver output, as measured by an averaging meter, equal to that from the noise signal. Measurements were taken at two frequencies, 300 kilocycles and 4000 kilocycles. Since those at 300 kilocycles were always larger, for the sake of brevity only they will be given. The laboratory set-up is shown in Fig. 1.

Using sharp needle points about 10 centimeters long, with a separation of 40 centimeters between point and plate, results were obtained which are given in Table I. When dull or damaged needles were tried, noise measurements as great as 400 microvolts were observed.[4] Next, the experiment was repeated with short lengths of wire parallel to the plate, so as to duplicate, roughly, the trailing wire discharger. The results obtained are not given, because they are comparable to those obtained with the sharp needle points, except that the radio noise was much greater. In supplementary flight experiments, it was found that if very long lengths of wire, say 400 feet in length, were trailed behind an aircraft in flight, the entire wire exhibited corona and maintained the aircraft at a low potential. Although effective in some respects, such a discharger is not practical because of the radio noise generated, the difficulty of handling such a long wire, the undesirable alteration of the radio transmission characteristics of the aircraft, and the lightning hazard involved. The short trailing wire and the blunted needle point are practical but suffer from the defect, already explained, that the corona discharge from them causes noise in nearby radio receivers. In fact, it is possible to use either type of discharger with some degree of success only when it is suitably attached to the aircraft by a series decoupling resistor of about ½ megohm or more, and when it is properly installed on the tail of the aircraft, where the interference radiated will be shielded as much as possible from the overhead antennae. This means that trailing wire dischargers or needle points (whose sharp points soon become dull or damaged) should not be installed on the wings where good inductive coupling with the antennae exists. Such dischargers, therefore, are undesirably limited in use.

TABLE II. Characteristics of dischargers with thermal ions.

Source of thermal ions	Distance D to plate	Voltage	Discharge (micro-amperes)	Radio noise at 300 kc**
Acetylene flame* (blue cone—1 cm long)	60 cm from flame to plate	+30,000	6	<3 μv
		+45,000	16	<3 μv
		+60,000	28	<3 μv
		−30,000	−12	<3 μv
		−45,000	−26	3 μv
		−60,000	−44	4 μv
Gasoline blowtorch (flame length—13 cm)	54 cm from flame to plate	+45,000	14	Radio noise input less than 3 μv
		+60,000	20	
		−45,000	−27	
		−60,000	−43	
Manufactured gas flame from Mecca burner (flame, 15 cm long)	45 cm	+45,000	19	<3 μv
		+60,000	35	<3 μv
		−45,000	−28	<3 μv
		−60,000	−53	4 μv
Signal flare (flame—10 cm long)	60 cm	+60,000	10	<3 μv
		−60,000	−20	<3 μv

* Flame consumes about 225 cc acetylene (N.T.P.) per minute.
** Noise measurements are uncertain and may show large values for changing electric fields.

The problem remains of devising a discharger without such limitations and of investigating whether or not profuse generation of ions will improve the output of the discharger. Taking the second part of the problem first, several possible ion sources must be reviewed. Of these, the electric arc appears to be quite promising because of the known high ionization intensity existing in the arc. Also, it is known[5] that the superposition of a high frequency field upon a d.c. field at a point can be made to prevent discharge bursts causing interference. Based on this knowledge, experiments intended to measure the effectiveness of the electric arc as a static discharger have been carried out at several laboratories, including the Naval Research Laboratory. The discharger investigated at this Laboratory consisted of a blunt tungsten point supplied with radiofrequency energy from a resonant circuit and mounted on one of the two parallel plates in the d.c. field previously described. The discharge currents for an arc of about ½ inch length, requiring some 50 watts of oscillator power at a frequency of 8.0 megacycles, are given in Table I. With the receiver tuned to 300 kilocycles, the radio interference from the arc discharge was negligible; at 5 megacycles, it was serious. Evidently, therefore, the arc frequency should be several times that of the receiver frequency

[4] Needles employed in these experiments were common polished steel sewing needles of various sizes, the size having negligible effect upon the results. However, even a barely visible deformation of the point was sufficient to make the discharge from the point become noisy.

[5] M. O'Day, Civil Aeronautics Adm. Tech. Dev. Report No. 27 (August, 1940).

TABLE III. Characteristics of wick* dischargers.

Type	Distance D to plate	Voltage	Discharge (micro-amperes)	Radio noise at 300 kc
Glycerol impregnated (after 25 hours flight time on aircraft)	30 cm	+40,000	13	Less than 3 μv
		+60,000	36	Less than 3 μv
		−40,000	−18	Less than 3 μv
		−60,000	−48	Less than 3 μv
Metallized (with silver)	30 cm	+30,000	12	Less than 3 μv
		+45,000	25	Less than 3 μv
		+60,000	44	Less than 3 μv
		−30,000	−11	Less than 3 μv
		−45,000	−26	Less than 3 μv
		−60,000	−50	Less than 3 μv
Metallized (with silver)	2.5 cm	+15,000	20	Less than 3 μv
		+30,000	125	Less than 3 μv
		+53,000	350	Sparkover above this
		−30,000	−130	Radio noise less than 3 μv
		−45,000	−350	
		−60,000	−620	

* Each wick of cotton fibers, over-all diameter ¼ inch, length approximately 6 inches.

for noise-free operation of the discharger. Results were disappointing, in that the amount of r-f power dissipated in the arc, provided it was large enough to reduce corona static, had only a small effect on the discharger current. This was determined by varying the oscillator power over the range from 50 to 150 watts; the arc length varied from ½ to 1½ inches over this range.

Parallel experiments seeking the effect of thermal ions on discharge characteristics were conducted in the apparatus already described, using flames in place of the r-f arcs previously used. It had been observed before that a flame could be made to ignite and burn in a slipstream by using a specially designed nozzle, and by using a fuel, such as acetylene, with a high heat of combustion. In the laboratory experiments, much radio noise resulted if any metallic projections having high field intensities sufficient to cause corona were present in the flame itself; however, flames could be made to discharge with no measurable radio noise. The results obtained in the laboratory using acetylene flames, gasoline, and solid fuel are given in Table II.

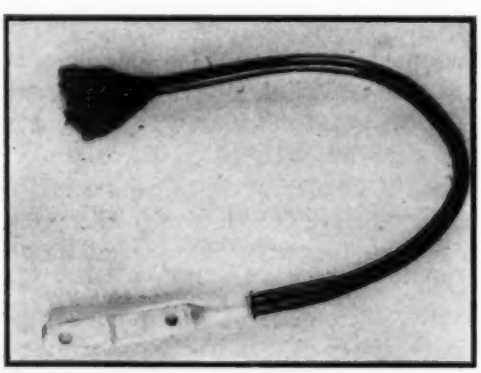

FIG. 2A. Wick type static discharger.

Next, exhaust gases from the aircraft reciprocating engines were considered for use in the discharge process; however, the low temperature, relatively speaking, of exhaust gases as they leave the exhaust pipe of this type of engine, results in ion densities too small to be of any real help. For example, calculations based on exhaust gas conductivity of eight electrostatic units (obtained from other data) indicate currents from the exhaust will be of the order of 10 to 20 microamperes per 1000 horsepower engine. This approximate result has been checked by experiment.[6] Discharge possibilities using the exhaust from jet type engines have not been investigated.

Certain observations may now be made, based on the data of Tables I and II. These data show that the point discharger, the arc discharger, and the flame discharger have roughly the same discharge current. The major part of the differences in discharge current which exist may be ascribed to differing geometries at the discharger, or to different separations between the parallel plates across which the d.c. test voltage was maintained. Neither the relatively diffuse ionized region of the flame, nor the intense ionization of the high frequency arc significantly increased the output of the discharger. The only conclusion which can be drawn is that all of these dischargers are space-charge limited and, therefore, are unavoidably limited in output.[7,8] With this

[6] R. G. Stimmel, E. H. Rogers, F. E. Waterfall, and R. Gunn, Proc. I.R.E. **34**, 175 (April, 1946).

[7] During discharge there is about any of the dischargers a narrow region or layer of intense ionization; the rest of the space between the plates is free from the action of the ionizing agent. Also, the discharge current to the opposite plate is only a small fraction of the maximum corresponding to the ionization. Hence, the situation is quite analogous to that discussed by J. J. Thomson, reference 8, for the case where ionization is confined to a thin layer between parallel plates. Thomson shows that in this case, the discharge current, i, is given by

$$i = A(V^2k/l^3)$$

where A is a constant, V is the potential difference between the plates, l is the separation, and k is the mobility of the ion carrying the charge. It is apparent that the current, i, is

in mind, it becomes evident that improvements in the static discharger of this type can be realized only by making the discharger noise-free, cheap, easy to install, and capable of being attached at a number of points on the aircraft. The last improvement is the only one which can be expected to drain off larger and larger amounts of electric charge from the aircraft.

In the search for improvements along these lines, a "wick" discharger was developed by the author at the Naval Research Laboratory. It is essentially a small, flexible, treated cotton wick enclosed in a plastic tube, with many conducting fibers exposed at the end to serve as discharge points (see Fig. 2). The multitude of points in the wick have high resistance paths back to the aircraft, a negligible capacity, and provide a completely noise-free discharger of this type. Other fibers than cotton may be used, obviously, but none have been found more satisfactory. The cotton wick is treated to make it conducting, either by soaking the wick in an aqueous glycerol solution, chosen because it provides the desired low conductivity and has a very low rate of evaporation, or by metallizing the wicks with very thin deposits of metal. Either treatment is satisfactory, except that the glycerol treated wick is subject to a diminution in effectiveness as the glycerol evaporates or is diluted with rain water, and is more prone to become dirty in use on aircraft. The latter point is important, because wicks that are dirty may become noise. Metallized wicks using silver were found to have an indefinite life, except for mechanical wear. The discharge characteristics of some wicks made by the author are shown in Table III. These wicks generated no radio noise whatever at normal frequencies when properly made (so as to be free of metal flakes or bulky metal deposits), up to the limit of discharge which could be taken from the wicks before spark breakdown of the surrounding air occurred.

The "wick" discharger, or any discharger of this class, has limitations of the following nature. First, it must be placed on the aircraft in an exposed position where it will begin to discharge before other parts of the aircraft exhibit interfering corona. For best performance of these dischargers, therefore, they must be placed at the points of maximum electric field about the aircraft, as shown in Fig. 3. Two dischargers on each wing tip, and two to four on the empennage, represent a practical installation, though more could be used for improved performance. Second, no matter how many "wick" dischargers are used, precipitation static will occasionally be observed. This occurs when the charging current to the aircraft becomes significantly greater than the discharge current from the wicks. In such

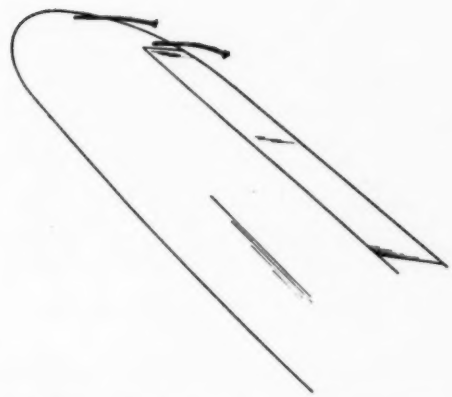

FIG. 2B. Wick type static discharger sample installation on wing.

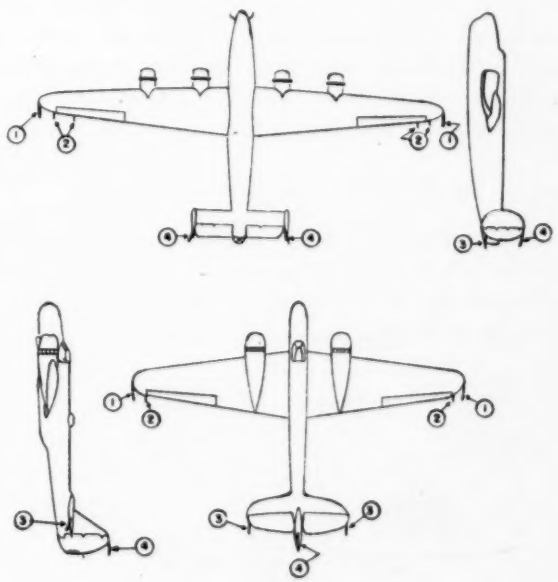

FIG. 3. Preferred localities for dischargers.

independent of the intensity or amount of ionization, and is thus space-charge limited.

[8] J. J. Thomson, *Conduction of Electricity through Gases* (Cambridge University Press) third edition, p. 206.

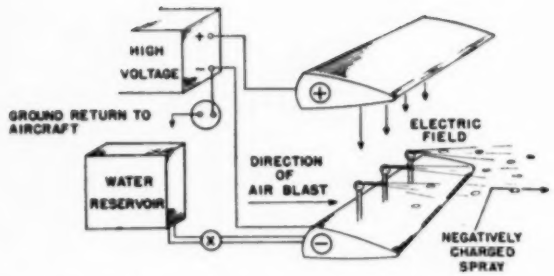

FIG. 4. Schematic of a water spray discharger.

cases, observed in severe atmospheric conditions, the aircraft will experience precipitation static, though usually for brief periods of time. For example, in the case of heavy rain, when precipitation static is heard, it will be difficult to remove. In this case, the streamers of water from the trailing edges of the airplane or other projections, such as the antenna, become, effectively, blunt points subject to corona discharge. Such streamers of water in an electric field under laboratory conditions are observed to cause intense radio static.

Another important point with regard to dischargers of this class should be made. It is known that atmospheric electrification of the aircraft may raise it to an extremely high potential with respect to its surroundings; for example, to a potential of one-half million volts. Consideration of this fact will lead to a realization that boosting the potential of a discharger relative to the aircraft by some 20,000 volts, such as may be obtained by a high voltage rectifier on the plane, will have little effect on the discharge current. Experimental results confirm this conclusion.

HEAVY PARTICLE DISCHARGERS

The second class of electrostic dischargers involves heavy particles, such as charged water droplets, as charge carriers. Charged particles like these are produced, for example, in a liquid spray exposed to a strong electric field. Alternatively, these charge carriers are produced by a triboelectric process where certain finely divided materials, such as powdered quartz, flowing through friction tubes take on one sign of charge, leaving the other charge on the friction tube. Such particles have mobilities of the order of 0.002 centimeter/second per volt/centimeter.

Dischargers of this class have some advantages, in that:

(1) The external electric field about the aircraft does not necessarily affect the amount of charge induced upon the particles sprayed from the discharger; hence, the discharge currents are relatively unlimited, and the point of attachment is unimportant.

(2) The aircraft's external field does not necessarily determine the induced charge; therefore, discharge current of either sign may be obtained.

The induction type of discharger, using a water spray, is illustrated by Fig. 4. It exposes water droplets to a strong electric field as the water droplets are removed from a nozzle by a high speed blast of air. This discharger has been used very successfully to charge aircraft in flight under fair weather conditions for the purpose of simulating precipitation static conditions.[9] In flight tests using a large number of spray nozzles, discharge currents of 250 microamperes have been measured for a water discharge of approximately 75 grams/second. By stepping up the rate of flow of the water through the spray nozzle, this discharger could be made to discharge quite an appreciable current. If the auxiliary electric field that is established at the spray nozzle to charge the droplets is maintained slightly below a value sufficient to cause corona, there will be little radio noise generated. There are engineering drawbacks to such a discharger, however; for example, the discharger requires an auxiliary high voltage of some 20,000 volts, a bulky and heavy tank of non-freezing liquid such as alcohol, and it increases the aerodynamic losses of the aircraft.

The triboelectric discharger, on the other hand, is illustrated in one form that it takes in Fig. 5. Here the friction between the tube and particles moving through affects the amount of charge carried away by the particle. Since the friction

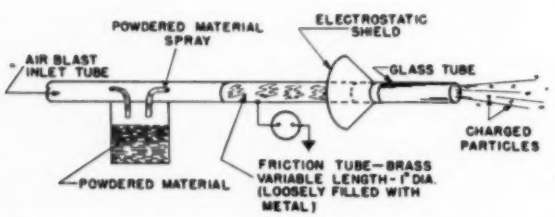

FIG. 5. Schematic diagram of triboelectric discharger.

[9] R. C. Waddel, R. C. Drutowski, and W. N. Blatt, Proc. I.R.E. **34**, 161–166 (April, 1946).

is partially determined by the velocity of the air blast through the tube, the data to be reported on the triboelectric discharger are for one air velocity only, namely, 250 miles per hour at the inlet tube. Table IV has been prepared to show the performance characteristics of this discharger under the given conditions. As high as 84 microcoulombs of charge per gram of material was obtained when using finely divided quartz (Santocel). Making the reasonable assumption that the average radius of the particles of the diatomaceous earth used (largely silica) was 10^{-4} centimeter, the theoretical limit of charge which could be carried by the powdered material per cubic centimeter of solid material (before pulverization) becomes $3E/4\pi R$, where E is the electric field at breakdown of the surrounding air. This corresponds roughly to a figure of 80 microcoulombs per cubic centimeter, or 30 microcoulombs per gram.

With this type of discharge, the substance of the powdered material usually determines whether the sign of charge will be positive or negative. Many materials, when blown through the friction tube, came out with a negative sign. This would be desirable, because in nearly all cases of charging by atmospheric particles, the airplane became negatively charged and would require a discharger of negative electricity. Noise measurements on the triboelectric discharger gave erratic results; at times a high level of noise intensity was observed. These and other drawbacks, of an engineering and practical nature, are believed to be sufficiently important to prevent any commercial use of this discharger.

TABLE IV. Characteristics of triboelectric dischargers using powdered materials.

Material	Discharge current (microamperes)	Discharge of material (grams/second)	Remarks	Efficiency microcoulombs per gram of material
Colloidal carbon*	+7#	1.4	Not dried	5
Infusorial earth*	−14#	1.4	Not dried	10
Diatomaceous earth*	−18	1.7	Not dried	10.6
Diatomaceous earth*	−13	1.1	Dried 2½ hrs. at 200°C	12
Diatomaceous earth**	−18	1.4	Dried 2½ hrs. at 200°C	13
Santocel (powdered quartz from Monsanto Chemical Co.)**	−50	1.0	Not dried	50
Santocel (powdered quartz from Monsanto Chemical Co.)***	−33	0.4	Not dried	84
Diatomaceous earth***	−12	0.36	Dried 2½ hrs. at 200°C	33
Santocel****	−9.5	0.13	Not dried	73
Santocel****	−25	0.30	Dried 1½ hrs. at 180°C	83
Titanium dioxide****	−5.5	0.60	Not dried	9
Graphite****	0	1.0	Not dried	0
Wheat flour****	+2.5	0.4	Not dried	7

# Denotes sign of charge on powder.
* Brass friction tube encloses ten copper tubes, ½ cm diam., 30 cm long.
** Brass friction tube, 75 cm long, loosely filled with steel wool.
*** Brass friction tube, 245 cm long, loosely filled with copper turnings.
**** Brass friction tube, 40 cm long, loosely filled with copper screen, mesh = 16/inch.

SUMMARY

To summarize, it appears that static dischargers are a practical necessity on aircraft using present-day methods of radio communication. Wicks or trailing wires, being simple and having relatively good performance, are to be preferred over other types. The wick discharger, if properly made, is completely noise-free and is applicable to the airplane at a number of points; hence, it appears to be the best available discharger. No discharger, alone, however, offers a complete solution to the problem.

Slow Transverse Magnetic Waves in Cylindrical Guides

G. G. Bruck and E. R. Wicher
Specialties, Inc., Syosset, Long Island, New York
(Received March 24, 1947)

The fundamental physical phenomenon upon which linear electron accelerators and traveling beam tubes depend is the fact that the phase velocity of guided *TM* waves can be reduced to a fraction of the velocity of light. There are various practical ways of achieving these reduced velocities, such as diaphragms or spiral grooves in the guide wall. An open helix has been used by Pierce.

An accurate knowledge of the field pattern would greatly facilitate an understanding of these devices. It is of particular importance to have exact information about the field in the region in which the charge actually travels, namely, in a region located at least a considerable fraction of a wave-length from the guide walls. Because of the complex shapes assumed by actual guide walls calculations of the field are inevitably somewhat inexact and complicated.

The authors propose that, for the purposes of theory, the well-established proposition concerning the equivalence of true and simulated dielectrics in producing a slow field be used. We propose to think of slowing down the phase velocity by lining the guide walls with a natural dielectric. The essential properties of the slow field, particularly in the important region referred to above, will not be affected by this method of obtaining it while, on the other hand, the field calculation becomes quite easy and exact.

Although this procedure is intended in the main as a device to facilitate the theoretical calculation of the field, the authors believe that such a step—replacement of periodic metallic structures by dielectrics—might prove useful in some actual applications.

THE solutions of Maxwell's equations appropriate to the description of a TM_{01} mode propagated axially in a cylindrical tube, may be written

$$\begin{aligned} E_z &= AJ_0(\kappa\rho)+BN_0(\kappa\rho) \\ E_r &= (2\pi i/\kappa s)[AJ_1(\kappa\rho)+BN_1(\kappa\rho)] \\ E_\varphi &= 0,\ H_z=0,\ H_r=0 \\ H_\varphi &= (2\pi ic\epsilon/\kappa)[AJ_1(\kappa\rho)+BN_1(\kappa\rho)] \end{aligned} \tag{1}$$

where $\rho=r/\lambda$, $s=v/c$, λ = free space wave-length, c = velocity of light, v = phase velocity actually present in tube, (z, r, φ) are standard cylindrical coordinates, $\kappa=2\pi c(\mu\epsilon-1/v^2)^{\frac{1}{2}}$, ϵ = inductive capacity of medium, μ = permeability, (E_z, E_r, E_φ), are components of electric field strength, (H_z, H_r, H_φ), are components of magnetic field strength, A, B are arbitrary constants to be adjusted to fit assigned boundary conditions.

Georgi rationalized units are used. It is understood that the factor $\exp(i\omega t-\gamma z)$ has been omitted from the right members of all of (1). Here ω is the angular frequency, equal to $2\pi c/\lambda$, and γ is the propagation constant. We neglect conductivity so that $\gamma=i\omega/v=2\pi i/s\lambda$.

We apply the solutions (1) to the case of a pair of infinitely long coaxial cylinders with radii $r_1=\rho_1\lambda$ and $r_2=\rho_2\lambda$, $\rho_1<\rho_2$. The inner cylinder is evacuated and the region $\rho_1<\rho<\rho_2$ is filled with a dielectric of inductive capacity ϵ_2. The outer cylinder is bounded by a perfect conductor. In the following we call the region $\rho<\rho_1$, region I, and the region $\rho_1<\rho<\rho_2$, region II. Parameters referring explicitly to these regions are distinguished by the use of subscripts 1 and 2.

In medium I, $B_1=0$ because the N functions are infinite at $\rho=0$. Hence,

$$\begin{aligned} E_{z1}&=A_1J_0(\kappa_1\rho),\quad E_{r1}=(2\pi i/\kappa_1 s)A_1J_1(\kappa_1\rho), \\ E_{\varphi 1}&=0,\quad H_{z1}=0,\quad H_{r1}=0, \\ H_{\varphi 1}&=(2\pi ic\epsilon_1/\kappa_1)A_1J_1(\kappa\rho), \end{aligned} \tag{2}$$

$$\kappa_1=2\pi(1-1/s^2)^{\frac{1}{2}}. \tag{3}$$

We now examine three cases.

Case *I*. κ_1 is real. Then by (3), $s>1$ and $v>c$. The z component of the electric field is described by the function $J_0(\kappa_1\rho)$ which is unity at $\rho=0$, and which tapers off to a zero at $\kappa_1\rho=2.4048$. In general, the fact that $J_0(\kappa_1\rho)$ is a decreasing

TABLE I.

ρ_2	$\rho_2-\rho_1$	ϵ_2/ϵ_1
0.9564	0.00064	154000.0
0.05530	0.00530	2499.0
0.05943	0.00943	774.4
0.06164	0.01164	524.3
0.07187	0.02187	174.4
0.08958	0.03958	74.44
0.10000	0.05000	57.25
0.1500	0.1000	34.27
0.4897	0.4397	25.63

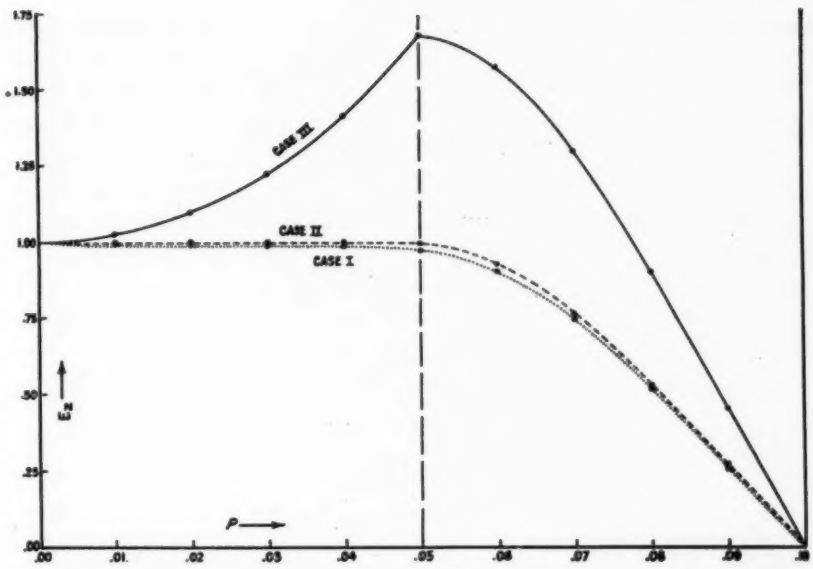

FIG. 1. Distribution of the longitudinal component of electric field strength through a cross section of the tube.

function for real κ_1 makes it usable in any case where $v>c$.

Case *II*. κ_1 is zero. Then by (3), $s=1$ and $v=c$. This gives $E_{z1}=A_1$, a constant. If region *I* were bounded by a conductor, this result would be trivial since all field components would have to vanish. Here, the result will have application to cases of electron accelerators, or traveling wave tubes in which the electrons have an energy of more than 10^6 electron volts.

Case *III*. κ_1 is imaginary. In this case $s<1$ and $v>c$. This gives an E_{z1} distribution described by $J_0(i|\kappa_1|\rho)=I_0(|\kappa_1|\rho)$, an increasing function of ρ. This type of distribution is of particular interest because it permits slowing down the phase velocity of the field to any desired value.

In region *II* the fields will be given by

$$E_{z2}=A_2J_0(\kappa_2\rho)+B_2N_0(\kappa_2\rho)$$
$$E_{r2}=(2\pi i/\kappa_2 s)[A_2J_1(\kappa_2\rho)+B_2N_1(\kappa_2\rho)] \quad (4)$$
$$E_{\varphi 2}=0,\ H_{z2}=0,\ H_{r2}=0$$
$$H_{\varphi 2}=(2\pi ic\epsilon_2/\kappa_2)[A_2J_1(\kappa_2\rho)+B_2N_1(\kappa_2\rho)] \quad (5)$$
$$\kappa_2=2\pi[(\epsilon_2\mu_2/\epsilon_1\mu_1)-(1/s^2)]^{\frac{1}{2}}.$$

The boundary conditions may be written

$$E_{z2}(\kappa_2\rho_2)=0,$$
$$E_{z1}(\kappa_1\rho_1)=E_{z2}(\kappa_2\rho_1), \quad (6)$$
$$\epsilon_1E_{r1}(\kappa_1\rho_1)=\epsilon_2E_{r2}(\kappa_2\rho_1).$$

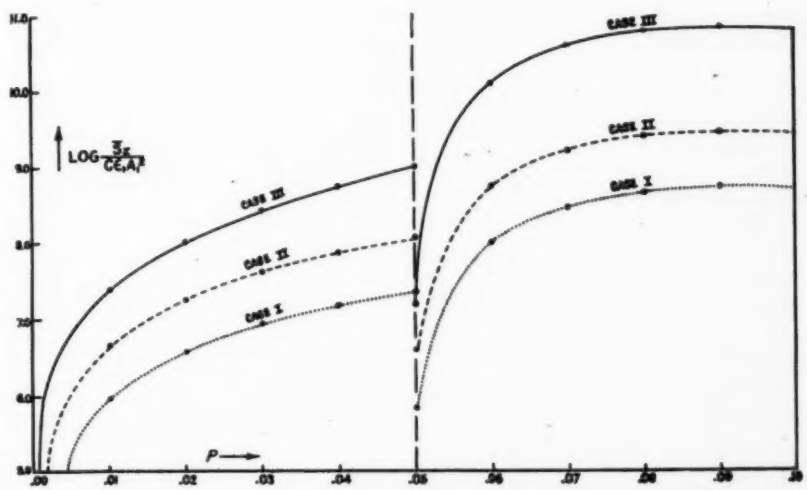

FIG. 2. Energy distribution. The logarithm of the real part of the complex Poynting vector plotted against the radial coordinate of the tube. The logarithm has been used to obtain a convenient scale.

From (2), (4), and (6) we get

$$A_2/A_1=(\pi\kappa_2\rho_1/2)[(\epsilon_1/\epsilon_2)(\kappa_2/\kappa_1)N_0(\kappa_2\rho_1)J_1(\kappa_1\rho_1)-N_1(\kappa_2\rho_1)J_0(\kappa_1\rho_1)],$$
$$B_2/A_1=(\pi\kappa_2\rho_1/2)[J_0(\kappa_1\rho_1)J_1(\kappa_2\rho_1)-(\epsilon_1/\epsilon_2)(\kappa_2/\kappa_1)J_0(\kappa_2\rho_1)J_1(\kappa_1\rho_1)]. \quad (7)$$

In these formulas A_1 is simply the amplitude of the z component of the electric field along the axis. From (6) and (7) we obtain

$$\frac{\epsilon_1}{\epsilon_2}\frac{\kappa_2}{\kappa_1}\frac{J_1(\kappa_1\rho_1)}{J_0(\kappa_1\rho_1)}=\frac{N_0(\kappa_2\rho_2)J_1(\kappa_2\rho_1)-J_0(\kappa_2\rho_2)N_1(\kappa_2\rho_1)}{N_0(\kappa_2\rho_2)J_0(\kappa_2\rho_1)-J_0(\kappa_2\rho_2)N_0(\kappa_2\rho_1)}. \quad (8)$$

This formula, taken with the definitions of κ_1 and κ_2, is a relation between field velocity, tube radii, and the dielectric constant of region *II*. In order to have a definite Case *III* to discuss, we chose $s=v/c=0.2$ and let $\rho_1=0.05$. These choices are arbitrary, and are simply meant to be illustrative. Having made this selection, (8) can be solved by a combination of patience with a variety of numerical procedures. The result is shown in Table I.

One particularly useful device in obtaining these points is to select the product $\kappa_2\rho_2$ to be a zero of either $J_0(\kappa_2\rho_2)$ or $N_0(\kappa_2\rho_2)$. For general points, (8) may be transformed to read

$$\frac{\epsilon_1}{\epsilon_2}\frac{\kappa_2}{\kappa_1}\frac{J_1(\kappa_1\rho_1)}{J_0(\kappa_1\rho_1)}=\frac{|H_1^{(1)}(\kappa_2\rho_1)|\sin(\psi-\theta_1)}{|H_0^{(1)}(\kappa_2\rho_1)|\sin(\psi-\theta_0)}, \quad (9)$$

where $\psi=\arg H_0^{(1)}(\kappa_2\rho_2)$, $\theta=\arg H_0^{(1)}(\kappa_2\rho_1)$, $\theta_1=\arg H_1^{(1)}(\kappa_2\rho_1)$.

The tables in Watson† are simply applicable to this form. We did the calculations from (9) to four significant figures and checked the results by substitution into (8). It will be noticed that for a given ϵ_2/ϵ_1, a denumerable set of numbers ρ_2 exists; we tabulate only the lowest ρ_2.

To compare field strength distributions, energy distributions, and field patterns in the three cases, we selected $v=0.2c$ (Case *III*), $v=c$ (Case *II*), and $v=5c$ (Case *I*), and fixed $\rho_1=0.05$ and

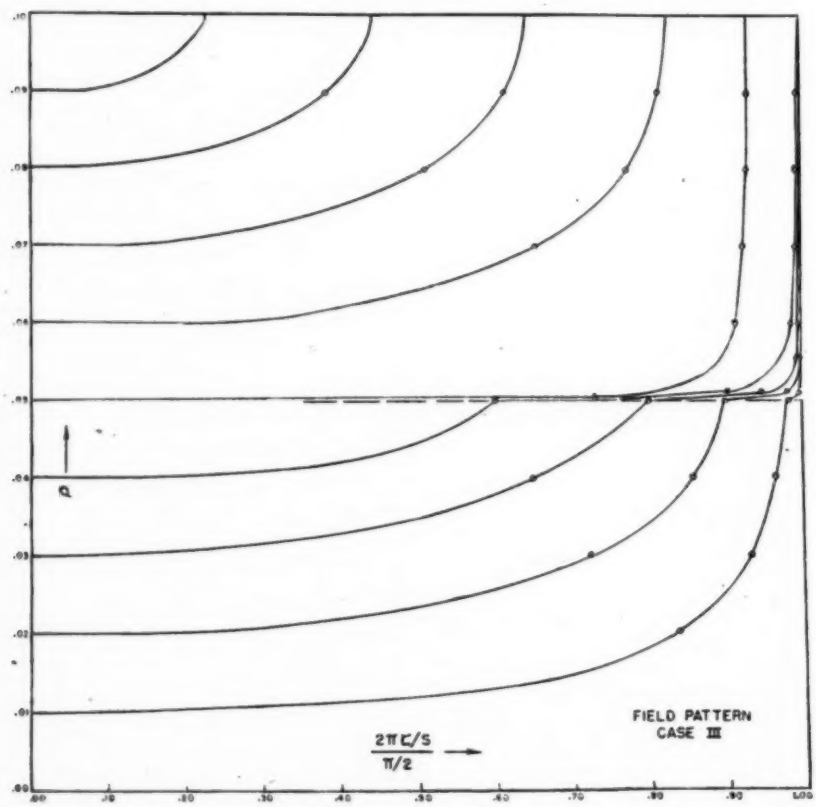

FIG. 3. Longitudinal field pattern, showing lines connecting points of equal electric field strength along a longitudinal cross section of the tube. The slope of the lines gives the direction of the field. $\zeta=z/\lambda$, and $s=v/c=2/10$.

† G. N. Watson, *Theory of Bessel Functions* (The Macmillan Company, New York, 1945), Chapter XX.

$\rho=0.10$ in all cases. This gives $\epsilon_2/\epsilon_1=57.25$ (Case *III*), $\epsilon_2/\epsilon_1=32.80$ (Case *II*), $\epsilon_2/\epsilon_1=31.82$ (Case *I*).

The results of this comparison for the distribution of the z component of the electric field are seen in Fig. 1.

The real part of the complex Poynting vector is given by

$$\bar{S}_{z1}/c\epsilon_1 A_1^2=(2\pi^2/\kappa_1^2 s)[J_1(\kappa_1\rho)]^2,$$

$$\bar{S}_{z2}/c\epsilon_1 A_1^2=\frac{2\pi^2}{\kappa_2^2 s}\frac{\epsilon_2}{\epsilon_1}\left[\frac{A_2}{A_1}J_1(\kappa_2\rho)+\frac{B_2}{A_1}N_1(\kappa_2\rho)\right]^2. \quad (10)$$

Figure 2 shows the logarithm of this quantity as a function of ρ for the three cases. It is obvious that practically all the energy is carried in region *II* in each case.

The field pattern is given by integrating the relation

$$dz/dr=ReE_z/ReE_r. \quad (11)$$

Letting

$$\zeta=z/\lambda, \quad (12)$$

(11) yields

$$\kappa_1\rho J_1(\kappa_1\rho)=C_1\sec(2\pi\zeta/s)$$
$$\kappa_2\rho[A_2J_1(\kappa_2\rho)+B_2N_1(\kappa_2\rho)]=C_2\sec(2\pi\zeta/s), \quad (13)$$

where C_1 and C_2 are integration constants. The obvious requirement on these constants is

$$\frac{C_1}{C_2}=\frac{\kappa_1\rho_1 J_1(\kappa_1\rho_1)}{\kappa_2\rho_1[A_2J_1(\kappa_2\rho_1)+B_2N_1(\kappa_2\rho_1)]}. \quad (14)$$

In Case *II* the first of Eqs. (13) may be replaced by

$$\rho^2=C_1\sec 2\pi\zeta, \quad (15)$$

so that (14) becomes, for this case

$$\frac{C_1}{C_2}=\frac{\rho_1^2}{\kappa_2\rho_1[A_2J_1(\kappa_2\rho_1)+B_2N_1(\kappa_2\rho_1)]}. \quad (16)$$

It develops that if the pattern be drawn by plotting ρ against $2\pi\zeta/s$, there is no appreciable difference between the three cases. This means that the effect of decreasing the field velocity is simply to compress the pattern in the direction of propagation. Figure 3 shows the pattern for Case *III*.

Incandescent Lamps as Electrical Load for Testing

S. KEILIEN
Pass and Seymour, Inc., Syracuse, New York
(Received March 25, 1947)

Because of the positive coefficient of resistivity of tungsten, incandescent lamps permit a current considerably greater than the normal lamp current to flow for a short initial period. When lamps are used as load for testing electrical apparatus, the factors affecting this inrush must be considered. Size of power source, its distance from the load (lamps), and frequency of switching the lamps (employing repetitive operations for endurance testing) are evaluated.

From the given curve the necessary cooling time for the desired current inrush may be determined, and thus the frequency with which the lamps could be switched "on" and "off" may be calculated. Practical means for obtaining the required cooling time are described.

ONE of an electric control device's usual function is switching. In this operation the electrical load is either connected to or disconnected from the source of power supply and, to be acceptable, the switching element should be capable of performing with least deterioration.

There are 3 basic types of loads, and their characteristics affecting the performance of switching devices may be summed up as follows:

Non-inductive-resistance load-current rise to reach the Ohm's-law value and its fall to zero (when disconnected) is instantaneous; the values of steady-state conditions are not exceeded.

Inductive load-current rise is gradual, depending on the rate of magnetic flux build-up; on disconnection of this load the stored electromagnetic energy is dissipated quickly, causing momentarily a high voltage, frequently far above that of the supply.

Tungsten-filament lamp load-current rise is very rapid and the maximum exceeds that of the steady-state value; current decay to normal value, following its reaching the peak, is relatively slow; upon the disconnection the fall of current to zero is instantaneous.

TABLE I.* Ratio R for various size lamps.

Size of lamp watts	Ratio R
100	9.1
500	8.7
1000	6.8

* R. W. Gillette, "Control of Multiple Street Lighting," Elec. World **94**, 419 (1929).

From the above grouping it will be seen that the inductive and the tungsten-filament lamp loads call for special precautions to be taken: the former upon interruption of the circuit (because of presence of high voltage) and the latter at completion of the circuit (because of current inrush).

In practice, the usual non-inductive-resistance loads are heating appliances of various kinds; the inductive load is typified by magnets and motors; the lamp-load characteristics are present in tungsten-filament lamps and condensers. For determination of suitability of a switching device, it is usually tested under various load conditions, and it is important to give proper consideration to these loads if the results of tests are to be used as criteria.

Tungsten filament lamps are employed extensively for testing the devices which are designed for such loads, or which are intended for loads with initial inrush of current. It is important, therefore, to have a clear conception of lamp characteristics and of limitations to assure their proper application as loads for testing.

TABLE II. Ratio R for various size lamp loads and their distance from busbars.

Load connecting circuit		Load (watts) and number and size of lamps (w)			
Length (ft.) and wire size (B and S gauge)	Total wire res. ohms	2400 w 4–500 w 2–200 w	1200 w 2–500 w 1–200 w	520 w 8–60 w 1–40 w	500 w 1–500 w
+ 163′—No. 10 16′—No. 14	.203	—	—	9.4	—
+ 148′—No. 10 16′—No. 14	.188	—	—	9.6	—
163′—No. 10	.163	7.7	9.1	—	11.0
148′—No. 10	.148	8.1	9.3	—	11.2
+ 10′—No. 10 + 10′—No. 11 + 16′—No. 14	.063	—	—	10.9	—
+ 10′—No. 10 10′—No. 11	.023	8.9	10.3	—	11.4

Notes: 1. All lamps—115 volts.
2. Power derived from specially designed 125 volts d.c. generator.
3. Values of "length" in first column—length of conductors between load and busbars.
4. Plus sign (+) in first column indicates series connections.

Because of the positive temperature coefficient of resistivity of the metal, the tungsten-filament lamps possess low resistance when cold and higher resistance when heated. It must be noted that carbon-filament lamps have the reverse characteristics because of the negative coefficient of resistivity of carbon. For regular 115- or 120-volt tungsten-filament lamps, sizes 40 to 1500 watts, the operating temperature of the filament varies between 4400°F and 4900°F, and the resistance of a hot lamp is 15 to 17 times that of a cold lamp. Consequently, if a cold lamp is connected to a source of supply, a current considerably greater than the normal lamp current will flow for a short time. Because of heating by the passing current, the temperature of the filament will rise and so will its resistance, thus causing a corresponding decrease in current. It would appear that the ratio of inrush current to the normal lamp current would be also 15 or 17 to 1. However, these values are not attained usually, for the inrush current also depends on such factors as the capacity of the current source, impedance of the circuit, and voltage stability, all of these tending to reduce the magnitude of the peak.

It is difficult to determine quantitatively the effect of some of the above factors, but definite conclusions may be drawn on the basis of experimental data.

The source of power should be of ample capacity to furnish the necessary inrush current. It is apparent that the source should not be the limiting factor, since the characteristics of the filament determine these inrush values. The ratio R of the peak current to nominal current of the lamp may be used as the criterion in evaluating the suitability of the generator.

A small generator having a relatively slow current response and a small amount of available power will give a smaller value of R, for the same lamp load, than would a larger machine. A 5-kw, 125 volt, direct-current generator controlling tungsten-filament lamps gave the current ratios R shown in Table I. A generator used for routine and experimental testing of switches produced

considerably greater values of R, as shown in Table II. It will be observed that such generator permits a current inrush to produce a value of R as high as 10.3, for 1200-watt load (compare a corresponding value of 6.8 for 1000-watt load with a smaller generator).

A generator for testing switching devices with lamps as load must be properly designed, for its rated capacity is not the only consideration. Factors like armature reaction, commutation, and voltage stability for a specific load will affect the values of R. The Underwriters' Laboratories, Inc., standard for switches specifies a generator capable of producing a current inrush of eight times the normal value of current, using a 20-ampere (normal) lamp load. Values of R considerably in excess of this can be obtained with specially designed generators.[1]

Size of conductors and distance between the lamp and the generator affect the resistance of the circuit. Since the current inrush is of transient nature, the impedance of this circuit must also be considered. The last four columns of Table II give values of the ratio R for various conductor sizes and their lengths. From this table it may also be observed that, for the same wattage, the larger the number of lamps in the circuit, the lower is the value of R (compare last two columns). This may be explained as follows: The rate of heating of a small lamp is considerably higher than that of a large lamp.[2] Because of this, with smaller lamps there will be considerably greater overlapping of the initial period when the current is limited by the circuit inductance and of the period when resistance of filament has risen sufficiently to reduce the current. Therefore, with same current, inductance and resistance of the circuit, smaller lamps would produce a lower value of R than would one large lamp of the same wattage. The R in the case of smaller lamps is further diminished by their lower final filament temperature, as compared with that of the larger lamp.

The use of tungsten-filament lamps for repetitive operations (connecting to and disconnecting from power source) should be conducted

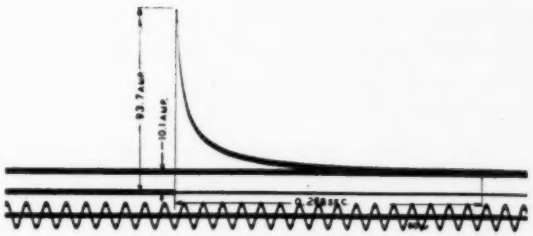

FIG. 1. Oscillogram showing current rise and decay in 1200-watt lamp circuit (2–500-w and 1–200-w lamps) upon its connection to 125-volt d.c. generator.

with discretion because of the time required to bring the filament to final temperature and the time needed for cooling it to the ambient temperature. The filament-heating time is relatively short. From oscillogram, Fig. 1, it will be seen that normal current was reached within 0.268 second. For lamps of lower rating this time is correspondingly shorter. Since the current decay in the lamp after reaching inrush peak is exponential, it is difficult to determine with a great degree of precision the exact point where the current curve reaches its normal value. However, for practical purposes, the oscillographic determination is sufficiently accurate.

The rate of cooling of the lamp is important in the calculation of the frequency with which the device under test may be operated. The value of R (ratio of inrush peak current to normal lamp current) may be used as basis for the determination. Should a lamp be reconnected to the power source while the filament is still hot, the ratio R would not be as great as that for a completely cooled lamp. This is apparent,

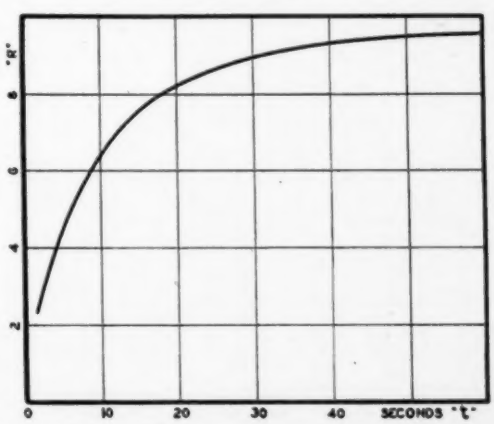

FIG. 2. Relation between cooling time t of tungsten-filament lamps and ratio R (ratio of initial peak current to normal current) for 1200-watt lamp load at 125-v d.c.

[1] S. Keilien, "Improving products through research and test for quality," Product Engineering 10, 24 (1939).

[2] W. E. Forsythe, M. A. Easley, and D. D. Hinman, "Time constants of incandescent lamps," J. App. Phys. 9, 209 (1938).

for under such a condition the differential in temperature would be lower. Results of experiments conducted with lamps which were cooled for varying intervals are represented by a curve, Fig. 2. In order to obtain stable data the readings of current inrush (from oscillograms) were obtained after constant ambient temperature had been established.

The curve is particularly valuable when rhythmic operation of switching *on* and *off* of lamps is to be employed. In testing current-interrupting devices for endurance, it is important to have a specific current inrush. From Fig. 2, it is possible to determine the cooling time (duration of the *off* period) for the desired current inrush, and then the frequency with which the testing is to be conducted may be readily calculated.

If, for endurance testing, only one lamp (or one bank of lamps) were used, it would be necessary to allow considerable time for its cooling in order to obtain the desired current peak on the subsequent *on* operation. Such procedure would be quite lengthy and would impede testing, especially if a large number of specimens is to be tested to keep up with production schedules.

To facilitate testing, a number of lamps (or banks of lamps) may be employed, so arranged that while one is being used (*on*) the others are cooling (*off*). This method makes possible any desired rate of specimen operation, the limitations being only those of the specimen itself, such as heat dissipation of its current carrying parts, velocity of its moving system, etc., and the time required to bring the filament to maximum temperature.

For repetitive operation of switches at a uniform rate, the number of lamps required to produce a desired cooling time may be calculated from Eq. (1),

$$N=\frac{t+a}{b+a} \tag{1}$$

where:

N—number of lamps (or banks of lamps),

t—lamp-cooling time to produce the desired value of R in seconds (obtainable from curve Fig. 2, for specific load),

a—time, per cycle of operation, during which the switch is *on*, in seconds,

b—time, per cycle of operation, during which the switch is *off*, in seconds.

If the *on* and the *off* periods of switch operation are equal, then Eq. (1) becomes

$$N=\frac{1}{60}(t\times f+30) \tag{2}$$

where f = rate of switch operation, in cycles per minute.

In testing switches, a is usually greater than the time required to heat the lamp and since the heating time is quite negligible in comparison with that needed for cooling the lamp, it was not considered in the formulae.

A very satisfactory scheme for the simultaneous testing of a number of switches is to connect the cold lamp in the circuit containing the specimen under test while this specimen is *off*, and to disconnect the lamp while the specimen is in the succeeding *off* position. Thus, the lamp-selecting device does not *make* nor *break* the circuit while it is alive; it is done by the device undergoing the test. The actual equipment for accomplishing such selection is shown in Fig. 3, which is a part of an installation for simultaneous testing of 10 switches, each with a 1200-watt lamp load, or a smaller number of switches with a proportionately greater load.

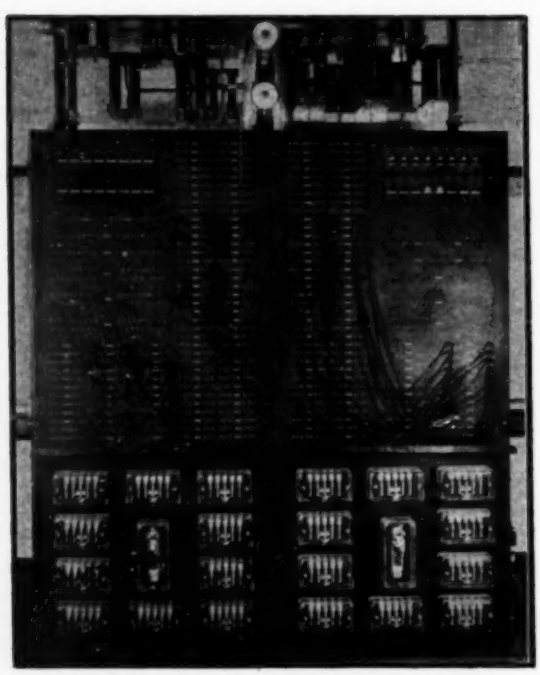

FIG. 3. View of switchboard with equipment for automatic selection of lamp circuits.

The cool lamps are connected in the test circuits by means of a magnetically-operated, step-by-step selector, which is driven in synchronism with the switches under test. The selector actually controls the coils of heavy-duty contactors, the contacts of which introduce into or remove from circuits the lamps for loading the switches. Other means of selection of cool lamps, such as continuously or intermittently-operated commutators, or cam-operated contacts of either spring or mercury type may be employed.

In some cases it is desired to obtain the inrush current with lesser equipment, or at quite rapid rate. Then, it is possible to connect resistance loads in such a way that the low resistance (allowing high current inrush) is removed from the circuit a short time after the switch under test has established the contact, leaving a higher resistance in the circuit (corresponding to normal current of lamp), thus permitting only normal current interruption by the switch. This arrangement does not duplicate actual lamp operation, because if current equivalent to inrush value is *on* for a considerable time the contacts are subjected to excessive heating. Furthermore, in the event of contact vibrations the contact erosion and welding are aggravated. Consequently, such testing may become unduly severe. In this scheme, shown in Fig. 4, the normal current is determined by resistance R_a, while the inrush current is limited by resistance R_b. After a predetermined interval following the closure of switch S, the timing contacts T open, thus permitting the switch S to break only the normal current, as determined by R_a. The current rises and decays abruptly since non-inductive resistances are used. Contacts T are synchronized with S so that they *close* and *open* before S is subjected to respective operations.

Another method is based on the characteristic curve of charging a condenser. A condenser of suitable capacity is connected in the test circuit before the switch is *closed;* this produces the necessary current inrush and decay. The condenser is then disconnected by a relay after a desired lapse of time, restoring the circuit containing a resistance to a current equal to that of normal value of the lamp. Essentially this arrangement is a modification of that shown in Fig. 4, the difference being in the introduction of

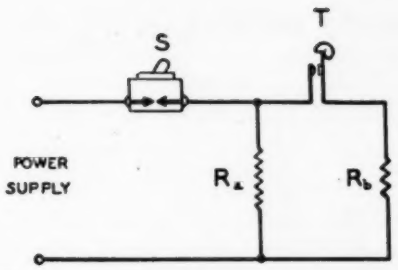

FIG. 4. Schematic wiring diagram of connections for producing initial current inrush.

capacitance C (not shown in diagram) in series with resistance R_b. As in the previous scheme, the resistance R_a determines the final value of current flowing through switch (normal lamp current), resistance R_b determines the peak current, while condenser C defines the rate of current decay during the transient period upon closure of switch S. Contacts T disconnect the condenser C (and resistance R_b) when the current through this path has decayed to a desired magnitude (near zero). This is done before S is opened. The operation of the timing contacts T may be accomplished either electrically or mechanically. Provision must be made for discharging the condenser C prior to its reconnecting into the circuit.

Because of presence of some inductance in the circuit, it is difficult to predict by calculation the initial peak current that would result. It is, therefore, necessary to adjust the parameter of the circuit until the desired values are obtained. These constants will differ from the calculated values.

While it is possible to duplicate relatively closely a current rise and decay of a tungsten-filament lamp, such synthetic-load testing equipment has been found less desirable from the standpoint of stability, reliability, and maintenance for large scale testing.

The tungsten-filament lamps should be employed as electrical load with due consideration given to their characteristics. Particular attention should be given to the frequency of operation of specimens under test, in order to obtain the desired current inrush during the *on* period. The source of power supply and the impedance of the circuit must also be evaluated if it is planned to duplicate the conditions to which the switching device would be subjected under actual field operations.

The Capacity per Unit Length and Characteristic Impedance of Coaxial Cables with One Slightly Non-Circular Conductor

PHILIP PARZEN*
New York, New York
(Received April 9, 1947)

It is possible to calculate approximately the electrostatic field in a coaxial line with one slightly non-circular conductor as a perturbation of that existing in the usual coaxial line. General expressions are then derived for the capacity per unit length and the characteristic impedance of such lines. In particular, these results are applied to the coaxial line with outer square conductor.

INTRODUCTION

THE calculation of the capacity per unit length, C, of a coaxial line depends upon the derivation of a potential distribution function, V, which satisfies $\nabla^2 V=0$, with the boundary conditions: $V=0$ on inner conductor, $V=V_1$ =constant on outer conductor. Thus,

$$C=-K\int \frac{\partial V}{\partial n}ds/V_1 \quad \text{(m.k.s. units)} \qquad (1)$$

where the numerator is the total charge per unit length which is given by the line integral of the normal derivative of the potential along either conductor, and K is the dielectric constant of the medium.

The characteristic impedance, Z_0, of a resistanceless line is:

$$Z_0=1/Cv,\ v=\text{velocity of light in medium.} \qquad (2)$$

This may be seen physically as follows: an outgoing progressive wave will advance a distance vdt in time dt, during which an amount of charge $dq=CvVdt$ will appear across that portion of the line. Hence the current $I=CvV$ and $Z_0=V/I=1/Cv$. A rigorous proof may be found in Smythe.[1]

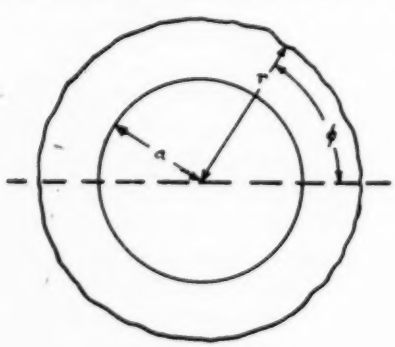

FIG. 1.

While the solution for concentric circles is quite easily obtained, only approximately correct solutions are obtainable for non-circular cables. In this paper we shall consider lines wherein one conductor is circular and the other slightly non-circular. The potential distribution is then calculated as a perturbation of that due to concentric circles. Finally we shall apply these results to the case where one conductor is square.

CALCULATION OF C AND Z_0

In Fig. 1 the inner conductor is a circle of radius a and the outer conductor is specified by its polar equation, $r=f(\phi)$, which can be sufficiently approximated by a Fourier series with p harmonics. Thus,

$$r=f(\phi)=A_0(1+\sum_1^p A_j\cos j\phi) \qquad (3)$$

with

$$\frac{p}{2}A_j^2\ll 1. \qquad (4)$$

The inclusion of sine terms in the Fourier series will not add anything of general value to the discussion. Moreover, most conductors in practice are symmetrical about an axis. Hence we seek a potential distribution $V(r\ \phi)$ such that,

$$\nabla^2 V=0 \qquad (5)$$

with boundary conditions,

$$V=0 \text{ on } r=a \qquad (6)$$

$$=V_1 \text{ on curve (3).} \qquad (7)$$

*Consulting Engineering Mathematician.

[1] W. R. Smythe, *Static and Dynamic Electricity* (McGraw-Hill Book Company, Inc., New York, 1939), p. 471.

Let

$$V = L \log r + M + \sum_1 (E_n r^n + F_n r^{-n}) \cos n\phi. \quad (8)$$

This expansion[2] will automatically satisfy (5), and to satisfy (6)

$$0 = L \log a + M \quad (9)$$

$$0 = E_n a^n + F_n a^{-n} \quad n = 1,2,\cdots \quad (10)$$

To satisfy (7), we have after expanding $\log r$, r^n, and r^{-n} in Taylor series about $r = A_0$,

$$\begin{aligned} V_1 = {} & L \log A_0 + M + L \\ & \times [\Sigma A_j \cos j\phi - \tfrac{1}{2}(\Sigma A_j \cos j\phi)^2 + \cdots] \\ & + \Sigma E_m A_0^m [1 + m \Sigma A_j \cos j\phi \\ & + \tfrac{1}{2} m(m-1)(\Sigma A_j \cos j\phi)^2 + \cdots] \cos m\phi \\ & + \Sigma F_m A_0^{-m} [1 - m \Sigma A_j \cos j\phi \\ & + \tfrac{1}{2} m(m+1)(\Sigma A_j \cos j\phi)^2 + \cdots] \cos m\phi, \end{aligned} \quad (11)$$

where . . . denotes higher powers of A_j. Now equating coefficients of $\cos n\phi$ in (11),

$$\begin{aligned} -LA_n = {} & E_n A_0^n + F_n A_0^{-n} \\ & + \tfrac{1}{2} \Sigma\Sigma m (E_m A_0^m - F_m A_0^{-m}) A_j + \cdots \\ & n = 1,2,\cdots \end{aligned} \quad (12)$$

and the double summation is taken over $m+j=n$, $m-j=\pm n$.
For $n=0$,

$$\begin{aligned} V_1 = {} & L(\log A_0 - \tfrac{1}{4}\Sigma A_j^2 + \cdots) + M \\ & + \tfrac{1}{2}\Sigma j (E_j A_0^j - F_j A_0^{-j}) A_j + \cdots \end{aligned} \quad (13)$$

We now have the linear set of Eqs. (9), (10), (12), and (13) to solve for L, M, E_n, and F_n. We should, however, point out that C depends upon L only, since by applying (1) to the inner circle, the line integral of the cosine terms in (8) vanish; thus

$$C = 2\pi K L / V_1. \quad (14)$$

We now solve Eqs. (10) and (12) for E_n and F_n by successive approximations. For a first approximation, we neglect the double summation and higher order terms in (12) and solving, we have,

$$E_n = -\frac{A_n L}{a^n [(A_0/a)^n - (a/A_0)^n]}, \quad (15)$$

$$F_n = \frac{a^n A_n L}{(A_0/a)^n - (a/A_0)^n}. \quad (16)$$

[2] See reference 1, p. 63.

Substituting these expressions in (13) and subtracting (9) from (13), we have to a first approximation,

$$C = \frac{2\pi K}{\log A_0/a - \sum_1 A_j^2 (\frac{1}{4} + \frac{1}{2} j R_j)} \text{ farads/meter} \quad (17)$$

$$R_j = \frac{(A_0/a)^j + (a/A_0)^j}{(A_0/a)^j - (a/A_0)^j}. \quad (18)$$

Thus we have an approximation which is of the order of jA_j^2. We can now obtain further approximations by substituting (15) and (16) in the neglected part of (12) and resolving for E_n and F_n, and so forth. This, however, will result in corrections to C which are of higher powers in jA_j^2 and hence may be neglected because of (4). It should also be noted that A_0 is always greater than a; otherwise there would be points on the outer conductor for which r is less than a, which is impossible.
Also, by (2),

$$Z_0 \text{ in air} = 60[\log A_0/a - \sum_1 A_j^2 (\tfrac{1}{4} + \tfrac{1}{2} j R_j)] \text{ ohms} \quad (19)$$

since $v = 3 \times 10^8$ meters/sec., and $K = 8.85 \times 10^{-12}$ farads/meter.

A case of interest is where A_0/a is of the order of 3 or greater. Then R_j is approximately 1 and

$$Z_0 = 60[\log A_0/a + d] \quad (20)$$

$$d = -\sum_1 A_j^2 (\tfrac{1}{4} + \tfrac{1}{2} j). \quad (21)$$

Since d is at most of the order of a few percent, we may replace d by

$$\log(1+d) \text{ and } Z_0 = 60 \log A^*/a \quad (22)$$

and A^*, which is $A_0/1+d$, may be considered as the outer radius of an equivalent coaxial (concentric lines) line, with the same characteristic impedance.

APPLICATION OF RESULTS TO SQUARE OUTER CONDUCTOR

For a square of side $2b$, the polar equation is,

$$\begin{aligned} r &= b \sec\phi \quad 0 \le \phi \le \pi/4 \\ r &= b \csc\phi; \ \pi/4 \le \phi \le \pi/2 \end{aligned} \quad (23)$$

with a periodicity of $\pi/2$. Hence only $\cos 4j\phi$ terms will appear in the Fourier series, and

$$A_0=\frac{4b}{\pi}p_0$$
$$A_0A_{4j}=\frac{8b}{\pi}p_j;\quad p_j=\int_0^{\pi/4}\sec\phi\cos 4j\phi d\phi. \tag{24}$$

Now,

$$p_{j-1}-p_j=2\int_0^{\pi/4}[\cos(4j-3)\phi-\cos(4j-1)\phi]d\phi$$
$$=(-1)^{j+1}2.828/(4j-3)(4j-1).$$

Thus knowing p_0, p_j is easily calculated; and $p_0=.881$, $p_1=-.062$, $p_2=.019$, $p_3=-.010$, $p_4=.005$, $A_0=1.12b$; $A_4=-.14$, $A_8=.044$, $A_{12}=-.021$, $A_{16}=.012$. Thus condition (4) is approximately satisfied with p equal to 12. Thus,

$$Z_0=60[\log b/a+.108-039R_4-.008R_8-.002R_{12}], \tag{25}$$

with

$$R_4=\frac{1.570(b/a)^4+.636(a/b)^4}{1.570(b/a)^4-.636(a/b)^4}, \tag{26}$$

and R_8 and R_{12} are given by similar expressions, with the constants replaced by (2.480, .403) and (3.870, .258), and the exponents by 8 and 12, respectively.

For b/a of the order of 2, the equivalent outer radius defined by (22) is $1.06b$. This value compares more or less favorably with $1.08b$, obtained by Frankel.[3] For b/a less than 2, Frankel's derivation does not apply, and the correct Z_0 is given by (25).

For b/a equal to 1, Z_0 from (25) is .06 ohms, which is fairly close to the actual value of Z_0, namely, 0. This constitutes a partial check upon the accuracy of this formula.

Finally I wish to thank Mr. Benjamin Parzen for suggesting the problem.

[3] S. Frankel, "Characteristic Impedance of Parallel Wires in Rectangular Troughs," Proc. I.R.E. **30**, 182 (1942).

Thermal Conductivity of Aluminum; Solid and Liquid States

C. C. Bidwell and C. L. Hogan
Lehigh University, Bethlehem, Pennsylvania
(Received April 9, 1947)

Thermal conductivity measurements on lead, tin, and zinc extending over the liquid as well as the solid states were reported by one of the authors in 1940. The present report extends this work to cover aluminum in both the liquid and solid phases. An improved technique is described. The law $k/\rho C=K(1/T)+K'$ is found to hold for aluminum also, with the intercept, K', the same for both states. The thermal conductivity (k) decreases with rise of temperature as it does for lead, tin, and zinc. On this point previous workers have published very conflicting data.

INTRODUCTION

DATA on the thermal conductivity of aluminum in the handbooks, the critical tables, and as collected and published in *The Aluminum Industry*[1] are conflicting particularly as to the change with temperature. No data for the liquid state are reported. Several observers report a rise of thermal conductivity with temperature; only one, Konno,[2] reports a decrease. The present data on a specimen of purity 99.20 percent is in exact agreement with Konno's values (0.50 at 0°C; 0.36 at 600°C). A specimen of purity 99.95 percent is found to have a higher conductivity, *viz.*, 0.54 at 25°C, decreasing to 0.44 at 657°C. On this specimen, measurements were extended into the liquid state at points 740°C and 900°C.

[1] Edwards, Frary, and Jeffries, *The Aluminum Industry* (McGraw-Hill Book Company, New York, 1930).
[2] S. Konno, Phil. Mag. **40**, 542 (1920).

THE METHOD

The Forbes bar method previously used was further modified and adapted to high temperature work. A cylinder of the material under study, 25 cm long, 2.5 cm in diameter, was

centered vertically in a tubular furnace and surrounded with finely screened silocel. Thermojunctions were previously fastened to the rod every 3 cm by insertion into small holes drilled about 1.5 mm deep, and the junctions peened in. At the upper end, just above the top junction, was placed a heater coil of about 10 turns of B & S No. 26 nichrome wire, insulated from the bar by mica or asbestos. The junction wires, encased in fine quartz tubes, were led down and out the bottom of the furnace tube, the heater wires going out the top. A reference junction was inserted into the furnace from below to a point just below the bottom of the test rod but not touching it. Another reference junction, as a spare, was inserted from above to a point about half-way down the specimen but placed near the furnace tube so as not to be affected by the heater at the top of the rod. The junctions could be connected in turn differentially with either of the reference junctions and led directly to the galvanometer (Leeds and Northrup Type R 2500 a). At any particular temperature steady conditions were indicated by the galvanometer readings. (The zero was adjusted to the right hand end of the scale at 30, thus making the whole scale available.) Deflections were differentials between the given junction and the reference. At room temperatures all junctions would read alike at 30. At higher temperatures there was always a residual temperature difference, and initial readings for each junction had to be taken and the heater turned on only when steady readings were obtained. A deflection of 60 divisions meant approximately 6°C. At upper temperatures the deflection for the bottom junction was very small, while that for the top junction (No. 1) might be as much as 20 divisions. The elimination of this gradient while desirable was not necessary. Also a slight drift of all junction readings due to temperature drift had to be tolerated and corrected for.

PROCEDURE

When all junctions show fairly steady condition, the time is noted, and the readings from top to bottom of the specimen and back again are recorded and again the time noted. This is repeated several times in order to determine the drift. Then the time is again noted, the heater turned on and, after about three minutes, the readings again taken from top to bottom and back and the time noted before and after. This is immediately repeated, and then the switch is opened. The cooling data are immediately obtained, using the top junction and taking readings every half minute. The readings should all be taken within about ten minutes from the time of closing the heater switch, otherwise the reference points become uncertain. Only the cooling data from the top junction are significant, the other junctions indicating too low a rate because of the inflow of heat from the upper part of the bar. The cooling rate for the top junction (which is about 4 cm from the top of rod) is approximately corrected with respect to the heat flow down the rod although for the first minute even this rate is low. This shows up on the dT/dt, T curve which is a straight line except possibly for the first few points. We have now two sets of data, the gradient data and the cooling data. The actual temperature is observed by connecting one of the reference junctions (or any junction) to a potentiometer. The gradient data and the cooling data are now plotted. First the temperatures (galvanometer deflections) are plotted for the gradient data, the deflections as ordinates, the distances down the rod as abscissa, taking the position of the top junction as $x=0$. This is the T, x curve. Slopes of this curve are measured graphically and the dT/dx, x curve plotted. Then the slopes of this curve are measured and the d^2T/dx^2, x curve plotted. The cooling data are plotted giving the T, t curve (T as ordinates and t (time) as abscissa). The slopes of this curve are measured and plotted, dT/dt as abscissa, T as ordinates. Corresponding* values of dT/dt and d^2T/dx^2 for the various values of T are plotted, d^2T/dx^2 as ordinates, dT/dt as abscissa. The straight lines usually go through the origin but not always. The constant value of $dT/dt/d^2T/dx^2$ is called m (actually the reciprocal of the slope considering the way the curves are plotted), and $m=k/\sigma\rho$, where k is the thermal conductivity, σ the specific heat, ρ the density. k is thus determined if σ and ρ are

* Corresponding values are values for the same temperature T. dT/dt values are read directly, but d^2T/dx^2 is found by finding the value of x for the given T (on the T, x curve) and for this value of x moving vertically to the value of d^2T/dx^2.

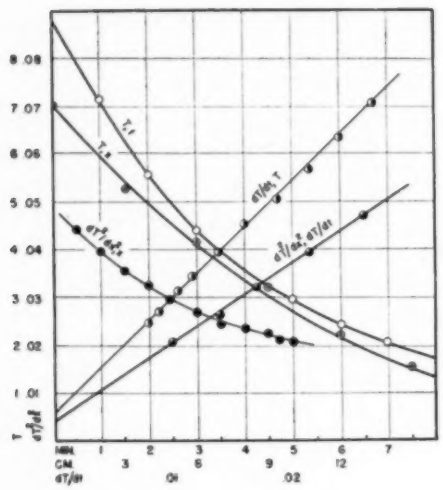

FIG. 1. Sample set of data for thermal conductivity of aluminum at 650°C.

known. Figure 1 is a sample of the plots. A similar set of curves is obtained for each value of k determined.

THEORY

This is the old Forbes method described by Forbes in 1868. The difference in the heat flowing down the rod at one level and out at a slightly lower level is $kA(dT/dx)_1 - kA(dT/dx)_2$, and this difference is $\sigma\rho AldT/dt$. A, the cross section cancels, l is the difference between the two levels, and

$$\frac{(dT/dx)_1 - (dT/dx)_2}{l} = d^2T/dx^2.$$

The equation is

$$\sigma\rho dT/dt = kd^2T/dx^2$$

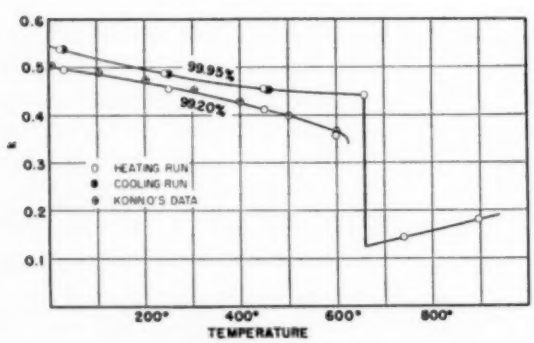

FIG. 2. Thermal conductivity and temperature of aluminum.

or

$$dT/dt = \frac{k}{\sigma\rho} d^2T/dx^2.$$

This calls for a straight line through the origin. Often the curve does not go through the origin. In taking the data one has to compromise—one cannot wait until conditions are completely steady. The reference junction readings are slowly changing, and hence one must be satisfied even though the temperatures are still slightly rising. This introduces a term $\sigma\rho dT/dt_H$ on the left side of the above leading to the equation

$$\frac{dT}{dt_C} = \frac{k}{\sigma\rho}\frac{d^2T}{dx^2} - \frac{dT}{dt_H}.$$

$\sigma\rho dT/dt_H$ is the residual heating, $\sigma\rho dT/dt_C$ is the observed cooling. Careful study of the data shows that the intercept is thus accounted for.

When measurements in the liquid state are desired the specimen must be contained in some inert container. In this work graphite was used —a long cylindrical crucible being bored out of a graphite electrode. The walls were about 3 mm thick, and the junctions were placed in small holes drilled into these walls but not clear through. The wires encased in quartz tubes were tied on with threads, the silocel packing holding them in place when the threads burned away. The heater was wound on the graphite cylinder (insulated with mica) and measurements made as before. The equation now is

$$\sigma_a\rho_a A_a dT/dt + \sigma_g\rho_g A_g dT/dt = k_a A_a d^2T/dx^2 + k_g A_g d^2T/dx^2$$

or

$$\frac{dT}{dt} = \left[\frac{k_a A_a + k_g A_g}{\sigma_a\rho_a A_a + \sigma_g\rho_g A_g}\right]\frac{d^2T}{dx^2}.$$

If one takes account of the slight heating, the term dT/dt_H is to be subtracted from the right side as above. The subscripts refer to aluminum and graphite. Values of $\sigma_a\rho_a$ were obtained from *The Aluminum Industry* or determined experimentally. The latter was necessary for the graphite. For this purpose observations were made as above on a graphite rod at room temperature and at 700°C. This gave values of $k_g/\sigma_g\rho_g$. $\sigma_g\rho_g$ was obtained by an auxiliary experi-

ment in which a graphite rod with an axial heater was held at various temperatures and the watts input noted. Later cooling curves were taken through these temperatures. The equation $\sigma_a\rho_a AldT/dt = VI/4.18$ permits the computation of $\sigma_v\rho_v$.

RESULTS

The values of the thermal conductivity of aluminum (99.95 percent) are as follows: at 25°C, 0.538; at 240°C, 0.486; at 250°C, 0.486; at 450°C, 0.452, 0.456; at 650°C, 0.445; at 740°C (liquid), 0.143; at 900°C (liquid), 0.180. For the aluminum (99.2 percent**) the values are: at 25°C, 0.500; at 245°C, 0.457; at 450°C, 0.414; at 590°C, 0.365. These values are shown graphically in Fig. 2, together with Konno's points. The error in these values does not exceed ±.005, assuming the accuracy of the values of $\sigma\rho$ (taken from *The Aluminum Industry*). The 99.95 specimen shows higher conductivity throughout, and the change with temperature is a decrease paralleling the change for the commercial specimen. Figure 3 shows the data for the c.p. specimen plotted to test the relation $k/\rho C = K(1/T)+K'$. This relation is found to hold with the intercept, K', the same for the solid and liquid phase, exactly as was found for tin, lead, and zinc.[3] (C in this equation is the atomic heat.) Since only two points were found for the liquid state it probably is more proper to state that the data are at least consistent with this equation.

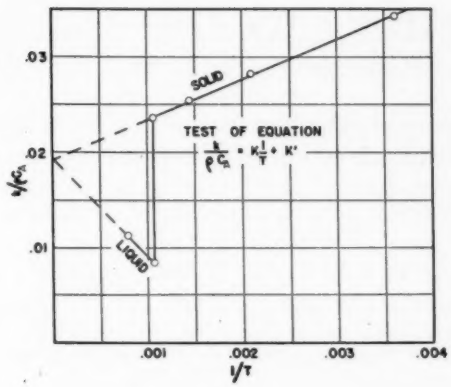

FIG. 3.

THERMAL CONDUCTIVITY OF GRAPHITE

The thermal conductivity of graphite as here determined was found as 0.30 at 25°C. Buerschaper[4] finds 0.26 for radial and 0.40 for longitudinal, while Powell and Schofield[5] find 0.34 at this temperature. The value here found for 700°C, 0.123, is consistent with an extrapolation of the data of the above observers.

ACKNOWLEDGMENT

The aluminum specimens and the analyses were furnished by The Aluminum Company of America together with a grant of funds to facilitate this work. For this help the authors express their appreciation to this Company.

** Analysis of the 99.2 percent specimen: Si 0.10 percent, Fe 0.67 percent, Cu 0.01 percent, Mn <0.01 percent, Mg <0.01 percent.

[3] Bidwell, Phys. Rev. **58**, 561 (1940).

[4] Buerschaper, J. App. Phys. **15**, 452–454 (1944).

[5] Powell and Schofield, Proc. Phys. Soc. **51**, 153–172 (1939).

Letters to the Editor

Stabilization, Tempering, and Relaxation in the Austenite-Martensite Transformation *

J. H. Hollomon,† L. D. Jaffe, and D. C. Buffum
Watertown Arsenal Laboratory, Watertown, Massachusetts
Received May 12, 1947

TRANSFORMATION in steels of the face-centered cubic phase, austenite, to the body-centered tetragonal phase, martensite, ordinarily takes place only during cooling. The temperature (Ms) at which the transformation begins is independent of the cooling rate. The extent of transformation at any temperature below Ms is less, the lower the cooling rate.[1] Moreover, holding at a constant temperature below Ms decreases the extent of transformation on subsequent cooling to a fixed lower temperature.[2] This phenomenon, termed stabilization, is believed to arise from a change in microstresses with time. This change might result from (*a*) decomposition of the metastable martensite (tempering) and consequent dimensional change, or (*b*) stress relaxation (viscous flow) of microscopic regions.

Specimens of a quenched steel containing 1 percent C, 1.5 percent Cr, were stabilized at various temperatures and times. The specific volume at room temperature (*R.T.*) was then determined before and after cooling to −196°C. The results (Fig. 1) indicate that the time and temperature

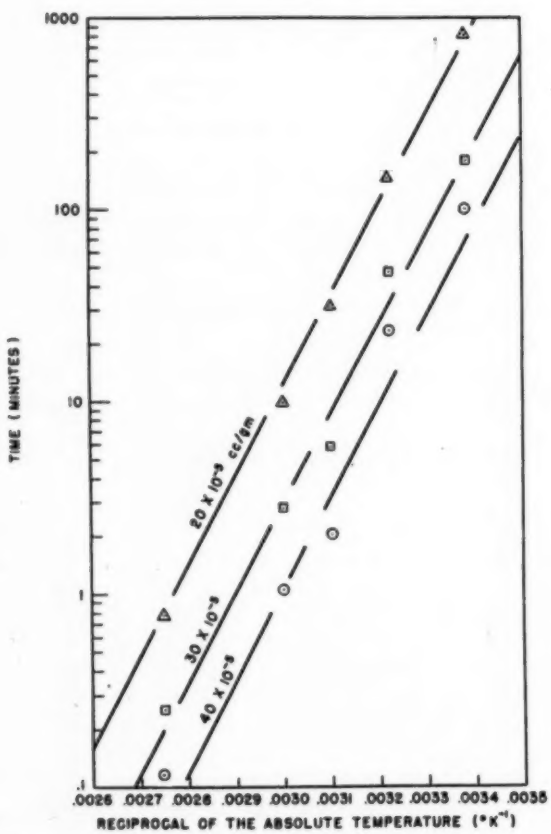

FIG. 1. Relation between time and temperature of stabilization for a fixed change of specific volume upon subatmospheric cooling.

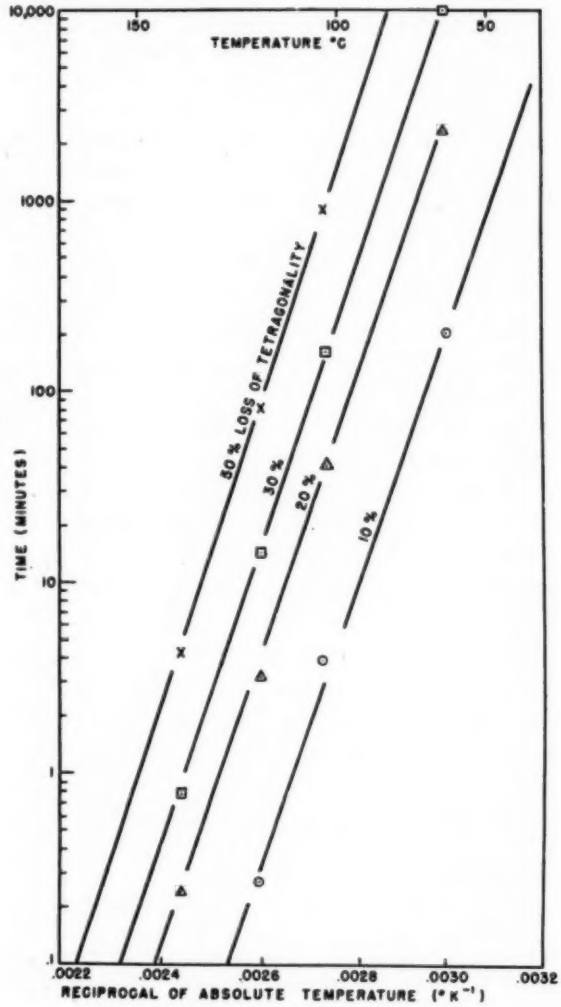

FIG. 2. Relation between time and temperature for fixed loss of tetragonality.

for a fixed degree of stabilization are related through an activation energy of about 21,500 cal./mole.

Specimens of a quenched plain-carbon, 0.95 percent C, steel were cooled to −196°C, then tempered at various temperatures and times. The tetragonality, $c/a-1$, of the martensite lattice at *R.T.* was determined by x-ray diffraction methods. The results (Fig. 2) indicate an activation energy of 34,000 cal./mole for the first stage of tempering.

Rods of quenched plain-carbon steel, 1.25 percent C, were heated to 100°C and twisted a fixed amount, not enough to cause permanent set. After holding 30 min., the specimens were cooled to lower temperatures and released. The anelastic twisting, measured as a function of time

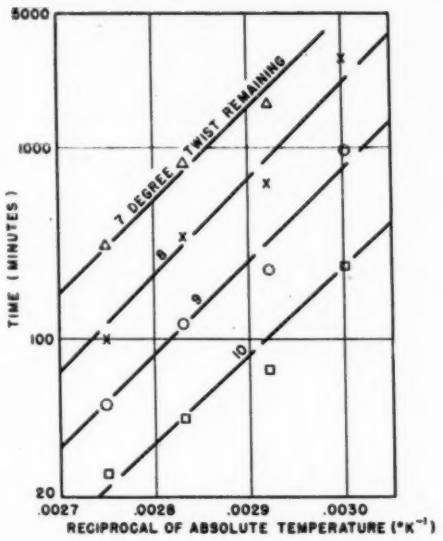

FIG. 3. Relation between time and temperature of untwisting for a fixed amount of untwisting. Twisted 30 degrees at 100°C. Held 30 minutes.

(Fig. 3), corresponds to an energy of about 22,500 cal./mole for stress relaxation. The energies observed for stabilization and relaxation are approximately equal to that reported [3] for stress relaxation in plastically deformed iron (ferrite).

Different steels were used for the different tests to obtain the required accuracy. However, changes in steel composition are unlikely to affect the activation energies materially, particularly in the light of the above agreement between the heats of activation for stress relaxation. It is concluded that stabilization in the austenite-martensite reaction does not arise from tempering of martensite, and probably arises from stress relaxation. Apparently, the relaxation centers responsible for stabilization are produced by local plastic flow caused by austenite-martensite transformation and perhaps by non-uniform thermal contraction.

This work will be discussed in detail elsewhere.

* The statements and opinions in this letter are those of the authors and do not necessarily express the views of the Ordnance Department.

† Now at General Electric Research Laboratories, Schenectady, New York.

[1] J. A. Matthews, Trans. A.I.M.E. **71**, 568 (1925).

[2] G. Tammann and E. Scheil, Zeits f. anorg. allgem. Chemie **157**, 1 (1926).

[3] W. A. West, Tech. Pub. 1993, A.I.M.E., Metals Tech. **13**, No. 5 (1946).

Remarks on Compressive and Tensile Strengths

Concerning a Paper by P. W. Bridgman

STANLEY THOMPSON
North American Aviation, Inc., Los Angeles, California

April 9, 1947

IN a recent paper[1] Bridgman has discussed a series of tests on the effect of hydrostatic pressure on the fracture of brittle materials. The remarks of this letter are considered pertinent to Bridgman's paper, since they explain some of the anomalies mentioned.

Tests to failure in compression by Föppl[2] indicate that the magnitude of the compressive strength, as well as the type of failure observed, depends markedly on the end conditions of loading. Föppl tested his specimens under two end conditions of loading, lubricated and unlubricated loading faces; and with two types of compressive loading, one-dimensional and two-dimensional. With a specimen of concrete, the compressive strengths in the four cases were related as shown in Fig. 1.

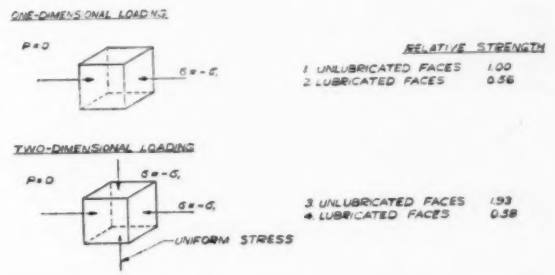

FIG. 1.

With the surfaces unlubricated, failure occurred by breaking off wedge-shaped pieces, while with lubricated surfaces failure occurred in planes parallel to the direction of compression—as if a tension existed at right angles to the direction of compression—with almost the same load for the one-dimensional case as for the two dimensional. The variation between lubricated and unlubricated surfaces is attributed by Föppl to the effect of shear stress across the loading faces. Since a compressive specimen must be comparatively short to prevent buckling, the end conditions are rarely negligible.

For an analysis of the type of failure produced and a prediction of the comparison between compressive and tensile strengths, it is desirable to consider the load systems shown in Fig. 2. Figure 2(a) shows a two-dimensional compressive loading ($-\sigma_1$); Fig. 2(b) shows a hydrostatic pressure, numerically equal to the compressive loading of Fig. 2(a) on which is superimposed a one-dimensional tensile loading numerically equal to the hydrostatic pressure. Neither the theory of elasticity, nor any test, can differentiate between these two loading systems, since they are physically identical.

In that which follows, aside from the entire equivalence of load systems (a) and (b) in Fig. 2, one assumption is made: the equivalence of breaking stress under one- and two-dimensional loading, as found experimentally by Föppl for lubricated loading faces, and as predicted by the

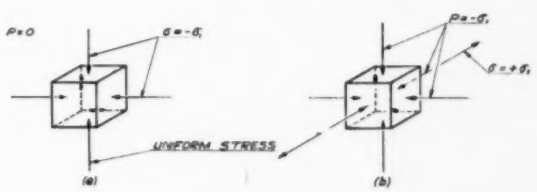

FIG. 2.

semi-empirical shear and octahedral-stress theories. As a result any given one-dimensional compressive breaking stress ($-\sigma_1$) superimposed on a given hydrostatic pressure ($-P_1$) is equivalent to a one-dimensional tensile breaking stress ($+\sigma_1$) of equal magnitude superimposed on a hydrostatic pressure ($-P_1-\sigma_1$). A plot satisfying this condition of breaking stress $\sigma(P)$ against hydrostatic stress P is shown schematically in Fig. 3. Positions above the horizontal axis represent tensile breaking stresses, those below compressive breaking stresses; positions to the right of the vertical axis represent hydrostatic tensions (triaxial tension), those to the left, hydrostatic pressure (triaxial compression). Tensions are considered positive, compressions negative. It should be noted that σ_P is zero when P is positive, which corresponds to failure under hydrostatic (triaxial) tension only.

The relationship shown in Fig. 3 can be expressed mathematically by the equation

$$f(P)=-g(P+f), \tag{1}$$

where $f(P)$ represents either branch of the curve for breaking stress σ_P, and $g(P+f)$ represents the other branch.

It is interesting to compare the slope $df(P)/dP$ of the branch $f(P)$ at any abscissa P with the slope $dg(P+f)/d(P+f)$ of the branch $g(P+f)$ at the corresponding $(P+f)$. From Eq. (1):

$$\frac{dg(P+f)}{d(P+f)}=-\frac{\dfrac{df(P)}{dP}}{1+\dfrac{df(P)}{dP}}. \tag{2}$$

These slopes correspond to the pressure coefficients of stress for the two branches of the curve. It can be concluded from Eq. (2) that a pressure coefficient of tensile strength at P between 0 and 1 corresponds to a pressure coefficient of compressive strength at $(P+f)$ between 0 and ∞, and the coefficient for compressive strength is always the larger.

Bridgman reports that "the effect of hydrostatic pressure is markedly greater in increasing the compressive strength of glass than in increasing its tensile strength." Equation (2) and Fig. 3 give a measure of this effect for any function $f(P)$. If either the compressive or tensile breaking stress is known experimentally as a function of hydrostatic stress, the other may be obtained without experiment by use of Eq. (1) or Fig. 3.

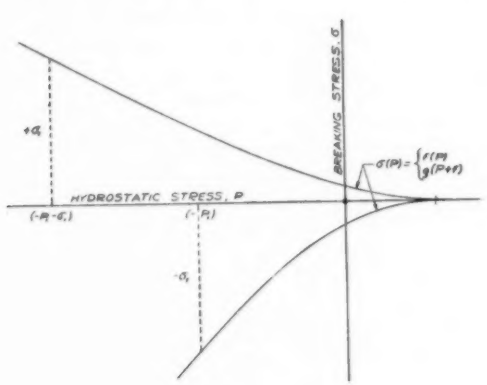

FIG. 3.

Since actual compressive failures of homogeneous materials under hydrostatic pressure cannot occur, it is concluded that failure of a material under compressive loading, in one or two directions, will occur in a manner typical of tensile failures for that material under corresponding hydrostatic pressure. Any departure from this type of failure, or from behavior predicted by a plot similar to Fig. 3, is a measure of the experimental departure from idealized end conditions or inhomogeneity of material. It is believed that the angular fracture of glass in simple compression when supported by hydrostatic pressure, shown in Bridgman's Fig. 3, may be due to the end effects investigated by Föppl and that the numerical results thus obtained for compressive strength are unreliable.

[1] P. W. Bridgman, J. App. Phys. **18**, 246 (1947).
[2] A. Föppl, Mitteilungen ausdem Mech. Tech. Lab. in München (1900).

Reply to "Remarks on Compressive and Tensile Strengths"

P. W. BRIDGMAN
Harvard University, Cambridge, Massachusetts
April 22, 1947

THANK you for letting me see the remarks by Stanley Thompson on my paper on brittle fracture under pressure. These remarks are interesting as showing the consequences of carrying through to a mathematical conclusion the implications of a literal acceptance of the results of the equivalence of one and two dimensional loading in compression. I think, however, that one would not expect the bearing on the experimental situation to be any too close. Föppl's results were obtained only for a single material of not very typical properties, namely, cement and furthermore were obtained only at atmospheric pressure. In developing his mathematics Thompson had to make an additional assumption not covered by the experiments of Föppl, namely, that the equivalence of one and two dimensional compression would continue to hold if the experiment were performed in a medium to which any hydrostatic pressure whatever is applied in addition to the compressions. I very much question whether this is legitimate. One of the conclusions that could be drawn is that when the effects of terminal friction are eliminated, only one type of fracture occurs, the same under simple tension as under simple compression. It is tacitly assumed that this type of fracture is the simple tension type, but I can see no intrinsic reason in the argument for preferring this to the ordinary simple compression type except the highly special experiments of Föppl. The point of view of Thompson also commits him to the position that the same type of fracture will prevail along the entire course of both the upper and lower

branches of the curves in his Fig. 3. This seems to me highly improbable.

Of course I will have to admit that there is some justice to his last sentence, namely, that terminal friction modifies the figures for the fracture stresses that would be given by using only the figures for hydrostatic pressure and compressive stress. But, I think the modification would not be large, and I think the effect is in the wrong direction. The most complete fracture experimentally was obtained near the ends, where the effect of friction in fictitiously raising the strength is the greatest according to Thompson's suggestion. If this is correct it seems to me that fracture should have occurred first at the center and should have been most complete there. Furthermore, I think substitution of the numerical values into a diagram like his Fig. 3, both for glass and Carboloy, would show that a rather improbable state of affairs is demanded.

Certain aspects of Thompson's analysis of the stress system into hydrostatic pressure and superposed simple stresses are much like my analysis in Mechanical Engineering, February 1939, in which similar questions are discussed.

European Induction Accelerators

ROLF WIDERÖE
Zürich, Switzerland
(April 21, 1947)

I have read with interest in the January number of this journal H. F. Kaiser's account concerning "European Induction Accelerators" and should be grateful if you would allow me to augment and also to correct some of the statements contained therein.

First of all, as regards the historical data concerning the development of the betatron: in the autumn of 1922 I had already invented the "ray transformer" (my own designation for the electron induction accelerator) in Karlsruhe during my studies there, quite independently of Slepian. In 1925 I applied for a German Patent on this invention, but this patent application was subsequently abandoned. After the completion of my experimental work under Professor Rogowsky in Aachen (1925–1927),[1] it was only in the autumn of 1942 that I learned of the work done by Kerst and other investigators in the meantime.[2] Subsequently, up to June 1943 I was able to make a number[3] of inventions during my work at the Norsk Elektrisk Brown Boveri in Oslo, these inventions being confiscated in the autumn of 1943, however, by the German authorities. Slepian's U. S. Patent, which had not been mentioned by Kerst in his first publication, only came to my knowledge accidentally some time later, so that it appears to me that Slepian's proposals can only have been of slight importance as regards the development of the induction accelerator.[4]

In Kaiser's account it is stated that the formula for the average electron ray current was found by me. This is an error, and in my work[5] it is clearly stated that this formula and its derivation originate from Kerst. According to this formula it should not be possible to obtain an appreciable amount of γ-rays with a 15-mv transformer at such a low frequency as 50 cycles. With $\Delta r = 2$ cm and $dr = 0.1$ cm, for instance, the formula gives an injection voltage of about 170 v and an average current strength of only about 0.0085 μA. Compared with this we used an optimum injection voltage of 7–10 kv and attained an average current of about 0.03 μA, the maximum obtainable current strength for this injection voltage being probably about 10 times higher. The remarkable fact that small ray transformers can still be operated to advantage with such a low frequency as 50 cycles was entirely novel in 1944 and certainly represents the most important result obtained from the work performed in Hamburg.

Our experimental results obtained with the 15-mv transformer can, as shown by Touschek and myself, be explained by elaborating the original Kerst-Serber assumptions.[6] When in accordance with our theory the electron source is placed inside the potential channel of the stabilizing forces, the efficiency of the electron injection can be calculated approximately from:

$$\eta = \mathrm{Eksp}\left(\frac{-16\sqrt{2}}{3\pi^2}\frac{Ui}{\Delta U}\left(\frac{b}{2\Delta r}\right)^{\frac{1}{2}}\arcsin\frac{h}{2\Delta z}\right),$$

where

Ui = injection voltage
ΔU = induced voltage per turn
b = width of electron source
h = height of electron source
Δr = radial oscillation amplitude of electrons
Δz = axial oscillation amplitude of electrons.

If the electron gun is located outside the potential channel ("injection from outside"), the efficiency of the electron injection will depend on the divergency of the injected electron beam, because only very small deviations from the optimum direction of injection are permissible for catching the electrons. With the 15-mv transformer, the angular deviation for $Ui = 10$ kv may for instance only amount to about 0.16°–0.32°. It can be shown that in this case the efficiency of the injection in first approximation will be proportional to:

$$\left(\frac{\Delta U}{U_i}\right)^x \text{ where } \tfrac{1}{2} \leqq x \leqq \tfrac{3}{4}.$$

In conclusion I should like to state that our work in Hamburg was performed quite independently and without knowledge of that done by Siemens-Reiniger and other investigators. An account given at a mutual discussion in Erlangen (Nov. 1944) concerning the favorable results obtained by us with the 50-cycle ray transformer probably may have given the impetus for the later construction of corresponding 50-cycle apparatus by Siemens.

[1] Described in Achiv für Elektrotechnik **21**, 387 (1928).
[2] Phys. Rev. **59**, 110 (1941); **60**, 47 (1941).
[3] E.g., "Premagnetising the control field," German Pat. Appl. W 113740 VIIIc/21g. "Elimination of the air gap by reverse magnetisation," German Pat. Appl. W 113763 VIIIc/21g. "New injection system for electrons," German Pat. Appl. W 113563 VIIIc/21g. "Electron lenses," German Pat. Appls. W 113742 and W 113925 VIIIc/21g.
[4] I presume that the well-known phenomenon of an electrodeless annular discharge, developing in a poor vacuum chamber under the influence of high frequency magnetic fields, provided the first impulse for my own inventions.
[5] Archiv für Elektrotechnik **37**, 391–408 (1943).
[6] A detailed report of this work will shortly appear in the "Schweizer Archiv."

Direction of Maximum Crystal Elongation during Metal Cutting*

G. H. Townend
Metropolitan-Vickers Electrical Company, Ltd., Manchester, England
March 17, 1947

IN an interesting paper by Dr. M. E. Merchant on "Mechanics of the Metal Cutting Process,"[1] an error was made in the expression connecting shear angle, rake angle, and direction of maximum crystal elongation (Eq. (1), page 269). I have written to Dr. Merchant and he confirms the new expression derived below.

Let α = rake angle,
ϕ = the angle between the shear plane and the surface of the workpiece.

Consider a section of the workpiece $ABCD$ such that $<CBD = 90°$. Then after shearing this section will become the parallelogram $BFEC$. The dimension perpendicular to the shear plane must be unchanged during shearing.

$$\therefore \quad BD = BH = a.$$

Consider a line CG in the chip making an angle ψ with the plane of shear. Then the corresponding line in the workpiece is DJ. The condition that CG shall be the direction

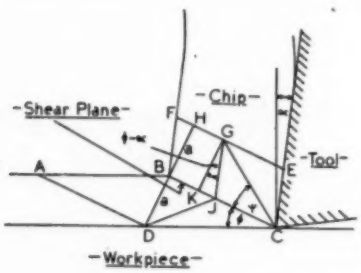

FIG. 1.

of maximum crystal elongation is that CG/DJ is a maximum.

$$CG = a \operatorname{cosec}\psi,$$
$$DJ = \{a^2 + (a\cot\phi - a\cot\psi + a\tan\langle\phi-\alpha\rangle^2)^2\}^{\frac{1}{2}}.$$

The condition is that

$$\{\sin^2\psi + (\cot\phi\sin\psi - \cos\psi + \tan\langle\phi-\alpha\rangle\sin\psi)^2\}^{-1}$$

is a maximum. That is,

$$\sin^2\psi + \{\sin\psi(\cot\phi + \tan\langle\phi-\alpha\rangle - \cos\psi)\}^2$$

is a minimum. Let

$$\cot\phi + \tan\langle\phi-\alpha\rangle = \epsilon,$$
$$\epsilon^2\sin 2\psi - 2\epsilon\cos 2\psi = 0.$$

If $\epsilon \neq 0$

$$2\cot 2\psi = \epsilon,$$
$$2\cot 2\psi = \cot\phi + \tan\langle\phi-\alpha\rangle.$$

Alternatively it is easily shown that a circle on the workpiece becomes an ellipse on the chip and that the principal axes of the ellipse make an angle ψ with the shear plane, where

$$2\cot 2\psi = \cot\phi + \tan\langle\phi-\alpha\rangle.$$

* This letter was published in the May issue of the Journal of Applied Physics, but through an error Fig. 1 was omitted.

[1] J. App. Phys. **16**, 267 (1945).

Here and There

New Appointments

A recent issue of *Science* reported the following new affiliations:

E. C. Watson, Professor of Physics at California Institute of Technology, has been appointed chairman of the Division of Physics, Mathematics, and Electrical Engineering.

C. J. Gorter, Professor of Physics and Co-Director, Physical Institute, University of Leiden, and formerly Zeeman Professor of Physics, University of Amsterdam, is a visiting lecturer at Harvard University for the 1947 summer term. He is conducting one course in advanced dynamics and one in relaxation phenomena. The latter treats magnetic and dielectric absorption and dispersion in alternating fields, a subject in which Professor Gorter has made outstanding contributions.

H. P. Robertson, a member of the faculty of Princeton University since 1928, has been appointed Professor of Mathematical Physics, California Institute of Technology, effective July 1.

Distribution of Concentrated Boron 10

Concentrated isotope boron 10, which enables scientists to make more sensitive neutron-detection tubes and thereby speed up results in atomic research problems, is now available, the Isotopes Branch of the Atomic Energy Commission has announced. However, only a limited quantity is ready for general distribution. Requests will be carefully reviewed and allocations will be restricted to reasonable quantities for the proposed investigation.

Boron 10 atoms are normally quite stable. They have, however, a great affinity for neutrons. When a boron 10 atom captures a neutron it is transmuted into two energetic nuclear particles, one lithium and the other helium. The latter is the well-known alpha-particle. Either particle serves as an excellent trigger for a tube designed to count neutrons. Boron found in nature contains only 20 percent boron 10. Hence a neutron-detection tube five times more sensitive can be made by employing nearly pure boron 10 rather than an equal quantity of ordinary boron. The boron 10 was produced by concentrating the isotope from natural boron in studies of isotope concentration.

Boron 10 will be packaged for shipment in the form of the solid complex boron trifluoride-calcium fluoride. The complex contains 6.9 percent elemental boron, of which 96 percent is B 10. Approximately 6.5 grams of $BF_3 \cdot CaF_2$ are needed to obtain one liter of BF_3 at normal temperature and pressure (assuming 100 percent liberation). The boron trifluoride may easily be released as a gas by heating to temperatures above 260°C in a vacuum.

The price of $BF_3 \cdot CaF_2$ complex is $2 per gram, independent of quantity. Shipping charges will be added to the invoice. There is no additional handling fee per shipment. Standard units of 1, 5, 10, and 50 grams have been packaged in glass containers with moisture-proof plastic

screwtops. Requirements will be filled in single units or multiples of these standard sizes. Clinton Laboratories, Oak Ridge, Tennessee, will act as the supplier.

Exhibit of Technical Photographs

A special section devoted to photographs of technical and scientific subjects will be included again this year in the annual exhibition of the Photographic Society of America. The exhibition will be hung at the Oklahoma Art Center, Oklahoma City, and contributors are invited to submit prints for the technical section prior to September 8. Prints should be mailed to W. F Swann, 343 State Street, Rochester 4, New York

Subject matter may cover any phase of technical photography save pictorial photographs of technical or mechanical operations. Scientific and industrial photographs illustrating original and novel photographic techniques may be submitted. These include photographs in such fields as astronomy, geology, medicine (except diagnostic radiographs), metallography, mineralogy, and physics. Both black-and-white or color photographs are acceptable. Technical data pertaining to each photograph should be lettered neatly in the lower left-hand corner of each mount, if possible, and the maker's name should appear on the face of the mount. There is no limit to the number of prints which may be submitted by a competitor.

Brookhaven Advisory Committee

Dr. Edward U. Condon, Director of the National Bureau of Standards, and Dr. Detlev W. Bronk, Chairman of the National Research Council, have accepted appointments as members of the Scientific Advisory Committee of Brookhaven National Laboratory, Long Island, New York.

Louisville Research Institute Dedicated

The University of Louisville Institute of Industrial Research (affiliated with Speed Scientific School) dedicated its new research building on June 12, 1947.

Herman F. Mark Accepts Belgian Chair

Herman F. Mark, Director of the Institute of Polymer Research and Professor of Organic Chemistry, Polytechnic Institute of Brooklyn, has been invited to accept the Chair Franccki at the University of Liége, Belgium, for the academic year 1947–1948. The guest professorship involves a six-month lecture tour of several Belgian universities.

Spectrochimica Acta Re-Established

The journal *Spectrochimica Acta* has been re-established as an international organ for spectroscopists and spectrochemists, to be published in the Vatican under the editorship of Dr. Alois Gatterer, assisted by a group of coworkers in other countries, as follows: Dr. R. Breckpot of Belgium, Dr. H. Kaiser of Germany, Dr. E. Van Someren of England, and Dr. Lester W. Strock of America. It is expected that the first number of the journal will be ready for press by August 1, and that from six to eight numbers a year will be issued thereafter. Papers in English from America should be submitted to Dr. Strock at 21 Madison Avenue, Saratoga Springs, New York. The official languages of *Spectrochimica Acta* are English, French, and German, and papers will also be accepted in Italian and Spanish.

Second Instrumentation Exhibit

Over ninety manufacturers of instruments and devices for measurement, inspection, testing, and control have already signed up to exhibit their latest developments at the coming second annual Instrument Conference and Exhibit at the Stevens Hotel, Chicago, September 8–12, 1947, sponsored by the Instrument Society of America.

Lehigh to Remodel Two Buildings

Lehigh University is remodelling its physics and chemistry buildings at an approximate cost of $105,000. Work is expected to be completed before the opening of the fall semester. The physics building will be equipped with new laboratories for high voltage x-ray equipment, electronics, electric waves, and optical and spectroscopic work.

Awards

Otto Stuhlman, Jr., Professor of Physics, University of North Carolina, received the Poteat Award at the 64th annual meeting of the North Carolina Academy of Science, May 9–10, in recognition of his biophysical paper "A Dynamical Analysis of the Movements of the Lobes of the Venus' Flytrap."

Presidential Medals for Merit were presented on May 5 to the following scientists for outstanding contributions to the Navy's war effort: John T. Tate, Chairman of Research and Professor of Physics, University of Minnesota; Frederick V. Hunt, Chairman of the Department of Engineering Sciences, Harvard University; Gaylord P. Harnwell, Chairman of the Department of Physics, University of Pennsylvania; and William V. Houston, President of Rice Institute.

Detection of Isotopes by Tracer Micrography

A method for the more effective tracing of radioactive isotopes in materials in which they have been intentionally introduced has been developed by L. Marton of the National Bureau of Standards with the cooperation of P. H. Abelson of the Department of Terrestrial Magnetism, Carnegie Institution of Washington. In this procedure, by means of a magnetic focusing arrangement, the radiation given off by a radio-isotope within a sample material is made to form an image of the emitting surface upon a photographic plate. The image may then be used in studying the distribution and concentration of the radioactive element present in the sample.

In many chemical, biological, biochemical, and other fields of research, there is growing application of the method of tracers, in which the isotope of a given element

is used as an indicator to tag or label certain groups of atoms so that they may be distinguished from other atoms of the same kind. Identification of tracer elements is at present greatly facilitated through the use of radioactive isotopes, which, because of recent developments in atomic energy, are now available in large quantities and are relatively easily detected through their radiations.

In the well-known method of radio autography a radioisotope is introduced in a biological or other system, and the distribution of that particular element within the system is determined by bringing the sample in close contact with a photographic emulsion. This method lacks resolving power, because, even in case of perfect contact of the sample with the emulsion, the circle of confusion from every point of emission is so great that details less than a tenth of a millimeter are very difficult or impossible to distinguish.

In order to improve the resolution of this tracer method, it was decided to use electron optical image formation for determination of the distribution of a radioactive element within a given sample. This process, which may be called "tracer micrography," is based on the emission of high speed electrons (beta-rays) by many tracer elements and the use of magnetic lens elements for forming an image on a suitable recording surface.

In the absence of any means for correction of the chromatic aberration of electron optical lenses, the first micrographs were limited to those elements that emit electrons of uniform speed. After some attempts with columbium 93, yttrium 87, strontium 85, strontium 87, protactinium 233, and gallium 67, the latter was selected for the initial tests. Gallium chloride, prepared by chemical separation from zinc, was bombarded by heavy hydrogen nuclei in the cyclotron at the Carnegie Institution, and the solution was evaporated drop after drop on a $\frac{1}{4}$-inch tantalum disk. Radiation emitted from the surface of the disk, upon passing through a magnetic lens consisting of a small iron-clad coil with Armco iron pole pieces, was brought to a focus on a photographic film at a distance of about $3\frac{1}{2}$ inches. An image of the tantalum disk was thus obtained showing radioactive areas. The conditions were selected so that a linear magnification of 2 was produced.

For calibration of the instrument, the photographic film was replaced by a Geiger counter, and the lens current necessary to produce a maximum number of counts in unit time was determined for radiations of varying velocities. This established the focusing current for a given type of radiation.

In preliminary experiments with samples of different concentration and thickness of the radioactive layer, exposure times ranged from 2 to 12 hours according to the age and concentration of the sample and the numerical aperture of the lens. It was found that micrographs with good definition were obtained consistently when the layer was sufficiently thin to avoid considerable self-absorption. The best resolving power attained so far has been about 30 microns.

The simplicity of this method, both in apparatus and technique, is one of its more important features. Vacuum requirements are very moderate, since the mean free path of the electrons is large in comparison with the apparatus dimensions, even at forepump pressure.

Scientists at the National Bureau of Standards expect to obtain further improvements in tracer micrography through after-acceleration of the beta-particles by means of a homogeneous electrostatic field. Such after-acceleration may well result in reduced exposure time and in better resolution due to a reduction in spherical aberration. A further reason for after-acceleration is that chromatic aberration, which is always present, even in sources emitting particles of uniform speed, can be markedly decreased if the accelerating potential is at least comparable in magnitude to the energy of the primary emission.

Utah Symposium on Sound

In connection with the Utah Centennial Celebration a Symposium on Sound was held at the Salt Lake Tabernacle and the University of Utah on July 21 and 22. Invited papers were presented by eleven academic and industrial experts in the field of sound.

New Books

Scientific Progress in the Field of Rubber and Synthetic Elastomers

INITIATED BY THE LATE ELMER O. KRAEMER, EDITED BY H. MARK AND G. S. WHITBY. Pp. 453, $15\frac{1}{2}\times23\frac{1}{2}$ cm. Interscience Publishers, Inc., New York, 1946. Price $7.00.

This book which is volume II of *Advances in Colloid Science* is a sequel to volume I and describes recent advances in the physics of rubber and synthetic elastomers. The work and plans of the late Elmer O. Kraemer have been admirably carried out by the co-authors, H. Mark and G. S. Whitby.

This book consists of ten chapters on various phases of high polymer physics, each written by specialists; and they have all done an excellent job. In addition, a biography of the late Dr. Kraemer is included with a list of his many publications. Complete author and subject indexes are included. The book contains around 450 pages and over 800 references.

The first chapter or introduction gives some well-known facts concerning the origin, chemical nature, and some of the properties of the cured polymers of both natural rubber and the more common synthetic elastomers.

The second chapter, a real treatise on the subject of second-order transitions, is extremely well written and contains over 125 references. Tables on second-order transition temperatures and brittle points are given for over thirty different plastics, rubbers, and synthetic rubbers. The theory of second-order transitions is elabo-

rated upon with particular reference to the theory of segment rotation. Experimental results, together with factors influencing second-order transitions, make this section of particular value to workers in the high polymer field.

Chapter 3 is an excellent résumé of the past and most recent information and theories on crystallization phenomena in synthetic and natural rubbers. This section contains a complete bibliography of 150 references.

The fourth chapter goes into a study of crystal and molecular structure of high polymers by means of x-ray diffraction methods. There is some duplication of information in this and the previous chapter; however, it is not objectional, as crystallization phenomena are followed in the first instance primarily by dilatometer and other methods, and in the second instance primarily by x-ray diffraction methods.

There are also valuable chapters on thermodynamics of rubber solutions and gels, viscosity of high polymers, kinetic theory of rubber elasticity, vulcanization, rubber photogels, and photo-vulcanizates. The volume fittingly concludes with a chapter on reinforcing agents in rubber.

Some of the newer organic plastics and resins as vulcanizing agents and as reinforcing agents for rubber and synthetic rubbers are not covered in this volume.

The authors are to be congratulated on the general make-up and quality of the chapters on the timely subjects which are covered in this book.

Duplication of information is surprisingly low in a volume covering such a diversity of inter-related subjects by such a large number of authors.

This book will be a welcome library addition to all those interested in the field of high polymer physics.

R. S. HAVENHILL
St. Joseph Lead Company, Monaca, Pennsylvania

Electron and Nuclear Counters—Theory and Use

BY SERGE A. KORFF. Pp. 212, 22×14½ cm. D. Van Nostrand Company, Inc., New York, 1946.

In his book, *Electron and Nuclear Counters—Theory and Use*, Korff has gone a long way towards removing the aura of "magic" from detectors used in the field of nuclear physics. The student desiring to enter this field has had in the past practically no recourse but to learn peculiarities of nuclear detectors the hard way, namely, the trial and error method of making and using them. This same student now has available in this very readable book a fairly complete qualitative account of the operation and construction of ionization chambers, proportional counters, and Geiger counters.

The first chapter is devoted to the history and general operation of particle detectors. Korff points out that the main differences between the ionization chamber, proportional counter, and Geiger counter is the voltage region in which they are operated. The next three chapters give a more detailed account of the operation of these detectors. The last of these chapters, namely, the one covering the Geiger counter, is by far the most detailed and complete since this is the author's special field. Even though they have much theory and operation in common, Korff discusses separately the non-self-quenching counter and the self-quenching counter. Expecially interesting is the discussion of the quenching process caused by the presence of certain polyatomic gases in a Geiger counter. The presence of spurious counts or a continuous discharge in a Geiger counter is interpreted as being caused by the emission of photoelectrons and/or secondary electrons from the outer electrode because of photons or positive ions formed in the discharge striking this electrode. If certain polyatomic gases are present they are found to absorb the photons and neutralize the positive ions of the counter gas, the excitation energy of the polyatomic molecule then being dissipated harmlessly through the process of predissociation.

The last three chapters cover, respectively, the constructional aspects of nuclear counters, statistics of counting random events, and finally the auxiliary electronic circuits involved, such as quenching circuits, scaling circuits, coincidence circuits, and linear amplifiers.

The book contains several erroneous and conflicting statements and at least one incorrect circuit diagram. At one point the author speaks of reducing the alpha-particle background of an ionization chamber through the use of a positively charged grid which "would repel any alpha-particles approaching it and drive them back into the wall." The expression for the percentage of missed counts has been developed in Chapter 6 on the basis of very naive assumptions and is valid only for recovery times small compared to the average time between counts. The Neher-Pickering circuit as presented is obviously not capable of quenching. In several cases the circuits given in the book are not the most up-to-date ones used for that particular purpose.

This book, the reviewer feels, has provided the newcomer with a good way of getting acquainted with the field but does not fill the need for a critical and detailed review of the present status of our knowledge of counter mechanisms. A worker in this field will still have to refer to the literature for a complete and quantitative account.

ERWIN F. SHRADER
Case Institute of Technology

Colloids, Their Properties and Applications

BY A. G. WARD. Pp. 133, Interscience Publishers, Inc., New York, 1946; Blackie and Son, Ltd., Glasgow.

A book on colloid chemistry of this limited size can obviously serve, as the author intended it should, only as an elementary account of recent progress in colloid science, and as an introduction of the subject to those who are unfamiliar with it. In general it accomplishes these aims in a satisfactory manner, and can be recommended highly.

The book has three major subdivisions: I. The Nature of the Colloidal State; II. The Colloidal Systems; III. Colloids in Industry and Living Matter. The treatment throughout is descriptive in nature. The author has tried

to make the field of colloidal dimensions intelligible to the layman by giving all dimensions first in microns and then, in parenthesis, on a scale one hundred million fold enlarged. Thus a particle of tobacco mosaic virus is said to have a length of 0.5 μ (50 meters). This is rather disconcerting to one who opens the book at random, unaware of the convention adopted.

The author points out that the usual tendency to explain trends in scientific progress on the basis of social and economic needs of the community is not valid in the colloid field. The practice of colloid chemistry is one of man's oldest endeavors in such realms as textiles, pottery soils, paints, etc. Colloid science has lagged behind practice mainly because the tools which were needed to explore the colloidal domain are all fairly new. Hence he places special emphasis on these new tools.

It was a pleasure to read this book and see a broad field free from the complex technical and mathematical details which one needs for active work in colloid chemistry.

R. F. BOYER
The Dow Chemical Company

New Booklets

The National Research Council of the National Academy of Sciences, Prevention of Deterioration Center, Room 204, 2101 Constitution Avenue, Washington, D. C., can now offer the *Prevention of Deterioration Abstracts* on a yearly subscription basis. These abstracts are set up under the following headings: electrical and electronic equipment; finished assemblies; fungicides; lacquers, paints, and varnishes; leather; lubricants; metals; microorganisms; optical instruments; packaging; paper; plastics; resins, rubbers, and waxes; storage, textiles; and wood. Items abstracted include journal articles, patents, specifications, unpublished reports prepared by various Army, Navy, and other governmental groups, and unpublished British, Australian, and Canadian reports.

There will be approximately 1500 pages of the abstracts per year. The individual abstracts are in loose leaf form, so that they may be arranged in manner desired by the individual receiving them. Throughout the calendar year, all the abstracts classified under any one heading will be numbered consecutively.

Comments made by the personnel of the Prevention of Deterioration Center are added to many of these abstracts. In these comments attempts are made to relate a specific report with other relevant ones, to evaluate reports, or to make suggestions concerning further needed research.

The price, which includes two binders and index guides, will be $37.50 per year. Two binders are required for one year's subscription. The fiscal year will be from July 1 to June 30. For the year 1946 back issues will be supplied, since these abstracts started in April 1946.

Dow Corning Corporation, Midland, Michigan, has published a new silicone data sheet entitled *Specifications for Rewinding Motors with Silicone Insulation*. 2 pages, free on request.

The Gaertner Scientific Corporation, 1201 Wrightwood Avenue, Chicago 14, Illinois, has announced publication of two bulletins: 157–74, *Divided Circle Spectrometers and Accessories*, 20 pages; 158–74, *Wavelength Spectrometers and Monochromators*, 12 pages. Available free on request.

The Tube Department of Radiq Corporation of America, Harrison, New Jersey, has brought out a revised edition of the *Quick-Reference Chart on Miniature Tubes*. It is form MNT-30A. 4 pages.

North American Philips Company, Inc., 100 East 42d Street, New York 17, New York, has published a two-page chart (R-1066) entitled *Basic Characteristics of Useful Industrial Laboratory Instruments*. Data are presented in a convenient form to facilitate hanging on the wall for ready reference. Free on request.

Littelfuse, Inc., 4757 Ravenswood Avenue, Chicago 40, Illinois, has recently published its first completely new catalog since the beginning of the war. It is a manual of progress in the field of circuit protection, including a brief historical survey of fusing and the announcement of many new developments in the company's line of fuses, fuse mountings, and circuit indicators. The catalog's number is 9.

Dewey and Almy Chemical Company, Boston 40, Massachusetts, has issued a new catalog of *Darex* meteorological balloons, containing many new performance and data charts calibrated in both the English and metric systems. 30 pages. Free on request.

RCA Application Note for May 15, 1947, published by the Tube Department of Radio Corporation of America, Harrison, New Jersey, is entitled *Use of the 2E24 and 2E26 at 162 Megacycles*. 8 pages, available on request.

Interscience Publishers, Inc., 215 Fourth Avenue, New York 3, New York, has published a 50-page catalog of its recent releases in the fields of chemistry, physics, mathematics, engineering, and medicine.

Eastman Kodak Company, Rochester 4, New York, has issued a revised data book on *Infrared and Ultraviolet Photography*. Priced at 25 cents a copy, it is available through all Kodak dealers.